UNIVERSITY OF SOUTHAMPTON

SCHOOL OF ENGINEERING SCIENCES

MATERIALS RESEARCH GROUP

TOUGHNESS-STRENGTH RELATIONSHIPS IN HIGH STRENGTH 7XXX ALUMINIUM ALLOYS

By Nicolas Kamp

A thesis submitted for the degree of Doctor of Philosophy

November 2002

UNIVERSITY OF SOUTHAMPTON

ABSTRACT

FACULTY OF ENGINEERING AND APPLIED SCIENCES
MATERIALS RESEARCH GROUP

Doctor of Philosophy

TOUGHNESS-STRENGTH RELATIONSHIP IN HIGH STRENGTH 7XXX ALUMINIUM ALLOYS

By Nicolas Kamp

While there is now a considerable amount of knowledge in the area of failure analysis of aerospace Al-alloys, the use of higher strength 7xxx alloy for new airframe application requires a more comprehensive understanding of the failure mechanisms at play. As high strength is known to be detrimental for fracture toughness, which is a critical parameter in damage tolerant concepts and aerospace design, it is relevant to analyse the influence of strength, and the microstructural conditions related to this high strength, on toughness.

Systematic material characterisation has been carried out on three high strength 7xxx aluminium alloys in peak-aged and overaged conditions: 7150, Zr-containing 7449 and Mn-containing 7449. Various microstructural features controlling the fracture process were considered: differential scanning calorimetry (DSC) has been used to characterise the content of η/η' strengthening precipitates in the alloys, whilst the amount of coarse intermetallics, and particularly of the undissolved S-phase (Al_2CuMg), was studied via image analysis. The grain structure and grain boundary characteristics (precipitate free zone (PFZ) and grain boundary precipitates) were also assessed. Standard K_{Ic} tests were performed in accordance with ASTM E399. Several failure mechanisms have been revealed by fractographic analysis: coarse voiding at intermetallics, fine tensile voiding and a combined intergranular/transgranular shear fracture mode. In the Zr containing alloys in particular, the increase in toughness with increased overageing is accompanied by a change in fracture mode from predominantly intergranular/transgranular shear failure to coarse voiding. A fracture toughness model was derived based on the microstructurally dependent work hardening factor, K_A, introduced in Ashby's theory of work hardening, combined with the semi-empirical model for plane strain fracture toughness developed by Hahn and Rosenfield. This model predicts a linear relationship between K_{Ic} and $K_A^{0.85}/\sigma_{ys}^{0.35}$ which is shown to be consistent with the experimental data, independent of the failure mechanism.

The application of a recently developed retrogression and reageing (RRA) heat treatment to thick 7449 plates was also studied. The modelling approach considered the temperature within the plate as a function of time, derived from heat transfer models, combined with the influence of the temperature-time profile on the alloy microstructure, evaluated using a equivalent time variable, and showed that the suitable theoretical range of RRA treatment is narrow. Retrogression treatment holding temperature must be between 180°C and 200°C and the heating rate between 10°C/h and 100°C/h.

CONTENTS

Chapter 4-Experimental methods

Chapter 5-Microstructure and mechanical properties: results

Chapter 6-Microstructure and mechanical properties: Discussion

ACKNOWLEDGEMENTS

I would like to thank Drs. Marco Starink and Ian Sinclair for their excellent supervision and encouragement.

Furthermore I would like to thank Pechiney-Rhenalu for the provision of materials. The financial and technical support of DERA (Farnborough) is gratefully acknowledged, especially the personal attention during this work of Dr Peter Pitcher.

The support of the technical staff at the department is gratefully acknowledged; particularly that of E. Bonner, D. Beckett. I would also like to thank Mrs Sue Walker, Gill Rod and Gwyneth Skiller for their kindly help.

Many thanks to all my colleagues in the Materials Research group for their help and friendship: Fabien, Julien, Anne, Yannick, Nick, Yigeng, Nihong, Thomas, Mark, Diccon, Ben, Suresh, Nong, Neil…

Finally, I'd like to express my deep gratitude to Gaynor and to my parents for their full understanding and support.

Chapter 1

Introduction

Reducing cost and/or increasing performance has always been the goal of airframe manufacturers (see e.g. [1]). This can be achieved in the production of aluminium alloys in various ways:

- Weight savings due to enhanced mechanical properties, and hence higher capacity of the aircraft in terms of range, passenger load or freight load.
- Weight savings by reducing density of alloys used, particularly in the development of Al-Li-X alloys.
- Reduction in manufacturing cost.

It is particularly the first approach that has led to the development of the AA7449 alloy [2], which is especially designed for upper wing skin applications (a compression load dominated structure). In its development, Pechiney Rhenalu used both trials and metallurgical simulation of different alloy compositions and heat treatments [3]. Compared to the incumbent 7150-T651 aluminum alloy, AA7449-T651 has a 10% increased strength level. Whilst the increased strength satisfies one key property requirement, progress in the design of structures using Damage Tolerance theory and service experience have shown that enhanced toughness and stress corrosion cracking (SCC) resistance are also critical [1,4]. Apart from the improved yield strength, the AA7449 alloy also possesses an increased resistance to SCC [2]. However, the toughness, and particularly the relationship between the toughness and the microstructural features of this alloy, have not as yet been precisely determined. This is due to the complexity of the microstructure which typically does not allow an independent systematic variation in key parameters to determine their respective influence on the mechanical properties. In the complex Al-Zn-Mg-Cu based commercial 7xxx aluminium alloys, alloy processing parameters are interdependent. For instance, it is well known that increasing the solute content (Zn,Mg,Cu) of these precipitation

strengthened aluminium alloys will raise the maximum attainable yield strength, but, modifying the solute content will also influence grain boundary precipitate formation, quench sensitivity and precipitate free zone formation, all of which can be detrimental to the other mechanical properties. Therefore, progress in 7xxx alloy development must be accompanied by extensive study of the evolution of the mechanical properties in relation to microstructural changes as a whole during commercial alloy manufacturing. For 7449 and 7150 alloy applications, the compromise between strength and toughness properties in different ageing conditions is of particular interest.

Hence, the first aim of the present study is to compare, analyse and model the fracture behaviour of the 7449 and 7150 aluminium alloys and its evolution with ageing treatment in order to elucidate the relationship between the fracture toughness and the alloy microstructural features and strength. As such, a range of experimental tests have been carried out, including (a) mechanical testing: tensile tests, notch tensile studies, arrested crack tests and toughness tests, and (b) microstructural investigation: particularly, differential scanning calorimetry (DSC) experiments; and transmission electron microscopy (TEM). A fractographic study has been carried out to determine precisely the fracture mechanisms and their interaction with microstructural features such as grain and subgrain boundaries and coarse intermetallic particles. These results were subsequently used in the analysis of the fracture process and the modelling of the fracture toughness.

Ageing treatment is a fundamental aspect of precipitation hardened 7xxx alloy manufacturing. In recent years a three-step heat treatment known as retrogression and reageing (RRA) has been developed which gives enhanced SCC resistance properties while retaining commercial strength and toughness level. This ageing treatment has been commercially applied with success to 7xxx alloys. However, RRA treatment parameters, i.e. holding temperatures, heating rates, duration, vary with the 7xxx alloy studied. Furthermore, for thick 7xxx plates, the requirement for property homogeneity throughout the plate adds restrictions on RRA treatment parameters. The application of RRA treatment to 7449 alloys and more specifically to thick 7449 alloy plates is of commercial interest but requires calibration of RRA parameters. Hence, the second aim of this study has been developing an insight into the relationships between heat treatment, mechanical

properties and homogeneity properties. To this end, modelling of transformation using heat transfer models and an internal state variable approach has been implemented to give a systematic approach to RRA treatment calibration.

The present thesis is structured as follows: the main characteristics of the 7xxx aluminium alloys are reviewed in chapter two, including; the use of the 7xxx aluminium alloys in the aircraft industry, precipitation strengthening mechanisms in 7xxx alloys, the relationship between microstructure, strength and toughness properties, and the RRA heat treatment and its implications in the improvement of 7xxx aluminium alloy properties. Chapter three considers the application of fracture mechanics to the determination of plane stain fracture toughness and reviews fracture toughness modelling attempts. The experimental techniques used are detailed in chapter four. The results of the microctructural investigation and mechanical testing are presented in chapter five. The analysis of these results and the modelling of fracture toughness are described in chapter six. Modelling of RRA treatments applied to thick 7xxx alloy plate is developed in chapter seven. Finally, chapter eight presents the main conclusions from this study.

Chapter 2

High strength 7xxx aluminium alloys

2.1 Introduction

The materials investigated in this study are Al-Zn-Mg-Cu based alloys: specifically the 7150 and 7449 compositions. These alloys offer high strength levels and are commonly considered for upper wing skin in civil airframe manufacture.

The standard nomenclature for these alloys as well as their heat treatments is explained in section 2.2. An historical overview of the development of the 7xxx aluminium alloy in the aircraft industry is given in section 2.3.

The 7xxx aluminium alloys are particularly sensitive to precipitation hardening. Their high strength is due to the formation of precipitates during ageing heat treatment following a suitable processing route. The precipitation hardening and processing route background is covered in section 2.4.

The influence of the complex microstructural features of commercial 7xxx aluminium alloys on the strength and toughness is reviewed in section 2.5.

Improved property combinations in 7xxx aluminium alloys can be achieved through optimizing heat treatment. The use of retrogression and reageing (RRA), a relatively novel heat treatment developed to achieve a combination of high strength and stress corrosion cracking resistance, is reviewed in section 2.6.

2.2 Standard nomenclature: alloy and temper

The International Alloy Designation System (IADS) for wrought products, introduced in 1970, is widely accepted (see e.g. [5]). This system gives each wrought alloy a four digit number of which the first digit is assigned on the basis of the major alloying element. Hence, the 7xxx series is associated with zinc and magnesium as major

alloying elements.

The second digit commonly indicates purity or alloy modification. A zero indicates an early alloy specification; integers 1 to 9 refer to alloy modification, all alloys exhibiting a close relationship.

The IADS system also deals with temper designation in order to specify mechanical properties of an alloy and the way they were achieved. The system designates each temper with a letter and digits added as suffix to the alloy number. A summary of temper designation is presented in Table 2.1. Stress-relieved wrought products are designated by additional digits; e.g. the Tx51 temper refers to alloys stress-relieved by stretching (0.5-3% for a plate) and in the same way Tx52 refers to alloys stress-relieved by compression; Tx53 is stress-relieved by thermal treatment.

The most commonly used heat treatments for wrought 7xxx alloys are T6 and T7. T6 represents a temper design to achieve the peak strength of the alloy. T7 is an overaged temper. Several overageing temper have been developed for commercial use, they are differentiated by a second digit. The most widely used overageing tempers for aluminium alloys in the aircraft industry are T73 and T76.

Letter	Condition	Digit	Properties
F	As Fabricated		
O	Annealed-wrought products only		
H	Cold work	**1**	Cold worked only
		2	Cold worked and partially annealed
		3	Cold work and stabilized
W	Unstable temper ages spontaneously at room temperature after solution treatment		
T	Heat treated (stable)	**1**	Partial solutionizing+natural ageing
		2	Annealed-cast products only
		3	Solutionize+cold work
		4	Solutionize+natural ageing
		5	Artificially aged only
		6	Solutionize+artificial ageing
		7	Solutionize+stabilizing
		8	Solutionize+cold work+artificial ageing
		9	Solutionize+artificial ageing+cold work

Table 2.1: Temper designation system.

2.3 Historical overview of the 7xxx aluminium alloys in the aircraft industry

Al-Zn-Mg based aluminium alloys were first developed in the 1920s in Germany (see e.g. [6]). Development was driven by their relatively high static strength. The first use for aircraft wings was achieved in 1938 with the X74S alloy (5.2%Zn, 2.1%Mg, 1.5%Cu, 0.4%Mn), although this alloy was susceptible to SCC. Further development used an empirical approach, e.g. additions of Cr were made to the X74S alloy to obtain a higher resistance to SCC, although the underlying physical mechanisms were not well understood at the time. This led to the release of the 7075-T6 alloy (5.1-6.1%Zn, 2.1-2.9%Mg, 1.2-2%Cu, <0.3%Mn, <0.4%Si, <0.5%Fe) in 1943, used as sheet for the skin and the stringers of the upper wing skin of a late version of the B-19 Super Fortress, with a weight saving of over 180kg per airplane. Sheet, extrusions, forging and plate were available by 1946. The crash of three Comet jet airplane manufactured with 7075 type alloy in the 1950s highlighted the need for damage tolerance approach in material selection [7].

The demand of aircraft designers for improved strength, corrosion resistance and fracture resistance has lead to numerous advances in composition and heat treatment of 7xxx aluminium alloys. The two step T73 overageing treatment was developed following experiments which showed that ageing at temperatures above 150°C increased the resistance to SCC in the short transverse direction and that adding a first ageing step near 120°C minimized the strength loss of the aforementioned step. The first application of the 7075-T73 appeared in the DC10 aircraft [5]. Further heat treatments were developed to respond to specific problems, such as the T76 overaged temper used to address the issue of exfoliation corrosion.

As effects of the alloying elements became better understood, new alloys containing optimized combinations of these elements were studied. Under the sponsorship of the United States Naval System Command and the United States Air Force Materials Lab., from among 28 candidates an optimized alloy for property balance was released in 1971 as 7050 (6.2%Zn, 2.3%Cu, 2.25%Mg, 0.1%Zr). It became the main construction material of the F18 and was used in many other aircraft. At this time Boeing was looking for a high strength alloy to replace the 7075-T6 used for their upper wing

skins. The 7150-T6, a slightly modified 7050 alloy, proved to be successful and was used as extrusions and plate for Boeing's 757 and 767 aircraft.

Challenging technical and cost specification for new plane such as the Airbus A380 have led Pechiney Rhenalu to produce the 7449 alloy which is particularly suited in T651 and T7951 conditions for compression dominated structures such as the upper wing skin and in T6511 and T79511 for upper wing skin stringers [8]. Improved dimensional tolerances are also achieved through good age forming capability of the alloy in overaged temper T7951 and T7651 [9].

2.4 Precipitation strengthening of 7xxx alloys

2.4.1 Processing route

The mechanical properties of 7xxx alloys are achieved through a multistage processing route. Commercial processes are usually optimized for each alloy. The thermomechanical treatment of a conventional commercial alloy consists of five basic steps [10]:

- Homogenisation: After casting, ingots have a microstructure characterised by inhomogeneous concentrations of alloying elements, and the presence of coarse precipitates. Homogenisation heat treatments (typically around 470°C) are designed to reduce the amount of coarse precipitates by dissolving them and to homogenise the distribution of elements within the cast dendrite structure by diffusion.

- Hot rolling: During hot rolling the coarse cast grain structure is broken up to form a finer grain structure orientated in the rolling direction. Rolling also separates intermetallic clusters to some extent, leading to bands of intermetallics orientated in the rolling direction.

- Solutionizing: To obtain a solution of the alloying elements from which an

optimised hardening precipitation will occur, solution treatment is performed typically at 470-475°C for 7xxx alloys (7xxx alloys achieve complete solid solubility in the range 455°C-530°C [11]). Solutionising is designed to dissolve deleterious phase such as η (Mg_2Zn), T (Al_6CuMg_4) and S (Al_2CuMg).

- Quenching: The alloy is rapidly cooled to obtain a supersaturated solution of both vacancies and alloying elements.

- Ageing or precipitation hardening heat treatment: This leads to a decomposition of the supersaturated solution resulting in a fine dispersion of precipitates. Prior to this step commercial plates may also be stress relieved by stretching (which may also provide a degree of work hardening and dislocations for heterogeneous precipitation).

Precipitation reactions depend also on the composition of the alloy. In this sense, the Al-Zn-Mg-Cu system is complex [12,13,14]. Several examples of phase diagrams are given in Fig. 2.1.

a)

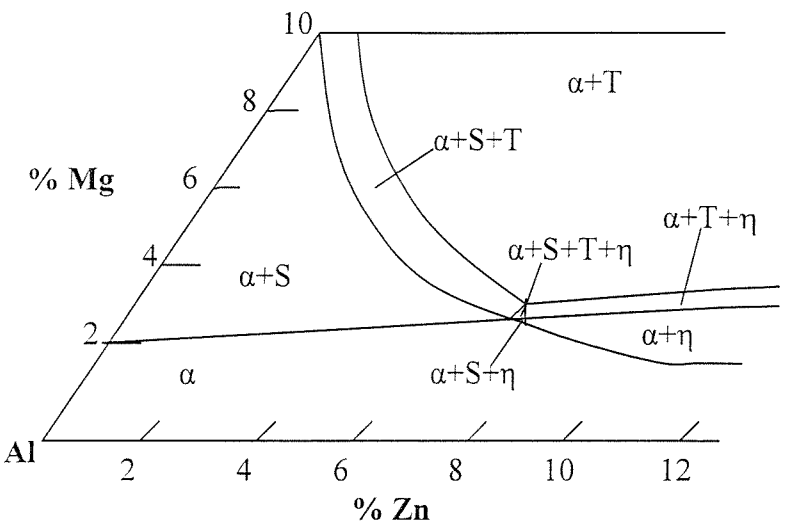

b)

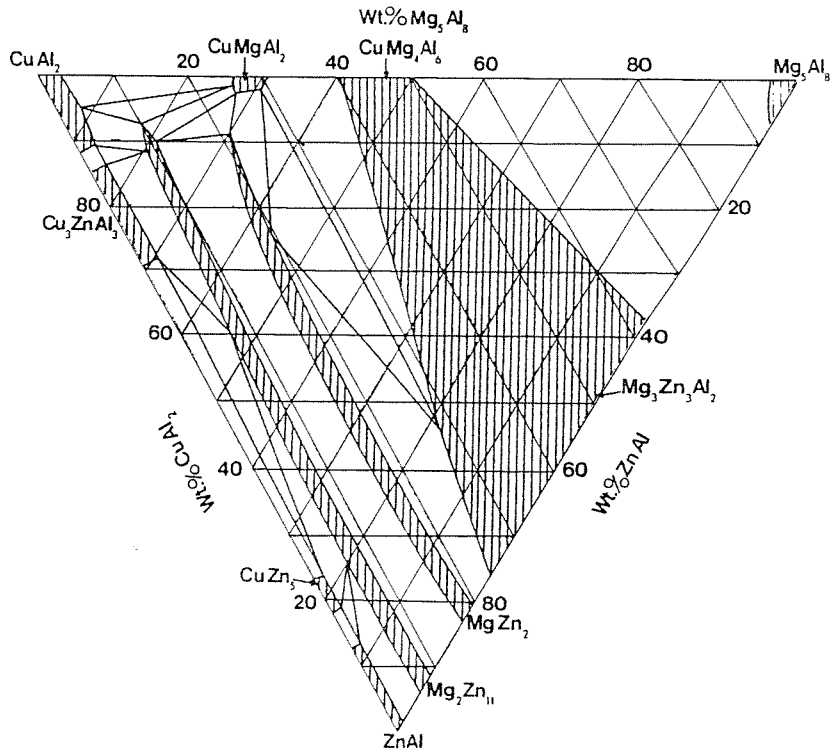

Figure 2.1: a) Phase diagram of Al-Zn-Mg-1.5%Cu at 460°C (S=Al_2CuMg, T=Al_6CuMg_4/$Al_{32}(Mg,Zn)_{49}$, η=$MgZn_2$) after Polmear [5]

b) Projection of the aluminium corner of Al-Cu-Mg-Zn diagram; phase distribution in the solid; after Mondolfo [12]

2.4.2 Precipitation strengthening

7xxx aluminium alloys are generally developed for high strength which is of course directly linked to the microstructure - particularly the finely dispersed precipitates formed during heat treatments. The quantity and distribution of these precipitates changes with the heat treatment applied. Although some authors have identified other precipitation mechanisms for non-commercial heat treatment [15], the mechanism of precipitation in copper containing 7xxx alloys is usually presented as (see e.g. [5,15,16])

Super Saturated Solution α(Al-Zn-Mg-Cu) $\rightarrow \alpha$ + GP zones $\rightarrow \alpha + \eta' \rightarrow \alpha + \eta$ or T

The main precipitates involved in this sequence are described below.

- Most studies consider two types of Guinier-Preston zones (GP zones) [17,18,19]. GP(I) are spherical solute-rich atom clusters that form during low temperature ageing, whilst GP(II) are vacancy rich clusters that form during quenching [18]. They are formed by diffusion of atoms over very short distances leading to a fine, high density dispersion. GP zones retain the basic structure of the matrix and are coherent with it [17]. The GP(I) zones solvus temperature is low, hence they often disappear rapidly during commercial artificial ageing [17,20]. GP(II) zones are more stable (they have been shown to coexist with η' after ageing treatments conducted at 100°C [18]) and act as preferential nucleation sites for η'. This fact provides the basis for double step ageing treatment applied to Al-Zn-Mg alloys. GP zones are formed during the first step ageing and η', and η, are formed during the second step. The positive influence of the presence of GP zones on the η' formation results from the fact that the number of zones acting as nucleation sites can be much larger than the number of η' nuclei formed in one-step ageing [19]. As GP(I) zones dissolve during commercial heat treatment, they do not directly influence the

mechanical properties in commercial heat treatment, except by promoting a fine dispersion of η′ and η (see below).

- If an Al-Zn-Mg(-Cu) alloy is aged at around 60-180°C for sufficient time, η′ will form. η′ nucleation sites can be a) concentration fluctuation following dissolution of low concentration GP zones, b) GP zones of overcritical size, c) quenched-in clusters rich in vacancies, d) impurity atom cluster [17]. The strength of the alloy is higher when this phase is homogeneously distributed in the alloy. η′ is a hexagonal phase believed to be partly coherent with the matrix [15]. η′ precipitates appear as plate shaped particles, approximately 30Å thick and 50Å in diameter [19] (up to 200Å in diameter when they form on dislocations [21]). They are present on different matrix planes with several orientation relationships [22]. The exact composition of η′ is difficult to estimate due to its small size. Early work by Auld and Cousland [23] reported a composition for an Al-Zn-Mg alloy as $Mg_4Zn_{11}Al$, although, in general, a $MgZn_2$ composition is accepted (see e.g. [5],[15]). Recent work using atom probe analysis has shown some evidence for a composition having the formula $Mg(Zn,Cu,Al)_2$ [24]. Li et al. [19] using high resolution electron microscopy have also proposed a model of the compositional structure for Al-Zn-Mg alloys which suggests a formula close to $Mg_2Zn_{5-x}Al_{2+x}$.
- η is the equilibrium phase in commercial alloys, it is also a hexagonal phase which is incoherent with the matrix. At high ageing temperatures (above 190°C) T phase, $(Al,Zn)_{49}Mg_{32}$, may appear [15]. η has a slightly different crystalline structure to η′, and is formed if the alloy is over-aged (ageing for a longer time or at a higher temperatures). Its composition is usually referred as being identical to η′ [15]. η forms heterogeneously on grain boundaries [25] and dislocations [26].

Precipitation hardening is the dominant strengthening mechanism in 7xxx alloys.

The strengthening of alloys by second phase particles can be considered in terms of their interaction with dislocations. The contribution of precipitates to the initial yield strength of the alloy can be modeled, in an idealized way, by considering those particles as point obstacles exerting forces on a dislocation (see e.g. [27]). The diagram in Fig. 2.2 represent a dislocation pinned by precipitates. The contribution to the flow stress, $\Delta\tau$, is expressed as

$$\Delta\tau = \frac{F}{bL} \tag{2.1}$$

Where F is the obstacle strength, b is Burger's vector and L is the effective spacing of the obstacles. This framework relates to the basic principles accounting for the incremental yield strength due to precipitates. The variation in distribution, size or nature of the precipitates will affect the strength of the alloy. Furthermore, considering the contact of the particle with the dislocation, further parameters are needed to describe the influence of precipitates on dislocations such as the elastic misfit of the particle, the surface energy and ordering energy.

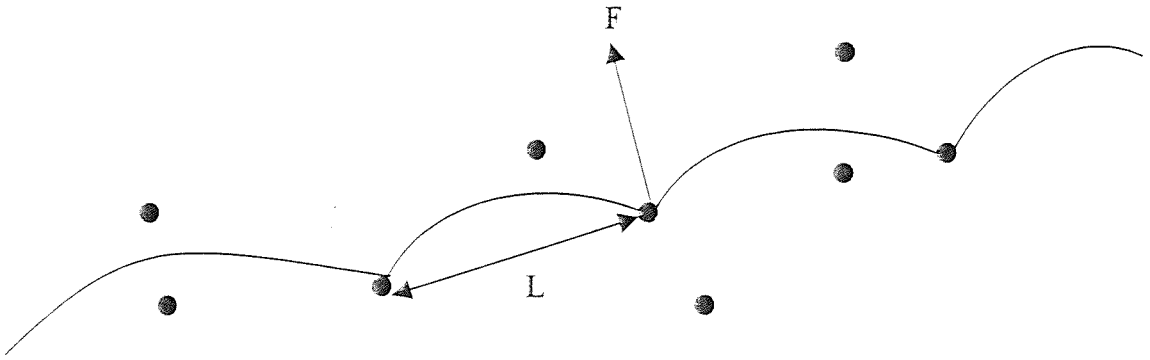

Figure 2.2: Schematic diagram representing a pinned dislocation.

Aluminium alloys (and of course other ductile crystals) will deform by the movement of dislocations under a certain amount of shear stress. Precipitates strengthen the alloy by impeding the movement of these dislocations. The precipitation strengthening depends on the force needed by the dislocations to shear or by-pass the precipitate obstacles. The main strengthening mechanisms for common precipitation

hardening systems are given below [27]:

1. Surface strengthening: due to the creation of increased surface energy due to particle shear
2. Stacking-fault strengthening: due to the difference in stacking fault energy between the particle and the matrix.
3. Modulus strengthening: due to the differences in the elastic moduli between the particles and the matrix.
4. Coherency strengthening: due to the elastic misfit of the particle in the matrix.
5. Order strengthening: due to the creation of an anti-phase boundary following the passage of a glide dislocation through an order phase.
6. Orowan strengthening: due to dislocations looping around a particle in the case of impenetrable obstacles

Expressions for these different mechanisms are given in Table 2.2.

Strengthening mechanism	Formula	Reference	Symbols
Surface	$\tau_{es} \propto \frac{1}{r}\sqrt{\frac{\gamma_s bf}{T}}$	[27]	b Burgers vector G shear modulus f particle volume fraction r particle radius T line tension of a dislocation γ_s surface energy γ_{sf} difference in stacking-fault energy between matrix and particle λ interparticle spacing E_1 modulus of the soft phase E_2 modulus of the hard phase ε_c misfit parameter γ_{apb} antiphase boundary energy
Stacking fault	$\Delta\sigma_{sf} \propto \frac{f^{0.3} r^{0.5}}{G^{0.5} b^2}\gamma_{sf}^{1.5}$	[28]	
Modulus	$\Delta\sigma_{E} \propto \frac{Gb}{\lambda}\left(1-\frac{E_1^2}{E_2^2}\right)^{0.5}$	[28]	
Coherency	$\Delta\sigma_{c} \propto \frac{Gr^{0.5} f^{0.5}}{b}\varepsilon_c^{1.5}$	[28]	
Order	for underaged alloys: $\Delta\tau_{ord} \propto \frac{\gamma_{apb}}{b}\sqrt{\frac{\gamma_{apb} fr}{T}}$ for overaged alloys: $\Delta\tau_{ord} \propto \frac{\gamma_{apb}}{b}\sqrt{f}$	[29]	
Orowan	$\sigma_0 \propto \frac{Gb}{\lambda}\ln\frac{r}{b}$	[28]	

Table 2.2: Particle strengthening mechanisms

The contribution of precipitates to the strength is influenced by the ageing condition, as broadly summarized in Fig. 2.3.

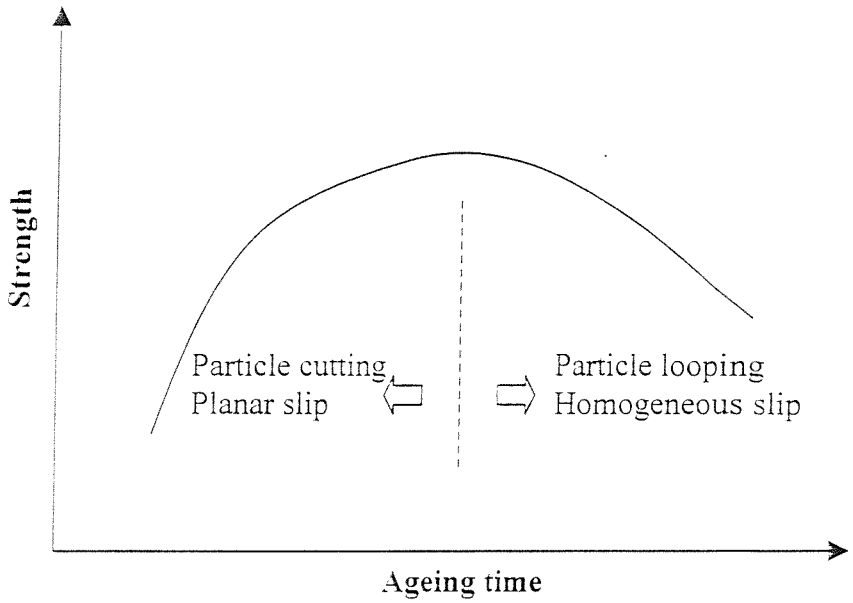

Figure 2.3: Effect of ageing on the alloy strength.

In underaged and peak aged 7xxx alloys, the shearing of GP zones, η′ and small η precipitates by dislocations effectively reduces the size of the precipitates on the slip plane (se e.g. [30]). Thus, the local resistance to further dislocation is decreased on that slip plane and dislocations then tends to concentrate in slip bands. This effect is related in peak aged conditions to high strength and limited work-hardening. In the over-aged condition coarser η precipitates can no longer be sheared, i.e. they are by-passed according to the mechanism described by Orowan (see e.g. [31]), see Fig. 2.4. Progressive looping around the particles becomes a further barrier for other dislocations, leading to dislocation pile-ups. The interaction of these loops with the interface between the matrix and the particle may indeed nucleate a void for relatively coarse particles (e.g. of a size typical of dispersoids, ~50nm), see Fig. 2.4.(c). Overall, the Orowan looping mechanism shown in Fig. 2.4.(a) leads to a fairly uniform strain distribution within a given material. Consequently, it decreases the tendency for shear band formation.

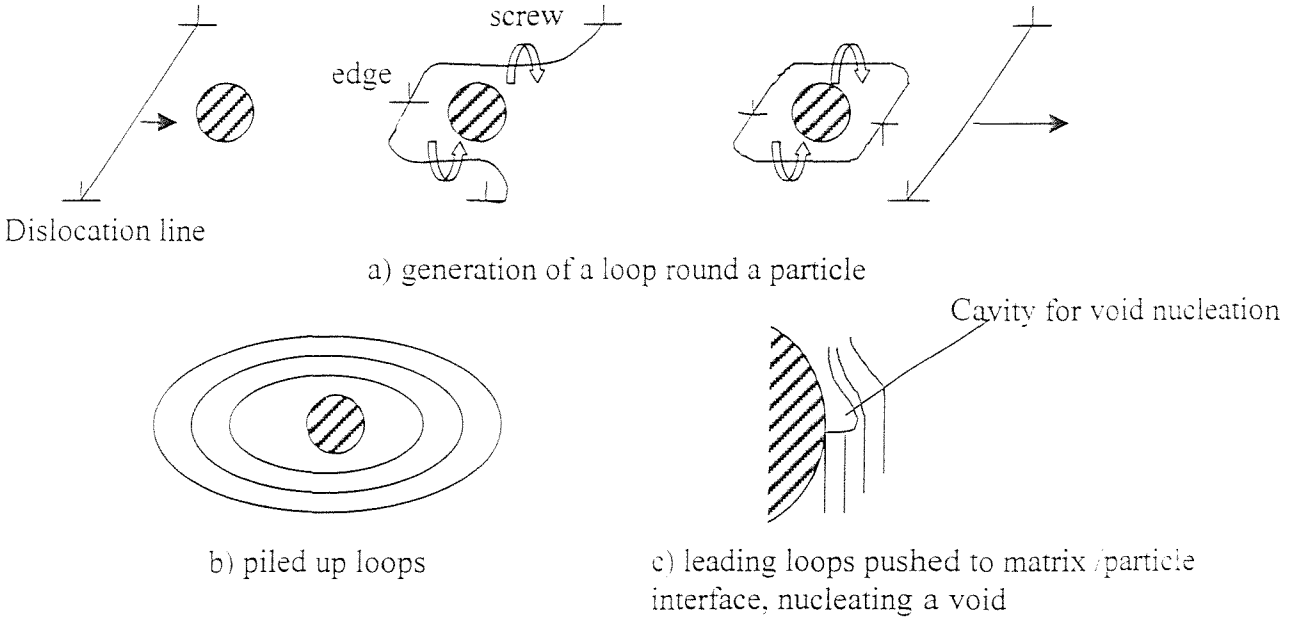

Figure 2.4: Formation and growth of voids around a particle [31].

Another rationalisation of the effects of hard second phase particles deforming elastically in a plastically deformed matrix has been proposed by Ashby [32]. Assuming that the interface matrix/particle does not fracture, Ashby concludes that secondary slip must occur locally round particles (see Fig. 2.5).

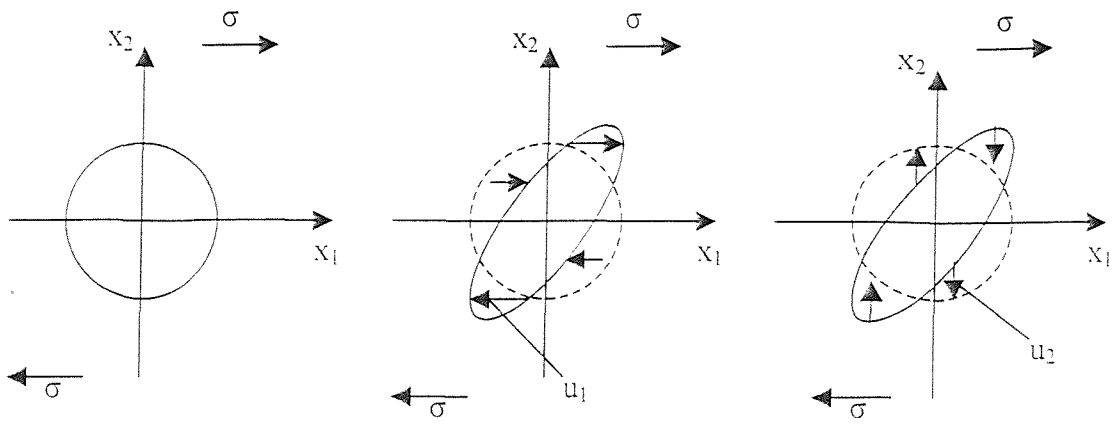

Figure 2.5: Schematic diagram of a) a hard spherical particle in an idealized single cubic, single crystal submitted to a shear stress σ along the axis x_1 causing a homogeneous plastic shear in the matrix a, b) when the particle is removed from its hole, and the matrix undergoes a uniform primary shear displacement $u_1=ax_2$, the hole is distorted as shown, c) to replace the particle in its hole, a secondary shear displacement u2=cx1 (where c is the shear strain in the secondary slip system) at the particle matrix interface is first needed if the particle is to be elastically distorted only. (After Ashby [32]).

The density of secondary slip increases with increased strain. These secondary dislocations act as a forest of obstacles which has to be overcome by primary dislocations for the latter to propagate. Therefore, Ashby derived a stress-strain relationship considering the secondary slip to be the main work hardening mechanism. Calculating the influence of a single secondary dislocation on the stress-strain dependency and estimating the density of secondary slip impeding primary dislocation, it is then possible to deduce the force opposing the motion of a dislocation. The stress-strain relationship is obtained by the requirement that this force equals an incremental force, above the yield strength, applied to the material. This theory of work hardening based on secondary slip forest interference involves a work hardening parameter K_A which depends on microstructural parameters:

$$\sigma = \sigma_{ys} + K_A \sqrt{\varepsilon_p} \tag{2.2}$$

$$K_A = 0.24 MG \sqrt{\frac{bf}{r_{ns}}} \tag{2.3}$$

where σ is the stress, σ_{ys} is the yield strength, b is Burger's vector, ε_p is the plastic strain, G is the matrix shear modulus, f is the volume fraction of non-shearable particles, r_{ns} the non-shearable particle diameter and M is a constant. M is sometimes referred as the Taylor factor [29,33,34]. This constant accounts for the polycrystalline nature of the material. Gomiero et al. [34] have assessed this model including the influence of the grain size and reviewed the different microstructural contribution to the strength, to give:

$$K_A = M\left[0.35G\left(\frac{b}{d}\right)^{1/2} + 0.24G\left(\frac{bf}{r_{ns}}\right)^{1/2}\right] \tag{2.4}$$

Where d is the grain size. In their work on the 2091 Al-Li based alloy, Gomiero et al. [34] have observed large discrepancy between theoretical estimates from equation 2.3, K_{Ath}, and experimental values from equation 2.4, K_{Aexp}. They attributed these large differences to the non-homogeneous nature of strain. They stated that the effective local strain ε^* from which hardening arises is larger than the macroscopic strain to an extent related to the volume fraction, V_f, of material that deforms plastically. Therefore the relation between K_{Ath} and K_{Aexp} can be expressed as

$$\varepsilon^* = \frac{\varepsilon}{V_f} \Rightarrow K_{A\exp} = \frac{K_{Ath}}{\sqrt{V_f}} \tag{2.5}$$

It should be noted that other factors participate in the strengthening of the alloy (intrinsic strength, solid solution strengthening, grain size effect...) some of which will be reviewed in the next section.

2.5 Microstructural influences on strength and toughness in 7xxx aluminium alloys

Microstructural features influence strength and toughness. The toughness is particularly influenced by various factors including [35]:

- The strength of the material, which in turn is influenced by such factors as shearable precipitates, grain size, etc.
- Spatial distribution, size and volume fraction of the particles that can be subjected to cracking
- Resistance of particles and their interfaces to failure
- Local strain concentration induced by fine shearable particles
- Particles on the grain boundaries and the relation between these decorated boundaries and the crack path

In the following we will consider the various types of microstructural features that influence toughness and strength.

2.5.1 Large particles

In wrought, high strength aluminium alloys, Fe and Si are essentially impurities forming coarse intermetallics particles that often cannot be dissolved during homogenisation or solution treatments. In 7xxx alloys, Fe and Si may lead to the formation of phases such as Al_7Cu_2Fe and Mg_2Si [36]. These intermetallics have no marked influence on the strength of the alloy [37]. Many authors have investigated the detrimental effects of coarse intermetallics on fracture toughness [35,36,38,39]. Toughness of a given alloy is generally seen to increase as concentrations of Fe and Si decrease [35,39]. It is therefore crucial to control the amounts of these impurities, hence the development of alloys with enhanced purity levels such as 7475 and 2124.

In terms of the influence of coarse intermetallics (generally 1-10μm in wrought products) on fracture behaviour, several processes have been identified. Hahn and Rosenfield [35] acknowledge that the cracking of the large particles occurs shortly after the onset of plastic flow because of high stresses generated around hard particles in a matrix undergoing plastic deformation and the intrinsically brittle character of the phases involved. It has been shown that from 25 to more than 50% of the coarse intermetallic inclusions in high strength aluminium alloys may be cracked after only 0.07 plastic strain [35]. Such particles will also rupture easily when engulfed by the plastic zone preceding a crack tip, creating a void. As more strain is confined to a much smaller zone adjacent to the crack tip, coalescence of the void and crack tip opening occurs, see figure 2.6. In this model crack propagation occurs when the crack tip opening displacement (CTOD) value, δ_t, equals the distance, X_o, from the crack tip to the nearest coarse void. In this model, the principal parameters for crack propagation are the volume fraction of coarse particles and their spacing [35].

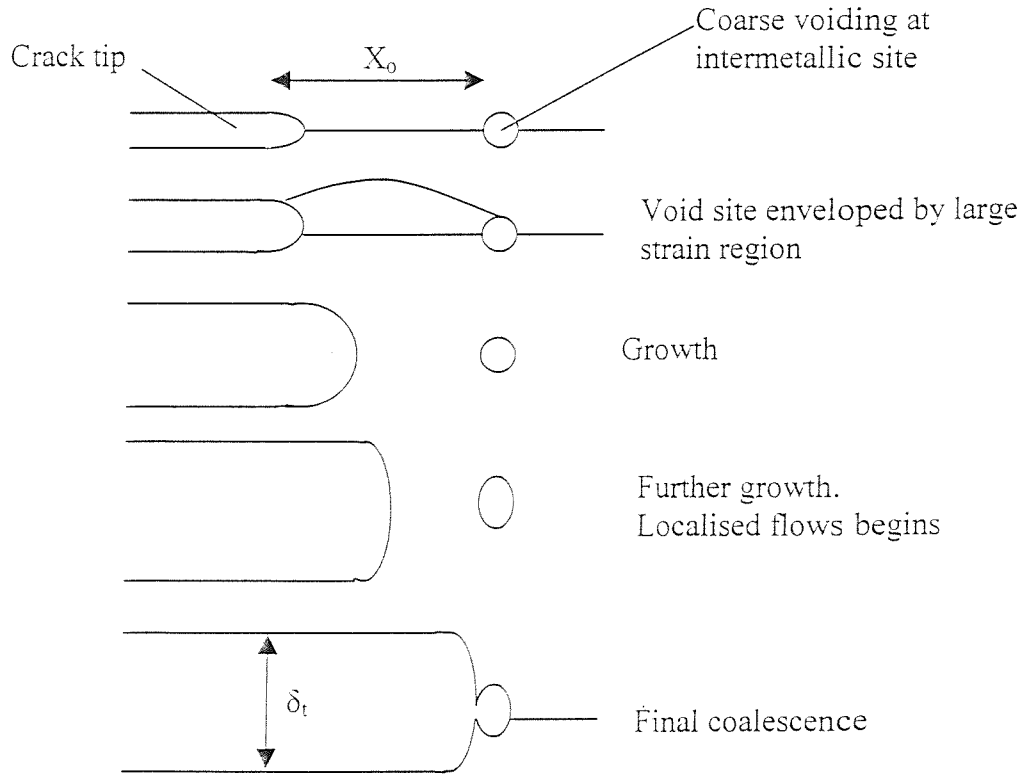

Figure 2.6: Transgranular crack propagation by linkage of voids surrounding large particles [40].

It is also important to note the presence of the so-called S phase (Al_2CuMg) in 7xxx alloys [41,42]. Whilst this is essentially a soluble phase in 7xxx alloys, incomplete solutionising and/or excessive alloying levels lead to the presence of coarse particles much like the Fe and Si containing intermetallics, having a similarly detrimental influence on toughness.

Intermetallic particles are heterogeneously distributed. The intermetallics can appear in cluster and are often orientated in the rolling direction. This may create a degree of anisotropy in the alloy mechanical properties.

2.5.2 Dispersoid particles

Zr, Cr and Mn containing particles are used to limit recrystallisation and grain growth [43] by pinning the grain boundaries in commercial wrought Al-alloys. These particles efficiency is function of their size, distribution and coherency with the matrix. The force applied by these particles on the grain boundary has been first calculated by Zener (see e.g. [10]). It was shown that the pinning efficiency decreases as the particle size increased and lost its coherency with the matrix [10]. In this respect, Zr, which precipitates as Al_3Zr (β' phase) particles (commonly ~10-50nm), is generally regarded as better than Cr or Mn (whose precipitates are larger and less coherent) in exercising strong control over grain structure whilst also increasing toughness and SCC [43].

The influence of the so-called "dispersoids" formed by Zr, Cr and Mn on toughness is twofold. As they limit recrystallisation, which is believed to be detrimental to the fracture toughness (see section 2.5.3 below) [44,45] dispersoids have a positive effect on fracture toughness. However, they may also nucleate voids by decohesion at the interface with the matrix, creating void sheets in high strength, low work hardening materials, which are then seen to limit the fracture toughness [46]. It has been assumed that a recrystallised structure could also enhance void growth at Al_3Zr dispersoids as they will become incoherent with the matrix during recrystallisation. The propagation of a crack by void sheet formed from dispersoids has been investigated and modeled by Chen

and Knott [46] for 7xxx aluminium alloys and Haynes and Gangloff [47] for Al-Cu-Mg-Ag-Zr. Overall, it may be seen that there is a complex relation between dispersoids, grain structure and toughness.

Dispersoids have an indirect influence on strength, particularly as a result of grain refinement. Fine grains increase strength: this will be reviewed in the next section.

2.5.3 Influence of the grain structure

Influence of the grain structure on the strength

Strength properties are enhanced by grain refinement. The contribution of the grain size effect to the yield strength can be described by the Hall-Petch law (see e.g. [34]). According to Hall and Petch, the stress increment due to the grain size is

$$\tau_y - \tau_0 = k_{HP} d^{-1/2} \tag{2.6}$$

where τ_y is the resolved yield stress of the polycrystal, τ_0 the yield stress of the corresponding single crystal, d the grain size, and k_{HP} a coefficient. A similar relation can describe the influence of the subgrain size d_{sub} on the material strength σ:

$$\sigma = \sigma_0 + k d_{sub}^{-p} \tag{2.7}$$

where σ_0 is the strength of the annealed material, k is the subboundary strength and p is constant. Strength increments of over 100% by producing fine, stable subgrain size through thermomechanical processsing have been reported in the literature [6].

Recrystallisation

The influence of the grain structure and recrystallisation on toughness has been substantially investigated in the literature [44,48,49,50,51] demonstrating different tendencies. Thompson and Zinkham [50], for instance, have illustrated the increase in toughness in the L-T direction for unrecrystallised structure in AA-7075. They assume

this to be due to a higher fraction of intergranular fracture in the recrystallised material. Staley [51] further suggests that increased boundary misorientation between grains in the recrystallised structure enhances grain boundary precipitation and, hence, decreases toughness (see section 2.5.4). However, work by Morere [48] on a 7010 aluminium alloy with relatively low recrystallised fractions showed no distinct influence of the boundary character on the fracture process, with the lower toughness for recrystallised alloys in this case being attributed to the presence of coarse intermetallics in soft recrystallised grains (see section 2.5.1).

Anisotropy

The grain structure is also believed to contribute to the anisotropy of toughness in wrought material. A wrought material with conventional pancake shaped grains (flat grains elongated in L and T direction after cross-rolling) can exhibit three different failure characteristics depending on direction of loading and crack growth [52]:

- Weak interface cracking during S-L and S-T loading, leading to strongly intergranular failure (Fig. 2.7.a).
- Intergranular failure perpendicular to the crack direction in L-S and T-S orientations (Fig. 2.7.b); the associated crack bifurcation (or blunting) will lead to a higher toughness as the blunted crack will decrease the overall crack driving force.
- Intergranular failure can also occur in L-T and T-L test orientations (Fig. 2.7.c), this process is called delamination. This delamination enables stress triaxiality to relax leading to increased fracture resistance, i.e. the specimen can be considered as if composed of several thinner through-thickness sections closer to plane stress conditions than plane strain.

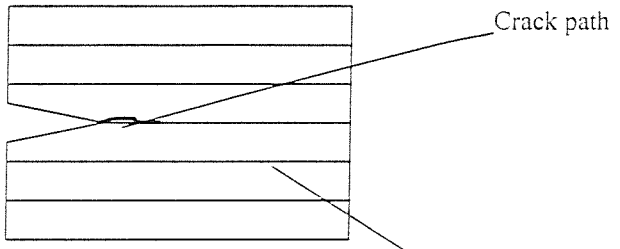

(a) SL orientation-propagation

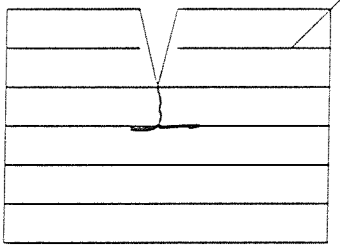

(b) LS orientation-crack blunting

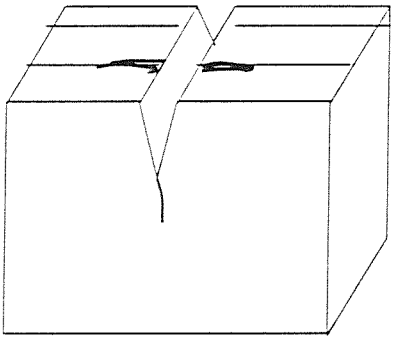

(c) LT orientation-delamination/crack dividing

Figure 2.7: Influence of the grain boundaries orientation on the crack propagation

- Fracture path deflection may appear in the L-S and L-T orientations due to shear strain localisation oriented at 45° to the crack plane, see Fig. 2.8. This deflection drives the crack away from the maximum tensile stress plane (i.e. plane perpendicular to the applied force) and hence reduces the crack driving force.

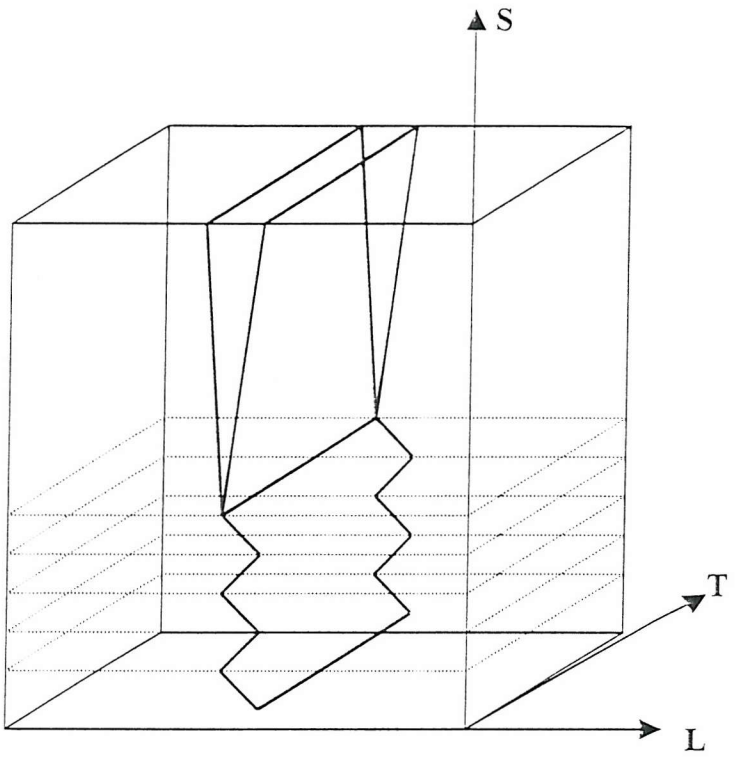

Figure 2.8: Schematic illustration of fracture path deflection in an L-S oriented specimen [52].

2.5.4 Influence of grain boundary precipitates and Precipitate Free Zones (PFZ)

Kirman [53] has shown, for a commercial 7075 aluminium alloy, that in an overaged condition the fracture is predominantly intergranular. In their review of grain boundary ductile failure, Vasudevan and Doherty [25] put forward three dominant mechanisms for this:

- Microvoid growth at larger grain boundary precipitates: fracture toughness then decreases as the area fraction of the grain boundary covered by precipitates increases [54]. The η phase, which nucleates heterogeneously on grain boundaries in 7xxx type alloys, is present during the entire ageing

treatment but tends to coarsen with an increased ageing time. It can be noted that a slow quench rate increases the density of η grain boundary precipitates [55] and, hence, may decrease toughness.

- Strain localisation in grain boundary PFZs: the interface between matrix and PFZ represents a high differential in yield stress that can favour void formation due to strain localisation. However, some authors [56] have also suggested that the PFZ may relax the stress at the end of a transgranular slip band and, therefore, enhance the toughness of an alloy. Other studies [57] have suggested that variation in PFZ width have little effect on fracture toughness.
- Slip band blocking: the shearing of matrix precipitates may promote the formation of planar transgranular slip bands, which then create a local stress concentration when they meet a grain boundary (see e.g. [58]). Such intersections are then believed to be sufficient to initiate a crack.

2.5.5 Fine precipitates

Toughness is typically greatest in the under-aged condition and decreases when approaching peak strength. Some improvement occurs with overageing with a reduction of yield strength, but for the same level of yield strength, underaged alloys exhibit better toughness than overaged alloys (Fig. 2.9).

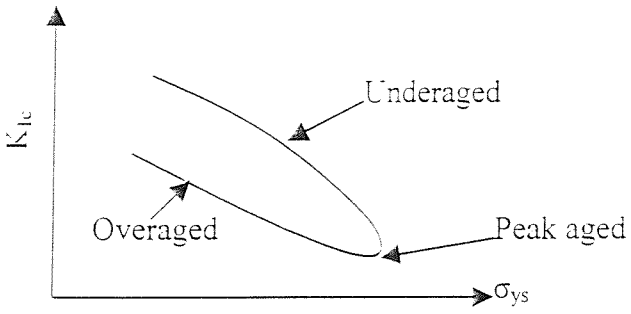

Figure 2.9: Schematic diagram of the evolution of the K_{Ic} vs σ_{ys} relationship during ageing.

The better strength/toughness performance of underaged alloys over overaged alloys is due in part to the formation in overaged condition of large η precipitates at grain boundaries, with PFZs adjacent to them, promoting intergranular fracture (see section 2.5.4). However, underaged alloys usually exhibit poor SCC resistance and are seldom used for commercial application. In overaged and peak aged conditions, a compromise is sought between properties that improve with overageing, like SCC resistance and toughness, and the ones that decrease on overageing, like yield strength.

The toughness recovery with overageing is usually associated with local interactions between dislocations and precipitates (GP zones, η′ and η) that provide an indirect though important influence on the fracture behaviour: when a material is under/peak aged, precipitate shearing may produce heterogeneous deformation (specifically, local planar slip bands) which may favour void initiation at dispersoids within the slip band, or at slip band/grain boundary intersections where high local stresses are generated. In overaged alloys, by-passing of larger η precipitates by dislocations creates a homogeneous distribution of strain in the alloy. Therefore, local cracking requires more additional strain to initiate.

2.6 Retrogression and Re-ageing (RRA) heat treatment

Overageing treatment, such as T73 and T76, have been applied to reduce the susceptibility of 7075 T651 aluminium alloy to stress corrosion cracking (SCC). However, overaged treatments result in a significant loss of strength. To address this, a heat treatment which aims to reduce the susceptibility of 7xxx aluminium alloys to SCC while retaining a strength comparable to the T6 heat treatment was developed by Cina [59]. This three-step heat treatment is called retrogression and re-ageing (RRA) treatment. The three steps are as follows:

- Ageing the alloy to a T6 temper
- Heating the alloy for a short time above the ageing temperature and below the solutionizing temperature (180°C-260°C) (i.e. within the (α+ η) region of the phase diagram) followed by either air-cooling or cold water quench.

- Re-ageing to a T6 heat treatment

From the T6 microstructural state, the retrogression treatment dissolves either partially or completely the smaller η′ precipitates [60] while some of the bigger η′ precipitates (which sizes exceed a critical size d_c) are transformed to a more stable phase η. For a temperature above 200°C, phase diagrams by Mondolfo [12] have shown the possibility of forming T phase, however this has been seldom observed in previous studies [60]. This step also leads to a coarsening of the η phase in the matrix and at the grain boundary. The re-ageing step induces the growth of the partly dissolved η′ and the re-precipitation of η′. Thus the main microstructural characteristics of the RRA treated alloy are a homogeneous distribution of η′ and η in the matrix with a broad particle size distribution and coarser η grain boundary precipitates. The matrix is similar to a T6 temper while the grain boundary is similar to a T73 temper (precipitates are larger and more widely separated).

The relevance of T7 and RRA treatment lies in the improvement of the SCC resistance with ageing. Although it is not the subject of this study to develop the influence of the microstructure on SCC, some basic notion of the mechanism of SCC is useful in understanding RRA treatments.

SCC is a complex mechanism involving interactions between the microstructure, mechanical deformation and the environment (see e.g. [5]). Two basic theories have been developed to explain SCC: anodic dissolution and hydrogen embrittlement. Both are believed to occur in 7xxx alloys, the relative importance depends on the particular alloy studied and the heat treatment applied to it. SCC in 7xxx alloy is an intergranular mode of rupture as both these mechanisms relate to grain boundaries.

The anodic dissolution concept considers that grain boundaries, PFZ and grain boundary precipitates act as an active path for corrosion due to high potential differential between the grain boundary precipitates and interior of the grain. Furthermore, stress, strain, grain boundary segregation and slip band intercepts with the grain boundaries enhance SCC sensitivity. The volume of grain boundary precipitates per unit grain boundary area has been found to be the most representative parameter of SCC susceptibility [60]. Also, the alloying element concentration within the PFZ changes the electrochemical potential and can therefore influence SCC sensitivity. For example a

higher concentration of Cu is believed to be beneficial to SCC resistance as Cu is thought to enter the grain boundary precipitates thus reducing the potential difference and retarding SCC [60].

The hydrogen embrittlement mechanism is also affected by the composition of the alloy and particularly the elements remaining in solution at the grain boundary. It has been suggested that Mg and Zn promote hydrogen dissolution in aluminium alloys, giving rise to hydrogen embrittlement (e.g. see [61]). A cathodic electrochemical process between water vapor and the alloy produces hydrogen. It enters the alloy via grain boundaries or dislocations, as hydrogen has a low solubility and mobility within the matrix (e.g. see [62]). Therefore the hydrogen is expected to be mainly present at grain boundary sites, and transport through grains can also occur by dislocations. When present in solution at the boundary hydrogen promotes brittle intergranular fracture [62]. However, several studies [60,62] have shown that grain boundary precipitates when they reach a critical size can act as hydrogen trapping sites, therefore reducing the amount of hydrogen in solution and subsequent embrittlement.

Therefore overageing and RRA heat treatments may improve SCC resistance by varying the grain boundary and matrix characteristics in several ways:

- The removal of dislocations due to the retrogression treatment decrease the rate of hydrogen transfer in the alloy [63,64], thus reducing hydrogen embrittlement.
- The coarsening grain boundary precipitates can act as trapping sites for the hydrogen [60]. They can also remove Zn and Mg from the PFZ.
- The homogenization of strain due to the replacement of η' precipitates by η during overageing reduce the localized stress at grain boundaries produced by coarse slip bands and thus reduce SCC sensitivity.
- Reducing potential difference and hence reducing anodic dissolution [65].

Among the many parameters which can affect the microstructure, the duration and temperature of the retrogression step are often recognize as the critical parameters of RRA treatments [60]. High temperature and/or long duration of the retrogression step can lead to severe overageing and poor strength/SCC resistance balance. Islam and Wallace [66] applied retrogression treatments of 10s at 280°C with a standard reageing procedure

(24h at 120°C) to a 7475 T6 alloy and noticed a 25% decrease in yield strength compared to the T7351 condition for a 5% increase in SCC resistance (from conductivity measurements). Rajan et al. [67] applied a 1h at 220°C retrogression step to their 7075 T6 alloy and after reageing found a 22% loss of strength compared to a standard T6 treatment. The optimum retrogression time and temperature is related to the microstructure evolution during this step. During retrogression, strength decreases very rapidly to reach a minimum before increasing to secondary peak and then decreasing again on further overageing as shown in figure 2.10. Dahn et al. [68] have divided this curve in three stages. In their study the first stage is associated with the partial dissolution of GP zones, stage II to η' formation and growth and stage III to the coarsening of all precipitates. Reaged material submitted to short retrogression time has a slightly higher yield strength/hardness as compared to T6 levels [68]. Longer retrogression time lead to a loss in the strength properties of the alloy.

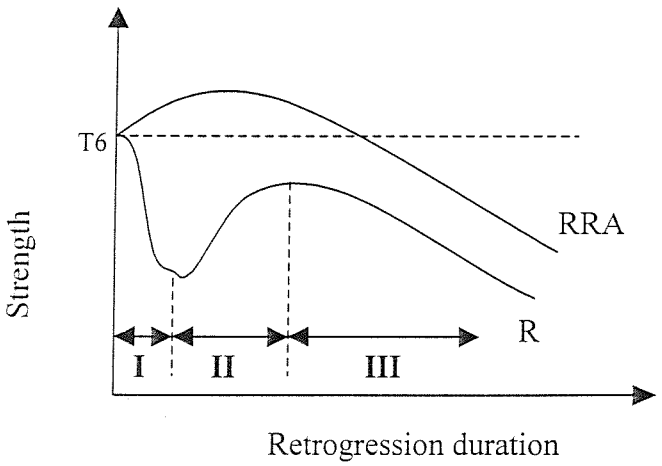

Figure 2.10: Schematic diagram showing the strength variation as a function of retrogression time. R: retrogressed alloy, RRA: retrogressed and re-aged alloy.

Cina [59] first suggested that the optimum retrogression duration corresponds to the minimum of the retrogression curve (Fig. 2.8). However, this minimum is attained for very short length of time, 20s at 240°C [60] up to 6min at 200°C [67], which is not applicable commercially for relatively thick products. Further investigation [67,69] have

shown that this peak is not necessarily the optimum for retrogression treatment. Rajan et al. [67] have shown that longer retrogression time associated with lower temperature can produce valuable strength/SCC resistance combination applicable to thick products.

A long retrogression treatment would lead to the coarsening of all precipitates. Therefore short retrogression times have to be applied to avoid the softening of the alloy. As heat up rates depend on plate thickness, there is a difficulty in applying the RRA treatment to commercial thick plates and optimisation of both time and temperature of the retrogression step have to be achieved. This optimisation is made possible by the understanding of the physics of heat transfer through an aluminium plate and thermodynamics of precipitation reaction. These topics will be studied in the next sections.

Chapter 3

Fracture mechanics and fracture toughness modelling

3.1 Fracture mechanics

3.1.1 The energy balance approach

In the 1920s, Griffith (see e.g. [31]) presented the first quantitative analysis considering the effect of cracks on the fracture behaviour of a material. Griffith suggested that in a cracked body under stress, fracture would occur when the rate of release of elastic strain energy due to crack propagation was equal to the rate of increase in surface energy associated with the formation of the free surfaces created. This energy balance approach was extended by Irwin [31] to the fracture of ductile materials by including a term in the energy balance accounting for the work done in plastic deformation during crack propagation.

A significant aspect of this approach is the determination of a crack driving force, G, which is the rate of elastic strain energy release during crack extension. Thus, G can be used to characterise the resistance of a given material to fracture through a critical value of energy release rate, G_c, i.e. G_c is the applied G to cause fracture. However, the use of energy balance approach is limited for most structural metals where plastic deformation significantly occurs during fracture as the strain energy release rates are based on purely elastic behaviour. Nonetheless, Irwin showed that G_c is still a meaningful expression for the fracture toughness when the scale over which plastic deformation occur is much smaller than the crack length and other characteristic dimensions of the specimen considered [31].

3.1.2 The stress intensity approach

The use of G_c as an engineering design criterion was found to be limited due to difficulties in measuring the work done in plastic deformation of the material during crack growth. In the 1950s, Irwin, to cope with practical difficulties of the energy approach, promoted the *stress intensity approach* to crack propagation [31]. Irwin shows that the elastic stress distribution ahead of a crack length a under a remote uniaxial load σ may be written in the following basic form:

$$\sigma_{ij} = \frac{K}{\sqrt{2\pi r}} f_{ij}(\theta) + \text{higher order terms in } r \qquad (3.1)$$

Where θ and r are defined as in Figure 3.1 and K is a constant giving the magnitude of the elastic stress field and called the *stress intensity factor,* given by:

$$K = \sigma\sqrt{\pi a}\, f(\text{specimen geometry only}) \quad (\text{MPa}\sqrt{\text{m}}) \qquad (3.2)$$

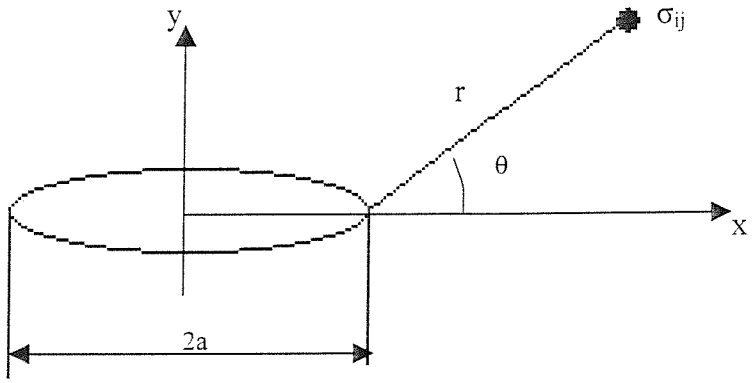

Figure 3.1: Stresses at a point ahead of the crack tip

It could then be shown using the principle of virtual work that G is related to K by the following expressions:

$$G = \frac{K^2}{E} \text{ under plane stress conditions} \tag{3.3}$$

$$G = \frac{K^2}{E\left(1-\nu^2\right)} \text{ under plane strain conditions} \tag{3.4}$$

Hence, G_c can be related to a critical stress intensity factor K_c which is a measure of fracture toughness. However, it should be noted that stress levels given in equation 3.1 tend to infinity when r approaches zero. In real metallic materials the onset of a plastic zone at the crack tip will limit the peak stress levels. The linear elastic fracture mechanics approach considers that the extent of this plastic zone is small compared to the zone at the crack tip where stress levels are dominated by K, therefore the elastic stress field surrounding the crack tip plastic zone will still be closely related to K. Subsequently, the attributes of the plastic zone, such as its shape or size, will be determined by the surrounding elastic stress distribution, and hence be related to K. This approach has the advantage that K is function of the crack length, the applied stress and the specimen geometry only, which can be directly quantified (using analytical or numerical methods).

3.1.3 Crack geometry

The crack geometry presented in Fig. 3.1 is rather simplified compared to most practical cases. Complex crack/loading situations may be analysed using three limiting cases: mode I (opening), mode II (in-plane shear) and mode III (out-of-plane shear), as illustrated in Fig. 3.2.

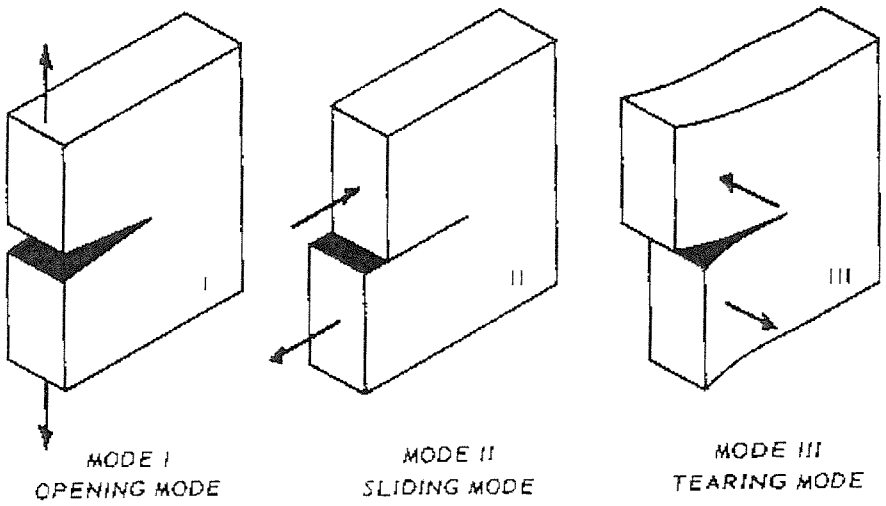

Figure 3.2: The three crack opening modes

Each crack opening mode can be quantified by a stress intensity factor as defined by an equation similar to Eq. 3.1. Hence, any crack/loading configuration can be characterised by a generalised expression following:

$$\sigma_{ij} = \sigma_{ij}^{I} + \sigma_{ij}^{II} + \sigma_{ij}^{III} \tag{3.5}$$

$$\text{with } \sigma_{ij}^{k} = \frac{K_k}{\sqrt{2\pi r}} f_{ij}^{k}(\theta) + \text{higher order terms in } r \tag{3.6}$$

Where $\sigma_{ij}^{I}, \sigma_{ij}^{II}, \sigma_{ij}^{III}$ are the stresses at the crack tip in the respective mode of loading I, II and III. K_k represent the stress intensity factor corresponding to the three loading configurations illustrated in Fig. 3.2. f_{ij}^{k} are the radial distribution functions.

The fracture properties of a given material associated with mode I loading are generally considered to be the lowest. The opening mode has therefore been the focus of research in fracture mechanics. The present study is based on mode I behaviour, therefore the following discussion is confined to mode I analysis.

3.1.4 Crack tip plasticity

Under mode I loading the size of the crack tip plastic zone for a given stress intensity is dependent on the specimen thickness. Two limiting cases are usually considered (see Fig. 3.3): (i) plane stress conditions, through thickness stresses are relieved by unrestricted plastic deformation in the through thickness direction, (ii) plane strain condition, plastic deformation in the through thickness direction is restricted by surrounding elastic material (see e.g. [70]).

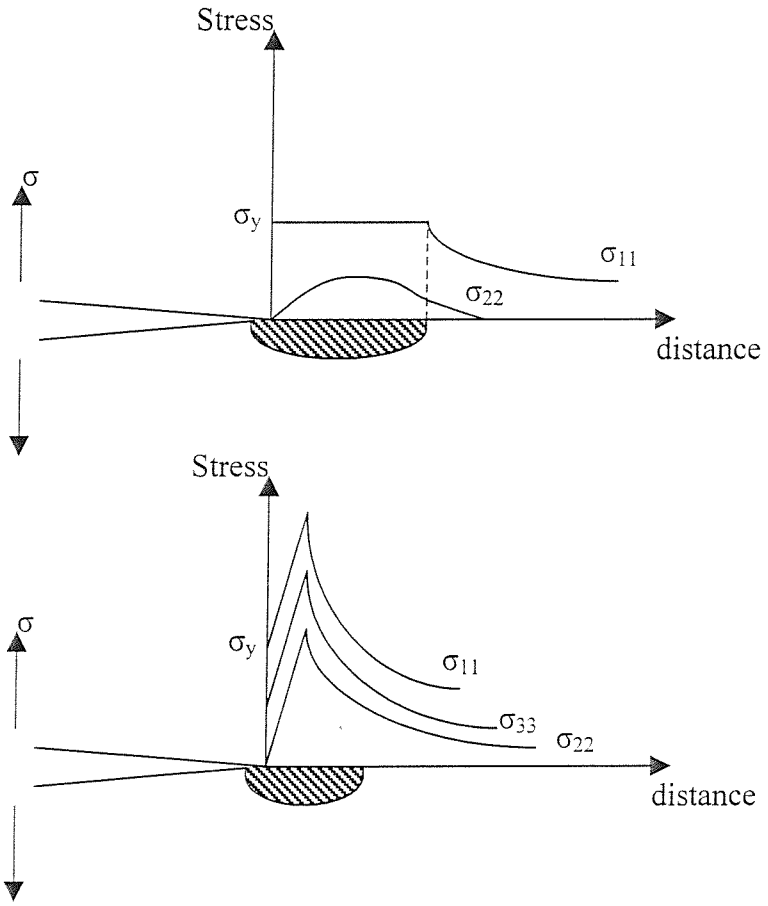

Figure 3.3: Schematic elastic/plastic stress distribution near a crack under, (a) plane stress and (b) plane strain conditions [70].

Plane stress is characteristic of thin specimens or edges of thick specimens whereas plane strain is characteristic of the middle plane of relatively thick sections (Fig. 3.4).

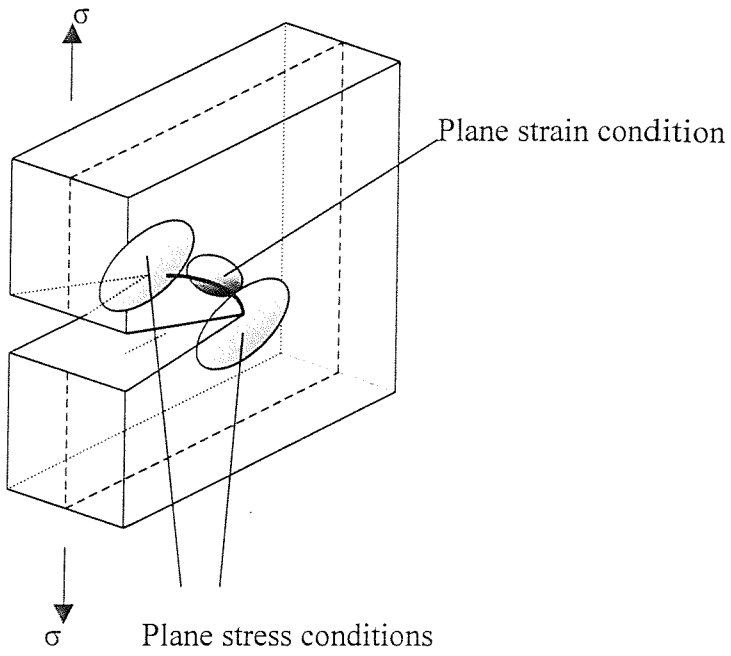

Figure 3.4: Schematic diagram of the stress state conditions in a specimen under mode I loading

In plane strain condition, tensile hydrostatic stress is present just ahead of the crack tip as a result of plastic flow constraint. Under such conditions, peak tensile stresses of the order of three times the material flow stress may develop. Plane strain loading is therefore considered the limiting condition in terms of mechanical properties. Plane strain fracture toughness, K_{Ic}, is most often used as engineering design parameter to evaluate a material's fracture resistance.

In a ductile material, a zone of plastically deformed material forms at the crack tip under the action of an applied far-field tensile load. Many calculation of crack tip plastic zone size have been presented in the literature (see e.g. [70,71]). These studies vary from first order approximation to finite element modelling. Irwin (see e.g. [31]) derived a first order estimate of the scale of deformation under LEFM conditions. The plastic zone

characteristic dimension, r_p, is related to the stress intensity factor following:

$$r_p = \alpha\left(\frac{K}{\sigma_y}\right)^2 \tag{3.7}$$

Where α is a constant, σ_y is the yield strength. In Irwin's analysis α is estimated to be $1/(2\pi)$ under plane stress condition for an (assumed) circular plastic zone of radius r_p. The constant α is usually divided by three to describe plane strain condition.

More accurate descriptions of the plastic zone in a ductile metal available in the literature (se e.g. [72]) show a plastic zone for a crack under mode I loading to be represented by two symmetrical lobes ahead of the crack tip (Fig. 3.5).

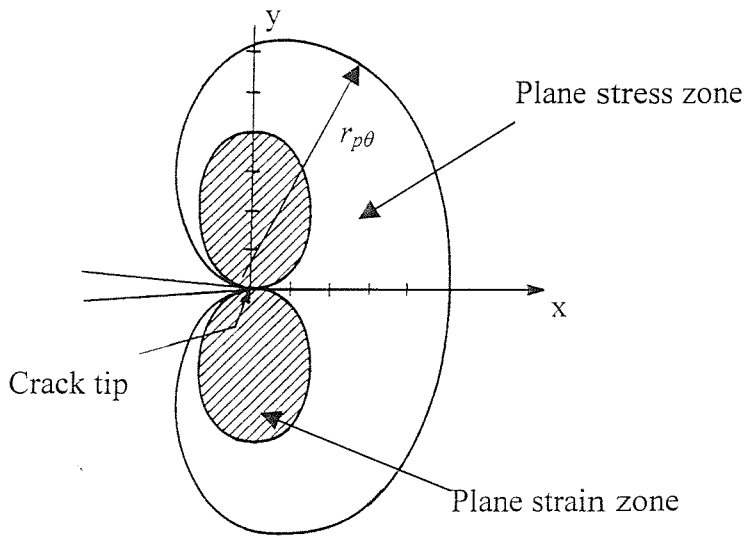

Figure 3.5: plastic zone shapes from the Von Mises yield criterion

The plastic zone size may then be expressed as:

$$r_{p\theta} = \alpha_\theta\left(\frac{K}{\sigma_y}\right)^2 \tag{3.8}$$

where $r_{p\theta}$ is as illustrated in Fig. 3.4 and α_θ is a function of θ.

3.1.5 Crack tip opening displacement

An initially sharp crack under an applied load will open up and become blunted due to plastic deformation. The crack tip opening displacement (CTOD), δ_t, gives a measure of this blunting. The CTOD is taken as the separation of the crack surfaces at the crack tip when the crack is loaded. The degree of blunting can be related to the maximum deformation condition and may therefore be used to characterise the behaviour of cracks in ductile materials (see e.g. [71]). Under LEFM conditions, the CTOD can be expressed as:

$$\delta_t = \beta \frac{K^2}{E\sigma_y} \tag{3.9}$$

where β is a constant. CTOD values are particularly significant as it has been shown that crack tip strain are particularly concentrated in a zone extending to approximately twice the CTOD value ahead of the crack tip (see e.g. [72]). Also, crack tip stress levels reach a maximum at a distance of approximately twice the CTOD [72].

3.2 Modelling of toughness

The dominant micromechanisms of fracture for high strength aluminium alloys that have been identified in chapter 2 are:

1. Decohesion and fracture of coarse constituent particles or intermetallics
2. Intergranular fracture
3. Transgranular shear at dispersoid particles.

Numerous attempts to model fracture toughness in relation to the microstructure and micro-mechanisms have been made in the literature. However, a number of problems exists:

- The strain-stress distribution in the plastic zone ahead of the crack is

complex.

- A "proper" fracture criterion must be chosen.
- Any fracture criterion can depend on many parameters that are difficult to determine. For example, the fracture criterion may state that fracture occurs when a critical strain is exceeded over a certain distance, such as particle spacing. Subsequently, the critical strain has to be determined, but it is a function of the stress state, which varies dramatically near the crack tip.
- Materials commonly show a mixture of failure mechanisms, making a simple single fracture criterion questionable.

As noted previously, Hahn and Rosenfield [35] have proposed a model which considers the critical element determining fracture toughness to be the propagation of the crack between large particles and not the cracking of the particles. It has been proved that large intermetallics crack at very low strain levels, therefore when a particle is near the crack tip, it has already cracked and toughness will depend on the linking up of the associated voids. The critical condition will then depend on the size and volume fraction of cracked particles and the size of the heavily strained region at the crack tip which depends on the yield strength and modulus.

When λ_c, the width of unbroken ligament to the next void forming particle ahead of the crack tip, is equal to the crack opening displacement, δ, the failure criterion may be said to be reached. K_{Ic} is then given by:

$$K_{Ic} = \left[2\sigma_{ys} E \left(\frac{\pi}{6} \right)^{1/3} D \right]^{1/2} f_c^{-1/6} \qquad (3.10)$$

Where D is the diameter of the void initiating intermetallics and f_c is their volume fraction. This model is to a certain extent in contradiction with experimental data. If the yield strength is raised for the same volume fraction and diameter of particles, the toughness is predicted to increase, contrary to general experience. The model also

predicts an increased toughness with increasing diameter of void initiating intermetallics which contradicts experimental studies [40]. Van Stone and Psioda [73] comment on this, stating that for an accurate model both void initiation and growth should be considered, and contrary to Hahn and Rosenfield, they expect the dispersoids to have an effect on fracture toughness. However, the Hahn and Rosenfield model has been shown to give a good approximation of experimental results for constant yield stress and constant particle size. Recently, Ehrstrom *et al.* [74] have shown that the basic principle of this model may be used to predict fracture toughness of 7xxx type aluminium with some success. They extended this model, considering the clustering of particles (the distance between intermetallics, λ, is replaced by a parameter proportional to the distance between clusters, λ_{cl}), they also considered a critical growth rate of cavities at the large particles to be the fracture criterion and used a finite element model for void growth behaviour in the clusters.

Following from the Hahn and Rosenfield model [75], Garrett and Knott [76], working on Al-Cu based alloys, have also derived an expression of toughness related to tensile properties, particularly yield strength and work hardening exponent, n. They make the assumptions that the average tensile strain in the region of intense plastic deformation (of length l) is half of the shear strain at the crack tip γ, and that the strain distribution in the plastic zone decreases linearly with distance from the crack tip (Fig. 3.6).

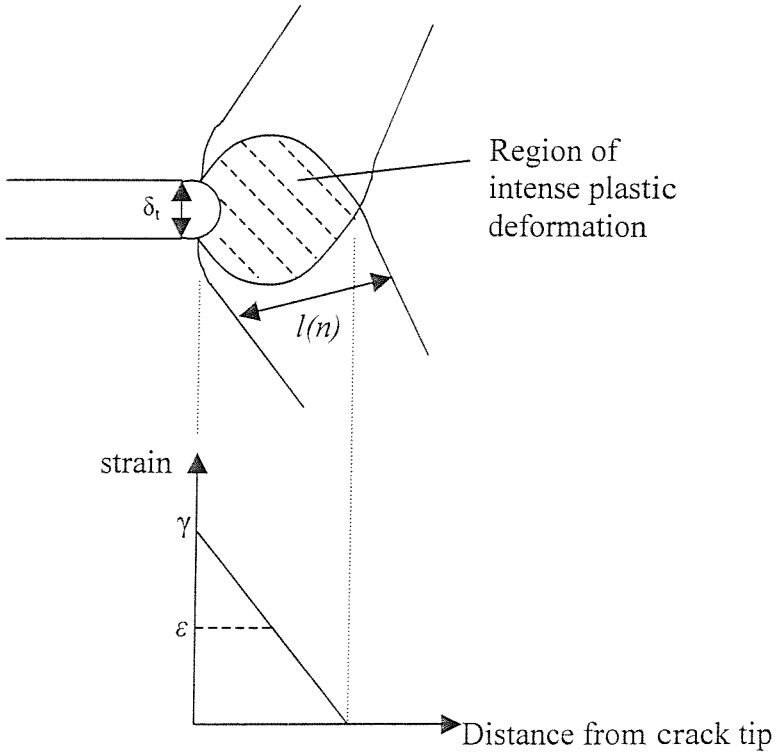

Figure3.6: Schematic illustration of Garrett and Knott model of plane strain plastic zone at the onset of instability [76]

From experimental work, Hahn and Rosenfield have deduced that $l \sim \frac{n^2}{40}$ [75]. Garrett and Knott then derive (for a constant void initiating particle dispersion) the following equation for the fracture toughness [76]:

$$K_{Ic} = Cn\sqrt{\sigma_{ys}} \tag{3.11}$$

Where C is a constant.

Chen and Knott [46], studying 7010 and 7475 alloys in different ageing conditions, have further developed this model by considering that the influence of dispersoids on crack propagation is greater than the influence of coarse intermetallics. Strain localization within shear bands in the plastic zone ahead of the crack tip may lead

to decohesion of the dispersoid/matrix interface. Therefore, the fracture criterion is reached when the stress at the interface dispersoid/matrix σ_c exceeds the cohesion strength. σ_c is shown to be given by:

$$\sigma_c = \frac{\gamma_c d}{2b\lambda} \tag{3.12}$$

Where b is the Burgers vector, λ the dispersoid spacing, d the diameter of dispersoid and γ_c is the critical shear strain.

This may then be shown to give:

$$K_{Ic} = \left(\frac{mb}{10A} E\sigma_c \sigma_{ys} n^2 \lambda d^{-1} \right)^{1/2} \tag{3.13}$$

Where m and A are constants.

The results of Garrett and Knott work, along with those of Chen and Knott's are presented in Figure 3.7. Their experimental results are shown to follow relatively accurately the linear relationships predicted.

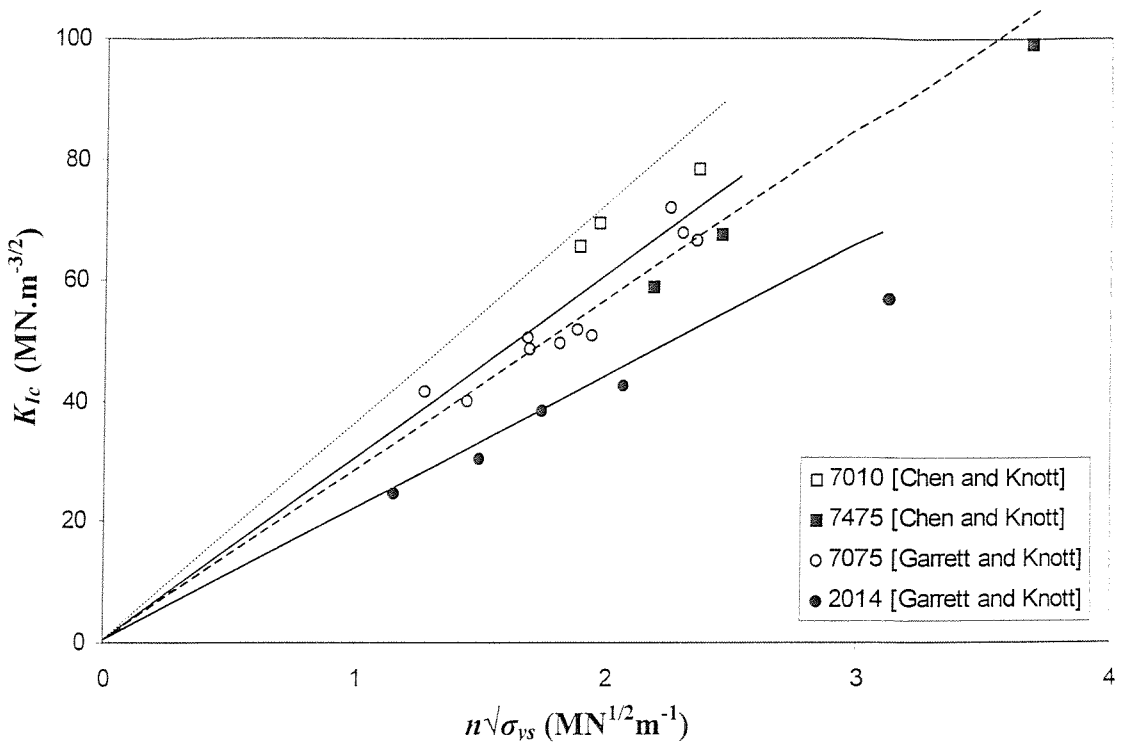

Figure 3.7: Experimental results and overall model prediction from Garrett and Knott [76] and Chen and Knott [46] studies

Also based on a ductile fracture approach, Haynes and Gangloff [47] have proposed a critical plastic strain model of toughness. This model is applicable for alloys failing by dimple rupture and couples three elements: crack tip stress-strain fields, stress state dependent tensile fracture strain, and a critical microstructural distance, l^*, over which microvoid fracture initiates. They consider the critical tensile fracture strain to be a function of the stress state triaxiality

$$\varepsilon_f^p\left(\frac{\sigma_m}{\sigma_{fl}}\right) = \alpha \exp\left(-1.5\frac{\sigma_m}{\sigma_{fl}}\right) \tag{3.14}$$

Where α is a constant, σ_m is the mean stress and σ_{fl} is the effective flow stress ($\frac{\sigma_m}{\sigma_{fl}}$ being a measure of the stress state triaxiality). This experimental relation has been deduced from the fitting of ε^p_f verses $\frac{\sigma_m}{\sigma_{fl}}$ curves obtained from notched tensile tests by considering

the reduction area (RA) of the specimens such that [47]:

$$\varepsilon_f^p = -\ln\left(1-\frac{RA}{100}\right) \tag{3.15}$$

$$\text{and}\frac{\sigma_m}{\sigma_{fl}} = \frac{1}{3}+\ln\left(\frac{d}{4R}+1\right) \tag{3.16}$$

Where d is the initial notch-root diameter and R is the notch-root profile radius, as shown in Fig. 3.8.

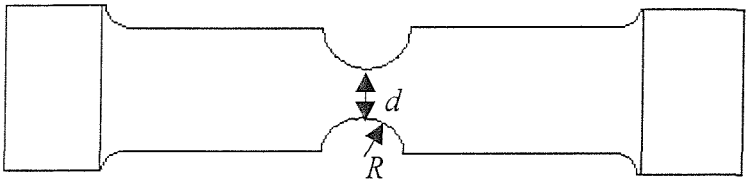

Figure 3.8: Schematic drawing of a notched tensile specimen geometry.

Fracture in a cracked specimen is considered to occur when ε exceeds its critical value over a distance l^*: fracture initiates by void impingement or void sheeting between the void nucleation site and the crack tip. Therefore, the predicted plane strain fracture toughness is equal to the applied stress intensity required for the crack tip plastic strain, ε^p, to exceed the stress-state dependent fracture strain, $\varepsilon^p_f(\frac{\sigma_m}{\sigma_{fl}})$, over a distance l^*. An illustration of this model is given in Figure 3.9: equations for ε^p and $(\frac{\sigma_m}{\sigma_{fl}})$ follow from crack tip stress-strain field calculations. The fracture criterion is satisfied at the intersection of the ε^p and $\varepsilon^p_f(\frac{\sigma_m}{\sigma_{fl}})$ curves, yielding an intrinsic fracture strain, ε^p_f, and a critical distance to CTOD ratio, l^*/δ_{Ic}.

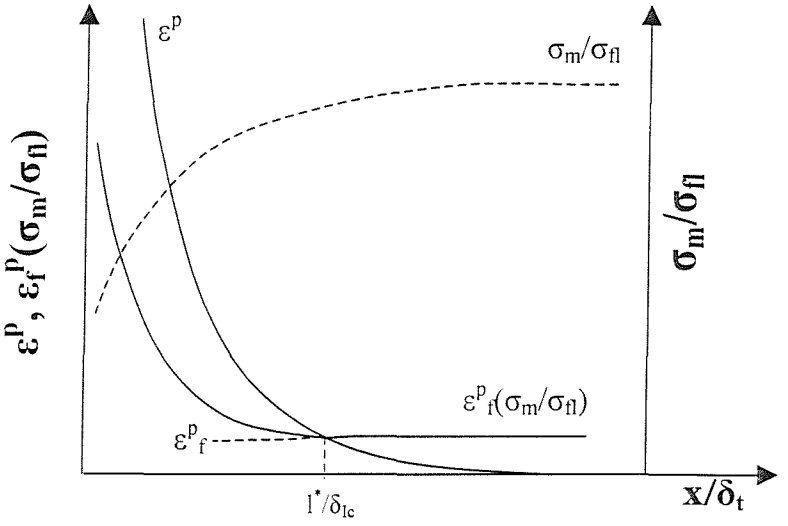

Figure 3.8: Illustration of the critical plastic strain-controlled model from Haynes and Gangloff [47].

The following equation for the plain strain linear elastic initiation fracture toughness K_{JICi} is given

$$K_{JICi} \approx \sqrt{\frac{\sigma_{ys} El^*}{d_n\left(1-\nu^2\right)}\left(\frac{\varepsilon_f^*}{7}\right)} \tag{3.17}$$

where d_n is a linear function of n. ε^*_f is the smooth tensile bar fracture strain. This model has been shown to give accurate prediction of fracture toughness dependence on temperature in the Al-Cu-Mg-Ag studied.

The models presented above are essentially based on ductile fracture considering mainly second phase particles and bulk material properties without taking into account the influence of grain boundaries. It has been shown that ageing promotes intergranular fracture in some alloys (see e.g. [35,53]). In materials containing a high fraction of incoherent grain boundary precipitates with PFZs of unspecified width, Embury and Nes [77] have identified as an empirical failure criterion the critical value for the grain boundary shear strain, γ_f, based on the area fraction of grain boundary precipitates, A_f:

$$\text{When } \gamma_f = \left[\left(\frac{1}{A_f}\right)^{0.5} - 1\right]/2 \tag{3.18}$$

When this critical shear strain is attained the voids around each particles will join up leading to the fracture of the specimen. Then, the energy absorbed on fracture is a function of γ_f and σ^*, the ultimate tensile stress of the weak PFZ, giving

$$G_c = \sigma^* \gamma_f \sim \frac{K_c^2}{E} \tag{3.19}$$

The relation between K_c^2 and $A_f^{-0.5}$ shows good agreement with experimental results as shown in Figure 3.9.

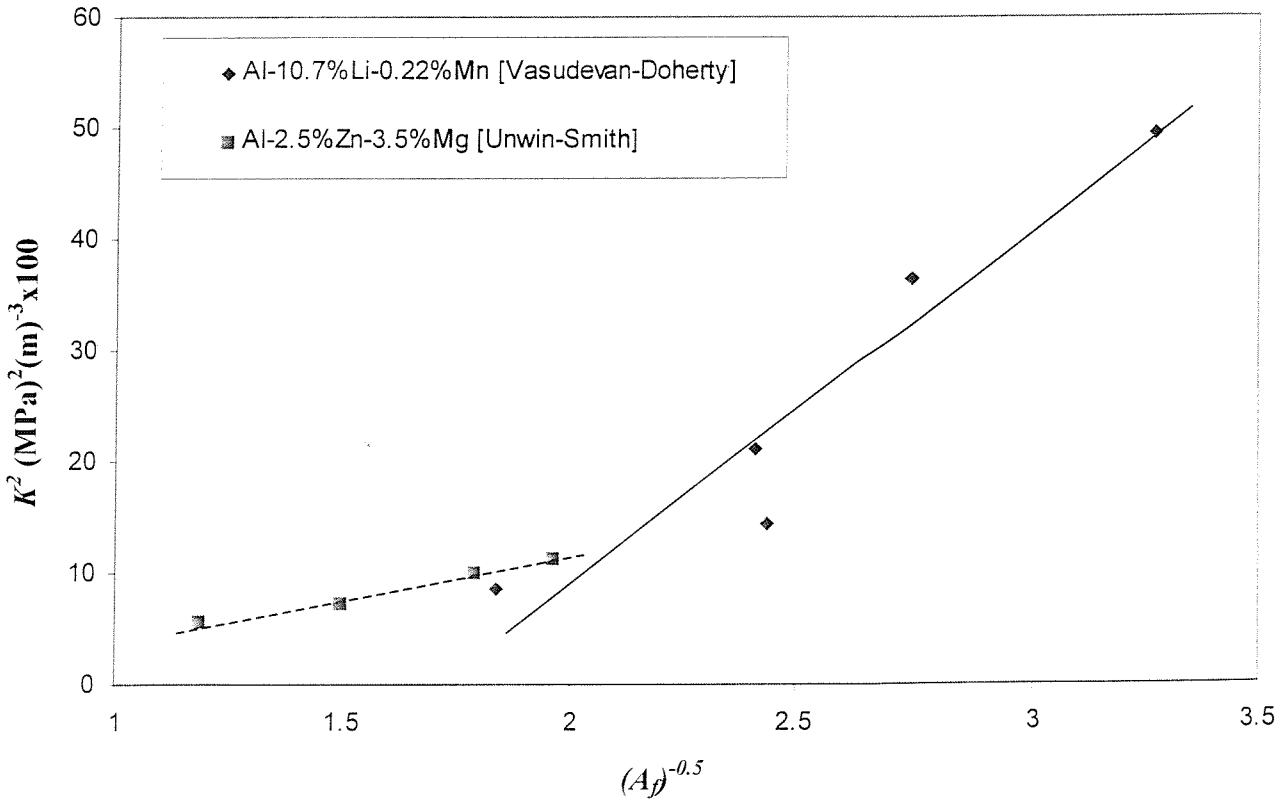

Figure 3.9: Variation of K^2 with $(A_f)^{-0.5}$ for alloys that show different matrix yield strength [25]

Localized shear in the PFZ is of course expected to have a detrimental effect on

fracture toughness, although there is still some debate on the exact influence [78]. Using a similar approach as Hahn and Rosenfield used, Hornbogen [79] has derived a fracture toughness model for the case when plastic deformation is restricted to narrow planar zones along the grain boundary. The fracture criterion is given by a critical value of the strain in the PFZ, ε_{fi}, then from Eq. 3.10. Hornbogen derived the following equation:

$$K_{Ic} = (lE\sigma_{yi} n_i \varepsilon_{fi} w / D_G)^{0.5} \tag{3.20}$$

Where l is a constant, σ_{yi}, n_{yi} are respectively the yield strength and the strain hardening coefficient, w is the PFZ width and D_G is the average grain size. ε_{yi} is considered to be dependent on the amount of grain boundary particles. These authors also make the assumption that plastic deformation is limited to the PFZ and, hence, σ_{yi} is much smaller than within the grains.

This model was later extended by Hornbogen and Graf [80] by considering that transcrystalline fracture can occur in the bulk alloy. The fracture is therefore composed of an intercrystalline portion p_i and a transcrystalline portion $p_t=(1-p_i)$ that are associated with partial fracture toughness levels K_{Ici} (Eq. 3.20) and K_{Ict} (Eq. 3.10) respectively. Hornbogen and Graf suggested that there is a critical angle of grain boundary, $\Delta\Phi_c$, that will experience maximum shear stress and which is more favorable to for a crack to follow an intergranular path. p_i is then expressed as a ratio of $2\Delta\Phi_c$ over the angular range $\pi/2$:

$$p_i = \frac{4\Delta\Phi_c}{\pi} \tag{3.21}$$

And the fracture toughness is estimated as a linear weighted summation of the partial fracture toughness levels:

$$K_{Ic} = K_{Ici} p_i + K_{Ict}(1 - p_i) \tag{3.22}$$

Gokhale et al [81] made clear that a comprehensive model should consider all the

modes of fracture and take account of the anisotropy of the alloy properties in terms of grain structure and clustering of coarse intermetallics. Sugamata et al. [82] have made some attempts to relate the fracture toughness to both intergranular and transgranular fracture in Al-Li alloys using a linear relation considering the area fraction of intergranular fracture, A_i, and the area fraction of transgranular fracture, A_t

$$K_{Ic} = K_{Ici} A_i + K_{Ict} A_t \tag{3.23}$$

K_{Ici} is derived from Eq. 3.20. K_{Ict} is derived from Roven's fracture toughness model for transgranular fracture [83]. This model assumes that the material surrounding the crack tip does not contain PFZ or coarse particles, slip is restricted to the slip bands emerging from the crack tip (see Fig. 3.10).

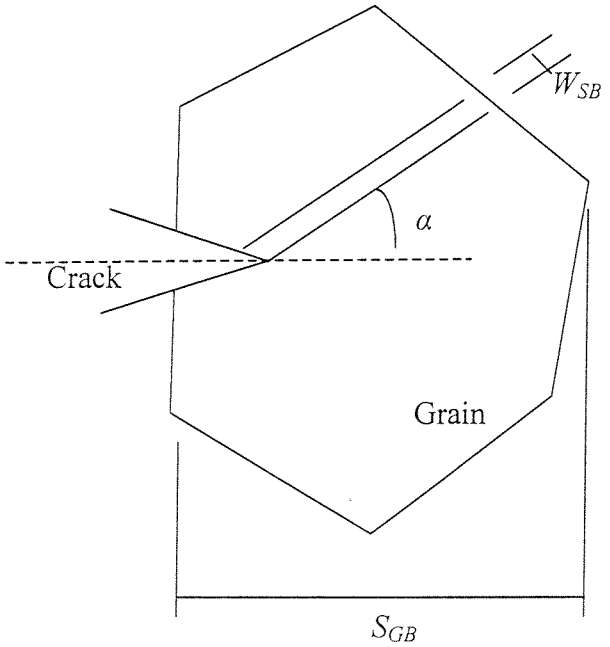

Figure 3.10: Assumed two-dimensional situation in an average section of the crack front. A slip band is emerging from the crack tip at an angle α and has a width W_{SB}. After Roven [83].

Roven considers the critical plastic strain, ε_p, to be:

$$\varepsilon_p = \frac{CTOD}{\left(\frac{S_{GB}}{S_{SB}}\right) W_{SB}} \tag{3.24}$$

Where S_{GB} is the spacing of the grain boundaries and S_{SB} is the slip band spacing. ε_p is also a function of the number of slip bands following:

$$\varepsilon_p = \frac{S_{GB}}{S_{SB} M \tan\alpha} \tag{3.25}$$

Where M is the Taylor crystallographic orientation factor. The transgranular fracture toughness is obtained by combining Eq. 3.10 with Eq. 3.24 and 3.25:

$$K_{Ict} = \left(\frac{2 S_{GB} W_{SB} \sigma_y E}{M \tan\alpha S_{SB}} \right)^{1/2} \tag{3.26}$$

Sugamata *et al.* have shown reasonable prediction of toughness with this model. However, Gokhale *et al.* [81] point out that this simple model is not physically reasonable as there is no basis for stress intensities to be linearly additive. Therefore, they proposed a model based on the energy release rate G_c additivity

$$G_{Ic} = G_{Ici} A_i + G_{Ict} A_t \tag{3.27}$$

$$\text{with } G_c = \frac{K_{Ic}^2}{E'} \text{ with } E' \text{ constant} \tag{3.28}$$

In their study Gokhale *et al.* [81] consider three micromechanism of fracture: intergranular fracture, transgranular fracture and coarse constituent particle fracture (area fraction A_p), such as:

$$A_i + A_t + A_p = 1 \Rightarrow A_i + A_t = 1 - A_p \tag{3.29}$$

Eq. 3.29 can be written as:

$$K_{Ic}^2 = (A_i + A_t)\left(K_{Ici}^2 - A_t K_{Ici}^2 + \frac{A_t}{A_i + A_t} K_{Ict}^2 \right) \tag{3.30}$$

Combining Eq. 3.30 and Eq. 3.9, a convenient way to express fracture toughness is:

$$\frac{K_{Ic}^2}{1 - A_p} = K_{Ici}^2 + \left[K_{Ict}^2 - K_{Ici}^2 \right] \left[\frac{A_t}{1 - A_p} \right] \tag{3.31}$$

K_{Ici} and K_{Ict} are constant for a given alloy chemistry, quench rate and ageing treatment. Therefore Eq. 3.31 predicts a linear relation between $\frac{K_{Ic}^2}{1 - A_p}$ and $\frac{A_t}{1 - A_p}$. This relation has been used to assess the fracture toughness of 7050 aluminium alloy [78] with some success (see Fig. 3.1) with varying specimen orientation and/or recrystallised volume. It should be noted that the slope and intercept of the linear prediction should yield the completely intergranular fracture toughness and completely transgranular fracture toughness.

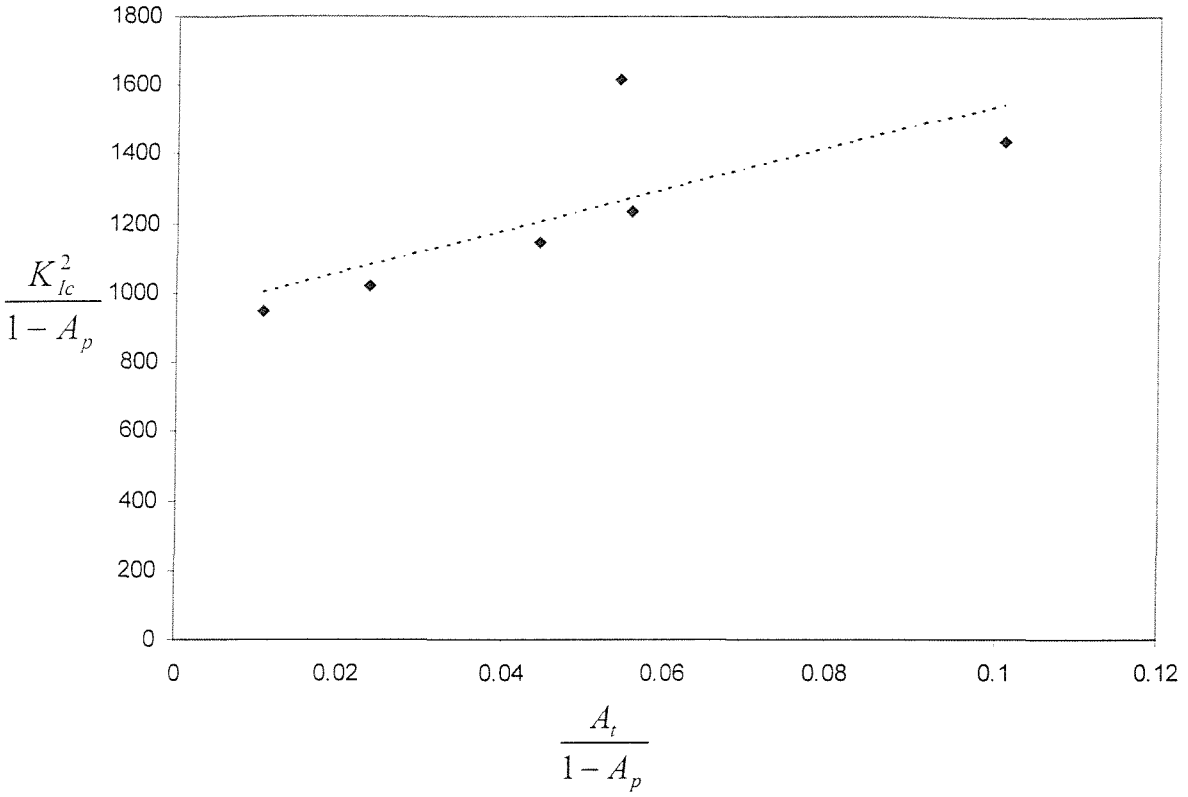

Fig. 3.11: Experimental data on water-quenched and peak aged partially recrystallised 7050 alloy specimens.

This last model appears more comprehensive than previous models. However, it fails to predicts the evolution of fracture toughness with ageing treatment and alloy composition which are fundamental to 7xxx alloy series processing.

Table 3.1 gives summary of the models presented above. A truly comprehensive model of fracture toughness has to consider all fracture modes (coarse voiding at large intermetallics, transgranular shear fracture, intergranular fracture), the parameters which influence these fracture modes (yield strength, grain boundary precipitation, PFZ, coarse intermetallics, grain structure) as well as the anisotropy of some of these parameters (distribution of intermetallics and dispersoids, orientation of the grain structure). All these processes are linked, and interactions between them may be expected.

Authors	formula	Advantages	Inconvenient	Ref
Hahn and Rosenfield	$K_{Ic} = \left[2\sigma_{ys} E \left(\frac{\pi}{6} \right)^{1/3} D \right]^{1/2} f_c^{-1/6}$	Give relationship between K_{Ic} and volume fraction of intermetallic particles.	Considers only one fracture mode (i.e. coarse voiding at intermetallics). The relationship between K_{Ic} and the yield strength is contrary to experimental knowledge.	[35]
Garrett and Knott	$K_{Ic} = Cn\sqrt{\sigma_{ys}}$	Give relationship between K_{Ic} and bulk material tensile properties.	No relation between K_{Ic} and microstructural properties. Valid only for a single fracture mechanism.	[76]
Haynes and Gangloff	$K_{JICi} \approx \sqrt{\frac{\sigma_{ys} EI^{*}}{d_n (1-\nu^2)} \left(\frac{\varepsilon_f^{*}}{7} \right)}$	Consider in more detail the influence of the stress state at the crack tip on fracture properties.	No relation between K_{Ic} and microstructural properties.	[47]
Hornbogen	$K_{Ic} = (lE\sigma_{ys} n_i \varepsilon_{fi} w / D_G)^{0.5}$	Consider the influence of the grain size and grain boundaries on fracture toughness.	Valid only for a single fracture mechanism (i.e. intergranular fracture)	[79]
Sugamata et al.	$K_{Ic} = K_{Ici} A_i + K_{Ict} A_t$	Multi-mechanistic approach to fracture toughness modelling.	No physical justification of the equation. The model does not take into account possible interaction between the fracture modes.	[82]
Gokhale et al.	$\frac{K_{Ic}^2}{1-A_p} = K_{Ici}^2 + \left[K_{Ict}^2 - K_{Ici}^2 \right] \frac{A_t}{1-A_p}$	Multi-mechanistic approach to fracture toughness modelling with physical justification of the equation.	The model does not take into account possible interaction between the fracture modes.	[81]

Table 3.1: Fracture toughness models.

Chapter 4

Experimental methods

4.1 Materials and heat treatments

Two Al-Zn-Mg-Cu alloys, 7449 and 7150, were provided by Pechiney CRV as 30mm thick plates. They were solutionised, quenched and stretched (corresponding to the commercial W51 heat treatment). These particular pieces were then naturally aged for several months before undergoing four different proprietary commercial heat treatments, which were:

- Ageing to achieve the peak strength of AA-7449, this heat treatment was referred to as T6 (7449)
- Ageing achieve to the peak strength of 7150, referred to as T6 (7150)
- Two slightly overaged double step treatments: T79 and T76 (the T76 treatment being more overaged than T79).

In addition more overaged heat treatments were performed for the 7449 aluminium alloy (Table 3.1). All heat treatments applied to these alloys should be referenced as Tx51, however we will refer to them as T6 and T7 heat treatments in the interest of brevity.

Another Al-Zn-Mg-Cu alloy containing Mn instead of Zr was provided by DERA as a 25mm thick plate. This alloy, which is not a commercial product, possesses Zn, Mg and Cu contents similar to 7449 and will be referred in the following as 7449(Mn). This alloy was furnished in as-rolled condition and naturally aged for several months before undergoing a solution treatment for 1h at 473°C, quench in water, and subsequent heat treatments, specifically T6, T76, and T7C.

Heat treatment denomination	Description
T7A	W51+ 24h at120°C + 12h at 165°C
T7B	W51+ 24h at120°C + 24h at 165°C
T7C	W51+ 24h at120°C + 39h at 165°C
T7D	W51+ 24h at170°C
T7E	W51+ 48h at160°C

Table 4.1: laboratory overaged treatments applied to the 7449 aluminium alloy

In terms of compositions, the main features of the two commercial alloys are a 33% increase in the Zn content in 7449 over 7150, and a slightly higher Cu content for 7150, see Table 4.2 (exact compositions are proprietary). 7449(Mn) contains slightly less Zn, Mg and Cu compared with the 7449 alloy.

	Zn	Mg	Cu	Zr	Fe	Si	Mn
7449	7.5-8.7	1.8-2.7	1.4-2.1	<0.25	<0.15	<0.12	-
7150	5.7-6.7	1.8-2.7	1.5-2.3	<0.25	<0.15	<0.12	-
7449(Mn)	8.1	2.2	1.75	-	<0.15	<0.12	0.4

Table 4.2: Composition ranges of 7449, 7449(Mn) and 7150 alloys (%Wt)

The DSC samples and the specimens used for the mechanical tests (toughness tests and tensile tests) are highlighted in Table 4.3.

Temper	DSC			Mech. Test.		
	7449	7150	7449(Mn)	7449	7150	7449(Mn)
W51	✓	✓				
T6 (7449)	✓	✓	✓	✓	✓	✓
T6 (7150)	✓	✓				
T79	✓	✓		✓	✓	
T76	✓	✓	✓	✓	✓	✓
T7A	✓			✓		
T7B	✓			✓		
T7C	✓		✓	✓		✓
T7D	✓			✓		
T7E	✓			✓		

Table 4.3: Heat treatments applied to the three alloys with corresponding experimental work. Heat treatments are given in order of increased ageing.

4.2 DSC

4.2.1 Principles

Differential Scanning Calorimetry is concerned with the measurement of energy changes in a substance (see e.g. [84]). It is an economical, fast, sensitive and reproducible method, as will be discussed later. Hence, it is one of the most commonly performed thermal analysis techniques in various areas such as mineralogy, but also polymer science, pharmaceutical studies or petroleum product analysis. As its name suggests, it uses the difference in heat evolution between the substance and a reference to quantify the response of the sample studied.

As the instrument signal records the energy change against time, DSC can be considered as a quantitative technique. However, DSC is often, particularly in studies of aluminium alloys, employed for qualitative study.

There are two main principles used for the DSC technique (see fig. 4.4) [84]:

- Power Compensation DSC: the signal is related to the differential heat provided to keep the sample and the reference at the same temperature.

- Heat flux DSC: the signal derives directly from the difference of temperature between the sample and the reference.

These two methods have both advantages and inconveniences, and their use is determined by each particular application.

One advantage of the DSC is the possibility to have fast heating or cooling (with rates of approximately over 100°C.min^{-1}). This, associated with the relative ease of use of the DSC, makes it available for application in the industry where, for example, a robotic system can test several samples at a time. Control of the sample environment is also possible, allowing testing at either high or low pressure.

The DSC has a high sensitivity that enables it to draw results from a very small sample (few mg), which makes the methods both cheap and reproducible, but, for heterogeneous materials, one single test can not give an overall view of the different properties. The preparation of the sample is also of great importance as the deformation induced in the material to cut and machine the samples can modify its properties [85].

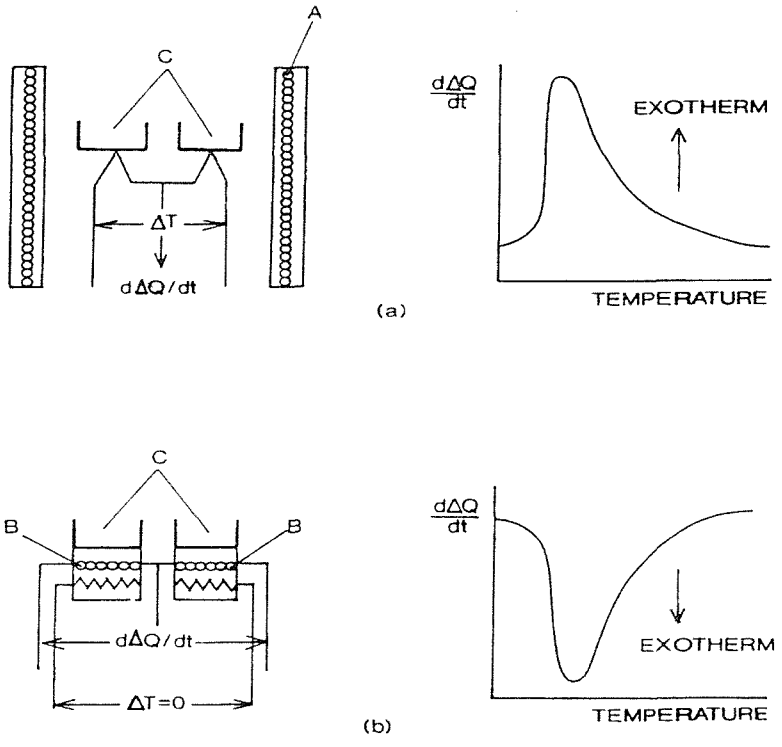

Figure 4.4: Schema of the basic principles of (a) Heat flux DSC and (b) Power compensation DSC

4.2.2 Experimental

Fine slices of 0.5mm thickness were cut and punched to obtain 5mm diameter samples. The samples were then put in a crucible in the DSC furnace. The reference employed was a pure aluminium disc of the same weight as the sample (±5mg). The DSC is a Shimatzu 50 heat flow DSC. The samples underwent the heating sequence as follows:

-Heating at 10°C /min to 520°C

-Cooling at maximum rate (-99°C /min) to 30°C

-Isothermal for 2 hours

-Heating at 10°C /min to 520°C

-Cooling at 2°C/min to 30°C

-Heating at 10°C /min to 520°C

-Cooling at -99°C/min to 30°C

The results displayed by the DSC were then corrected with a baseline correction, a heat correction and a temperature calibration. The aluminium alloy is also known to have a linear derivation of the heat flow, Q, measured with the temperature:

$$Q_{real}=Q_{mes}+a+bT \tag{4.1}$$

Where a and b are constant. As the heat flow is expected to be zero at 50°C and 520°C, these constants can be calculated for each alloy and then the curves can be corrected.

4.3 TEM

Several different samples were investigated with a Jeol JEM-2000FX TEM: 7150T7951, 7150T7651, 7449T7951, 7449T7651 and 7449T7E. The samples were 3mm diameter discs punched from the bulk material. The discs were subsequently ground with 1200 paper-grit to a thickness of about 0.3mm. They were electropolished with a Tenupol 3 electropolisher using a standard solution (30%

HNO_3, 70% methanol) at ~-20°C. The electropolisher was set with a voltage of 12V and a current of about 0.13A.

4.4 Image analysis of coarse intermetallics

Grinding and polishing

The quality and consistency of the preparation of the samples will determine the accuracy of image analysis results. Therefore a method of grinding and polishing that is identical for all the samples has been carefully applied. For the alloys considered in this study a three-step grinding (120, 600 and 1200 grit SiC-paper), and three-step polishing (6μm, 1μm, 1/4μm diamond paste) procedure has been used. An automated polishing machine was used to ensure consistency of results.

Image Analysis

Image analysis was carried out on a PC system connected to a Kodak Megaplus digital camera (1400x1000 resolution) mounted on an Olympus BH-2 optical microscope. High-resolution images are acquired from the digital camera, and subsequently analyzed using two packages: PC_Image workshop, and Optimas v. 5.2.

4.5 SEM & EDS

EDS has been performed on polished sections of the 7449, 7150 and 7449(Mn) alloys to identify coarse intermetallics.

SEM investigation of the fracture surfaces of failed specimens was carried out. This included edge-on observations linking the microstructural features in the LT and LS plane to the fracture surface features. For the edge-on observations, samples were cut from the middle of fractured specimens (to observe the fracture surface area which had been under plane strain conditions). The surface is subsequently coated with Lacomit varnish to be preserved during the later etching stage. The coated samples were mounted in resin support and polished to a standard metallographic finish. Finally, as for optical microscopy characterisation of the grain structure,

orthophosphoric etchant was used. The samples were etched for 1 to 3 minutes in a 10% H_3PO_4/90% distilled water solution heated to 50°C. Finally, the samples are broken out of the resin mount and the Lacomit varnish removed allowing the original fracture surface to be observed simultaneously with the underlying microstructure.

4.6 Toughness tests

To achieve a fatigue pre-crack front that meets the requirement of the ASTM standard and a reasonable pre-cracking time, a schedule of decreasing fatigue loads was used. Potential drop (PD) crack measurement was used. This enabled the loads to be chosen on the basis of a previously determined relationship between the potential V measured on the specimen during crack growth and the crack length a:

$$a/W = -0.9984 + 1.776\left(\frac{V}{V_0}\right) - 0.4276\left(\frac{V}{V_0}\right)^2 \qquad (4.2)$$

Where V_o is the initial potential and W the specimen length.

The present test methods followed ASTM E-399 [81]. This test method includes two parts:

- Recommendations and requirements for K_{Ic} testing
- Annexes such as displacement gauge design, fatigue cracking procedure, requirements for testing specimens

The test consists of loading a notched specimen which has been pre-cracked in fatigue. The compact tension (CT) specimen will be particularly considered, as this format was used in the present study (Fig 4.5). A specimen can be tested in different directions from the initial material as shown in Figure 4.6; in this study the L-T orientation has been tested.

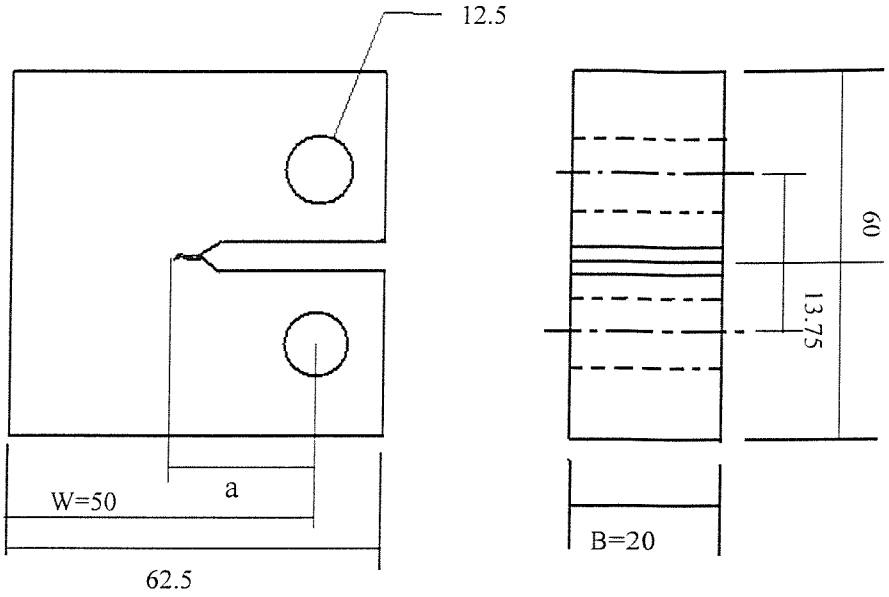

Figure 4.5: Schematic diagram of the CT specimen used for the present work (dimensions in mm)

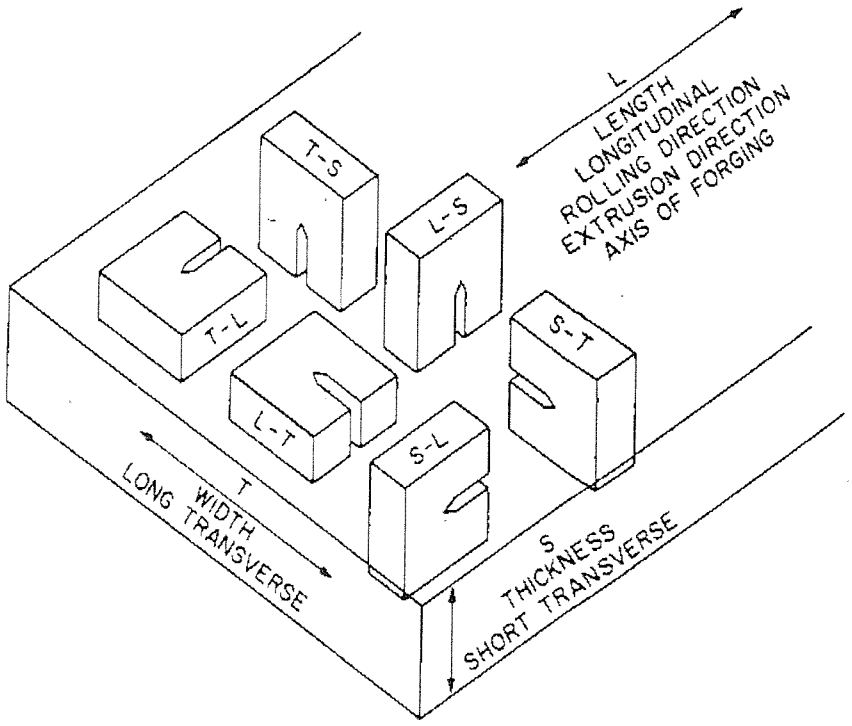

Figure 4.6: Crack plane orientation code [81]

The K_{Ic} value is derived from elastic stress analysis equations. This value is representative of a neutral environment with the presence of a sharp crack under

severe triaxial constraint. Prior cyclic loads may affect the results giving a K_Q value above K_{Ic} due to blunting of the pre-crack. Overall, K_{Ic} validity depends on a variety of conditions, the main ones being:

- Sharp pre-crack conditions created by a low prior fatigue load (the fatigue crack loading in the terminal stage of fatigue cracking must not exceed 60% of K_Q, where K_Q is the measured stress-intensity factor at fracture.
- The crack tip plastic region has to be small compared to the crack size or the specimen thickness. The following criterion is used:

  $2.5\left(\frac{K_Q}{\sigma_{YS}}\right)^2 < B,a$ Where B is the sample thickness, a is the crack length, K_Q is derived from the 95% offset load value, P_Q, as defined in the ASTM standard E399.
- $P_{max} / P_Q < 1.10$ where P_{max} is the maximum load experienced by the sample

When all the conditions are satisfied the K_Q value is then considered as K_{Ic}. If not, the calculation of the specific strength ratio, R_{SX} can be carried out to give semi-quantitative information about the properties of the material.

Three tests were performed for each condition (see Table 4.3) for the 7150 and 7449 alloys; two tests were performed for the 7449 (Mn) alloy due to limited available material.

4.7 Tensile tests

Tensile tests on the materials were carried out in general accord with ASTM standard E-8 with Hounsfield 'C' specimens (see Figure 4.7) for 7449 and 7150 in T651(7449), T7951, T7651 conditions, and Hounsfield 'A' specimens for 7449 and 7449(Mn) respectively in T7A, T7B, T7C, T7D, T7E conditions and T6, T76, T7C conditions. Three tests were performed for each condition. Specimens were taken in L orientation (i.e. parallel to the rolling direction). Tests were performed with specimens machined from the middle and quarter thickness positions of the 7449 and 7150 plates

for T651(7449), T7951 and T7651 heat treatments. Other tests were performed with specimens machined from the middle thickness position of the plates.

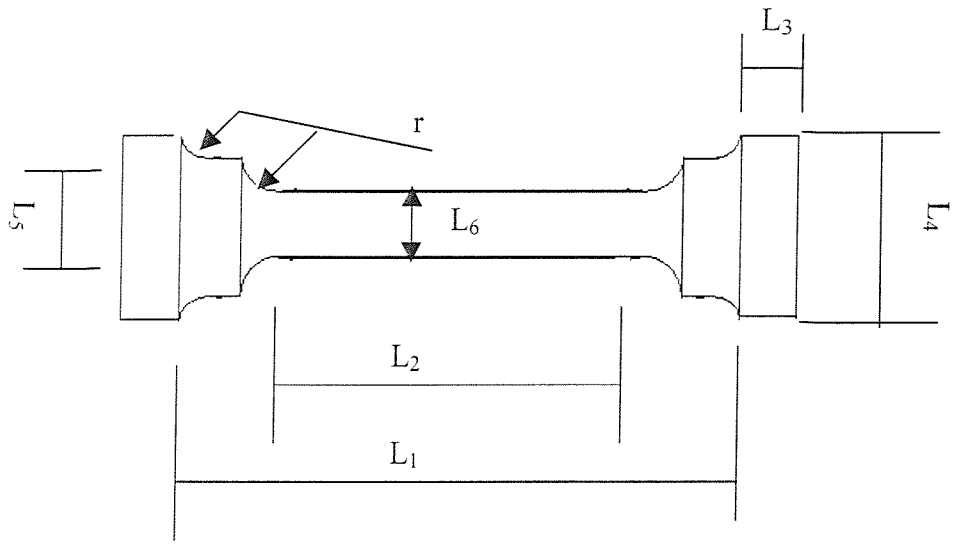

	Hounsfield 'A'	Hounsfield 'C'
L_1	21.7	31
L_2	12.6	17.9
L_3	3	4
L_4	7.5	10
L_5	5.5	7
L_6	3.5	5
r	1	1.5

Figure 4.7: Schematic drawing of the Hounsfield tensile specimen 'A' and 'C' with their respective dimensions (length in mm)

The strain was recorded using a 10mm gage extensometer for Hounsfield specimen 'C' and a 5mm gage extensometer for Hounsfield specimens 'A'. The yield strength was measured as the stress at 0.2% plastic strain. The ultimate tensile strength is the maximum nominal stress reached in the test. The strain hardening coefficient *n* has been measured from the stress-strain curves using the equation

$$\sigma_t = H\varepsilon^n \tag{4.6}$$

Where H is a constant, σ_t is the true stress and ε is the true strain

Therefore n is the slope of the curve log σ_t = f(log ε) and is calculated by a linear regression using 5 values for plastic strains between 1 and 5%.

4.8 Notch tensile tests

L-oriented, circumferentially notched tensile specimen of 7449, with varying notch acuity, were fractured to establish a stress-state dependent fracture locus ($\varepsilon^p_f(\sigma_m/\sigma_{fl})$) for the 7449 alloy. Stress-state triaxiality is expressed as the ratio of mean stress (σ_m) to effective flow stress (σ_{fl}) and is dependent on notch geometry [47]:

$$\frac{\sigma_m}{\sigma_{fl}} = \frac{1}{3} + \ln\left(\frac{d}{4R} + 1\right) \tag{4.7}$$

Where R is the initial notch root profile radius and d is the initial notch root diameter as illustrated in Figure 4.8. Three different geometries have been tested (see Table 4.4).

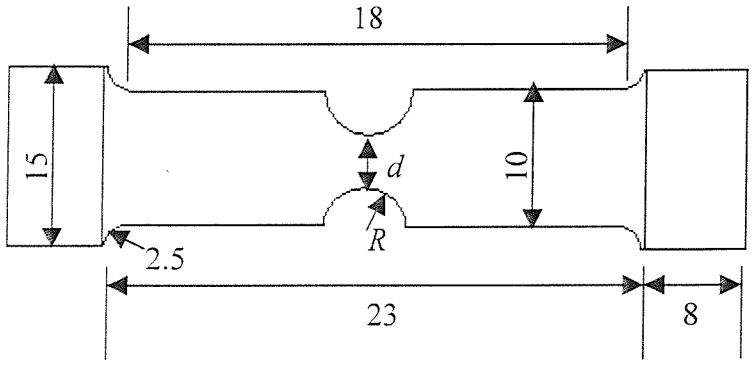

Fig. 4.8: Schematic drawing of the notch tensile specimen geometry (length in mm)

d(mm)	R(mm)	σ_m/σ_{fl}
5	1	1.144
5	2.5	0.739
4	3	0.621
Unnotched tensile specimen		0.333

Table 4.4: Notch geometry and corresponding triaxial-state values

The diameter at failure, d_f, was determined from two orthogonal measurements of the fracture surface. Effective plastic strain at fracture depends on diametrical contraction according to:

$$\varepsilon_f^p = 2\ln\left(\frac{d}{d_f}\right) \tag{4.8}$$

4.9 Arrested crack tests

The crack paths in the alloys have been studied using optical microscopy on polished and etched arrested crack specimens. The specimens were chevron-notched bars of rectangular cross section, as shown in Fig. 4.9. The specimens were taken in the same orientation as the toughness specimen (L-T). A bolt loading device was used to produce a crack within the samples, which would run and arrest due to the constant displacement conditions. The crack was then filled with an epoxy resin under pressure using a vacuum dessicator to preserve the specimen edges for subsequent sectioning and polishing.

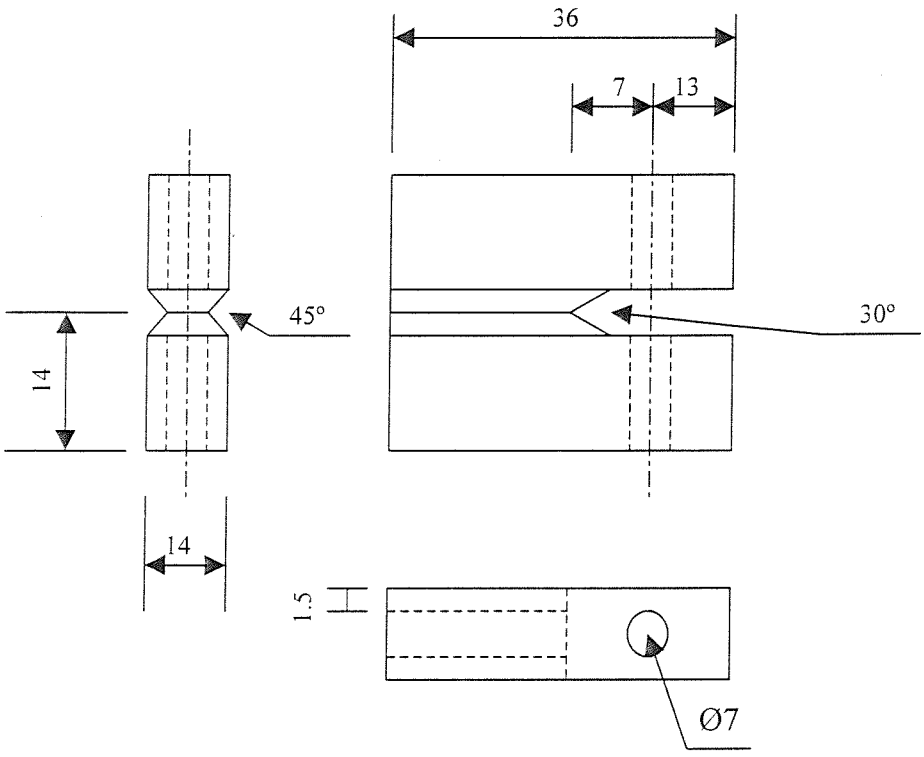

Figure 4.9: Schematic drawing of the chevron-notched specimen (length in mm)

Chapter 5

Microstructure and mechanical properties: results

5.1 Grain structure

Optical micrographs of the 7449, 7449(Mn) and 7150 alloy grain structures are presented in Fig. 5.1. The 7449 and 7150 alloys exhibit a similar grain structure, with the structure of both alloys being strongly elongated in T and L directions. The 7449(Mn) alloy grain structure is clearly less significantly elongated.

The three alloys exhibit a certain amount of recrystallisation. From optical micrographs, the amount of recrystallisation was estimated at 20% for the 7449 alloy and 30% for the 7150, whilst the 7449(Mn) alloy appeared to be fully recrystallised.

The grain size represented as the mean free path between boundaries in the short transverse (ST) direction, d_S, has been measured by the mean linear intercept method. For the 7150 alloy d_S is slightly larger (about 16μm) than for the 7449 alloy, for which d_S was about 12μm (Table 5.1). For both alloys, a wide range of subgrain sizes was seen (~3 to 10μm). The 7449(Mn) exhibit a much coarser grain structure, with d_S reaching 40μm.

5.2 Coarse intermetallics

Optical microscopy showed that coarse intermetallics were inhomogeneously distributed; they mainly appeared as bands of particles oriented in the rolling direction. Intermetallics were especially observed in recrystallised grains. The coarse intermetallic particles were examined in the SEM (see Fig. 5.2 and 5.3). This analysis identified two different kinds of Cu containing particles for the 7150 and 7449 alloy: one containing Al, Fe and Cu (which is believed to be Al_7Cu_2Fe) and the other Al, Mg and Cu (believed to be S phase [36]). In the 7449(Mn) alloy, Al-Fe-Cu, Al-Mn-Fe and Mg-Zn particles were observed. Similarly to 7449 and 7150, the Al-Fe-Cu containing particles were thought to be Al_7Cu_2Fe; the Al-Mn-Fe phase is possibly Al_6MnFe (Mn dispersoids, Al_6Mn, can

contain Fe when it is present in solution) [87]. Mg-Zn coarse particles are believed to be undissolved coarse η precipitates. EDS analysis of some of the smaller particles contained in the three alloys, which appear black in the optical micrographs, showed that they contained Si and Mg, and were therefore identified as Mg_2Si. The image analyser enabled particles to be distinguished by their grey level and their area fractions were determined (see Fig. 5.3). For all alloys, the area fraction of black particles (Mg_2Si) was between 0.1 and 0.2%. The 7150 alloy contained the greater amount of mid-grey particles (S and Al_7Cu_2Fe), corresponding to 1.6%, approximately the double of the amount contained in 7449 (0.9%) and 7449(Mn) (0.9%). Volume fractions of intermetallic phases are presented in Table 5.2.

5.3 TEM

The TEM experiments reveal aspects of the grain structure, with Fig. 5.5 showing both recrystallised and unrecrystallised regions. Details of the different precipitates are shown in Fig. 5.6: a homogeneous distribution of small (i.e. <50nm) precipitates and somewhat larger dispersoids (presumably Al_3Zr) were identified within the grains, with coarse η particles at the grain boundaries. The width of the grain boundary precipitate free zones (PFZ) was seen to vary between 40 and 70nm for the various treatments considered here (Fig 5.7); no simple variation of PFZ width with degree of overageing could be observed. Large variations in grain boundary precipitate size (see Fig. 5.8) and area coverage of the grain boundaries within single samples were observed (see Fig. 5.9). Grain boundary precipitates were generally of ellipsoidal shape, elongated along the grain boundary (see Fig. 5.10), with aspect ratios varying between 2 and 6. Grain boundary precipitates having preferential orientations at an angle with grain boundary have also been observed (Fig. 5.11). Grain boundary precipitates sizes vary between 20 and 60nm for the 7150 aluminium alloy, with no significant differences between T7951 and T7651, whereas for the 7449 aluminium alloy, precipitates sizes seem to vary from about 25nm in the T7951 condition to 55nm in the T7651 condition, with little apparent growth with further overageing to T7E.

5.4 DSC

All three alloys, in all the ageing conditions applied, were studied by DSC, and results are presented in figures 5.12, 5.13, 5.14 and 5.15. All the DSC curves show similar general features (Figs. 5.12, 5.13, 5.14 and 5.15). The nature of the different peaks has been detailed in the literature [88,89]. The peaks are numbered identical to earlier work [88], and their nature is discussed below.

It should first be noted that in freshly quenched 7xxx alloys GP zone formation (an exothermic effect) is expected to occur at temperature lower than 150°C during DSC scanning, but that in the present naturally aged, peak aged and overaged alloys no peak due to GP zone formation is observed (This exothermic zone formation peak (Peak I) has indeed been observed in the solution treated and quenched 7449 alloy, where it occurs in the range of 30 to 100°C [89]). The absence of this peak even in W51 conditions (see Figs. 5.13 and 5.14) suggests that in the present alloy GP zone formation has been completed very early on during the natural ageing process.

The first endothermic peak (peak II, see Fig. 5.12) shifts to higher temperatures as the ageing treatment becomes more severe (see Figs. 5.13 and 5.14). This corresponds to the results obtained in the literature (see e.g. [90]). For the W51 temper the first endothermic peak is usually associated with GP zones dissolution. For instance, Garcia-Cordovilla and Louis [20] found a GP zone dissolution peak temperature of 130°C that is in agreement with our work. For the peak-aged alloy the first endothermic peak occurs at higher temperature. Papazian [91], studying the reaction kinetics of 7075 Aluminium in the T6 condition, shows that the first dissolution peak is made up of simultaneous formation and dissolution reactions that can be GP-zone dissolution, η' formation and η' dissolution. Delasi and Adler [89] assume that the first endothermic peak represents mainly GP dissolution for the under-aged (UA) alloys, and represents mainly η' dissolution for the over-aged (OA) alloys, which explains this shift to higher dissolution temperature with increasing the ageing severity. However, it is not always clear whether this peak is dominated by GP-zone or η' dissolution as Delasi and Adler [89] consider that this peak represents both GP-zone and η' dissolution for peak-aged (T651) 7075 alloy.

According to the literature [89] the second peak (peak III, see Fig. 5.12) is a combination of up to three reactions, η′ formation and growth, η formation and T formation, leading to a three peak shape for underaged alloys. In the overaged temper, i.e. when most η′ phase is already formed, the triple peak becomes a double peak shape that may represent the formation of η and T. However, some authors [60] consider this double peak shape in peak aged alloys to be due to η′ and η formation. The total heat evolved decreases with the increase of the ageing treatment (Fig. 5.13, 5.14). This can be explained as follows. It is known that during ageing, η′ and η are formed. Hence, the amount of η′ and η forming during the DSC run, which depends on the remaining Mg and Zn dissolved in the Al-rich matrix to form the precipitates, is reduced, thus reducing the total heat evolved.

The second endothermic peak (peak IV, see Fig. 5.12) corresponds to the dissolution of the phases present after precipitation (mostly stable η). This reaction is to a large extent determined by the equilibrium solvus of the dissolving phase(s) (e.g. the thermodynamic equilibrium between η and the Al-rich phase) [21], and this equilibrium is temperature dependent. As the present T6 and T7 ageing treatments will have little effect on the microstructure that the DSC samples have developed by the time the start of peak IV (about 280°C) is reached, this peak is very similar for all the samples.

For the 7449 (Mn) alloy, a sharp endothermic peak is found around 480°C. Such peak has previously be observed for 7xxx alloys and was associated with the melting T or η phase [92].

For the 7150 alloy, a sharp endothermic peak is found around 500°C (peak VIII, see Fig. 5.13), which represents the melting of the S (Al_2CuMg) phase [41,88]. There is no evidence of any effect of ageing on this peak, as it does not seem to vary systematically with the heat treatment. This indicates that this peak is sample dependent, involving S phase formed during ingot casting.

Throughout the various heat treatments, both alloys have a similarly shaped peak II, but the complex precipitation peak (peak III) shows marked changes. In the peak aged condition the total heat evolved during peak III is higher for the 7449 alloy (see Fig. 5.12). This can be explained by the higher Zn content of the 7449 alloy. However, in overaged conditions, the trend is reversed and for T79 and T76 conditions the 7150 alloy

shows a higher exothermic heat evolution (Fig. 5.13 and 5.14). This suggests that the rate of Zn precipitation during T7 treatments is higher for the 7449 alloy than for the 7150 alloy, causing the η′ and η precipitation peaks to decrease in size faster for the 7449 alloy. The higher amount of η in the 7449 alloy is evidenced by the higher peak area of peak IV for all the ageing treatments. The peak VIII relating to S phase melting does not appear at all in the 7449 (Zr) alloy. In 7150 alloy, this peak seems to be dependent on the position within the plate suggesting that there is a higher amount of S phase at the quarter depth position of the plate (Fig. 5.16).

5.5 Mechanical tests

The present materials are relatively high strength aluminium alloys, with T6 yield strengths of 600 MPa for the 7150 alloy, 625 MPa for the 7449 alloy and 546 MPa for the 7449(Mn) alloy (Table 5.3). The high strength levels of the 7449 and 7150 alloys is illustrated in Fig. 5.17 by comparison with 7475 and 7075 alloys. The yield strengths of 7449 are at least 20 MPa higher than those of 7150 for all commercial heat treatments, which is in line with the literature [2]. The 7449 T6 yield strength is more than 100MPa greater than 7075 T6 for the same fracture toughness level [2]. It should be noted that the heat treatments considered in this study were designed for the 7449 alloy. Hence, the 7150 and 7449 (Mn) alloys in their respective heat treatment conditions are not an entirely fair comparison. The T651 treatment used in the 7449 alloy will in fact be a slightly underaged condition for the 7150. Similarly, The T6 treatment applied in this study to the 7449 (Mn) alloy is not strictly the designed ageing treatment to achieve peak strength for this alloy: reports on Mn containing Al-Zn-Mg alloys [93,94] suggest that our T6 treatment will also correspond to an overaged treatment for the 7449(Mn) material.

For the toughness tests, two valid K_{Ic} values were obtained for each condition for the 7150 and 7449 alloy. For the 7449 (Mn) alloy, only K_Q values were obtained due to the bowing of the fatigue pre-crack. However these values were coherent between them and compared to the other alloys, therefore for the clarity of the discussion these K_Q

values will be refered to in subsequent chapters as K_{IC} values*. As expected, the yield strength decreases and the toughness increases on increasing overageing, i.e. in going from T651 to T7E (Fig. 5.17). As overageing is increased from T651 to T7E for the 7449 alloy the strength decreases in an approximately linear manner with the increasing toughness. In the T7951 and T7651 conditions the 7150 and 7449 alloys show similar levels of toughness (but with better strength properties in the 7449 alloy). 7449 (Mn) alloy strength-toughness properties in T6 and T76 conditions are in the same range as the 7449 alloy strength-toughness property linear recovery trend. However, strictly comparing the 7449(Mn) alloy to the 7449 respectively in T6 condition and T76 conditions, Fig. 5.17 shows that 7449(Mn) exhibit a slightly better toughness value but with a much lower yield strength. In T7C condition, 7449(Mn) has a yield strength 80MPa above the 7449 T7C yield strength for the same level of toughness. 7449 (Mn) T7C alloy strength-toughness combination is in near the 7475 T6 aluminium alloy. The 7449 (Mn) alloy has a toughness recovery rate (i.e. associated with decreasing strength) greater than that of the 7449 alloy.

For all tensile tests performed, the applicability of Ashby's work hardening equation (Chapter 2 Eq. 2.2) was assessed and compared to the classical Ramberg-Osgood equation, by fitting the corresponding equations to the experimental stress-strain curves. The fitting of the experimental stress-strain curves by the exponential model and the Ashby model (Eq. 2.2) revealed that for $0.01<\varepsilon_p<0.05$ the Ashby model is more accurate than the exponential fit for most samples tested and at least equivalent for few of the samples. Table 5.4 shows the root mean squared error (RMSE) between the experimental data and the different work hardening models. The RMSE value is define as follows:

$$RMSE = \sqrt{\frac{\sum_{i=1}^{m}\left(\sigma_{\exp erimental,i} - \sigma_{\mathrm{mod}elling,i}\right)^2}{m}} \qquad (5.1)$$

* In subsequent chapters K_{Ic} values are plotted for each test.

where m is the number of data point considered, $\sigma_{experimental}$ and $\sigma_{modelling}$ are respectively the stress experimental value and the stress value derived from the models (taken at identical strain values). This table shows that over this range of strain, the Ashby model is accurate to about 2% of the experimental data whereas the Ramberg-Osgood model can deviate by up to 5% from the experimental values.

The strain hardening parameters K_A and n show different trends with ageing; n increases consistently with ageing for both alloys, whereas K_A is initially approximately constant (in the T6 and T79 conditions for 7150 and 7449 alloys, and in the T6 and T76 conditions for the 7449 (Mn) alloy) before a marked increase in the more overaged conditions (T76 for the 7150 alloy, T76 to T7E for the 7449 alloy and in T7C condition for the 7449 (Mn)).

The elongations to rupture of the 7150 and 7449 alloys are similar (Table 5.5). They range between 10.5 and 15%. The elongations in the 7449 (Mn) alloy are much smaller, from 5.3% in the T6 condition to 8.6% in the T7C. The critical strain for the 7449 alloy, calculated from the reduction area in smooth tensile specimens, showed a consistent increase with overageing.

Tensile tests conducted for the 7150 and 7449 alloys with samples extracted from the plate centre and plate quarter showed only limited differences in terms of yield strength, tensile strength or elongation (Table 5.5).

5.6 Notch tensile tests results

Notch tensile tests were performed to establish stress-state dependent fracture strains. The triaxial stress-state depends directly on the notch geometry and is systematically varied in the present tests. Fig. 5.18 shows the fracture strains related to their stress-state for different heat treatments for the 7449 alloy (see section 3.2 also). The figure shows that the critical strain to fracture increases with more severe heat treatments. The critical strain also decreases with more severe (triaxial) stress state conditions. The results for the 7449 alloy are broadly consistent with results reported in the literature for other 7xxx alloys [95].

5.7 Fractography

From the fracture surfaces of the failed toughness samples, various features can be recognized (Fig. 5.19 to 5.25). 7449 and 7150 alloys samples showed reasonably similar features, whilst the 7449 (Mn) alloy exhibited quite distinct fracture characteristics. Fractographic features of the 7449/7150 alloys and the 7449 (Mn) alloy are therefore reviewed separately below.

5.7.1 Fractographic analysis of the 7449 and 7150 alloys

The presence of coarse voiding was generally evident in the 7449/7150 samples, with large intermetallics visible inside the voids (see e.g. Fig. 5.19f). The presence of ridges in the T direction (which is the predominant grain boundary direction) also indicates some interaction with the grain boundaries (see Fig. 5.19a). The ridges were specifically linked to the grain boundary locations (Fig. 5.23), however fracture was clearly not wholly intergranular, i.e. linkage of grain boundary failure in the S direction was at least partly transgranular in keeping with the observation of Ludtka and Laughlin [96]. For both alloys it was clear that the rupture mode was influenced by the ageing condition; the T7651 condition is more 'ductile' (exhibits a higher proportion of coarse primary voiding), with less of the ridge-like features as compared to the T651 condition. On further ageing of the 7449 alloy to the T7E condition, a more complete transition occurs to principally coarse voiding.

Edge-on observation of the microstructure on the L-S plane and the fracture surface have clarified the nature of the linear ridges. They appear to be formed from the grain boundaries (Fig. 5.23). An important feature of the linear ridges is that the "valley" between ridges is rarely observed to propagate down the grain boundary into the bulk of the sample. The valleys between ridges are generally rounded in the L-S plane. Fig. 5.23 clearly illustrates the difference between rounded valley features and a secondary crack which has propagated down the grain boundary, marked by "X" in the figure. Such true delamination has only been observed occasionally. It is interesting to note the link between grain boundaries which are well decorated by particles, and the ridge separations

(Fig. 5.24). From the fractographic results, it is difficult to determine whether the more decorated boundaries are grain or subgrain boundaries. However, Fig. 5.23 and 5.24 show that boundaries between unrecrystallised and recrystallised grains exhibit these features suggesting that the more decorated boundaries are high angle boundaries.

Edge-on observations of the fracture surface and the L-T plane in the 7449 and 7150 alloys (Fig. 5.25) (i.e. parallel to the crack growth direction) reveal further aspects of the multimechanistic nature of the fracture process. Transgranular shear through both unrecrystallised and recrystallised areas is evident, whilst there was clearly some influence of the boundaries of recrystallised grains on the fracture path for the two alloys. Particularly, transitions from linear ridges to clear grain boundary failure was observed between recrystallised and unrecrystallised grains. Continuous linear features running across recrystallised and unrecrystallised areas were also identified. Whilst interactions between recrystallised and unrecrystallised grains were sometimes evident, little influence of substructure on crack growth was seen.

Optical microscopy observation on LS (Fig. 5.26) and LT planes (Fig. 5.27) of arrested crack specimens further illustrates the features revealed by the edge-on SEM observations for the 7449 and 7150 alloys. Figure 5.26 shows failure at grain boundaries where the adjacent grain has necked down to a relatively fine point (see locations X). However, many regions of apparent shear decohesion are also seen (see locations Y), illustrating the complex nature of the failure in this material. Multiple failure modes are highlighted in Fig. 5.27.

5.7.2 Fractographic analysis of the 7449 (Mn) alloy

The 7449 (Mn) material has a quite distinct mode of rupture compared to the 7150 and 7449 alloys, as shown in Fig. 5.21. The fracture mechanism is associated with fine tensile voiding. Large areas of the plane strain zone of the failed samples are covered by small voids (<5μm). Particles up to 1μm are visible within these voids (Fig. 5.22). These particles have an ellipsoidal or round shape. The voids surrounding these particles are only 2 or 3 times bigger than the particles. More coarse voiding was also seen in this alloy (Fig. 5.28), however, it was not a dominant feature of the fracture surface. Evidence

of interaction of the grain boundaries with the fracture process has been identified: lower magnification SEM micrographs show small ridges (<100μm) orientated in the T direction (Fig. 5.29). However, these ridges are not linked together and are widely spaced. The fracture mechanism for the 7449 (Mn) shows no obvious sign of evolution/change with ageing condition.

	Mean free path, average grain intercept (μm)		
	d_S	d_L	d_T
7150	16	79	34
7449	12	60	20
7449(Mn)	40		

Table 5.1: Grain sizes represented as "mean free path" in S, L and T direction of the 7449, 7150 and 7449(Mn) materials.

	Intermetallic phases (% volume fraction)		
	Mg_2Si	Al_7Cu_2Fe and Al_2CuMg	Al_7Cu_2Fe, Al_6MnFe, $MgZn_2$
7150	0.15	1.5	-
7449	0.17	0.75	-
7449(Mn)	0.13	-	0.79

Table 5.2: Intermetallic content of 7150, 7449 and 7449(Mn) alloys.

		σ_{ys} (MPa)	Standard Error (SE)*	σ_{UTS} (MPa)	SE	K_{Ic} (MPa$\sqrt{m}$)	SE	n	SE	K_A (MPa.m$^{-1/2}$)	SE	elongation (%)	SE
7150	T651	599	7	644	12	31.0	1.7	0.051	0.0007	391	27	12.9	0.5
	T7951	572	3	617	8	29.2	0.6	0.055	0.007	396	31	11.4	0.4
	T7651	566	4	617	4	31.3	1.4	0.059	0.003	435	13	10.5	0.3
7449	T651	627	8	665	5	25.6	1.6	0.041	0.002	365	4	12.6	0.8
	T7951	591	2	622	1	28.1	1.7	0.046	0.001	343	19	10.5	0.4
	T7651	584	12	614	3	31.3	0.9	0.047	0.007	392	1	11.1	1.1
	T7A	512	5	561	5	34.3	1.1	0.063	0.004	455	25	12.6	0.1
	T7B	472	10	535	12	39.4	0.9	0.082	0.002	549	4	13.2	0.4
	T7C	421	10	498	10	43.7	2.1	0.103	0.003	622	23	13.6	0.6
	T7D	426	3	500	4	42.7	0.3	0.104	0.002	569	18	14.5	0.2
	T7E	404	5	481	3	45.4	2.0	0.108	0.007	560	38	15.0	1.2
49(Mn)	T6	449	3	586	8	30.1	0.3	0.036	0.02	300	42	5.3	2.0
	T79	400	10	577	2	33.8	0.6	0.037	0.01	297	25	7.3	2.1
	T7C	363	6	545	4	44.5	1.0	0.063	0.01	422	23	8.6	1.2

ıe standard error (*SE*) for *n* tests having a range of value $\Delta Values$ is defined as: $SE = \frac{\Delta Values}{\sqrt{n}}$

le 5.3: Tensile and fracture toughness tests results.

		T6			T79			T76		
		1	2	3	1	2	3	1	2	3
7150	Ashby RMSE	-	0.70	0.53	0.51	0.50	-	1.54	0.26	0.40
	Ramsberg RMSE	-	1.20	1.04	0.66	2.24	-	1.90	0.61	0.70
7449	Ashby RMSE	0.43	-	0.23	0.16	0.19	0.25	0.07	-	0.37
	Ramsberg RMSE	0.73	-	0.62	0.12	0.16	0.10	0.33	-	0.23

		T7A			T7B			T7C			T7D			T7E		
		1	2	3	1	2	3	1	2	3	1	2	3	1	2	3
7449	Ashby RMSE	-	0.56	0.71	0.65	0.80	0.70	0.72	1.03	0.61	0.36	0.24	-	0.76	-	0.85
	Ramsberg RMSE	-	1.60	1.76	2.11	2.08	1.56	1.55	0.65	1.38	0.26	0.36	-	1.58	-	1.43

Table 5.4: Root mean square errors (RMSE) in fitting work hardening behaviour with the Ramsberg-Osgood and Ashby models

	7150					
	T651		T7951		T7651	
	center	quarter	center	quarter	center	quarter
yield strength (MPa)	599	595	572	577	566	557
UTS (MPa)	644	635	618	615	617	603
elongation (%)	12.9	12.7	11.4	11.1	10.5	10.4
strain hardening coefficient, *n*	0.0511	0.0508	0.0551	0.0516	0.0586	0.0559
	7449					
	T651		T7951		T7651	
	center	quarter	center	quarter	center	quarter
yield strength (MPa)	627	623	591	599	584	574
UTS (MPa)	664	657	622	625	614	607.5
elongation (%)	12.6	12.2	10.5	11.2	11.1	10.9
strain hardening coefficient, *n*	0.041	0.044	0.046	0.045	0.047	0.052

Table 5.5: Comparison of 7449 and 7150 tensile properties from samples extracted from the center position and quarter position of the plate

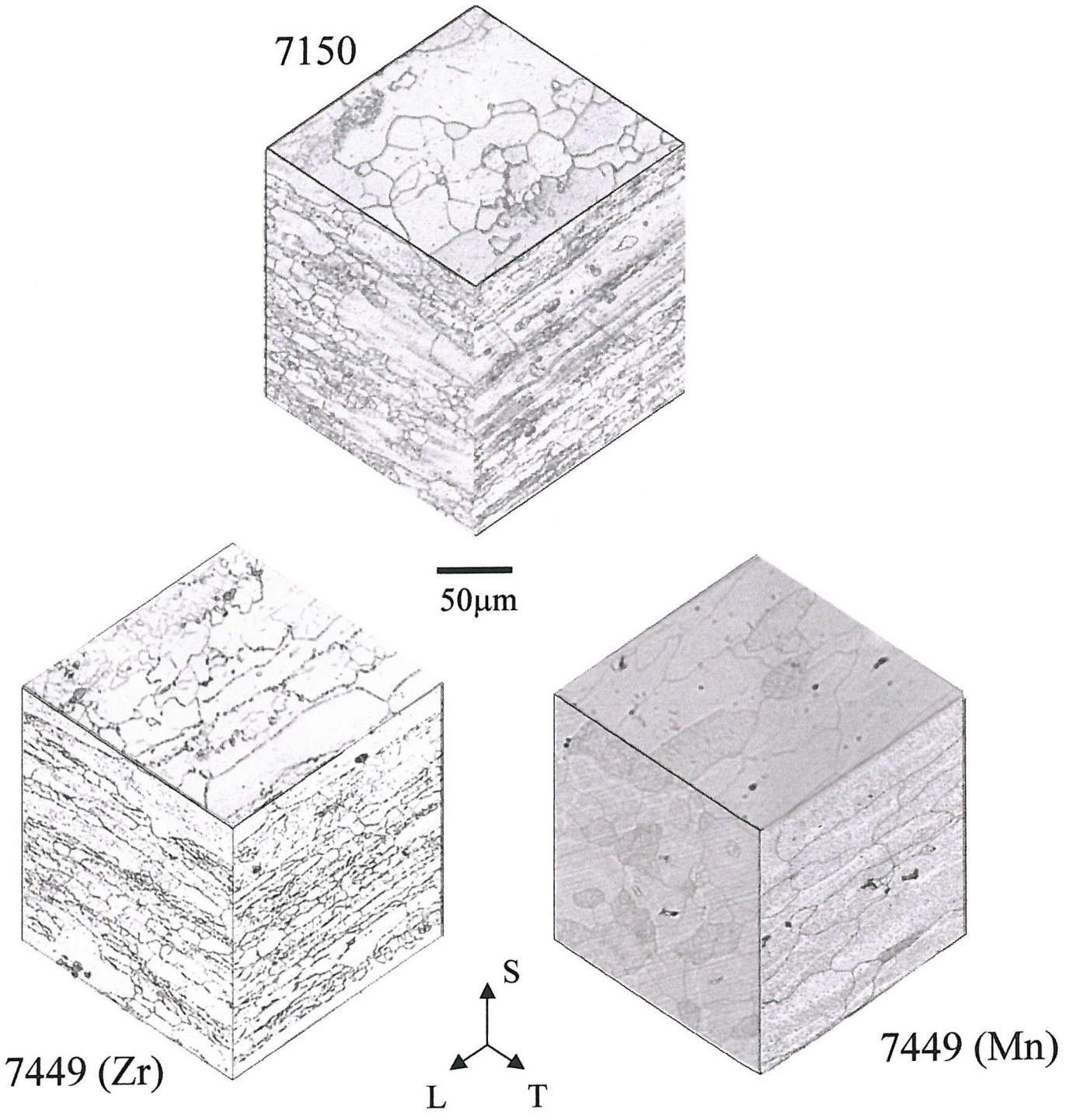

Figure 5.1: Optical micrograph of the 7449, 7150 and 7449 (Mn) materials: polished and etched sections

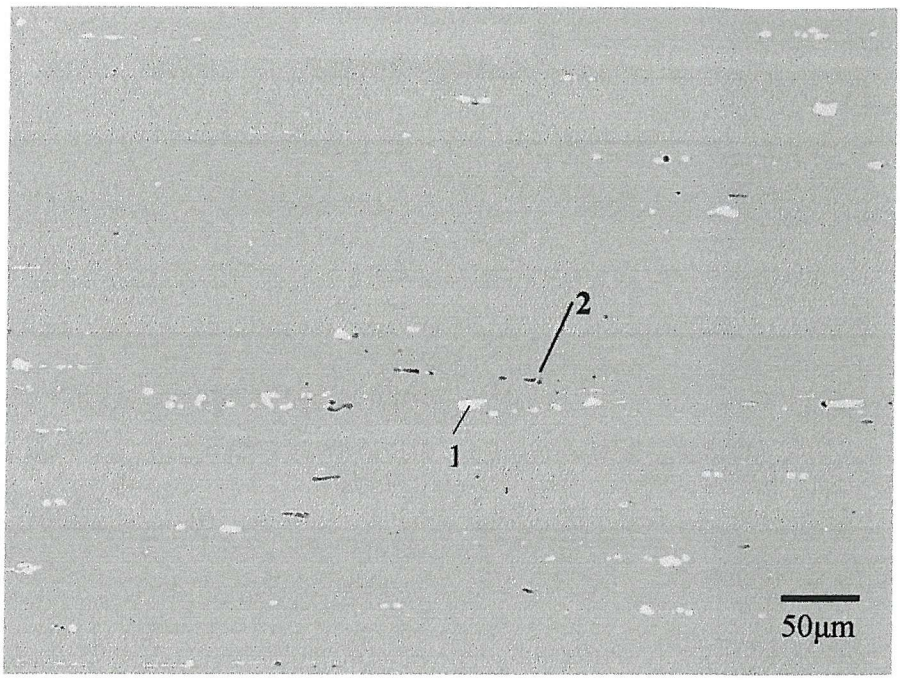

Figure 5.2: SEM backscattered image of LS polished section of the 7150W51 alloys where a systematic EDS analysis was performed on particles. Particles 1 was identified as 70%at Al-19.49%at Cu-9.43%at Fe-0.61%at Zn and particle 2 as 43%at Al-21.25%at Mg-34%at Si-0.5%at Cu-1.2%at Zn- Fe trace.

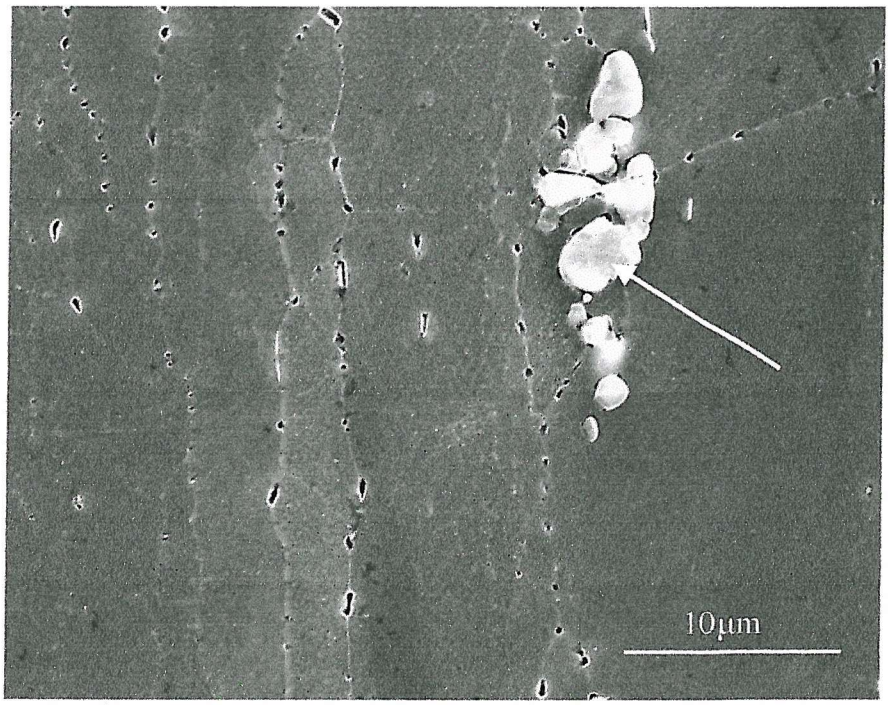

Figure 5.3: SEM backscaterred electron micrograph of a group of coarse Cu bearing intermetallics (arrowed) in the 7150W51alloy.

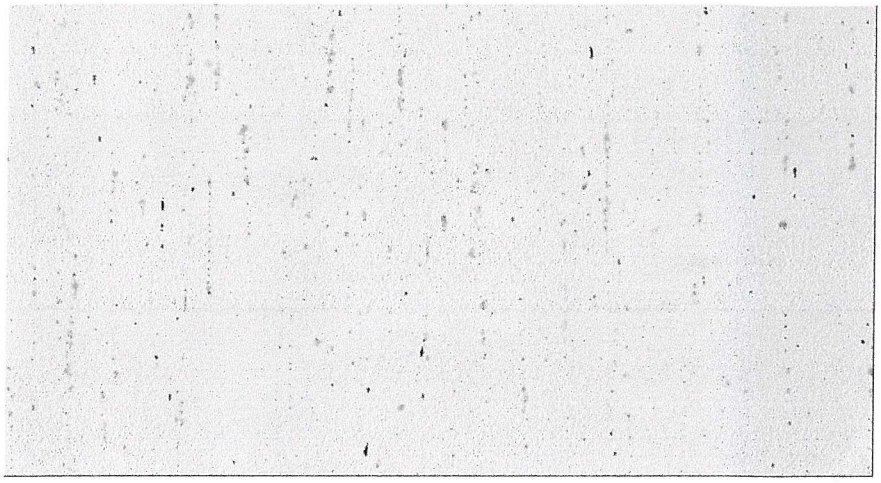

a)

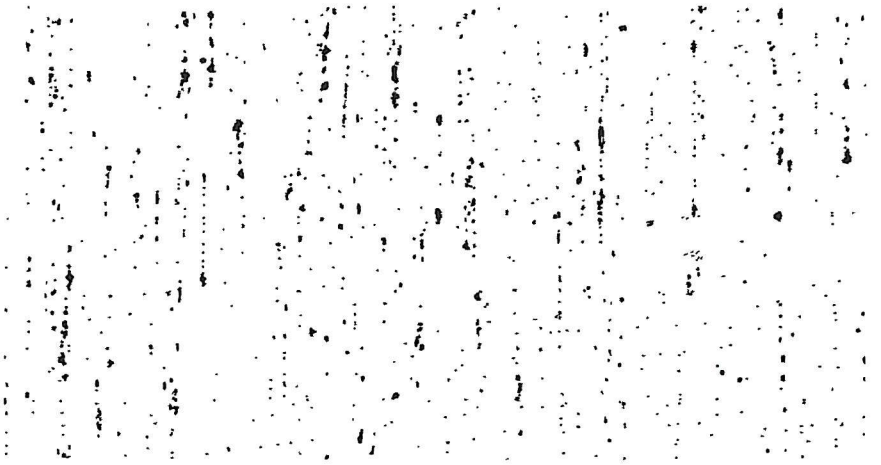

b)

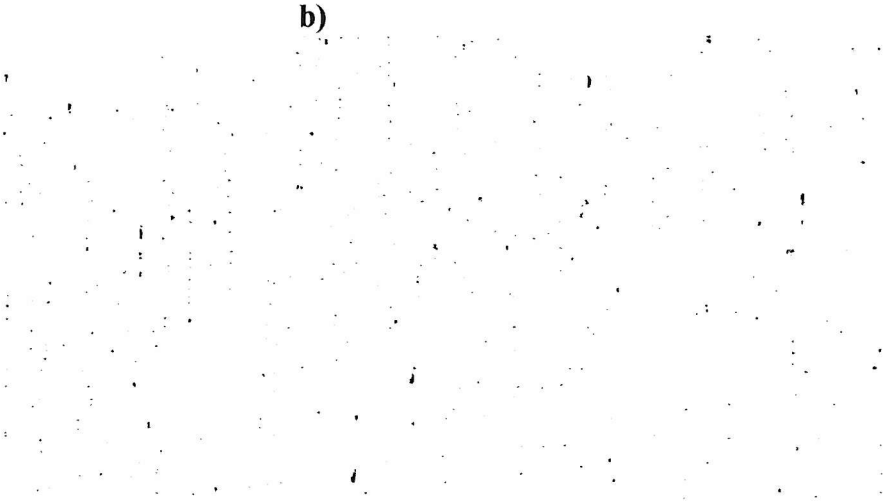

c)

Figure 5.4: a) Optical micrograph of the L-S face of the 7150 W51 alloy, polished and unetched, b) Binary image of Fig. 5.4.a) showing the black particles and grey particles, c) Binary image of Fig. 5.4.a) showing the black particles.

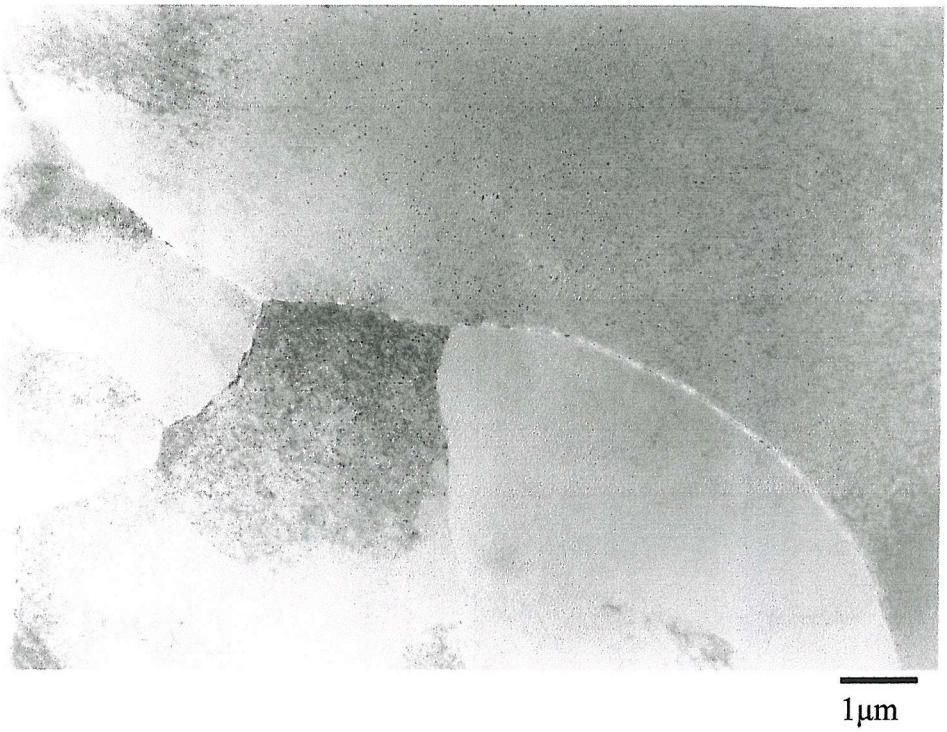

Figure 5.5: TEM micrograph of the grain structure of the 7449 T7951 alloy (bright field).

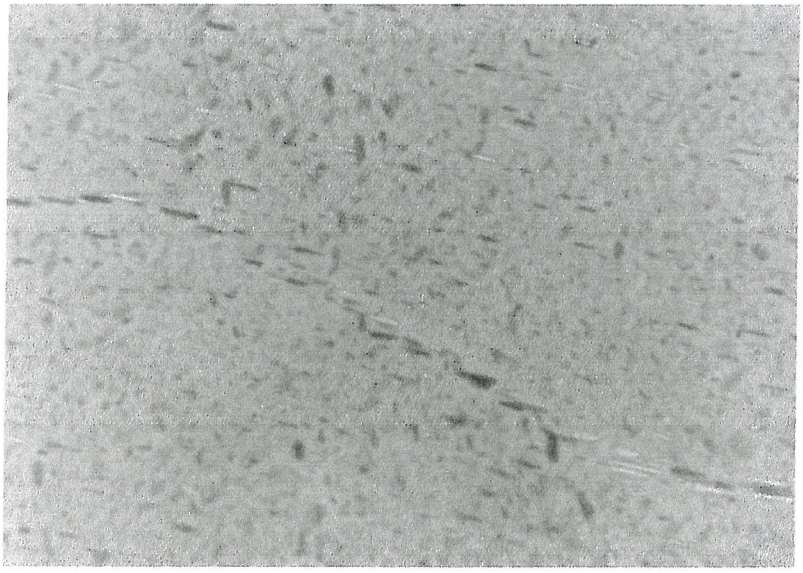

Figure 5.6: TEM micrograph of grain boundaries and matrix precipitation of the 7449 T7B alloy (bright field).

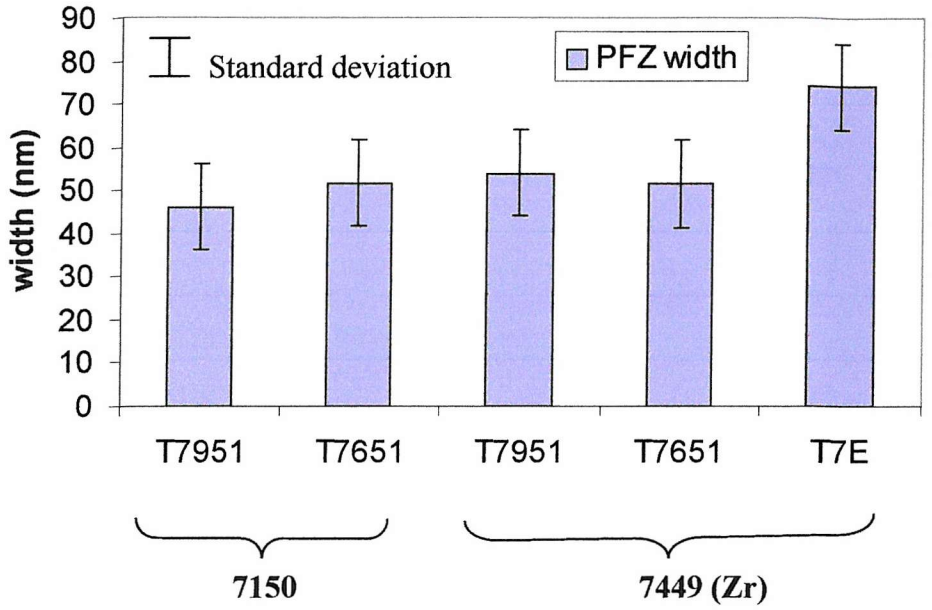

Figure 5.7: measured PFZ average widths for various heat treatments.

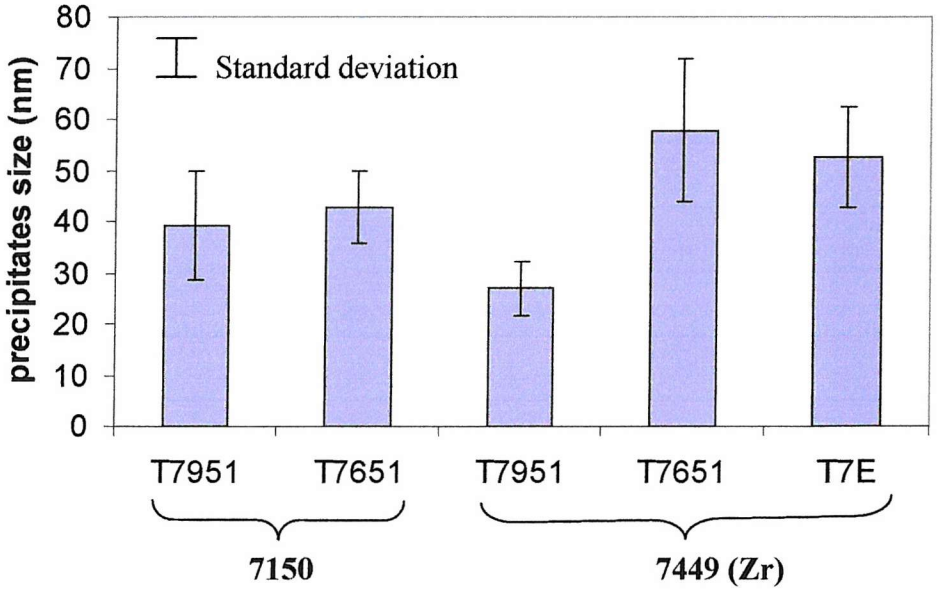

Figure 5.8: Grain boundary precipitate sizes (along maximum dimension) for various heat treatments.

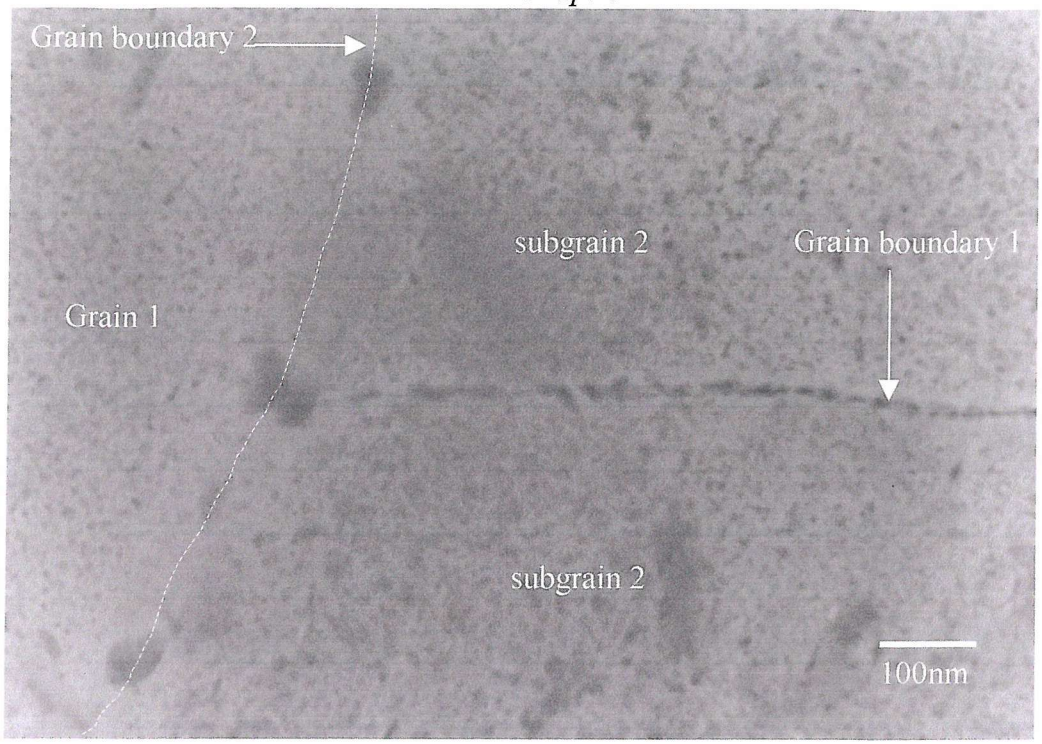

Figure 5.9: TEM micrograph of intersecting boundaries in the 7150 T7651 alloy. Grain boundary 1 exhibits a high area coverage of small grain boundary precipitates, whilst grain boundary 2 shows a low area coverage of large grain boundary precipitates. Grain boundary 1 is a boundary between two subgrains. Grain boundary 2 is a boundary between two grains.

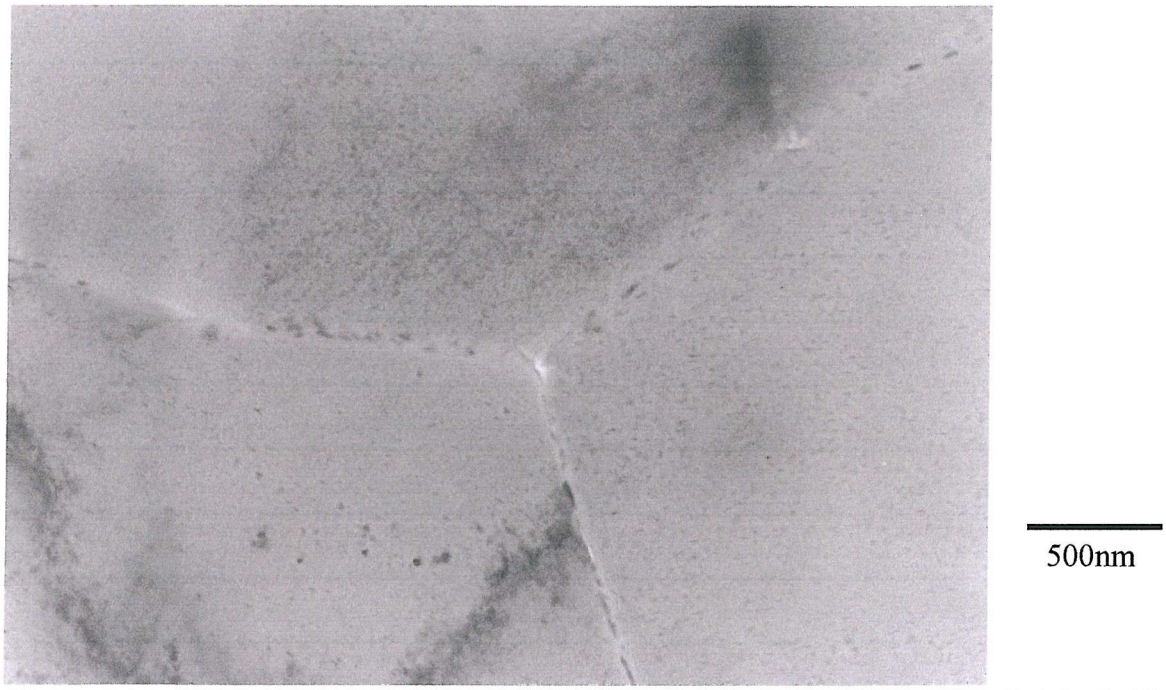

Figure 5.10: TEM micrograph of grain boundaries in the 7449 T7651 alloy (bright field).

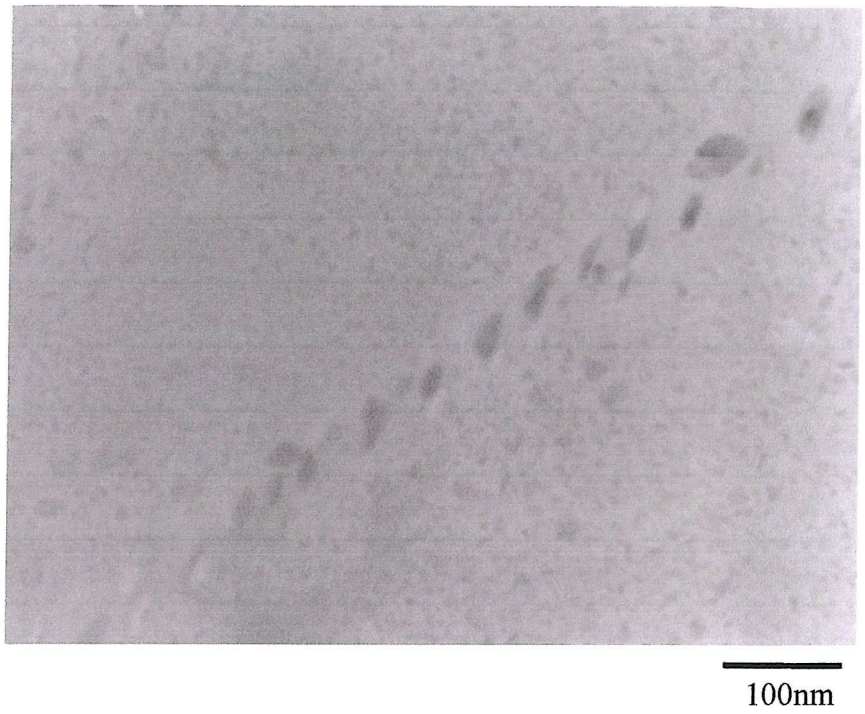

Figure 5.11: TEM micrograph of a grain boundary of the 7150 T7651 alloy showing grain boundary precipitates (brigth field).

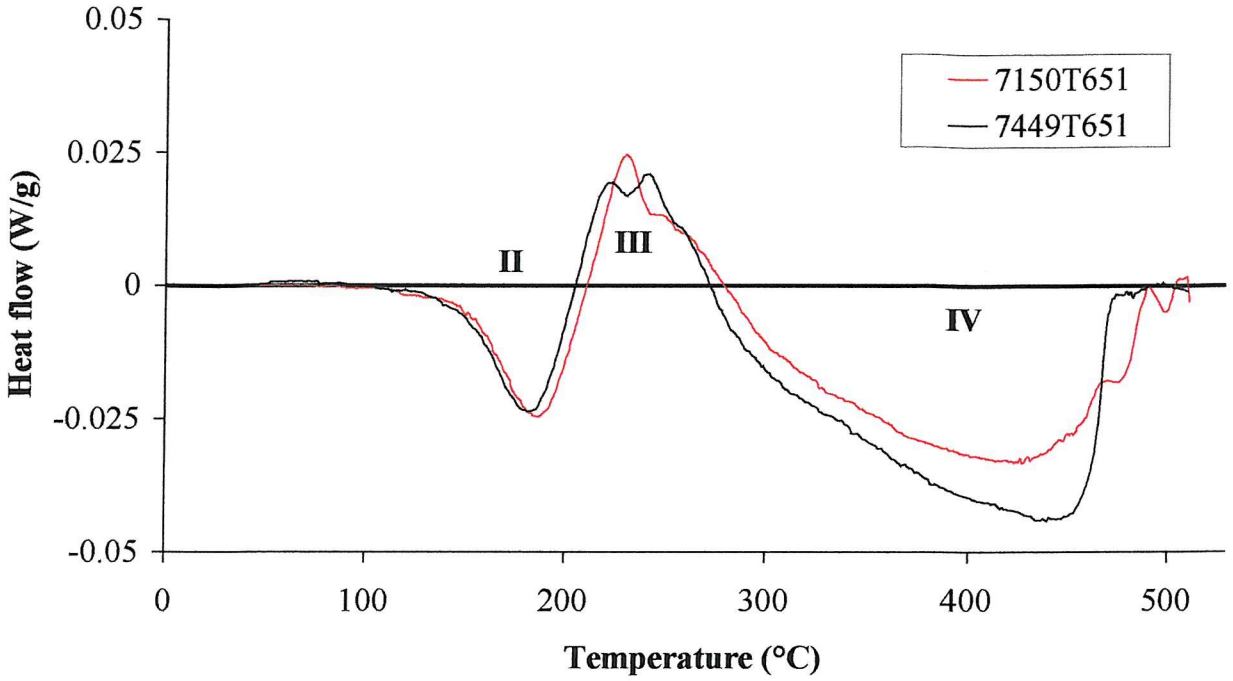

Figure 5.12: DSC curves of the 7150 and 7449 alloys in T651 heat treatment conditions.

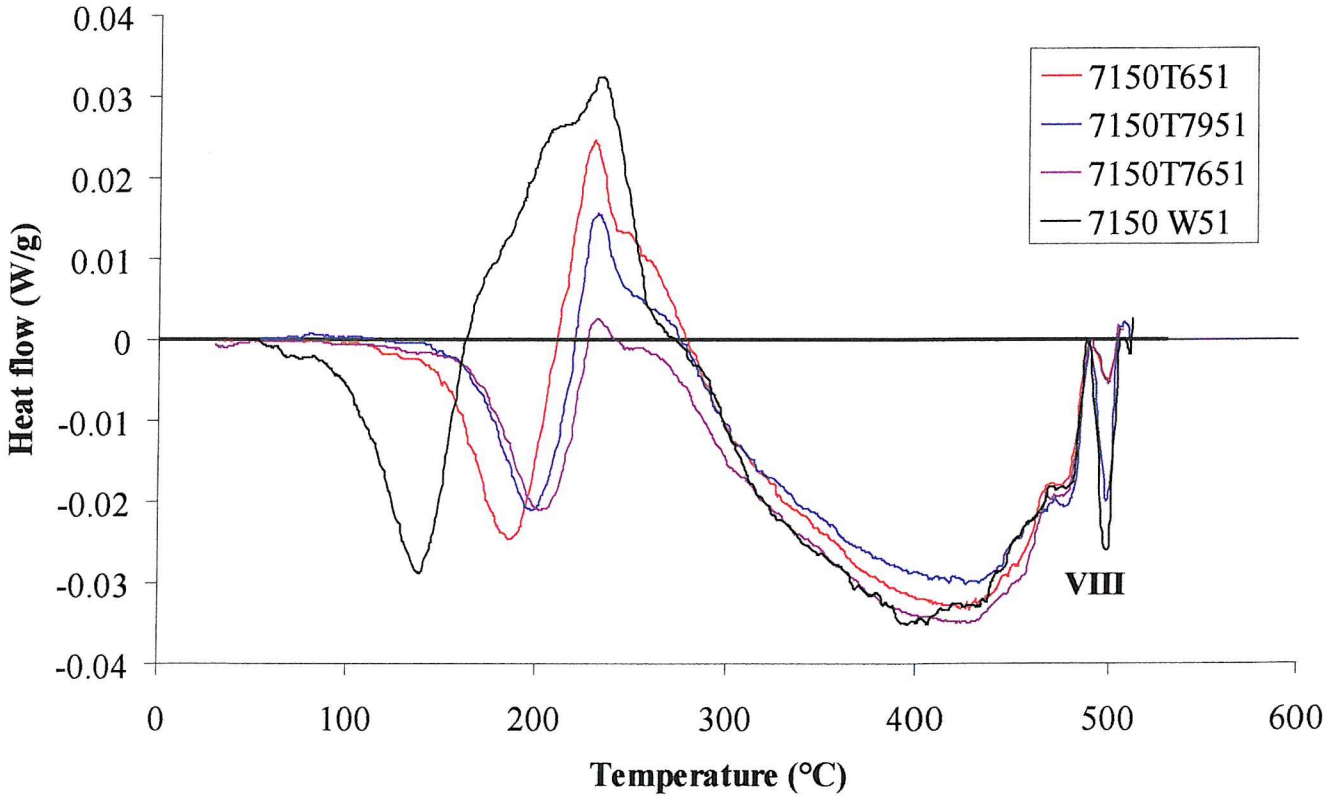

Figure 5.13: DSC curves of the 7150 alloy for various heat treatment conditions.

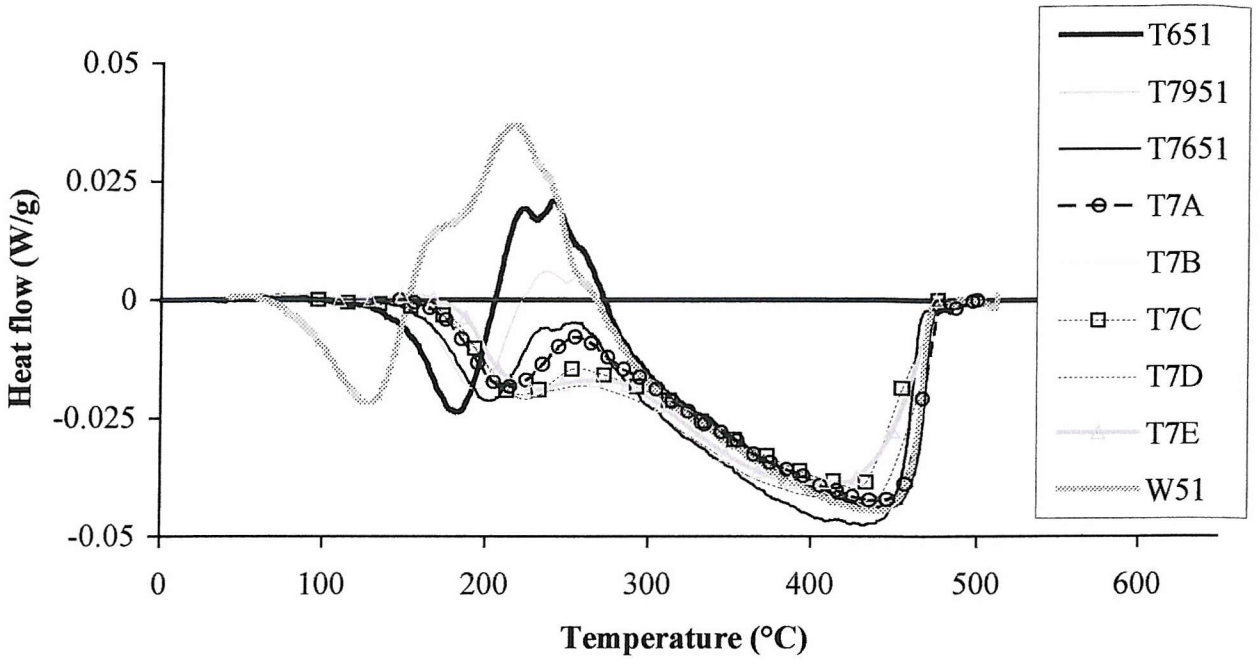

Figure 5.14: DSC curves of the 7449 alloy for various heat treatment conditions.

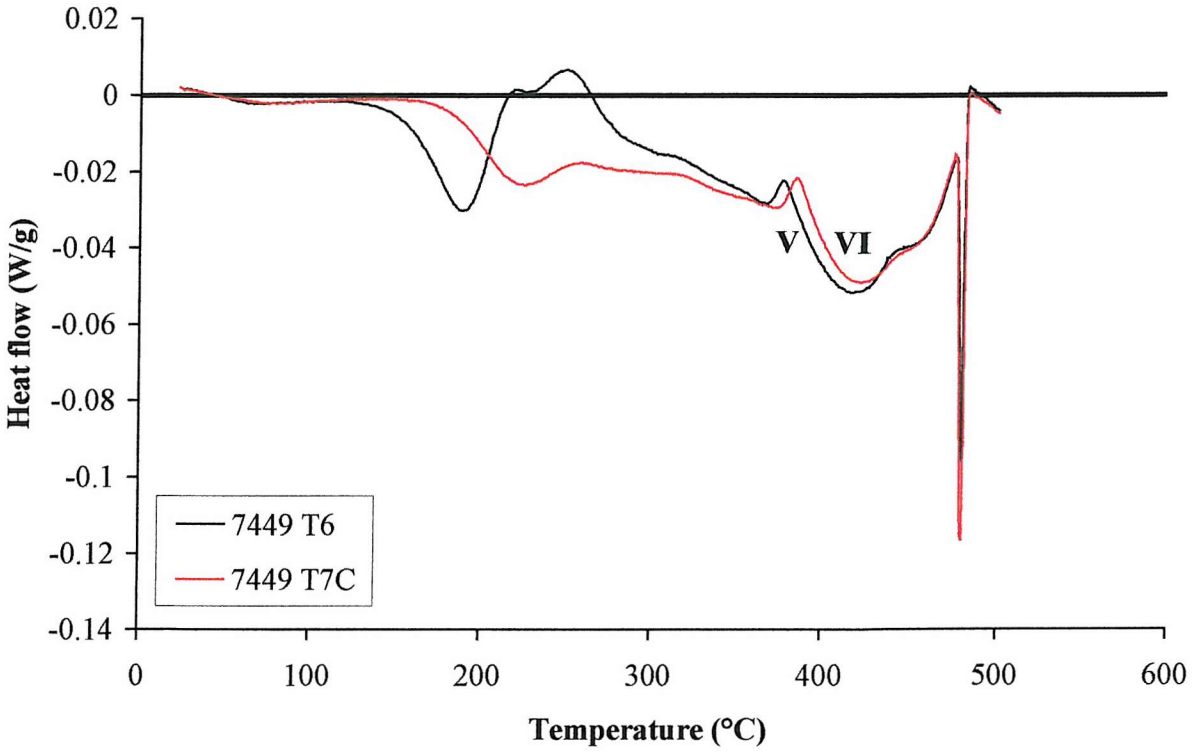

Figure 5.15: DSC curves of the 7449(Mn) alloy for various heat treatment conditions.

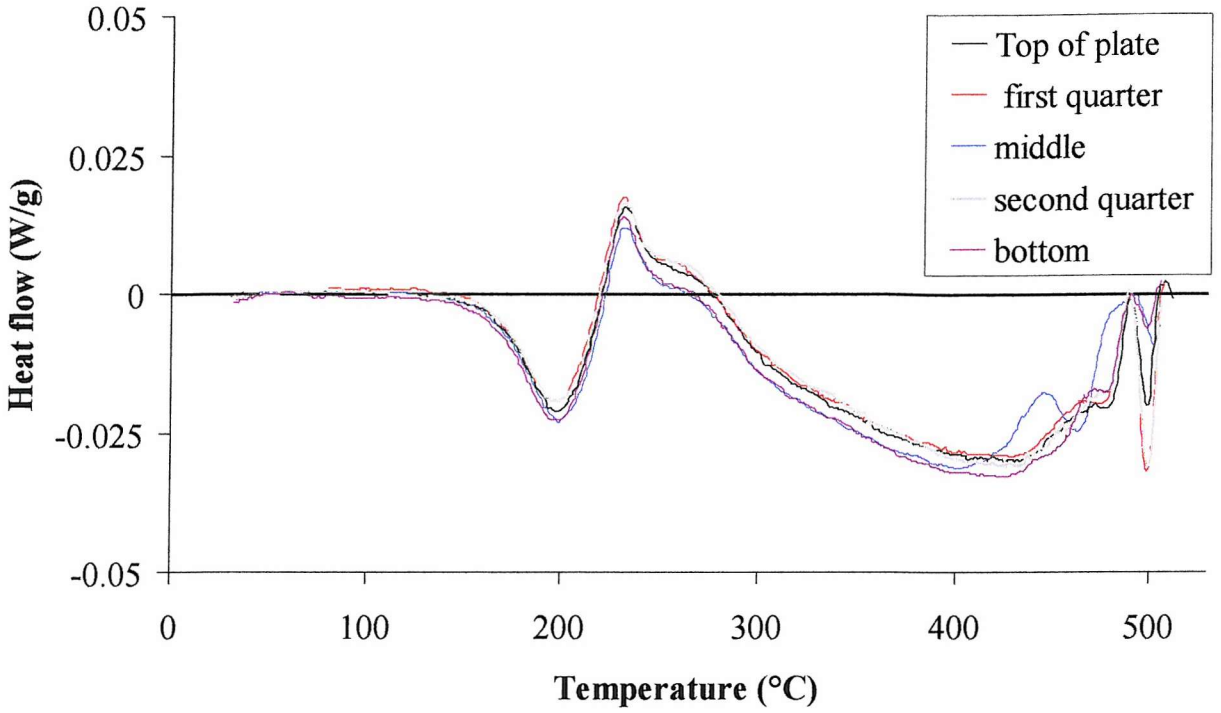

Figure 5.16: DSC curves of the 7150 T7951 alloy for various positions within the plate.

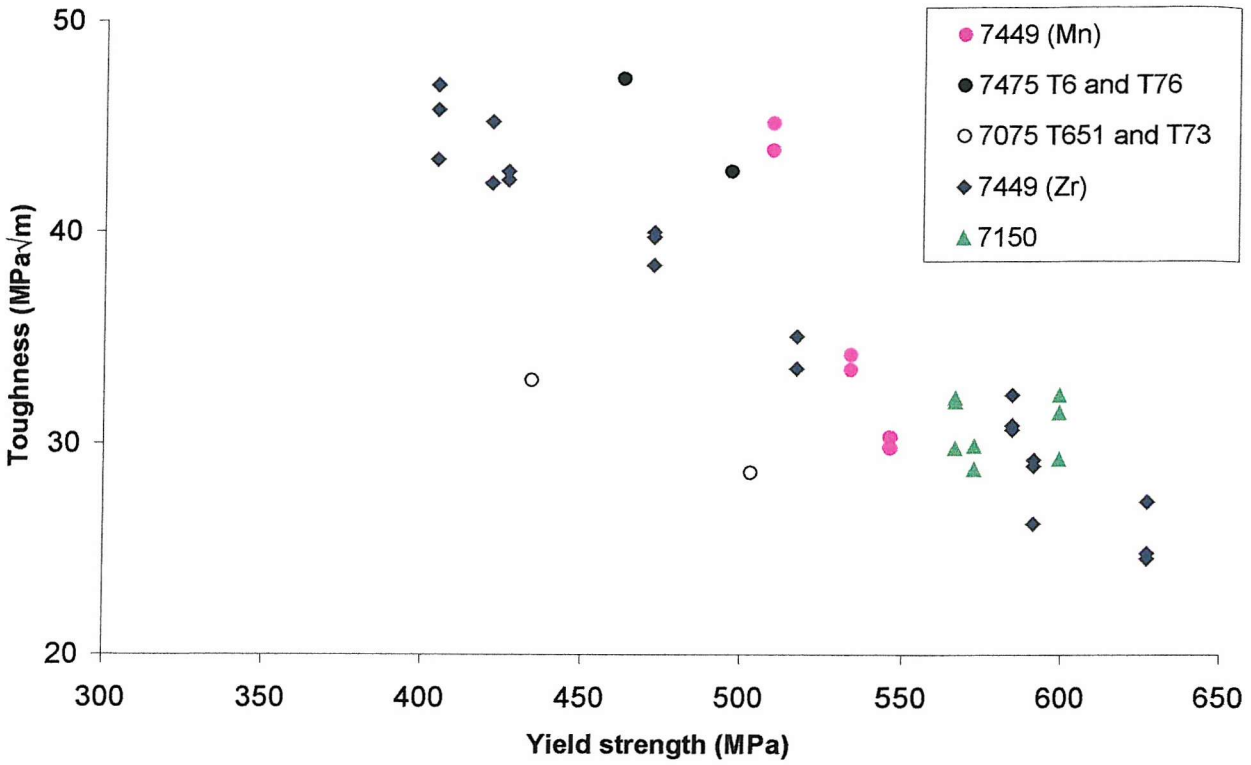

Figure 5.17: Toughness vs. yield strength results for 7449, 7150 and 7449(Mn) materials. Results for 7475 and 7075 are taken from [46].

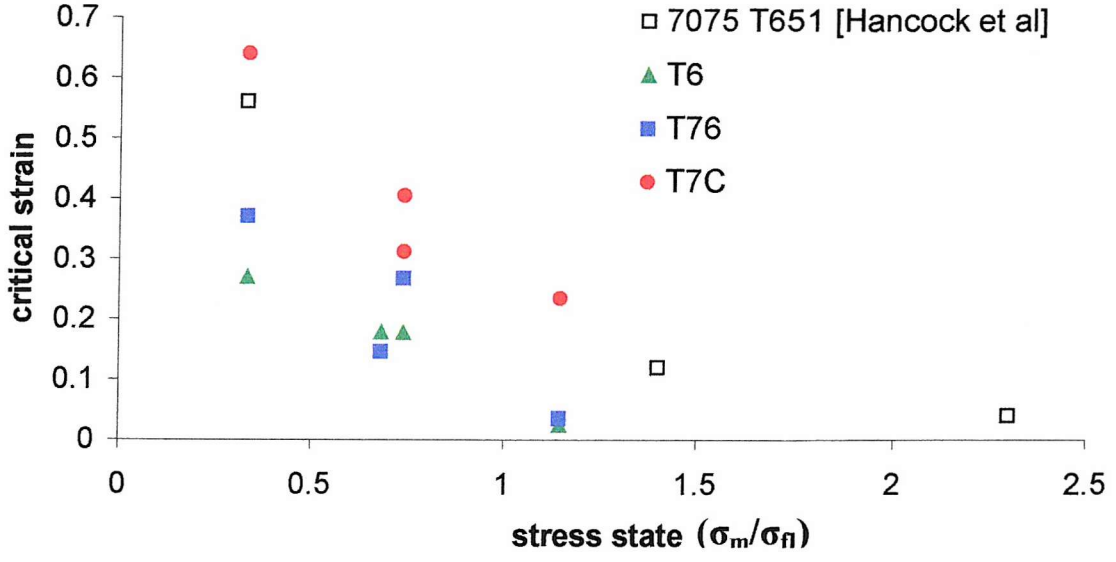

Figure 5.18: Critical strain vs. stress state curves for the 7449 alloy in different heat treatment conditions.

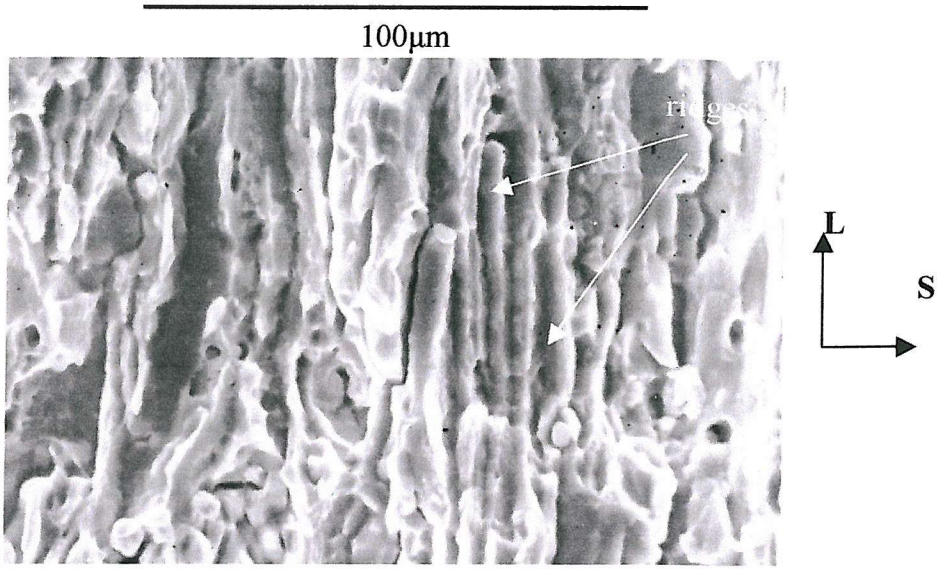

Fig. 5.19a: SEM micrograph of fracture surface (T-S plane) of 7449 T651.

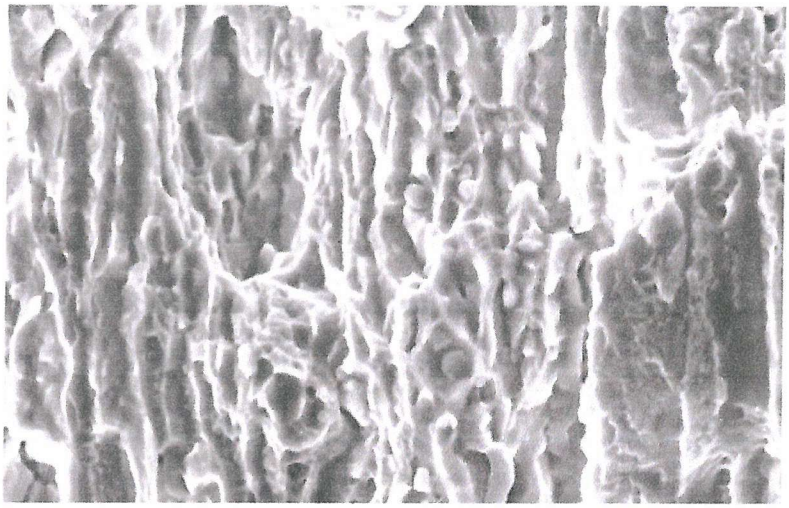

Fig. 5.19b: SEM micrograph of fracture surface (T-S plane) of 7449 T7951.

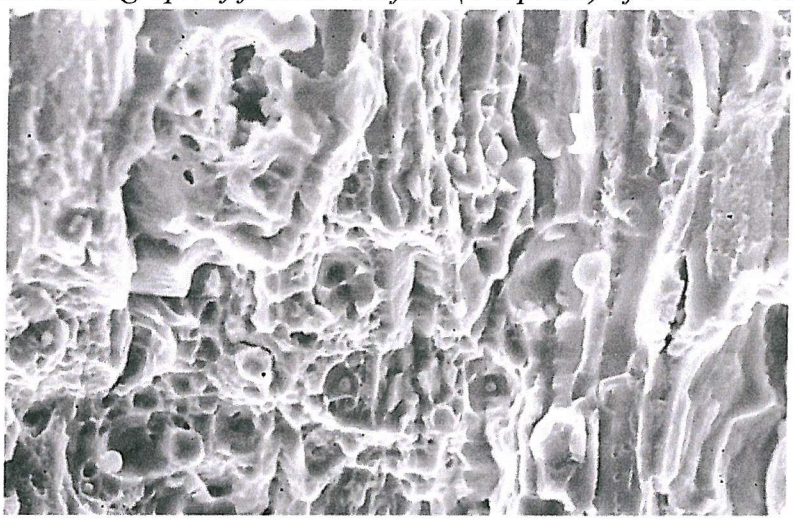

Fig. 5.19c: SEM micrograph of fracture surface (T-S plane) of 7449 T7651

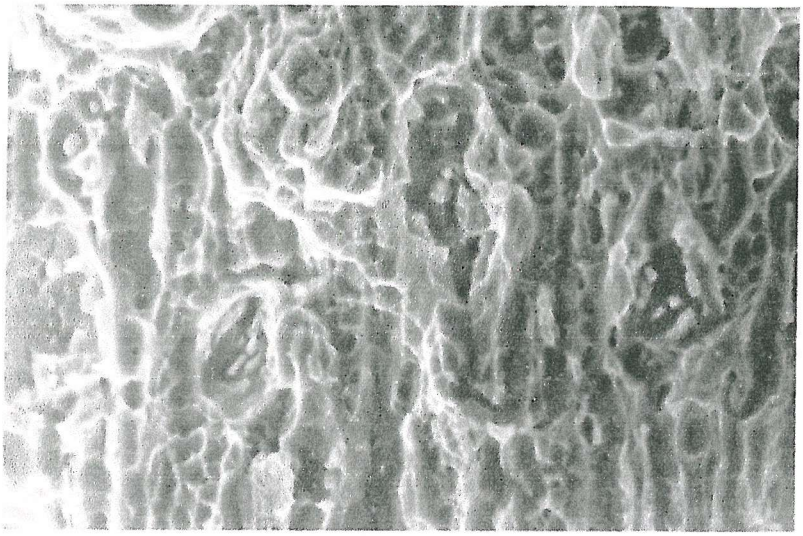

Fig. 5.19d: SEM micrograph of fracture surface (T-S plane) of 7449 T7A.

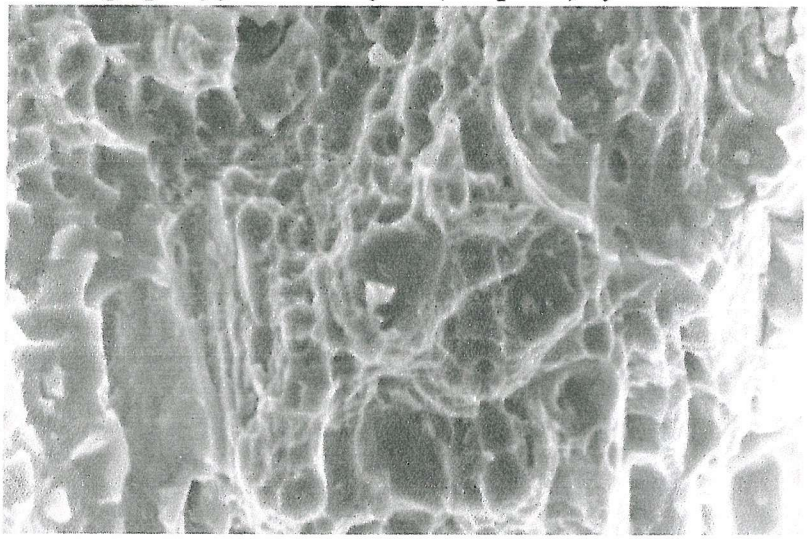

Fig. 5.19e: SEM micrograph of fracture surface (T-S plane) of 7449 T7B.

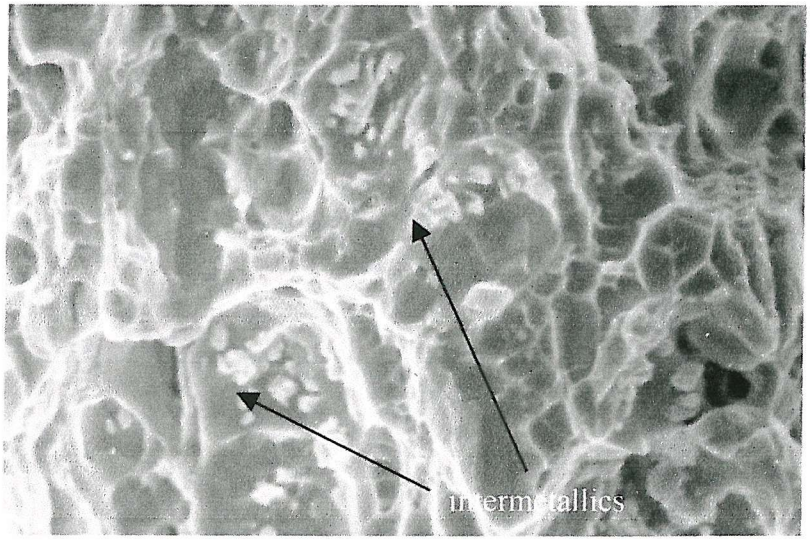

Fig. 5.19f: SEM micrograph of fracture surface (T-S plane) of 7449 T7C.

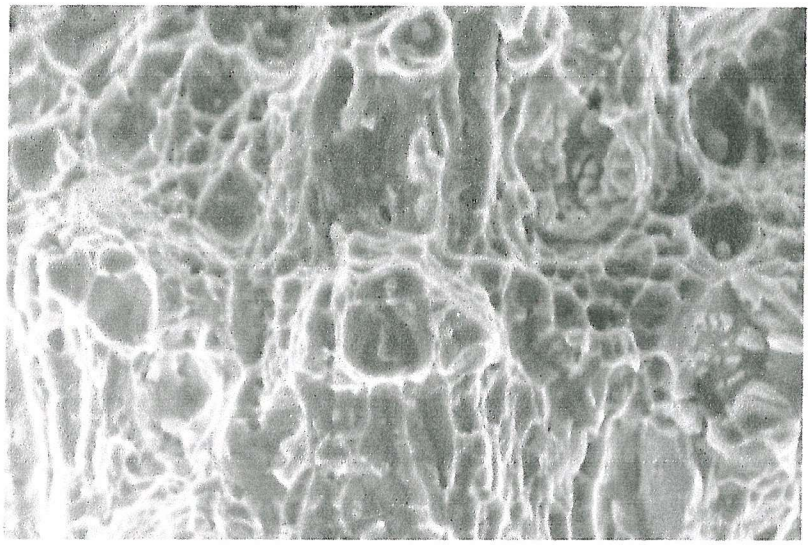

Fig. 5.19g: SEM micrograph of fracture surface (T-S plane) of 7449 T7D.

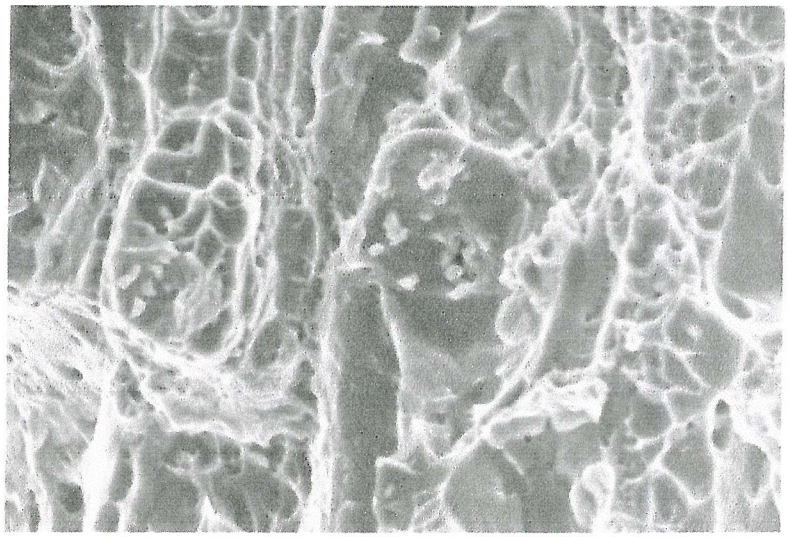

Fig. 5.19h: SEM micrograph of fracture surface (T-S plane) of 7449 T7E.

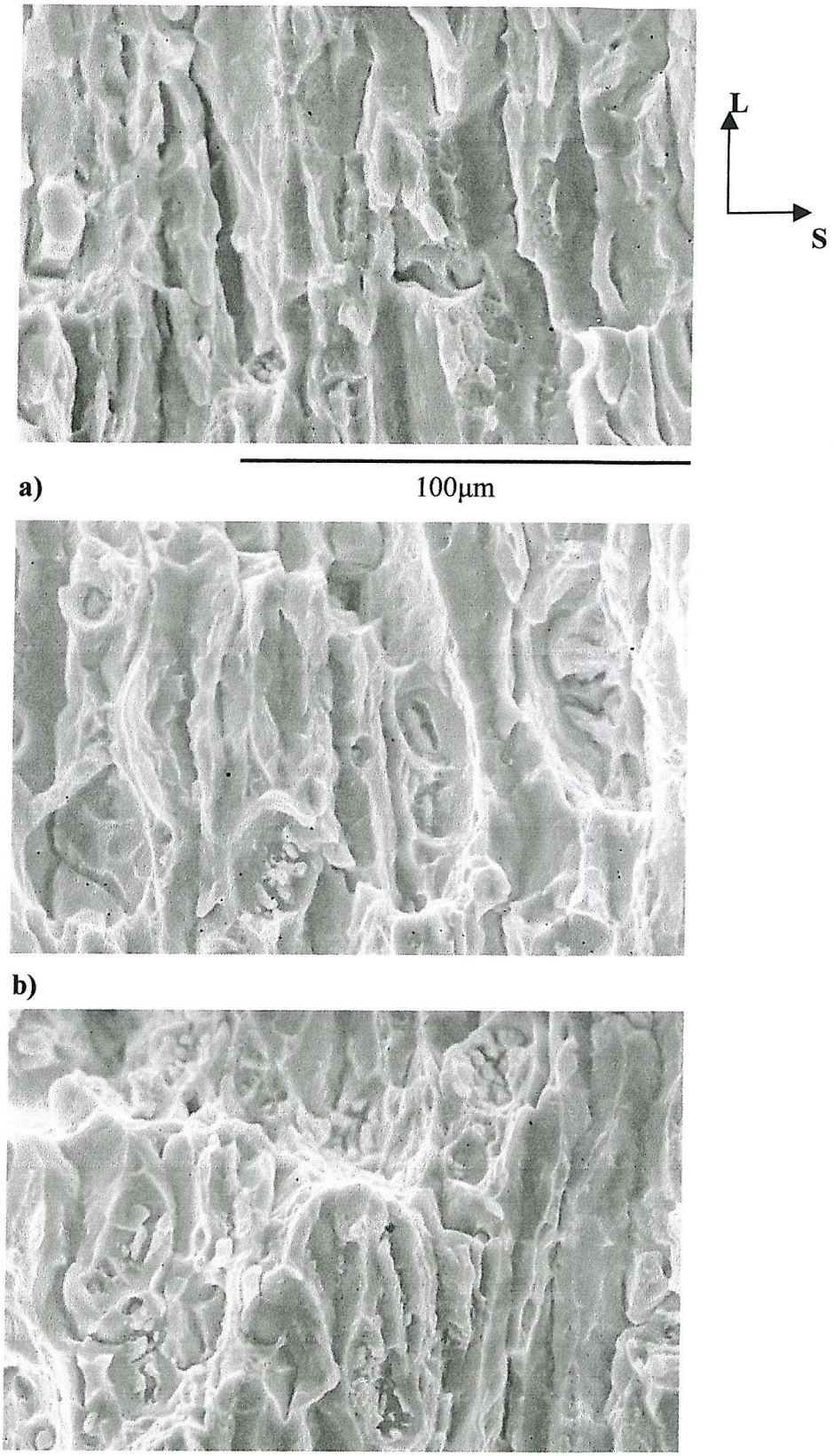

Figure 5.20: SEM micrograph of fracture surface (T-S plane) of a) 7150 T651, b) 7150 T7951 and c) 7150 T7651.

a)

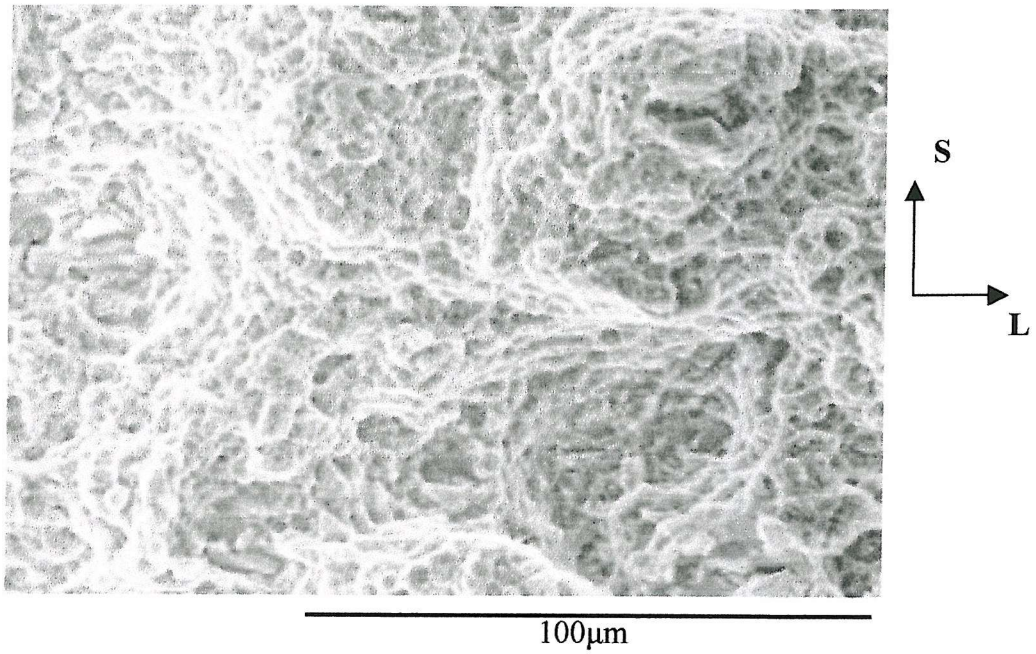

b)

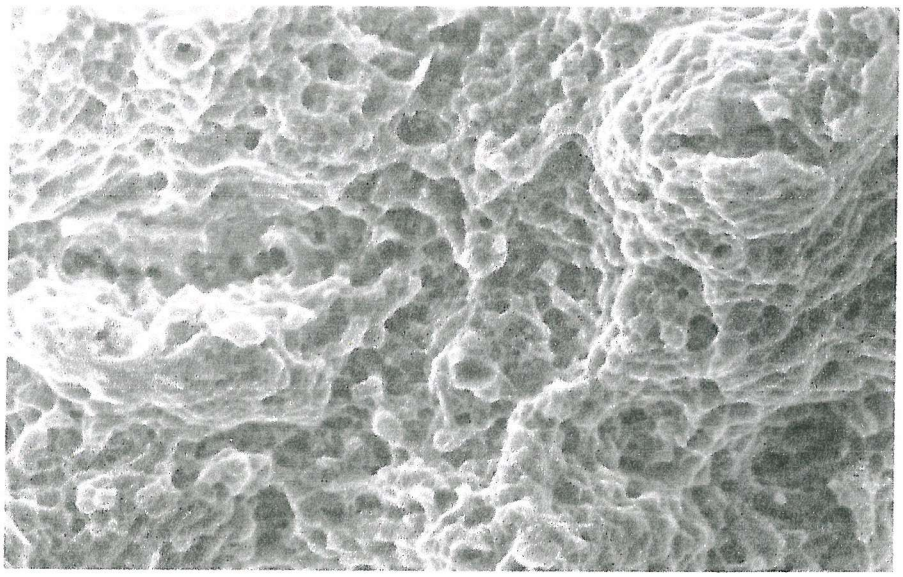

c)

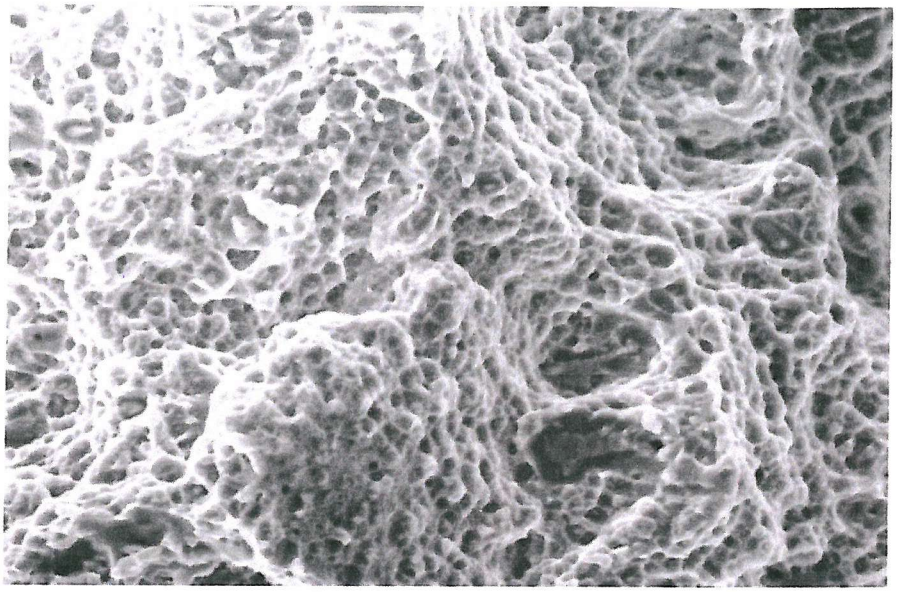

Figure 5.21: SEM micrograph of fracture surface (T-S plane) of a) 7449 (Mn) T6, b) 7449 (Mn) T76 and c) 7449 (Mn) T7C.

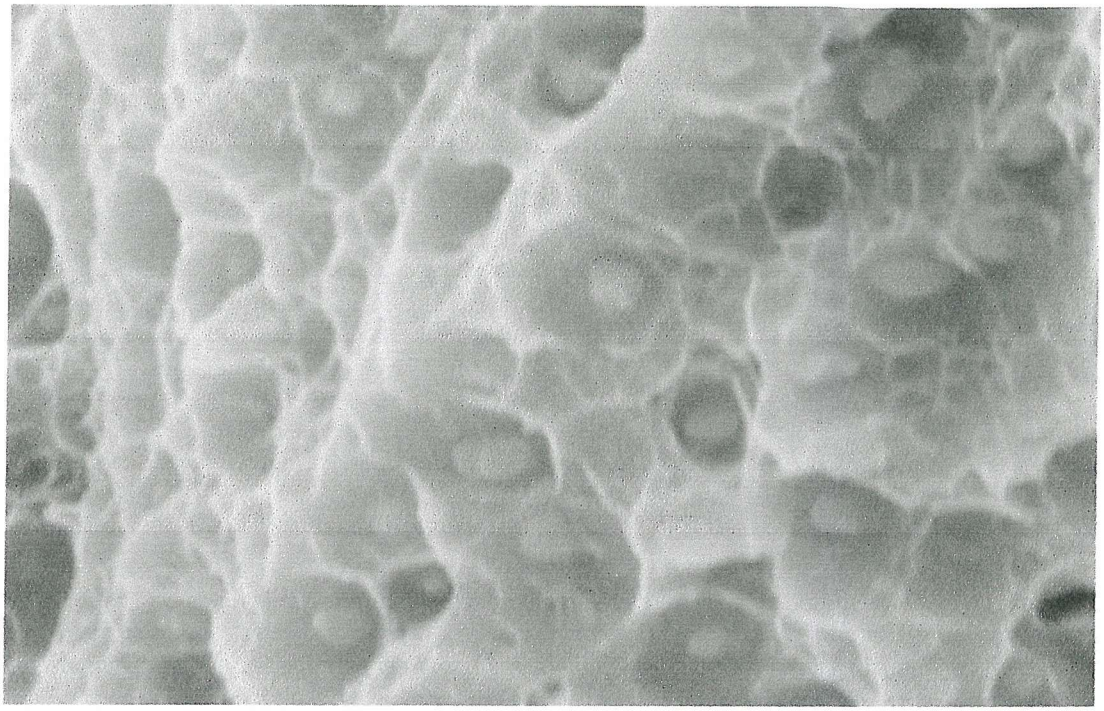

Figure 5.22: SEM micrograph of fracture surface (T-S plane) of 7449 (Mn) T6

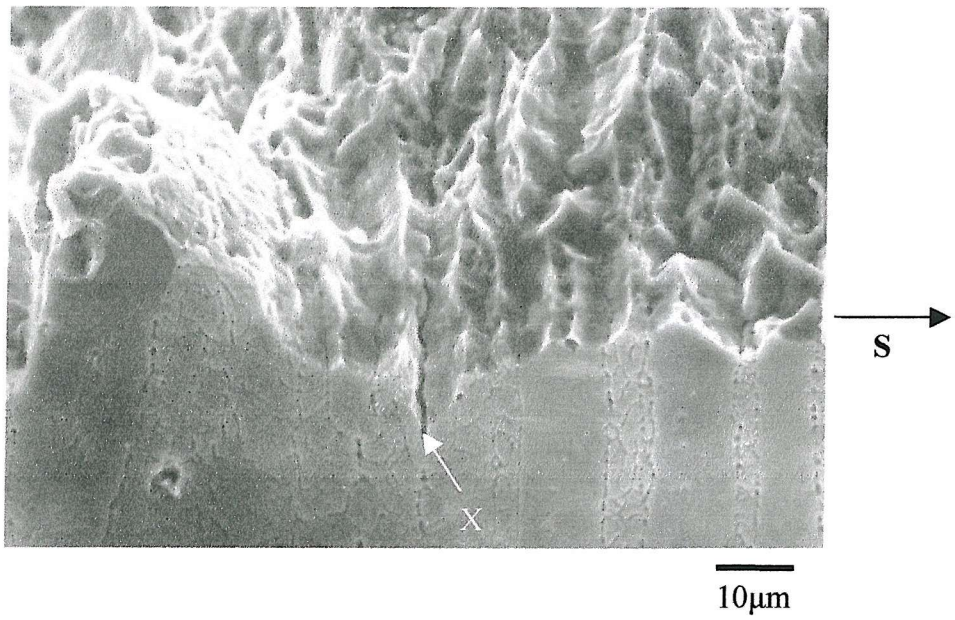

Figure 5.23: SEM edge-on micrograph showing the fracture plane (TS) and the polished and etched LS plane of the 7150 T7951 alloy. (X) secondary crack propagating down the grain boundary into the bulk sample.

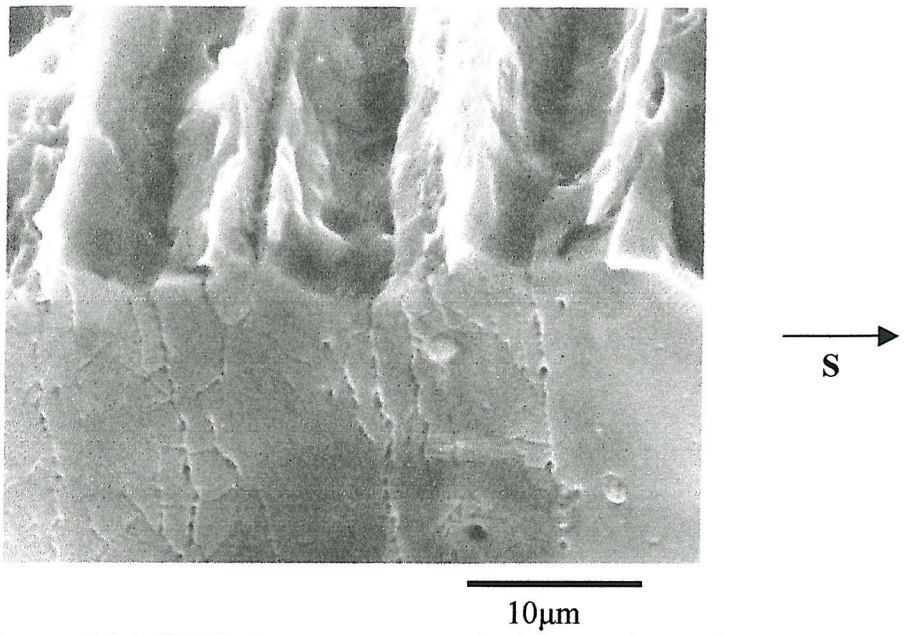

Figure 5.24: SEM edge-on micrograph showing the TS fracture plane and the polished and etched LS plane of the 7449 T651 alloy

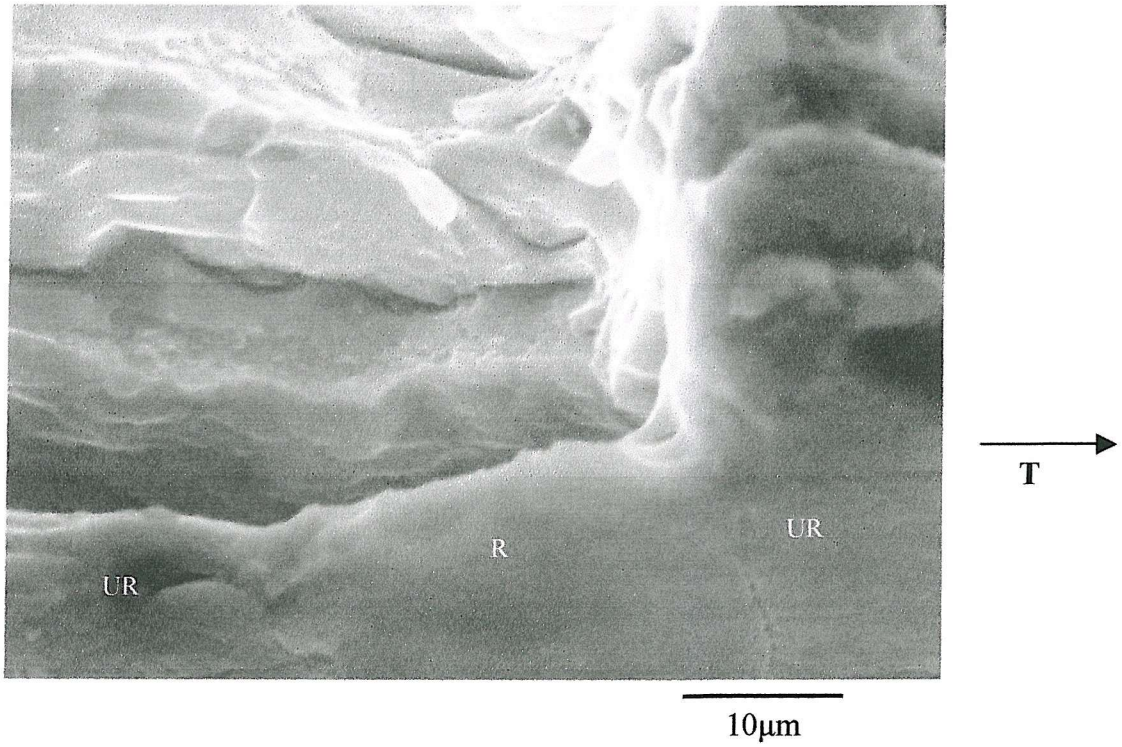

Figure 5.25: SEM edge-on micrograph showing the TS fracture plane and the polished and etched LT plane of 7150 T7951 alloy showing recrystallised (R) and unrecrystallised grains (UR)

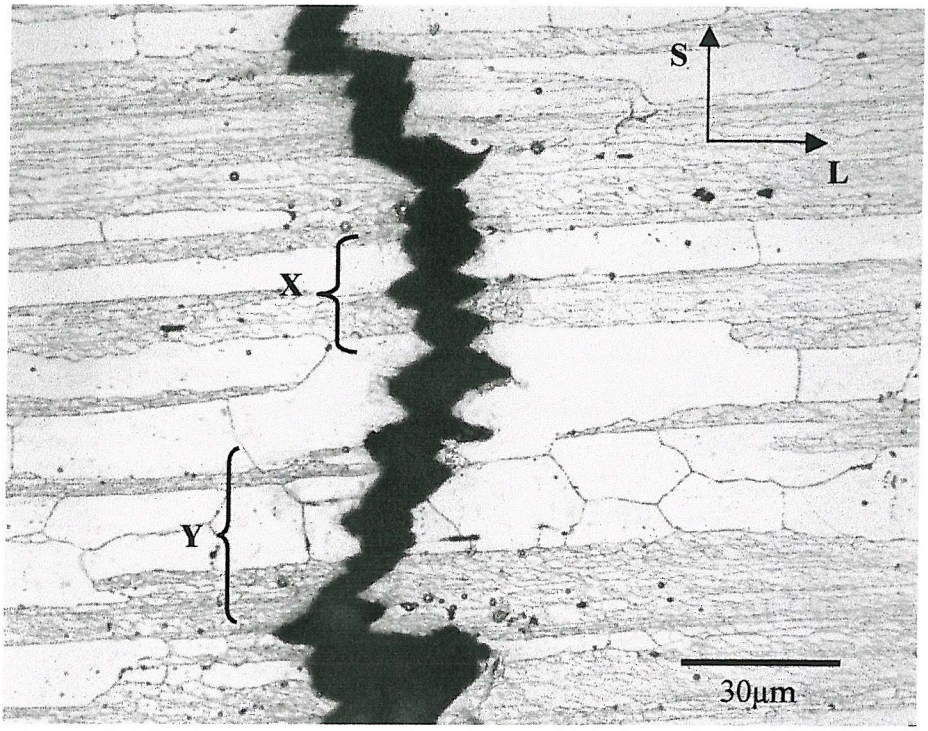

Figure 5.26: Optical section (LS) of an arrested crack in 7150 T7651: X highlights region of grain boundary failure and necking down of grains, whilst Y identifies a region of shear decohesion.

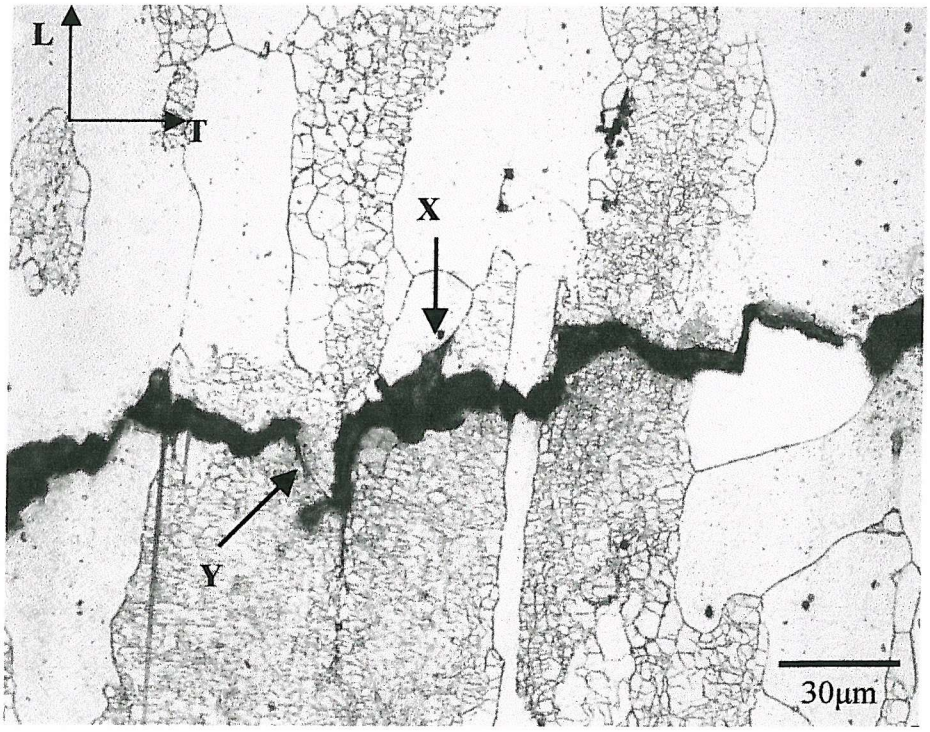

Figure 5.27: Optical section (LT) of an arrested crack in 7449 T651: X highlights a region of grain boundary failure and Y a region of shear decohesion.

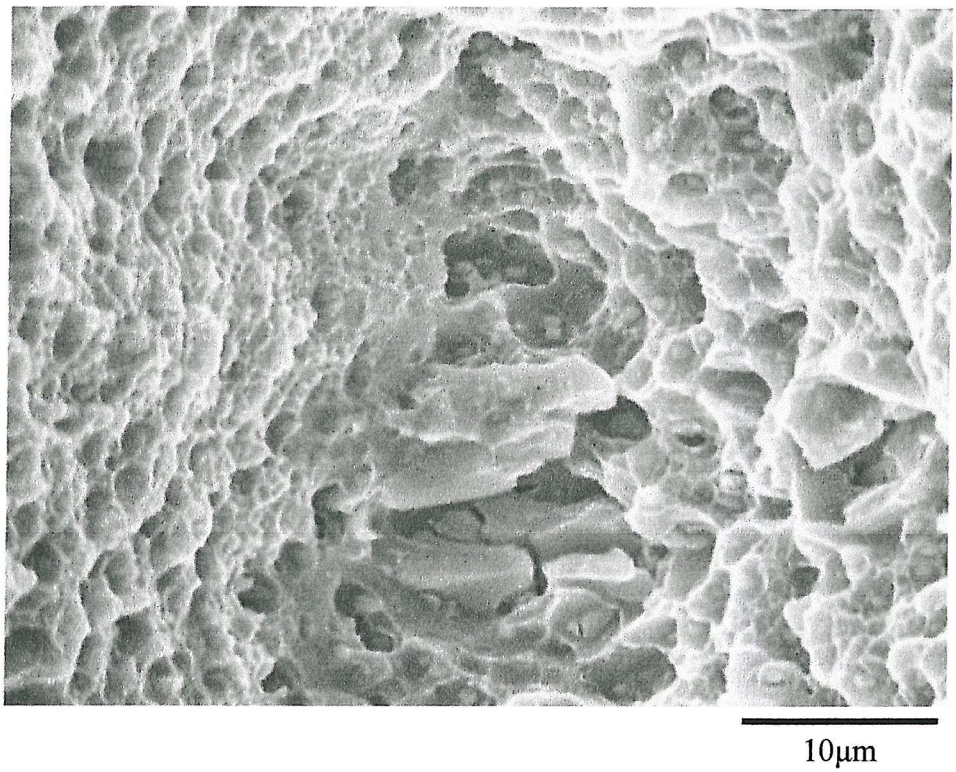

Figure 5.28: SEM micrograph of fracture surface (T-S plane) of 7449 (Mn) T6

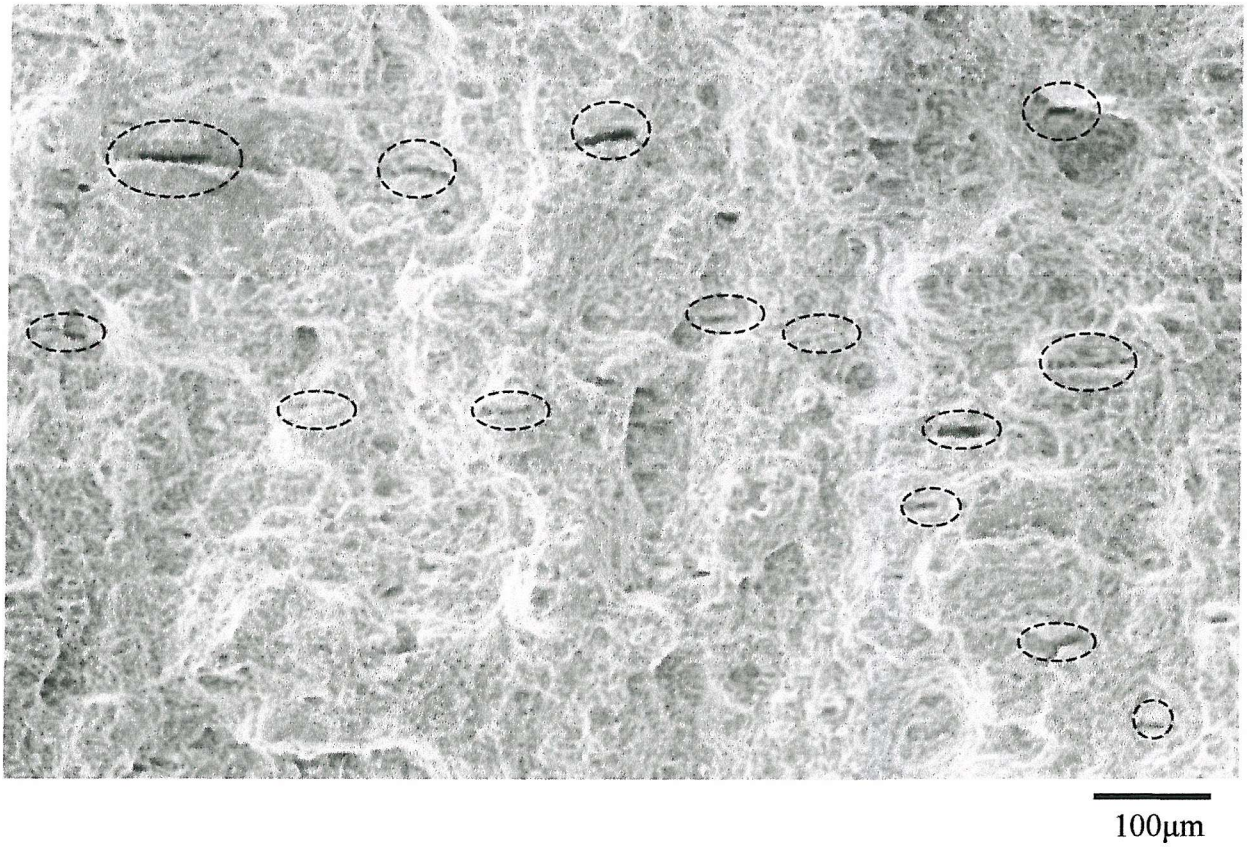

Figure 5.29: SEM micrograph of fracture surface (T-S plane) of 7449 (Mn) T6

Chapter 6

Microstructure and mechanical properties: Discussion

6.1 Introduction

As noted in the literature review, many microstructural parameters can influence the strength and fracture toughness of commercial 7xxx materials: intermetallic particles, dispersoids, strengthening precipitates, grain structure and grain boundary morphology may all play an important role in the fracture process. The direct application of basic physical metallurgy models to these commercial complex alloys is therefore problematic. However, a pragmatic approach aimed at acquiring sufficient description of the microstructural features combined with the analysis of the evolution of the fracture mechanism can provide significant information towards alloy or process optimization. Furthermore, developing the modelling of fracture toughness for these alloys using identified critical parameters while considering the limit of applicability of existing models can give valuable insight towards the manufacturing process of these materials and their applicability in engineering structure. The relationships between toughness and bulk properties such as work hardening and yield strength have been shown in the literature review to give valuable models whilst adopting relatively simple physical frameworks.

In the present chapter the results presented in the previous chapter will be analysed and discussed in three stages. The mechanisms of failure in the 7449, 7150 and 7449(Mn) aluminium alloys and associated microstructural influences are considered in Section 6.2, whilst in Section 6.3 new approaches to toughness modelling are presented. This new model is subsequently assessed and compared to other modelling approach in Section 6.4.

6.2 Mechanisms of failure

Several mechanisms of failure were indicated by the fractographic analysis: fine tensile voiding in the 7449 (Mn) alloy, coarse voiding at intermetallic particles, along with intergranular separation and transgranular shear fracture in the 7449 and 7150 alloys.

For the 7449 and 7150 alloys, it was difficult to separate accurately the amounts of transgranular shear and grain boundary failure, as well as the interaction between coarse voiding and the other fracture processes. SEM observation at a higher magnification on the edges of the linear ridge showed featureless areas, fine shear voiding, slip traces and fine intergranular dimples. Whilst exact identification of failure mechanisms was problematic, the controlling mechanism clearly varied with ageing, with the complex intergranular/transgranular shear 'ridges' dominating in the T651 condition, and coarse voiding becoming progressively more important as overageing became more severe. The T651 heat treatment is associated with the higher strength of the alloy. This high strength is due to a fine dispersion of η' precipitates which are obstacles to the movement of dislocations. When sheared, these precipitates may be expected to create a localization of the deformation [97]. Therefore, the ability of the alloy to accommodate strain, particularly near the crack tip where the particles are sheared due to the presence of the plastic zone, may be limited. This localization of the deformation may be expected to be strongest for the peak-aged alloys. A local critical strain sufficient to initiate transgranular shear fracture through the matrix may therefore be attained sooner for a given crack tip opening displacement in the T6 condition. As the strength in the matrix is high in the T6 condition, it is also significant to consider the strength differential between the matrix and the PFZ at the grain boundaries (i.e. where the strength is low), providing an additional strain localization mechanism that may encourage grain boundary failure.

The SEM edge-on observation linking the fracture surfaces to the L-S plane of microstructures illustrates the nature of the ridges representative of the intergranular/transgranular shear fracture, particularly indicating the influence of the grain boundaries and the grain boundary precipitates on failure (Fig. 5.23,5.24). Boundary particles may of course also be expected to favour boundary separation given

the strain/stress concentrations they cause and their co-location with the soft PFZs. It was seen that the fracture path was particularly influenced by grain boundaries that were decorated by coarse precipitates: when the precipitates were not present, the boundaries did not seem to influence the fracture path (see Figs. 5.23 and 5.24). Ludtka and Laughlin [96] have observed a competition process between intergranular and transgranular failure which exhibits features similar to some seen here. They suggested that this process is initiated by formation of voids at the coarse precipitates at the grain boundary, with voids subsequently coalescing and extending along the grain boundary. This step is followed by the necking down of the grain interiors until fracture occurs transgranularly. This mechanism is illustrated in Fig. 6.1. It is interesting to note that whilst failure in our samples is clearly influenced by the decorated grain boundaries, excessive delamination of the grain structure is not evident. As shown in Fig. 6.2, it would appear that for our alloy, once failure appears at the boundaries, separation of the material is more dominated by triaxial opening rather than ongoing planar separation of the boundary, i.e. the form of the crack path illustrated in Fig. 5.24 suggests that a degree of void growth occurs at the grain boundaries rather than a separation of the boundaries. It may be suggested that the presence of a low density of grain boundary precipitates be the cause of this mechanism: in this case, the voids formed at the grain boundary particles can grow but their low density is an obstacle for sustained propagation along the grain boundary. Precipitate sizes and PFZ features may also be expected to influence such behaviour, with further experimental investigation beyond the current experimental scope being required to clarify this issue.

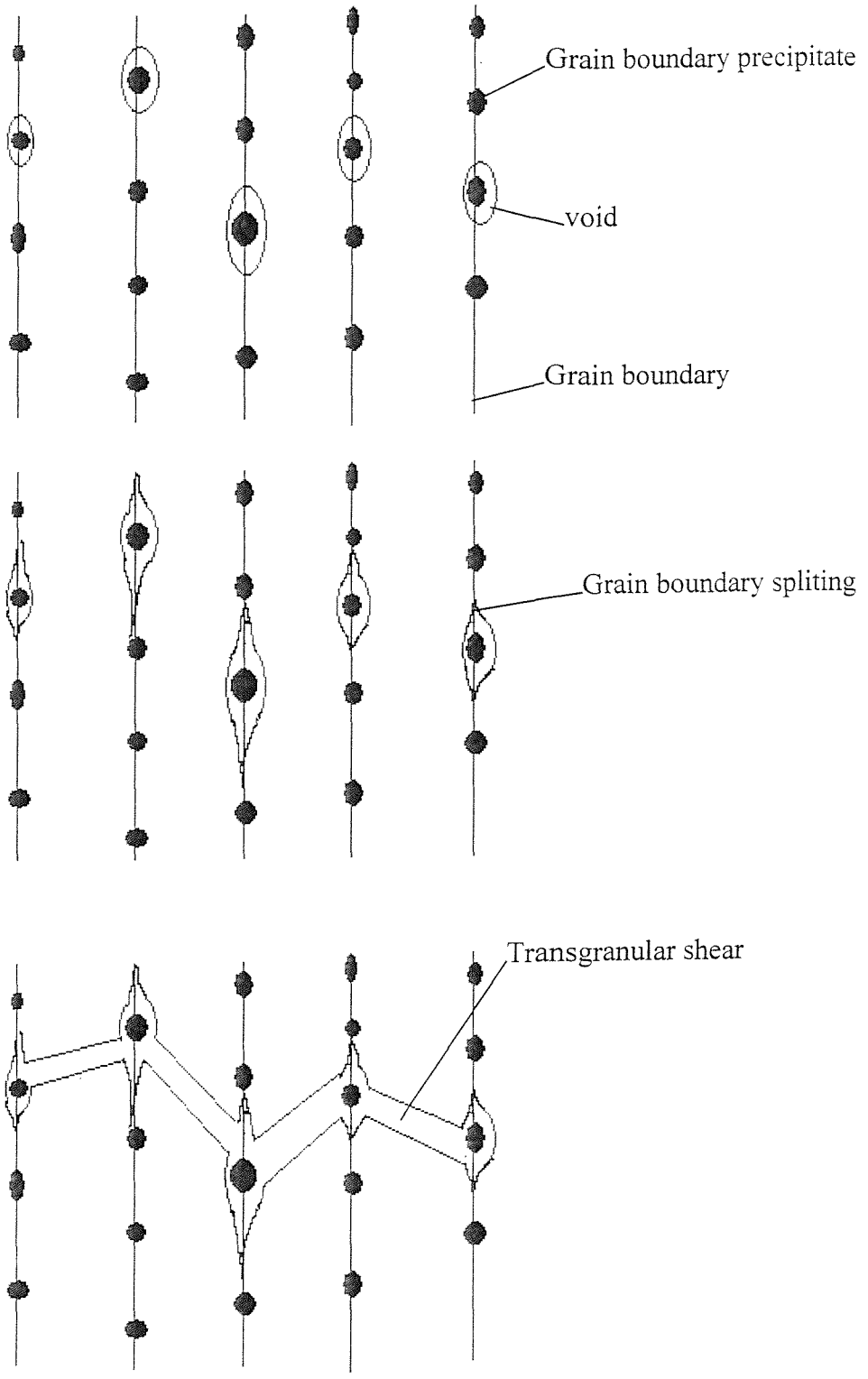

Figure 6.1: Schematic of the sequence of events during fracture of high strength Al alloys [96]

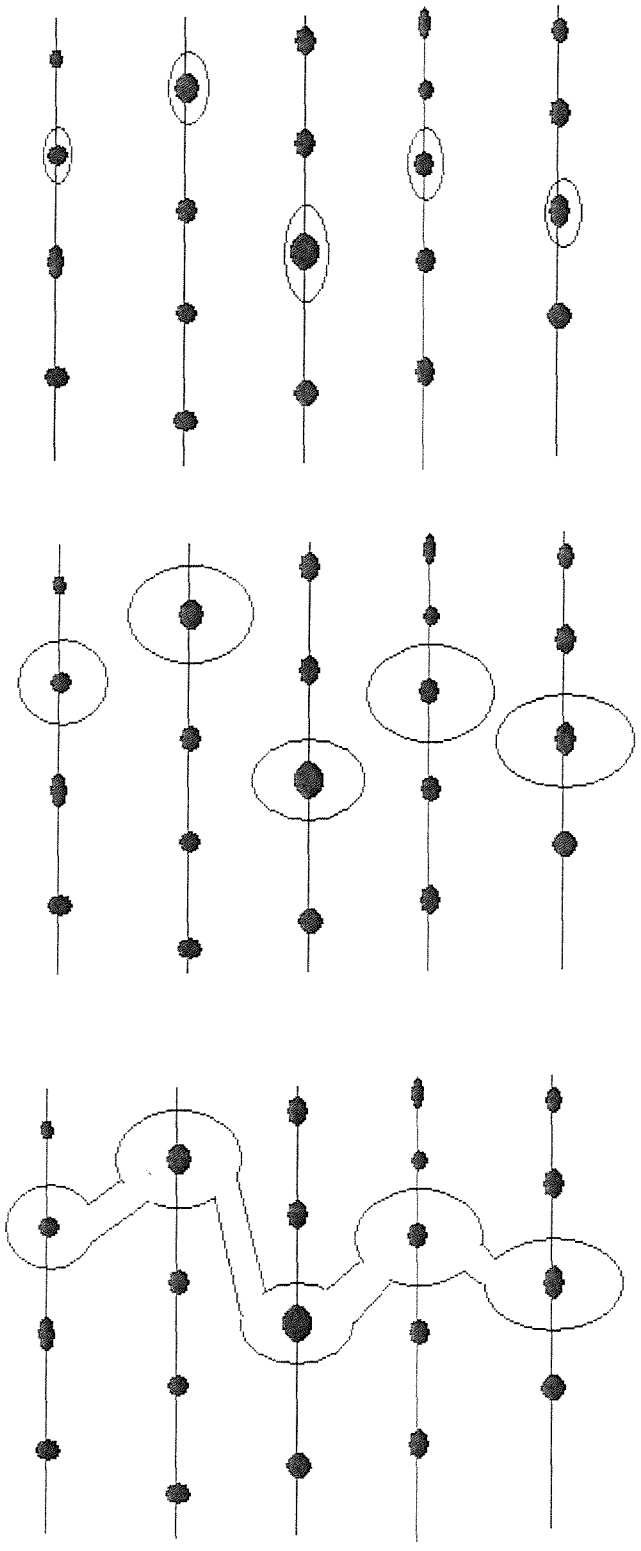

Figure 6.2: Schematics of a proposed model of intergraular/transgranular shear fracture.

It has been reported in the literature [35] that coarse particles fail early in the fracture process. However, the limited amount of coarse voiding in the T6 condition tests suggests that the growth of these voids would occur at a higher strain than the critical strain required for intergranular/transgranular shear fracture. During the ageing treatment, the strengthening precipitates become coarser and the coarsened η precipitates which gradually replace η′ can no longer be sheared. This is then identifiable with increased work hardening capacity and more homogeneous deformation, decreasing susceptibility to shear decohesion. At the same time, the strength differential between the matrix and any PFZs that are present is reduced, giving rise to increased relative deformation resistance at the grain boundary. A competition may then be identified between the improve fracture resistance at the grain boundary due to the reduction in matrix-PFZ strength differential and the coarsening of boundary precipitates with ageing. Several authors [25] have pointed out the detrimental effect of increased grain boundary coverage by precipitates on fracture toughness. Nevertheless, enhanced grain boundary failure on overageing has not been observed in this study. As such, matrix precipitation, and consequent influences on matrix-PFZ strain partitioning 'capacity' would appear to be dominant in the present alloys. Overall the transition to coarse voiding at intermetallics with overageing is identifiable with changing boundary failure characteristics and matrix deformation mode rather than any intrinsic change in coarse voiding processes.

In the 7449 (Mn) alloy, fine tensile voiding, evidenced by the predominance of fine dimples on the fracture surfaces, is clearly the main failure mechanism. Particles visible inside the voids are up to 1μm in size. Their size and distribution are consistent with the distributions of Mn containing particles in Mn containing 7xxx alloys [98]. The fact the fracture process was insensitive to heat treatment further suggests Mn dispersoids were involved, as opposed to phases such as T or η which would evolve during ageing. Earlier studies [46,96] have stressed the potentially damaging effect of dispersoids on fracture toughness. It has been suggested [46] that as shear strain begins to localize into narrow bands at the crack tip, decohesion of dispersoids may occur. This decohesion decreases the local deformation resistance of the material promoting further decohesion within the shear bands, and, subsequently, fracture of the bands. Such processes do not appear to apply in the present 7449(Mn) materials with voids exhibiting a predominantly

equiaxed (round) form, as opposed to assymetric shear forms. The fact that Mn containing dispersoids appear to be such potent void formation sites compared to the Zr containing particles of the 7150 and 7449 alloys may of course be linked to the increased size and incoherent interfaces of the Mn containing particles [93].

Large S phase intermetallics are of course expected to promote failure through coarse voiding [41,42] as seen in more heavily overaged 7449. S phase can be suppressed by a combination of high solution treatment temperature and a limited Cu and Mg content such that all S phase can be dissolved at the solution treatment temperature [42,92]. EDX investigation of coarse intermetallics and DSC results have shown that S phase is not present in the 7449 and 7449 (Mn) alloys. This can be analysed by considering Fig. 6.4 and 6.5 which show that, in the 7449 alloy, the suppression of S phase was achieved by decreasing the copper content relative to that in the 7150 alloy (the present 7449 alloy has a Cu content which is 0.3wt% lower than that of the 7150 alloy). Notwithstanding the difference in S phase content, the 7449 and 7150 alloys have a similar strength-toughness relation for T6, T79 and T76 conditions (see Fig. 5.17). In these cases it would appear that the higher content of S phase in the 7150 alloy than in 7449 alloy is not detrimental to the 7150 alloy as coarse voiding at intermetallics contributes only to a limited extent to the fracture process in these near peak aged conditions (as identified fractographically). Going to more overaged conditions, coarse voiding at intermetallics becomes progressively more important, and thus the S phase in 7150 might be expected to limit the recovery of toughness with decreasing strength of the 7150 alloy although such conditions were not part of the present test matrix.

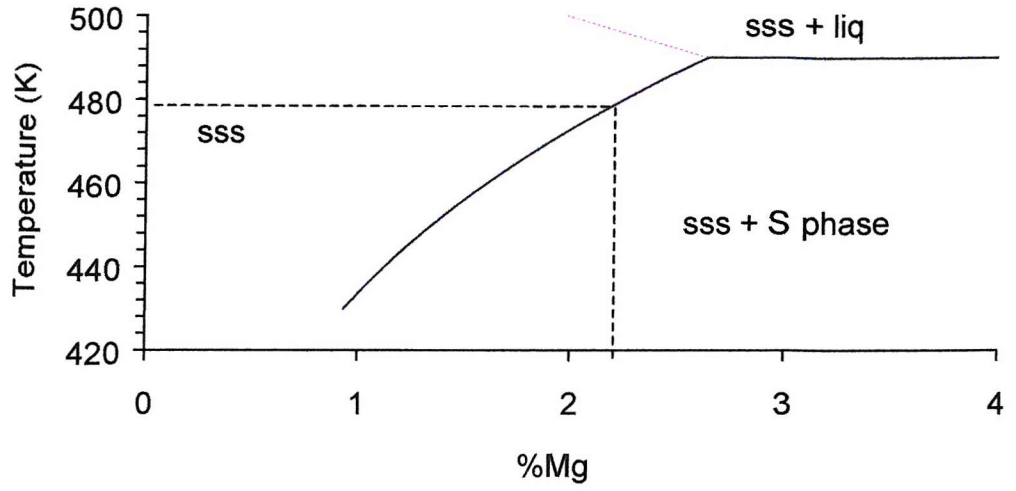

Figure 6.4: Estimated phase diagram of Al-Zn-Mg-Cu wih Zn=6wt%, Cu=2wt% with %Cu in the average composition range of the 7449 and 7150 [99].

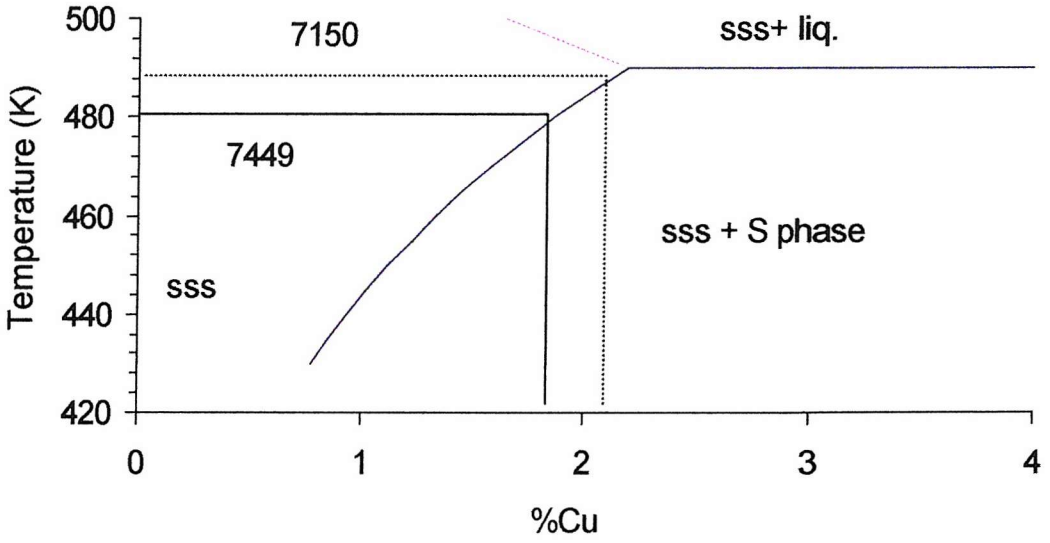

Figure 6.5: Estimated phase diagram of Al-Zn-Mg-Cu with Zn=6wt%, Mg=2.4wt% with %Cu in the average composition range of 7449 and 7150 [99].

6.3 Toughness modelling

6.3.1 Existing approaches

Several models to analyse toughness on the basis of microstructural parameters have been published in the literature (see e.g. Hahn and Rosenfield [75], Garrett and Knott [76]), as reviewed in Chapter Three. Garrett and Knott [76], as well as other researchers before them [75], have argued that the critical condition at the crack tip is reached when the strain exceeds a critical value ε_c^* over a critical distance. Using experimental studies by Hahn and Rosenfield [75], they expressed their model as:

$$K_{Ic} = Cn\sqrt{\sigma_{ys}\varepsilon_c^*} \qquad [6.1]$$

where K_{Ic} is the fracture toughness, C is a constant and σ_{ys} is the yield strength. The latter relation between K_{Ic}, n and σ_{ys} is common to the works of Garrett and Knott, and Hahn and Rosenfield and others (e.g. Chen and Knott [46]). We will refer to this equation as the Garrett and Knott model; the models mentioned above are applied and further analysed in recent literature [46,47] (see section 3.2).

This model gives a relationship between the fracture toughness and the tensile properties of the alloy, without providing any direct relationship to the microstructure. The work hardening coefficient, n, is an experimentally derived term and is not explicitly related to the microstructure. Furthermore, it must be noted that the use of n to describe work hardening is a matter of mathematical convenience, and does not provide a particular meaningful indication of work hardening itself. This is due to its mathematical formulation, whereby 'parallel' yielding curves, see Fig. 6.2, that only differ in initial yield point will in fact give different n values.

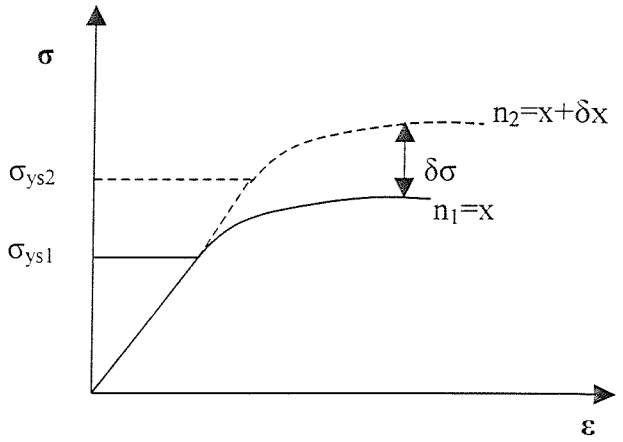

Figure 6.2: Schematic diagram of two stress-strain curves with different yield strength but 'parallel' yielding curves

These limitations of the Garret and Knott model reduce its value with regards to property optimisation studies of the heat treatable Al-based alloys, in which strength can be readily varied through variation in heat treatment and composition. Hence, a different approach to modelling, aimed at deriving quantitative expressions for the decrease in toughness with increasing strength incorporating clear microstructural influence on work hardening may be beneficial.

Macroscopic flow behaviour may be expressed in terms of yield strength and strain hardening. Whilst the first is reasonably well defined, strain hardening is less straightforward. Strain hardening mechanisms depend on microstructure, and are generally divided in several regimes with different corresponding equations, depending on the strain hardening mechanism at play [77]. Strain hardening is often quantified using a purely empirical, exponential equation, based on the Ramberg-Osgood equation, which is expressed as,

$$\frac{\varepsilon}{\varepsilon_0} = \frac{\sigma}{\sigma_0} + \alpha\left(\frac{\sigma}{\sigma_0}\right)^{\beta} \qquad [6.2a]$$

where ε is the strain, σ is the stress, ε_0, σ_0, α and β are constants. The plastic part can be approximated as:

$$\sigma = A\varepsilon^{n} \qquad [6.2b]$$

where A is a constant, ε the strain, and n is the work hardening exponent.

Contrary to the general exponential form of Eq. 6.2, the Ashby [32,100] theory of strain hardening due to non-shearable particles and grain boundaries leads to a square-root strain hardening expression which has been given as (see also [29,34]):

$$\begin{aligned}\sigma &= \sigma_{ys} + M\left(0.35G_m\sqrt{\frac{b}{d_g}} + 0.25G_m\sqrt{\frac{bf_{ns}}{2r_{ns}}}\right)\sqrt{\varepsilon_p} \\ &= \sigma_{ys} + K_A\sqrt{\varepsilon_p}\end{aligned} \qquad [6.3]$$

where M is the Taylor factor [33], b is the Burgers vector, d_g is the grain size, f_{ns} is the volume fraction of non-shearable particles, r_{ns} is the radius of non-shearable particles, K_A is the strain hardening factor and G_m is the shear modulus. For non-shearable particle types of varying sizes and volume fraction it holds:

$$K_A = M\left(0.35G_m\sqrt{\frac{b}{d_g}} + 0.25G_m\sqrt{\frac{bf_{ns,1}}{2r_{ns,1}} + \frac{bf_{ns,2}}{2r_{ns,2}}}\right) \qquad [6.4]$$

where $f_{ns,i}$ and $r_{ns,i}$ are respectively the volume fraction and radius of the different type of non-shearable particle.

Our results show that for our alloys K_A varies between 350 and 560MPa.m$^{-1/2}$. These values are slightly higher than theoretical values calculated from Eq. 6.4 using microstructural data [44] for typical 7xxx alloys in underaged conditions where precipitates are generally shearable, which indicate that K_A is about 150-300 MPa, with grain size having the most important influence. For overaged (T7) samples, coarsened precipitates will become non-shearable and contribute to an increase in K_A. It is unfortunately not possible to predict K_A values for the present materials, as $f_{ns,i}$ are not strictly known. It is interesting to note that the above equations are only valid over a limited strain range; roughly for ε_p between 0.01 to 0.05 [32]. This means that σ_{ys} in

Ashby's root-strain work hardening regime may deviate to some extent from a conventional 0.2% proof stress.

6.3.2 A new modelling approach

As noted previously, for a given absolute work hardening curve, n values will vary with σ_{ys} levels. Given the widely quoted significance of strain hardening capacity in fracture processes, it is clearly valuable to be able to separate work hardening and strength levels, whilst retaining an understanding/relationship with the established Garrett and Knott equation. Extensive assessment of medium to high strength Al-alloys (for ε_p=0.01 to 0.05) reveals the following relationship (details of this analytical fit can be found in Appendix I):

$$n = C_1 \left(\frac{K_A}{\sigma_{ys}} \right)^{\gamma} \qquad [6.5]$$

where C_1 is a constant. γ is found to have a value of 0.85(±0.1). As such, it may be seen that for a fixed absolute work hardening rate (K_A), n decreases with increasing yield strength.

In terms of toughness modelling, it may be assumed that if the relative contributions from different fracture mechanisms do not vary with strength, ε_c^* can be considered to be a constant. From Eq. 6.5 combined with Garrett and Knott's expression for ductile fracture (e.g. [76], see Section 3.2) the following expression for the toughness is derived:

$$\text{Model I:} \quad K_{IC} = \sqrt{\frac{2CE\varepsilon_c^* \sigma_{ys} n^2}{1-\nu^2}} = C_1 \sqrt{\frac{2CE\varepsilon_c^*}{1-\nu^2}} K_A^{\gamma} \sigma_{ys}^{0.5-\gamma} \qquad (6.6)$$

where E is Young's modulus, ν is Poisson's ratio and C is a constant. It is interesting to note that if K_A and ε_c^* are constant, i.e. if the distribution of non-shearable particles and

the grain structure is constant, with only one fracture mechanism occurring, K_{Ic} reaches a minimum when σ_{ys} reaches a maximum: i.e. by the proper separation of work hardening and absolute strength levels in this expression, an intuitively acceptable inverse relationship between strength and toughness is exhibited, as opposed to being convoluted with apparent hardening characteristics.

6.4 Application of the new toughness model and comparison to previous models

6.4.1 Applicability of the Garrett and Knott model

As compared to 7xxx alloys used to assess the Garrett and Knott type models in the past [46,76], the current 7150 and 7449 alloys possess a lower toughness, higher strength and lower work hardening coefficient n. Hence it is valuable to compare our present data with the prediction of the Garrett and Knott model. The Garrett and Knott model indicates that for samples failing through the same mechanism, K_{Ic} is proportional to $n\sqrt{\sigma_y}$. However, Fig. 6.6 shows that is not the case for the 7449 alloy over the range of ageing treatments studied and, in fact, the data on peak aged and slightly overaged conditions (until T7651) show a steeper slope than the more overaged conditions. This tendency is confirmed by the 7449 (Mn) alloy.

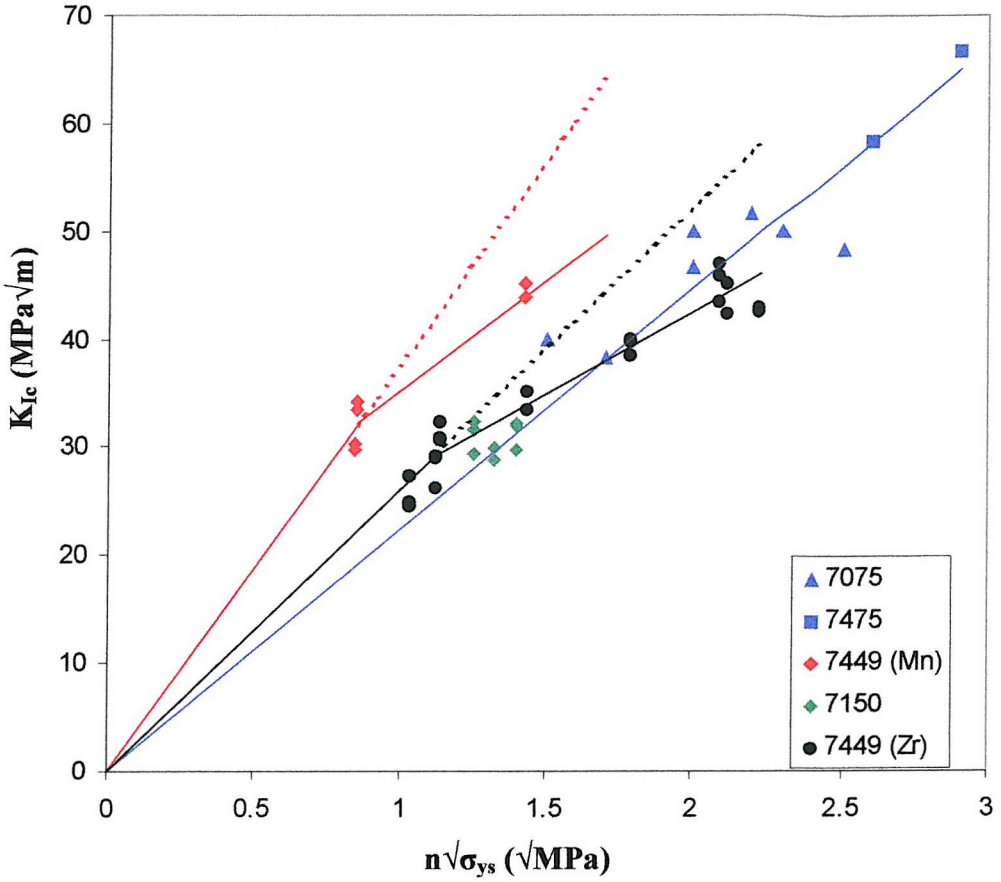

Figure 6.6: Relationship between K_{Ic} and $n\sqrt{\sigma_{ys}}$ for the 7449, 7449(Mn), and 7150 alloys studied. Data for 7075 and 7475 is from reference [46,76]

- *Influence of the critical strain:*

In the first instance, changes in critical failure strain may of course be identified with changing fracture modes for the 7449 and 7150 alloys. The Garrett and Knott model, which essentially is a single mechanism model would generally be expected to fail under these circumstances. For the peak aged and slightly overaged 7150 and 7449 alloys, the high strength condition is seen to promote multi-mechanistic aspects of the fracture process, with a competition between coarse voiding and the combined transgranular/intergranular failure mode. In more overaged tempers the fracture mode is dominated by a single mechanism: i.e. the coarse voiding at intermetallics. One may consider that including the critical strain as a variable parameter in the Garrett and Knott model may improve the model accuracy. This may be tested through the critical strain

data from smooth tensile tests, as originally suggested by Garrett and Knott [76]. The Garrett and Knott model incorporating the critical strain is re-plotted in Fig. 6.7.

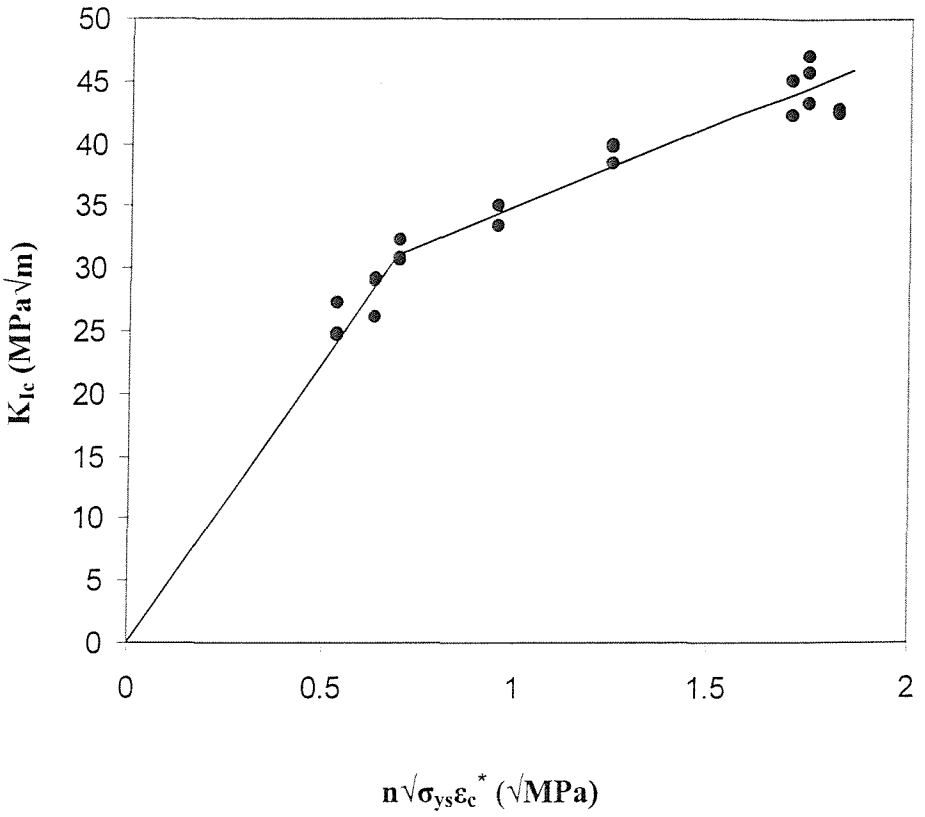

Figure 6.7: Relationship between K_{Ic} and $n\sqrt{(\sigma_{ys}\varepsilon_c^*)}$ for the 7449 alloy.

This figure shows that variable critical strains deduced by simple reduction of area in smooth tensile specimens does not enhance the linearity of the predicted relationship, i.e. the coarse voiding dominated T7A to T7E conditions are still below the linear prediction.

For the present work data from Fig. 5.18 were fitted to a theoretical estimate following Haynes and Gangloff [47] which is based on integration of the Rice-Tracey void growth laws under constant stress-state conditions, which gives:

$$\varepsilon_f^p\left(\sigma_m/\sigma_{fl}\right)=\alpha\exp\left(\beta\frac{\sigma_m}{\sigma_{fl}}\right) \qquad [6.7]$$

The fitting results are shown on Table 6.1 and the fitting of the curves is displayed in Fig. 6.8.

		α	β
7449	T6	1.043	-2.971
	T76	1.200	-2.870
	T7C	0.926	-1.240

Table 6.1: Fitting coefficients from Eq. 6.7.

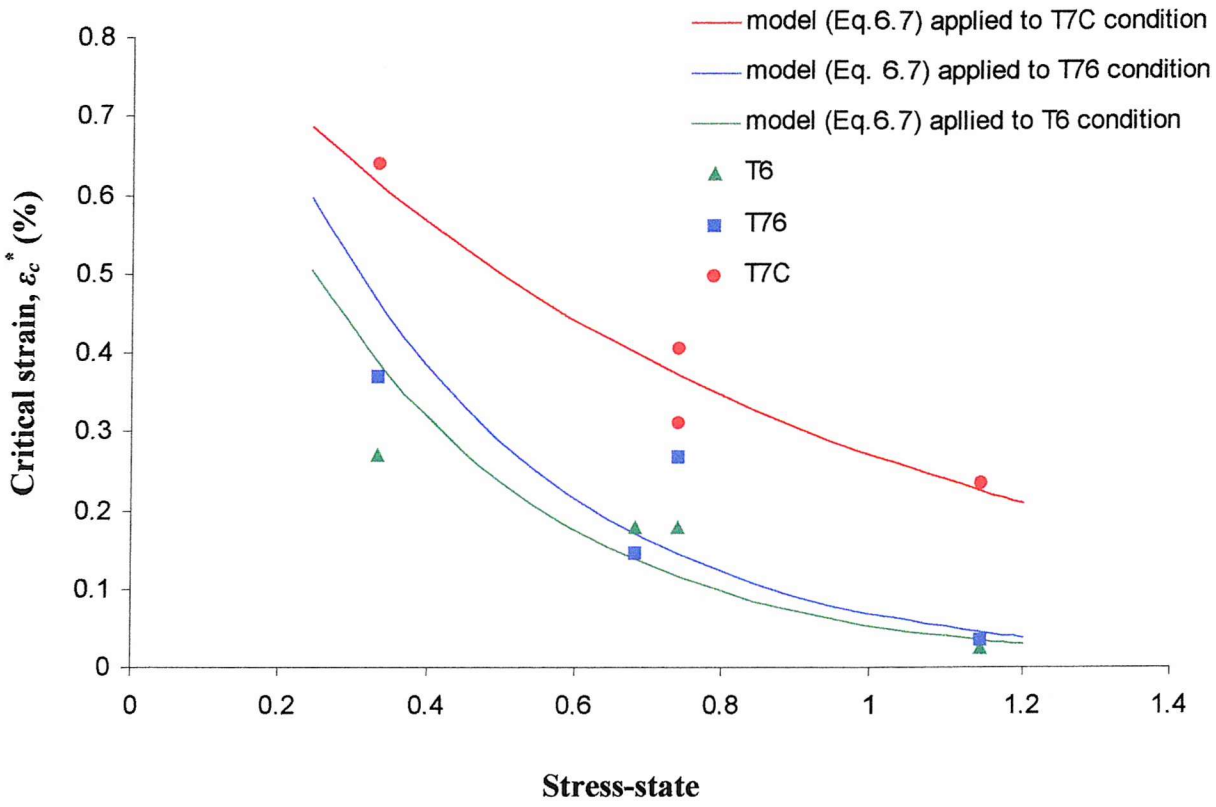

Figure 6.8: Critical strain vs. stress-state for the 7449 alloy in several heat treatment conditions and their fitted models (derived from the Rice-Tracey approach).

This approach may be judged to give a more accurate approximation of the stress-state/critical strain relationship. Critical strain values associated with the plane strain zone (corresponding to σ_m/σ_{fl} values ~2.1, see e.g. [75], extrapolated from Fig. 6.8) were incorporated in the Garrett and Knott model (Eq. 6.1) and the resulting toughness prediction is plotted in Fig. 6.9.

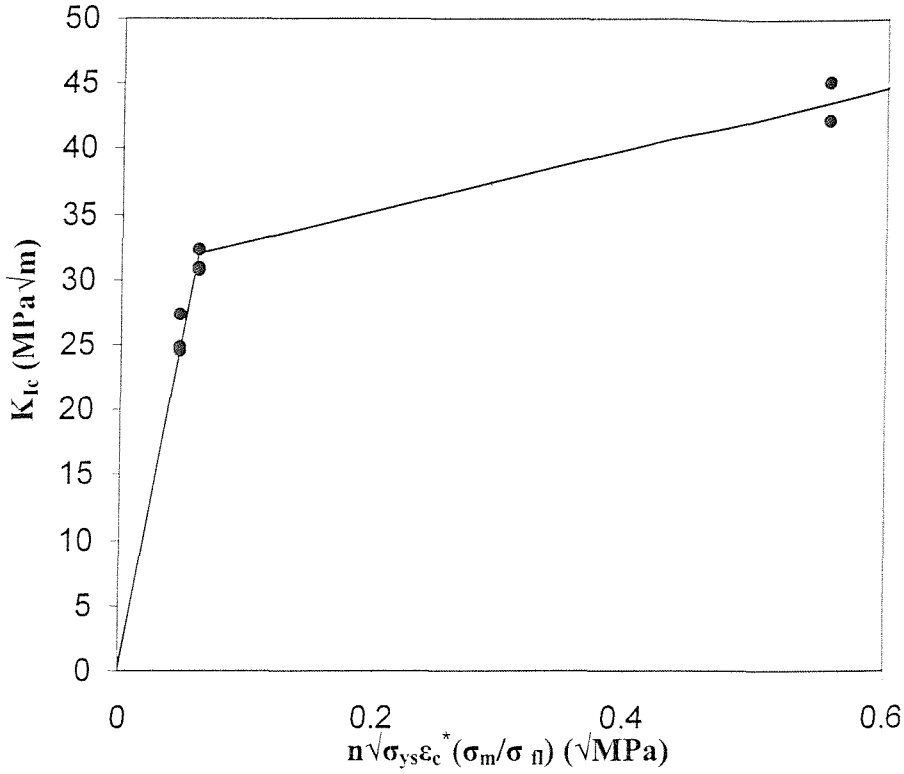

Figure 6.9: Relationship between K_{Ic} and $n\sqrt{(\sigma_{ys}\varepsilon_c^*(\sigma_m/\sigma_{fl}))}$ for the 7449 alloy for σ_m/σ_{fl}~2.1.

Figure 6.9 shows that the inclusion in the Garrett and Knott model of the critical strain dependence on stress state triaxiality does not seem to improve the model accuracy.

It may be noted that the approximation of fracture toughness failure mechanisms via bulk material testing (i.e. notched tensile tests) is open to debate. Such hypothesis appears valid when a single fracture mechanism occurs, such as in the T7C condition, i.e. a coarse voiding dominated fracture mechanism: however, the bulk material critical strain in T76 condition is used to describe both coarse voiding and intergranular/transgranular shear mechanisms. The underlying theory for the determination of the critical strain as a function of stress-state is based on void coalescence analysis, therefore the applicability of these concepts to partly intergranular fracture is questionable. Fig. 6.9 could be interpreted by considering that the stress-state triaxiality at the onset of fracture in coarse voiding dominated conditions is higher than for intergranular/transgranular shear conditions. The fracture mechanism may be more accurately described micromechanistically by relating fracture strains to each fracture mechanism: ε_{cv}^*, $\varepsilon_{i/t}^*$,

ε_{tv}^{*}. This method is a multi-mechanistic approach to toughness modelling, a concept considered further in section 6.4.3.

- *n and l^* relationship*

A further important approximation in the Garrett and Knott approach lies in the relation between the work hardening exponent, n, and the zone of intense deformation as identified in section 3.2. The parameter n is related to the capacity of the alloy to accommodate further strain and to develop shear bands during loading, i.e. a relation between n and l^* arises. The semi-empirical approach in the Garrett and Knott model which uses a linear relation between l^* and n^2 by a fit through results for aluminium alloys, as well as titanium alloys and steels needs confirmation. It may be shown that a different relation between l^* and n is in fact conceivable, based on the present results: considering the relationships between l^*, the CTOD at the onset of fracture (δ^*), K_{Ic}, E, σ_{ys} and the critical strain at the crack tip (ε^*) used by Garrett and Knott (see e.g. [31]), l^* can be obtained 'retrospectively' via:

$$\left.\begin{aligned} \varepsilon^* &= \frac{\delta^*}{2l^*} \\ \delta^* &\sim \frac{K_{Ic}^2}{E\sigma_{ys}} \end{aligned}\right\} \qquad l^* \sim \frac{K_{Ic}^2}{E\sigma_{ys}\varepsilon^*} \tag{6.8}$$

l^* values were calculated for the present 7449 data and plotted against n values (Fig. 6.10) and n^2 values (Fig. 6.11).

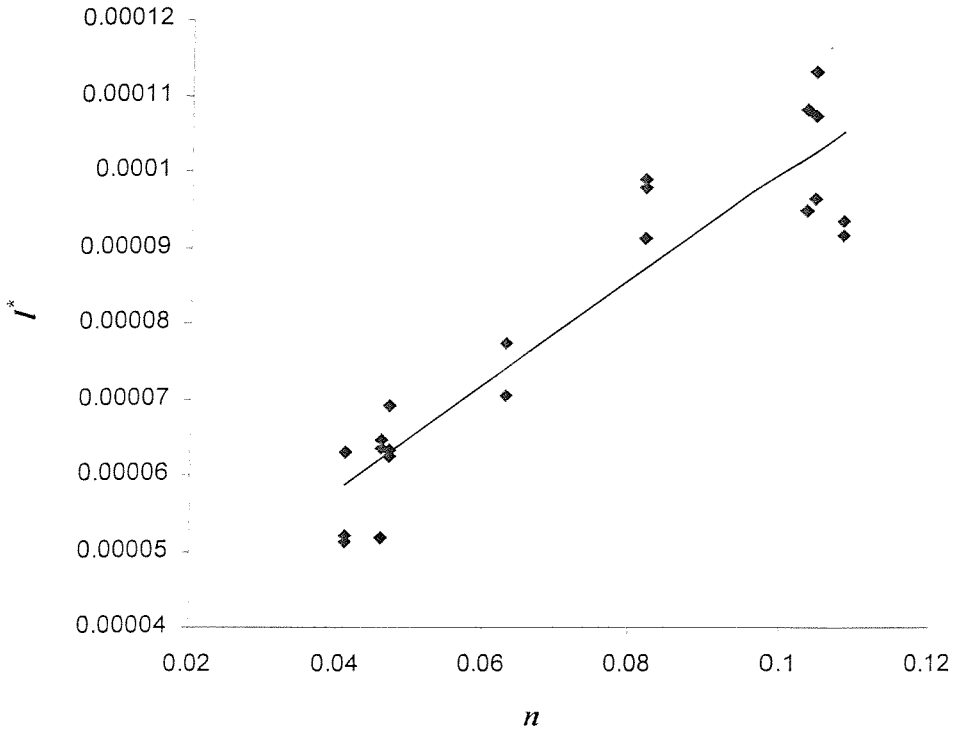

Figure 6.10: Relation between calculated l^* values and strain hardening exponent, n, for the 7449 a lloy with a linear trendline.

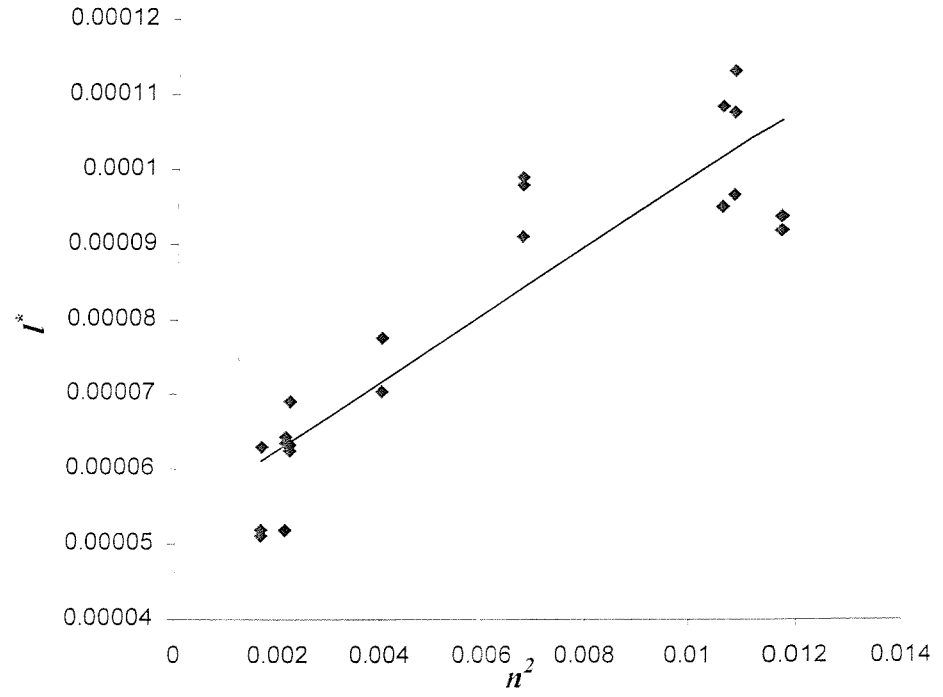

Figure 6.11: Relation between calculated l^* values and n^2 for the 7449 alloy with a linear trendline.

Figure 6.10 and Figure 6.11 show that within this framework, a linear relationship between n and notional l^* values is as much a reasonable approximation as assuming a linear relationship between l^* and n^2. A linear relation ship between l^* and n would give an alternative toughness model following:

Model II: $$K_{Ic} = C\sqrt{n\sigma_{ys}} \tag{6.9}$$

This relation is plotted in Fig. 6.12 for 7449 alloy data: whilst the data in this figure cannot be fitted satisfactorily with a single line through to the origin, the accuracy of the linear prediction of K_{Ic} is in fact enhanced by the simple modification, we may identify as model II.

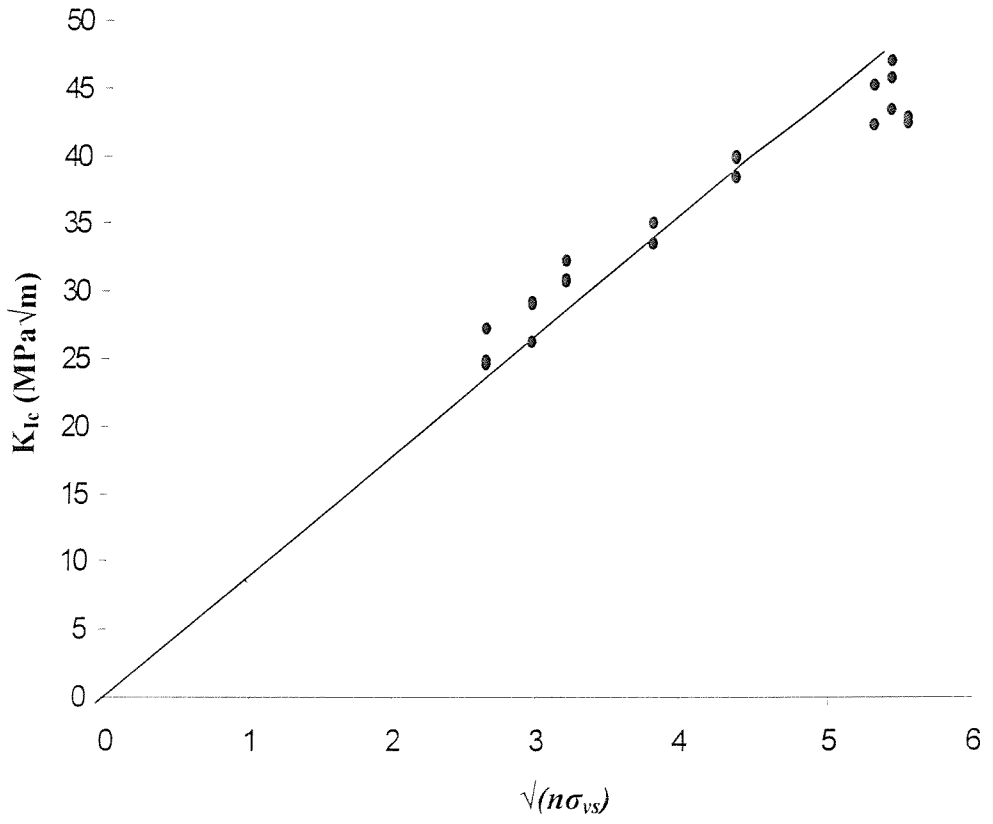

Figure 6.12: Relationship between K_{Ic} and $\sqrt{(n\sigma_{ys})}$ for the 7449 alloy in different heat treatment conditions.

The additional effects of the critical strain and the relation between l^* and n on the Garrett and Knott model then gives rise to:

$$K_{Ic} = C\sqrt{n\sigma_y\varepsilon^*} \tag{6.10}$$

The results for the data on 7449 are plotted in Figure 6.13.

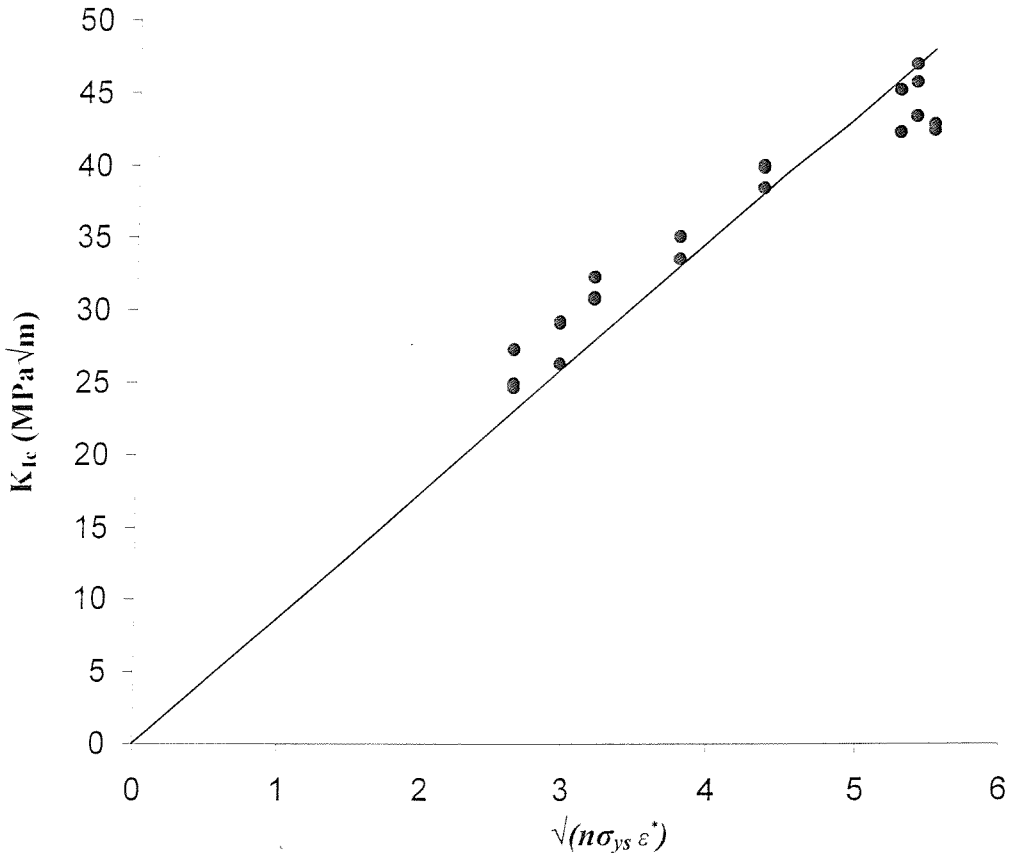

Figure 6.13: Relationship between K_{Ic} and $\sqrt{(n\sigma_{ys}\varepsilon^*)}$ for the 7449 alloy in different heat treatment conditions

This latter plot shows that with the determination of varying parameters such as critical strain and an alternative approximation of the size of the zone of intense deformation, an alternative model can be derived which fits our data reasonably well. However, seeing that the linear relationship between n and l^* which led to Eq. 6.9 was derived based exclusively on data for 7449, model II would need to be compared to other data before

any further conclusions can be drawn. Especially data on 7075 and 7475 which have been suggested to show a good correlation between K_{Ic} and $n\sqrt{\sigma_y}$ [46] would need to be considered in detail.

6.4.2 Applicability of the toughness model, model I, based on Ashby's work hardening theory

As may be seen from Eq. 6.6, the Ashby hardening modified model shows K_{Ic} to be proportional to $\frac{K_A^{\gamma}}{\sigma_{ys}^{\gamma-0.5}}$. Fig. 6.14 shows such a relationship for the present data on 7449 and 7449 (Mn) alloy: the prediction by the "new" model would appear to hold up better than the original Garrett and Knott model (Fig. 6.6), i.e. in Fig. 6.14 a straight line through the origin can fit the data, whilst this is not possible in Fig. 6.6 (or Fig. 6.7). Similar to Garrett and Knott's model, this new model is still only valid for a single mechanism of failure, but this does not seem to adversely influence its accuracy. In the first instance it must be noted that the fundamental derivation of Eq. 6.6 is of course a direct substitution between n and K_A, based on an empirically derived curve fit. As such the improvement in modelling accuracy between Eq. 6.6 and the Garrett and Knott approach cannot be given immediate micromechanical weight. However, key point to bear in mind are:

(A) A satisfactory translation from the non-micromechanical 'n' exponent, to the genuinely physically based 'K_A' has been made, and shown to retain a reasonable relationship between tensile deformation characteristics and toughness.

(B) Section 5.5 has shown that K_A actually provides a more accurate description of the work hardening of the present material compared to n.

(C) K_A may be related to quantifiable microstructural features such as the grain structure of the alloy and the non-shearable particles present in the matrix. As η particles are the only non-shearable particles that are susceptible to vary in density and size with ageing, the variation of K_A should be related to changes in the η precipitate sizes and density through ageing. Specifically, in overaged

conditions, a transition to Orowan looping is expected to increase the work hardening factor in the 7449 alloy.

As such, the present work may provide evidence for a more satisfactory micromechanical relationship between microstructure, tensile deformation characteristics and toughness than that provided by any modelling approach that uses '*n*' exponent values (such as Garrett and Knott).

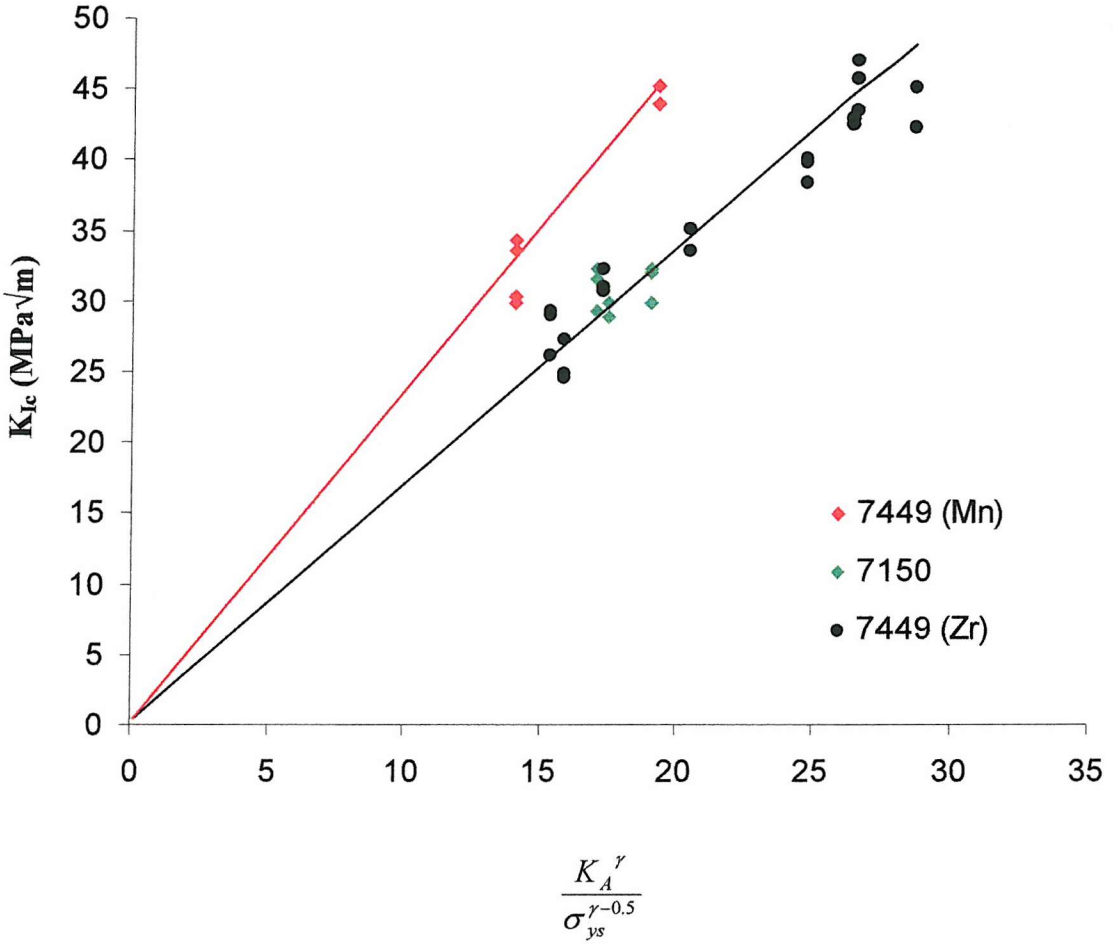

Figure 6.14: Graph of K_{Ic} vs. $\frac{K_A^{\gamma}}{\sigma_{ys}^{\gamma-0.5}}$ with γ=0.85

It is also valuable to note that the driving parameters of the fracture model are to a large extent uncoupled, i.e. the parameter describing macroscopic work hardening, K_A, does not depend directly on σ_{ys} (although some microstructural features, such as non-shearable particles, can effect both the strength and K_A, thus causing some interrelation to remain).

Similar to the approach used in deriving model II, also model I can also be modified to include the linear relationship between l^* and n as observed for 7449 (Fig. 6.9). Thus, an additional model can be derived by combining Eq. 6.9 and Eq.6.5.

$$\left.\begin{aligned} K_{Ic} &\sim \sqrt{\sigma_y n} \\ n &\sim \left(\frac{K_A}{\sigma_y}\right)^{\gamma} \end{aligned}\right\} \quad \Rightarrow \text{Model III:} \quad K_{Ic} \sim \sigma_y^{1/2-\gamma/2} \cdot K_A^{\gamma/2} \cdot \varepsilon^{*0.5} \qquad (6.11)$$

Figure 6.15 illustrates the relation predicted by model III (Eq. 6.11) for the 7449 alloy.

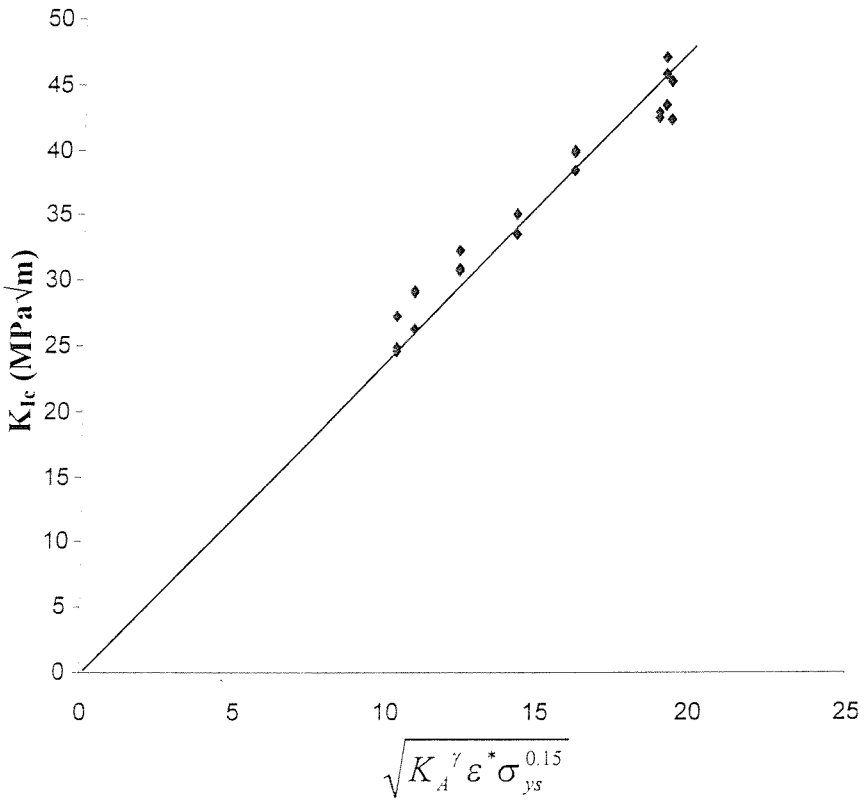

Figure 6.15: Graph of K_{Ic} vs. $\sqrt{K_A^{\gamma} \varepsilon^* \left(\frac{\sigma_{ys}}{\sigma_{ys}^{\gamma}}\right)}$ for γ=0.85, plotted with experimental data for the 7449 alloy.

It is clear from Fig. 6.15 that this additional model (model III) may exhibit a reasonable correlation with the experimental data. The relative accuracies of the different models have been evaluated by statistical means using RMSE between the experimental result and the linear predicted models for the corrected Garrett and Knott model (Fig 6.13), model I (from Eq. 6.6, Fig. 6.14) and the two further modifications (model II and model III) developed in this study.

	RMSE
Garrett and Knott model (Eq. 6.1)	3.9
Model I (Eq. 6.6)	2.3
Model II (Eq. 6.9)	3.7
Model III (Eq. 6.11)	1.9

Table 6.2: Root mean square error (RMSE) between experimental data and Garrett and Knott and new toughness models for the 7449 alloy.

The typical range in K_{Ic} measured in the tests for a given alloy/heat treatment combination was 2-3 MPa. The RMSE values in Table 6.2 clearly show that the accuracy of models I and III is of the same order as the accuracy of plane strain toughness tests results. Model I (Eq. 6.6) particularly presents a combination of relatively good accuracy, meaningful parameters and relative simplicity.

6.4.3 Multi-mechanistic approaches to toughness modelling

The need for a multi-mechanistic approach to toughness modelling for the 7150 and 7449 alloys has been highlighted in the previous sections. A multi-mechanistic interpretation of the model derived in Section 6.4 (Eq. 6.6) is illustrated in Fig. 6.16. A linear relation is associated with the fracture modes, with experimental results falling on these lines when a single failure mechanism occurs, or between the lines when there is combination of failure mechanisms.

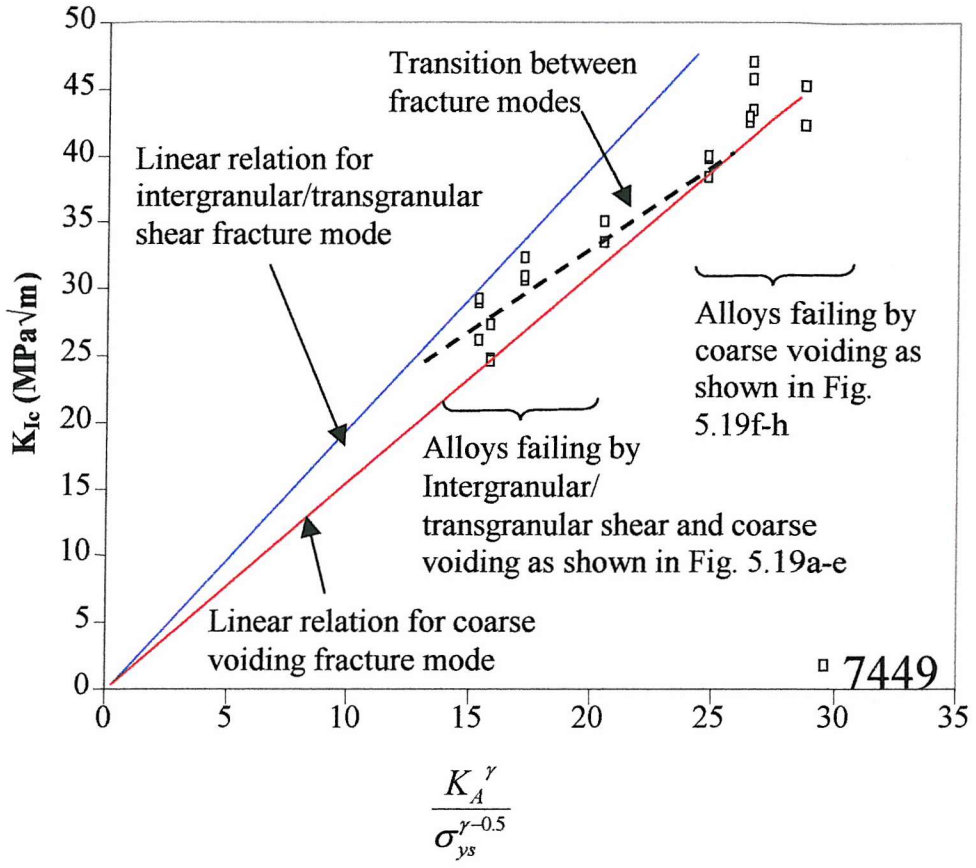

Figure 6.16: multi-mechanistic analysis of Fig. 6.13.

Several attempts have been made within the literature to model toughness with a multi-mechanistic approach, as noted in Section 3.2: Hornbogen and Graf [80] have proposed a linear summation of specific intergranular and transgranular fracture toughness, weighted by their respective area fraction on the fracture surface; whilst Gokhale et al [81], considering fracture toughness as an energy parameter, have used a squared summation of K_{Ic} for specific fracture mechanisms with a weight function based on the area fraction of the respective mechanisms. Following the same principles a multimechanistic model may be deduced attributing a critical strain specific to coarse voiding failure and a critical strain specific to the intergranular+transgranular shear fracture mode, with a specific toughness value being generated for a given failure mechanism. Following from this, a weighted summation of toughness contributions from the different mechanisms may be made, similar to Hornbogen and Graf;

$$K_{Ic} = A_{cv} K_{Ic,cv} + A_{i/t} K_{Ic,i/t} \tag{6.12}$$

where A_{cv} and $A_{i/t}$ are the area fraction of the specimen surface that failed respectively through coarse voiding and intergranular/transgranular fracture. $K_{Ic,cv}$ and $K_{Ic,i/t}$ are the fracture toughness values associated with the occurance of a single fracture mode (respectively, coarse voiding and intergranular/transgranular fracture). It shall be noted that critical strains specific to the fracture mode ε_{cv}^* and $\varepsilon_{i/t}^*$, defined in Section 6.4.1, can be used to define $K_{Ic,cv}$ and $K_{Ic,i/t}$:

$$\begin{aligned} K_{Ic,i/t} &= K_{Ic}\left(\varepsilon_{i/t}^*\right) \\ K_{Ic,cv} &= K_{Ic}\left(\varepsilon_{cv}^*\right) \end{aligned} \quad \text{with} \quad K_{Ic} = C \cdot K_A^{\gamma} \sqrt{\frac{\varepsilon_{fract.mode}^*}{\sigma_y^{\gamma}}} \tag{6.13}$$

where C is a constant. Following this formulation, Eq. 6.12 is then equivalent to a weighted sum of the specific critical strain. However, as discussed in Section 6.4.1, the determination of specific ε_{cv}^* and $\varepsilon_{i/t}^*$ values is problematic. Therefore, the influence of the critical strain will be expressed through fracture mode specific constants $C_{i/t}$ and C_{cv}. According to Eq. 6.6 and Eq. 6.13, $K_{Ic,cv}$ and $K_{Ic,i/t}$ may be expressed as

$$\begin{aligned} K_{Ic,i/t} &= C_{i/t} K_A^{\gamma} \sigma_y^{0.5-\gamma} \\ K_{Ic,cv} &= C_{cv} K_A^{\gamma} \sigma_y^{0.5-\gamma} \end{aligned} \quad \text{with} \quad C_{fract.mode} = C\sqrt{\varepsilon_{fract.mode}^*} \tag{6.14}$$

Combining Eq. 6.12 and 6.14 gives

$$K_{Ic} = K_A^{\gamma} \sigma_y^{0.5-\gamma} \left(A_{cv} C_{cv} + A_{i/t} C_{i/t}\right) \tag{6.15}$$

SEM fractographic observation of failed specimens was used to deduce semi-quantitative estimates of the percentage of the surface area failing by coarse voiding or the intergranular/transgranular shear fracture mechanisms: a grid was superposed to the fracture surface micrographs and the fracture mode occuring at the intersection of the

grid lines was recorded and weighted against the total number of grid point to give a percentage. These estimates are presented in Table 6.3.

7449-Temper	A_{cv} (%)	$A_{i/t}$ (%)	Range*
T6	29	71	20
T79	48	52	13
T76	63	37	18
T7A	84	16	12
T7B	100	0	-
T7C	100	0	-
T7D	100	0	-
T7E	100	0	-

* The range is defined as the variation between the maximum value and the minimum value obtained from the micrographs studied.

Table 6.3: Estimated area fraction of coarse voiding and intergranular/transgranular shear fracture from the SEM fractographic observation of the failed toughness specimens.

The constant C_{cv} is obtained by applying Eq. 6.15 to alloy 7449T7B to T7E test results (i.e. conditions where coarse voiding was clearly dominant). $C_{i/t}$ was then used as a fitting parameter. This then yields

C_{cv}=1.62

$C_{i/t}$=1.83

Using these parameters, Eq. 6.15 is plotted in Fig. 6.17.

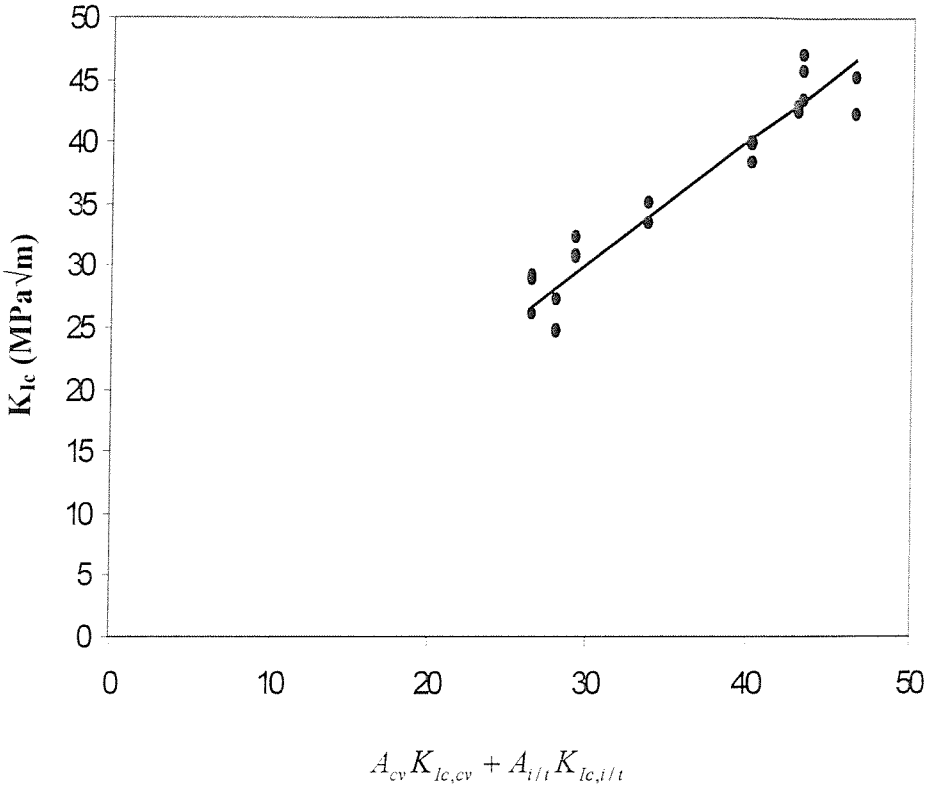

Figure 6.17: K_{Ic} vs. $A_{cv}K_{Ic,cv} + A_{i/t}K_{Ic,i/t}$, plotted with experimental data for the 7449 alloy.

Figure 6.17 shows that the linear relationship predicted by Eq. 6.15 is reasonably well respected. The RMSE value for this multi-mechanistic model is 2.1. The accuracy of this model would therefore appear only slightly improved compared to model I (see Table 6.2). In the first instance the approximation made in estimating the different fracture mode areas on the fracture surface may limit the accuracy of any associated model. Furthermore, the model represents a relatively simple description of multiple failure modes with no interaction occuring between the mechanisms.

Following the same approach but considering a squared summation of fracture toughness gives:

$$K_{Ic}^{\ 2} = A_{cv}K_{Ic,cv}^{\ 2} + A_{i/t}K_{Ic,i/t}^{\ 2} \tag{6.16}$$

Combining Eq. 6.16 with Eq. 6.14 gives:

$$K_{Ic} = K_A^{\gamma}\sigma_{ys}^{0.5-\gamma}\sqrt{A_{cv}C_{cv}^2 + A_{i/t}C_{i/t}^2} \tag{6.17}$$

Using the same parameters as above, Eq. 6.17 is plotted in Fig. 6.18.

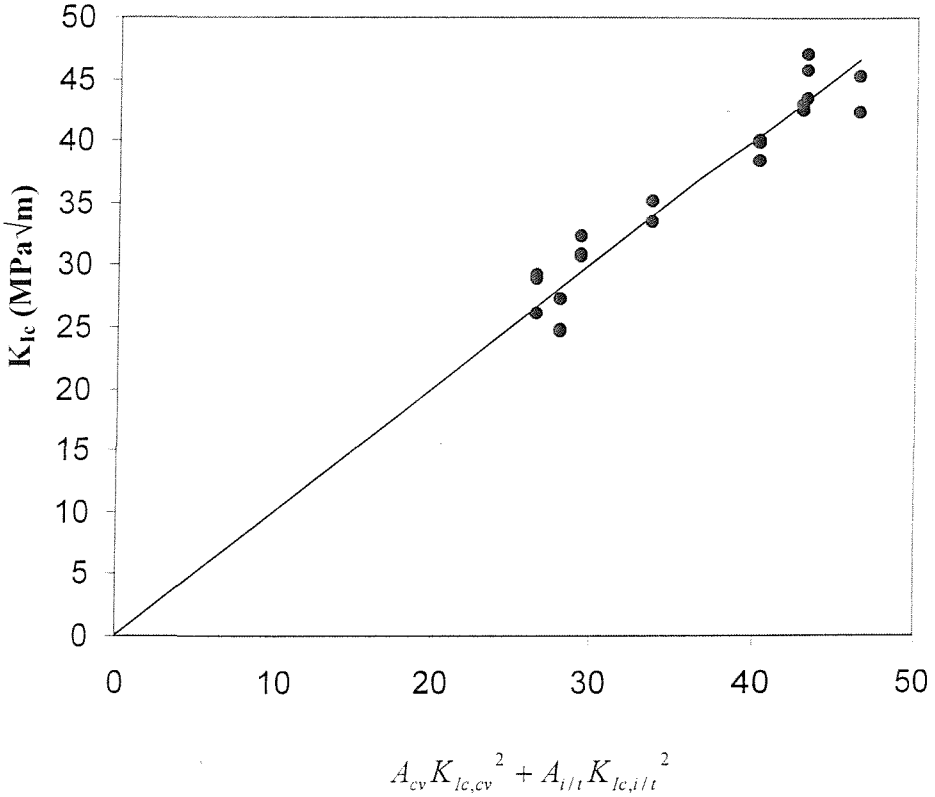

Figure 6.18: K_{Ic} vs. $A_{cv}K_{Ic,cv} + A_{i/t}K_{Ic,i/t}$, plotted with experimental data for the 7449 alloy.

The RMSE value for this multi-mechanistic model is 2.1 which shows little amelioration compared to the weighted summation model presented in Eq. 6.15.

6.5 Conclusions

- SEM analysis on fracture surfaces and polished sections through fracture surfaces and arrested cracks showed that fracture in 7449, 7150 and 7449(Mn) is multi-mechanistic: fine tensile voiding, grain boundary failure, transgranular shear and coarse voiding at large intermetallics occur. In the 7449(Mn) alloy, there is a marked influence of Mn-containing dispersoids on the fracture process. In the 7150 and 7449 alloy the occurrence of several fracture modes within a same sample, and the evolution of the dominant fracture mode with the ageing treatment, was linked to the amount of η' shearable precipitates within the matrix (i.e. controlling shear banding), as well as the weakening of grain boundaries by coarse η precipitates. The higher amount of coarse S phase in the 7150 alloy is believed to lower the alloy fracture toughness compared to the 7449 alloy.
- The work hardening behaviour of these high strength 7xxx aluminium alloys is better described by the Ashby work hardening model for hard particles in a soft matrix compared to the Ramberg-Osgood model.
- A new modelling approach, incorporating the Ashby model for work hardening with previous approaches within the literature was derived. The advantages of this new model are:
    - The model correctly predicts an increasing toughness with decreasing strength and independently describes the dependence of toughness on yield strength and work hardening for a given alloy.
    - The work hardening factor K_A is directly relatable to the microstructure
    - The significance of l^* and ε_c^* values has been considered in relation to model accuracy. The use of ε_c^* values from smooth and notched tensile tests was not seen to particularly improve model performance.
- The complex interaction between the failure mechanisms make the attempts to model fracture toughness using multi-mechanistic approaches problematic. Incorporation of

multimechanistic behaviour into the present data has been attempted, although the accuracy/validity of the approaches is difficult to clarify with the available data (multimechanistic model accuracies are not seen to improve dramatically upon single mechanism approaches).

Chapter 7

Heat treatment modelling

7.1 Introduction

The application of RRA heat treatment has proven commercially valuable for 7xxx aluminium alloys. This temper has been given the designation T77 and applied by Boeing to the 7055 alloy and by Alcoa to the 7150 alloy. However, the use of this treatment is still limited. In chapter 2 part 2.6, some of the problems related to the application of RRA treatment were reviewed. The present chapter describes a study that was conducted to provide some insight in the difficulty of applying RRA treatment to thick 7xxx plates. Commercial applications require both a good level of mechanical properties and homogeneity of these properties throughout the plate. A modelling approach has been applied to evaluate these properties depending on the parameters of the heat treatment, and especially the parameters of the retrogression treatment as this stage of the RRA treatment is the most significant for the process efficiency. The parameters considered were the retrogression treatment temperature and time as well as the heating rate from a T6 heat treatment temperature to retrogression temperature. Several cases of retrogression treatment were modeled: linear heating of the oven, immersion of the alloy in an oven set at the retrogression temperature. The presence of a medium between the alloy and the oven was also included in the study.

The temperature profile for the alloy was calculated from the basic principles of heat transfer as presented in part 7.2. The comparison of the different RRA treatments with their varying parameters was made using an internal state variable approach. This calculation was done for various plate thicknesses as explained in part 7.3. In part 7.4, the results of the modelling work are presented and discussed.

7.2 Basic principle of heat transfer

The description of the heating and cooling of a solid is based on an energy balance formulation (see e.g. [101]). This balance depends on the energy flow added to the system by an outside source, $\dot{E}_{in}$, the rate of energy exported out of the system, $\dot{E}_{out}$, the rate of energy generation inside the system, $\dot{E}_g$, and the energy storing rate, $\dot{E}_s$. The energy balance is then expressed as:

$$\dot{E}_{in} + \dot{E}_g = \dot{E}_{out} + \dot{E}_s \tag{7.1}$$

The energy balance is depicted schematically in Fig. 7.1.

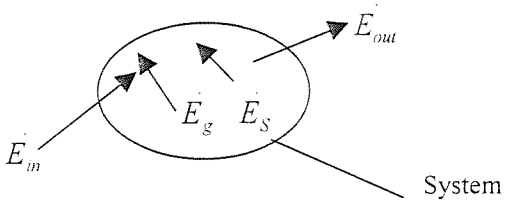

Figure 7.1: Energy balance description of a system

The generation of energy in a solid is due to the conversion of other energy forms into thermal energy, like for example an exothermic chemical reaction. Though chemical reactions are taking place during the heating of aluminium alloys (precipitation, dissolution), this effect is generally negligible compared to the overall heating of the material, provided no massive melting or solidification occurs.

The transfer of heat from an external source to the system for aluminium is achieved mainly by conduction. The conduction heat transfer is the transfer of kinetic energy from one atom to the next by direct contact between the two. The conduction in a solid with a heat flow propagating along an axis x is described by the Fourier law:

$$q = -kA\left(\frac{dT}{dx}\right) \tag{7.2}$$

Where q is the rate of heat flow in the x direction, k is the thermal conductivity, A is the system area normal to x direction, T is the temperature and x is the distance along the x-axis.

The phenomenon of energy storage occurs in a solid when the temperature changes with the time. It is then described as

$$\dot{E}_s = \rho Vc\left(\frac{\partial T}{\partial t}\right) \tag{7.3}$$

Where ρ is the density of the material, V is the volume, c is the specific heat, t is the time

Therefore heat diffusion problems are expressed as differential equations. The solution to the differential equation can be found if the boundary conditions are specified.

7.3 Heat flow modelling in a 7xxx aluminium plate

7.3.1 Internal state variable modelling

It has been stated earlier that the application of RRA treatment to thick plate would require different heat treatment as compared to RRA treatment applied to thin plate, i.e. slower heating ramp, longer retrogression time, lower retrogression holding temperature (see Fig. 7.2). Though apparently quite different, heat treatments such as presented in Fig. 7.2 can actually lead to the same microstructural state. The concept behind this is generally referred to at the equivalent time approach and has been used by a number of researchers [102,103,104]. The equivalent time approach gives some insight into the heat treatment/precipitation reactions in order to interpret and compare the temperature-time profile relative to each heat treatment undergone by the alloy.

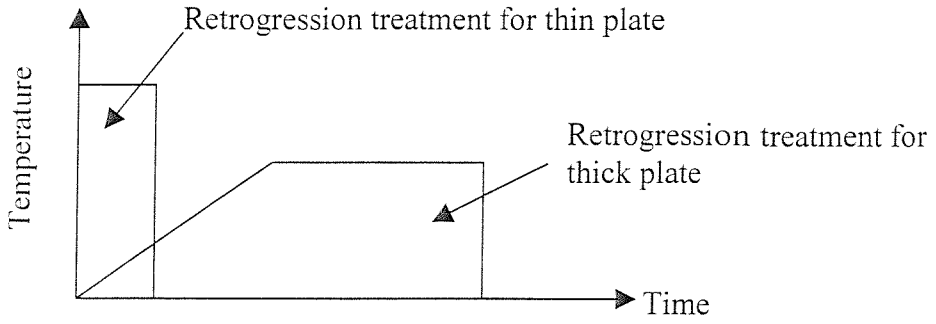

Figure 7.2: Schematics of two potentially equivalent heat treatments

Shercliff and Ashby have proposed a model for the ageing of heat treatable binary aluminium alloys [102]. Considering that over most of the ageing curve the particles coarsen at an almost constant volume fraction and applying simplifying assumption together with the cubic coarsening law, they relate the mean particle radius r at a time t for a heat treatment conducted at a temperature T to the mean radius r_0 at $t=0$ with the equation:

$$r^3(t) - r_0^3 = \frac{k_1 t}{T} \exp\left(-\frac{E_a}{RT}\right) \tag{7.4}$$

Where k_1 is a kinetic factor which depends on the matrix composition, E_a is the activation energy, and R is the gas constant.

Therefore, the extent of ageing can be defined by the "temperature corrected time" variable P:

$$P = \frac{t}{T} \exp\left(-\frac{E_a}{RT}\right) \tag{7.5}$$

However, most commercial heat treatments are not isothermal. Therefore Shercliff and Ashby [102,105] introduce the concept of kinetic strength J of a thermal cycle $T(t)$. J describes the microstructural state of the alloy and is expressed as:

$$J = \int_0^t \frac{1}{T(t)} \exp\left(-\frac{E_a}{RT(t)}\right) dt \tag{7.6}$$

A given isothermal heat treatment (at a temperature T_0 for a time t_0) corresponds to a P value which determines the microstructure. This same P value (i.e. the same microstructure) can be attained by a different isothermal heat treatment at a temperature T' for an equivalent time t_{eq}:

$$t_{eq} = PT' \exp\left(-\frac{E_a}{RT'}\right) \tag{7.7}$$

The same equivalent time approach can be used for non-isothermal heat treatment (using J). This approach enables the direct comparison of different heat treatments.

The same kind of concept has been applied earlier in an industrial context. For example, Dubost and Bouvaist [106,107] evaluated thermal treatments applied to 7xxx aluminium alloys using a function $R(T)$ having a similar form:

$$R(T) = A_1 \int \exp\left(-\frac{A_2}{\theta(t)}\right) dt \tag{7.8}$$

Where A_1 and A_2 are constant and $\theta(t)$ is the time dependent temperature applied for a duration t to the alloy.

Another version is given by Shahani et al. [45] in their optimisation of thick 7xxx alloy products:

$$t_{eq} = \frac{\int \exp -\frac{E_a}{k_B T} dt}{\exp -\frac{E_a}{k_B T_{ref}}} \tag{7.10}$$

Where T_{ref} is an arbitrary reference temperature.

Thus it is possible to compare the effect of different isothermal and non-isothermal heat treatments and gain some insight in the relation between microstructural state and ageing by the use of the equivalent time approach. This theory relies on the estimation of the activation energy which is specific to each reaction and a way to calculate these activation energies is described below.

7.3.2 Calculation of the activation energy

The rate of a precipitation reaction depends on the activation energy E_a of the different reaction. Several methods can be used to derive the mean activation energy of a thermally activated process [108]. The Kissinger method provides a means of deriving an activation energy from a set of experiments performed at a range of heating rates. Various types of thermal analysis experiments can be analysed. The Kissinger method predicts a linear relation between $\frac{1}{T_f}$ and $\ln\frac{\beta}{T_f^2}$ with a slope equal to E_a/k_B:

$$\ln\left(\frac{\beta}{T_f^{\,2}}\right) = -\frac{E_a}{k_B T_f} + C \tag{7.11}$$

Where C is a constant, T_f is the temperature at a fixed state of transformation, β is the heating rate and k_B is the Boltzmann constant.
T_f is related to an arbitrary fixed state of transformation, i.e. for DSC experiments a constant heat evolved, ΔQ, value [109].

DSC experiments give the heat flow $\frac{dQ}{dt}$ versus time. By integrating the heat flow of the peak corresponding to the reaction of interest, i.e. specific activation energy, over the time: $\int\frac{dQ}{dt}dt$, ΔQ values can be derived and ΔQ evolution with the temperature is deduced. At a fixed state of transformation, i.e. an arbitrarily chosen ΔQ value, a T_f temperature can be deduced. This can be achieved for several DSC runs with different

heating rates. Therefore, several T_{fi}-β_i combinations are obtained. The slope of the curve - $\frac{1}{T_f}$ vs. $\ln\frac{\beta}{T_f^2}$ gives the value of the activation energy.

7.3.3 Model of heating of a plate

The present problem of heating up of a thick plate is a transient, i.e. time dependent, heat conduction problem. Generally the boundary condition at the surface of the solid depends on convective heat transfer, depending on the relative efficiencies of conduction and convection for aluminium alloys. In the following treatment we will neglect this complication and instead assume that simple boundary conditions for conduction can be applied to describe the conditions on the contact surface of the two media [101]:

- The heat flux is continuous over the surface of separation, that is:

$$\lim_{x\uparrow l} k_1 \frac{\partial T_{medium1}}{\partial x} = \lim_{x\downarrow l} k_2 \frac{\partial T_{medium2}}{\partial x} \tag{7.12}$$

  Where k_1 and k_2 are the respective conductivities of the medium 1 and medium 2, $T_{medium1}$ is the temperature in the first media (air, oil, etc), and $T_{medium2}$ is the temperature in the second media (aluminium plate)(see Fig. 7.3).

- At the surface of separation the temperature of the two media are the same:

$$\lim_{x\uparrow l} T_{medium1} = \lim_{x\downarrow l} T_{medium2} \tag{7.13}$$

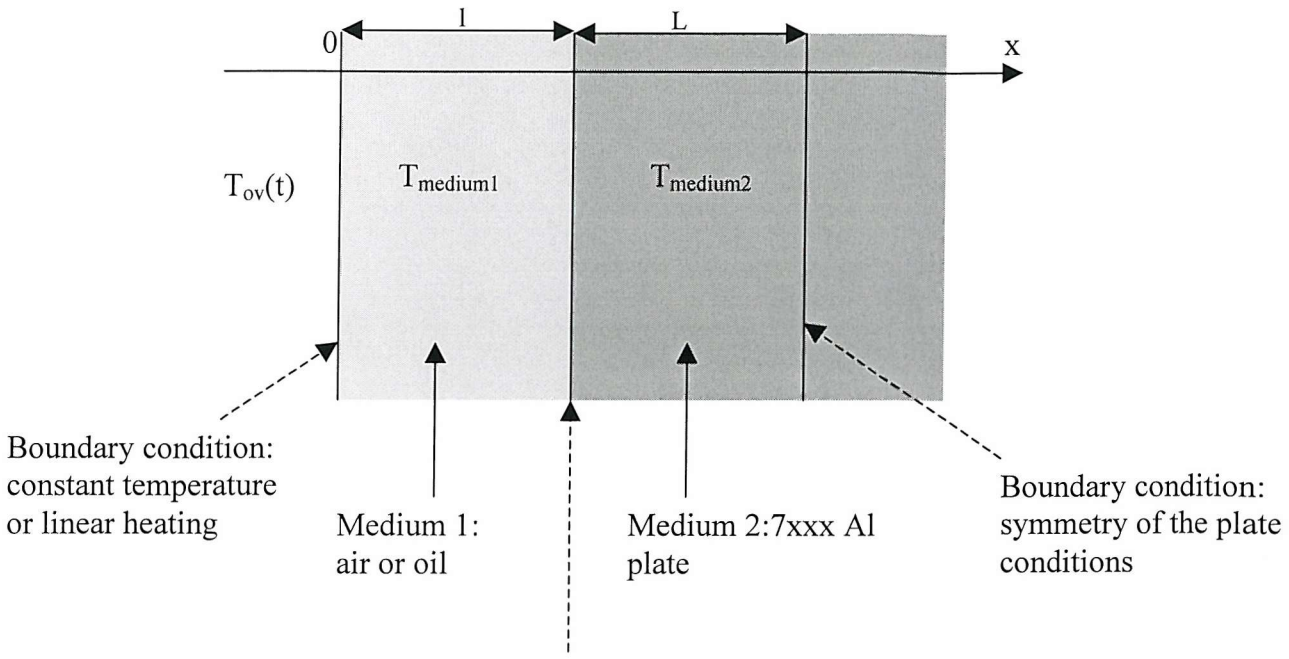

Figure 7.3: schematic illustration of the heat conduction problem with boundary condition.

Assuming that the generated energy is negligible, the differential equation defining this problem is (see e.g. [101]):

$$\frac{\partial^2 T}{\partial x^2} = \frac{1}{\alpha}\frac{\partial T}{\partial t} \tag{7.14}$$

$$\text{With } \alpha = \frac{k}{\rho c} \tag{7.15}$$

Other conditions are:

- at $x=0$, $T=T_{ov}(t)$
- symmetry: $T(x+l+L)=T(l+L-x)$
- at $t=0$: $T_{medium1}=T_1$ and $T_{medium2}=T_2$

If the temperature stays constant (T_1) at the surface of the aluminium plate, Eq. 7.14 can be solved analytically, and this gives [101]:

$$T_{media2} = T_1 + \frac{4(T_2 - T_1)}{\pi} \sum_{n=0}^{\infty} \frac{1}{2n+1} \exp\left[-\left({(2n+1)\pi}/{2L} \right)^2 \alpha t \right] \sin\left({(2n+1)\pi x}/{2L} \right) \qquad (7.16)$$

To solve the above equation for varying interface temperature, generally an iterative method needs to be employed. A readily usable iteration equation can be derived from Eq. 7.14.

$$\frac{\Delta T}{\Delta t} = \alpha \frac{\Delta^2 T}{\Delta x^2} \qquad (7.17)$$

Which gives:

$$T_{x,t} = T_{x,t-\Delta t} + \alpha \Delta t \frac{T_{x+\Delta x,t-\Delta t} - 2T_{x,t-\Delta t} + T_{x-\Delta x,t-\Delta x}}{\Delta x^2} \qquad (7.18)$$

Where $T_{x,t}$ is the temperature at the position x and at the instant t. Using this equation and the initial and boundary conditions given above, the temperature evolution with the time throughout the aluminium plate and medium can be obtained using an iterative method. Hence, evolution of temperature in the plate for different thermal treatments can be modeled. Several configurations are considered:

- Fixed T_{ov}, with initially $T_{medium1} = T_{ov}$ and $T_{medium2}$ equals the room temperature: this case is representative of a cold plate immersed in a hot bath in a stable furnace.
- T_{ov} is increasing linearly with initially $T_{medium1} = T_{medium2}$: this case is representative of the heating of plate in a fluid bath, which are both at the same temperature initially.

These cases have been programmed in Visual Basic using Microsoft Excel's built-in visual basic editor. The program code is presented in Appendix II.

7.3.4 Modelling parameters

The heat transfer through an aluminium plate during a retrogression treatment has been modelled using Eq. 7.18. The diffusivity α and conductivity k used in this model are summarised in Table 7.1.

	α ($x10^{-5}$ m^2/s)	k (W/m.K)
7xxx aluminium alloy	7.72	155
Air	3.19	0.024
Oil	1.76	0.14

Table 7.1: Diffusivity and conductivity constants

The plate thickness in the model was 20cm; it represents an upper limit for thick 7xxx alloy products [45,106]. Two thicknesses for the medium layer have been considered: 10cm and 50cm. The retrogression treatment follows directly after the T6 ageing treatment conducted at 120°C. A range of cases with a selection of parameters has been studied; including heat transfer from the furnace to the plate with and without an intermediate medium (oil and air), heating rates of 100°C/h, 50°C/h and 10°C/, holding temperature of 180°C and 200°C and holding times of 10min, 30min and 1h. Separately, the case of the immersion of a cold aluminium plate in a hot bath (with a 10cm medium layer) has been considered for the same holding times and temperatures.

All these heat treatments were subsequently evaluated using the equivalent time approach described in Eq. 7.10 (T_{ref}=120°C). Equivalent times are also compared to typical equivalent time for retrogression applied to thin plates.

7.4. Results

7.4.1 Preliminary experimental investigation of RRA

Analysis of T6 samples: the activation energy of η′ dissolution

The activation energy of η′ dissolution in 7449 has been determined applying the Kissinger method to analyse DSC experiments conducted at different heating rates (5°C/min, 10°C/min, 20°C/min) on the 7449 T651 alloy. Calculations have been performed on the first endothermic peak (η′ dissolution).

DSC runs conducted on the 7449 T651 alloy at different heating rates are shown in Fig. 7.4.

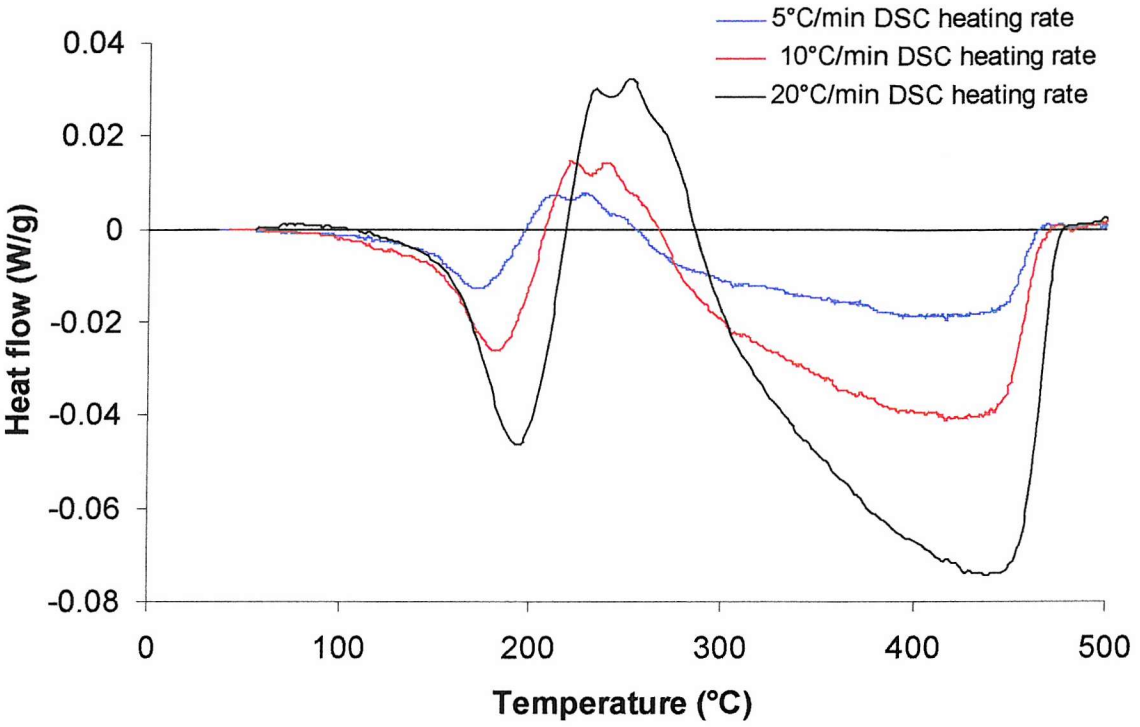

Figure 7.4: DSC curves of the 7449 alloy T651 with 3 different DSC heating rates.

As the DSC heating rate is increased, both the peak temperature and the heat flow increase. This graph also shows that the retrogression treatment takes place in the temperature range where η′ dissolution takes place. In more conventional commercial ageing treatment achieved at lower temperature, the phase transformation from η′ to η is expected to appear slowly and continuously. The efficiency of the retrogression treatment relies on the transformation of the grain boundary precipitates but also in ensuring that a sufficient amount of η′ precipitates will be dissolved or partially dissolved during the process. This provides that the strength can be restored to a T6 level during re-ageing treatment. As the grain boundary precipitate transformation process can not be analysed

from the DSC data, the progress of the retrogression treatment is evaluated in terms of η′ dissolution. Therefore the activation energy considered in the following model is the activation energy of η′ dissolution. Thus, only the first endothermic peak, i.e. the peak related to η′ dissolution, in the DSC runs has been considered in the determination of the activation energy E_a. These peaks have been integrated to give the total heat evolved as plotted in Fig. 7.5. To obtain T_f temperatures associated with a constant fraction transformed for the first dissolution peak for each of these runs, an arbitrary heat evolved value was chosen as 3 J/g.

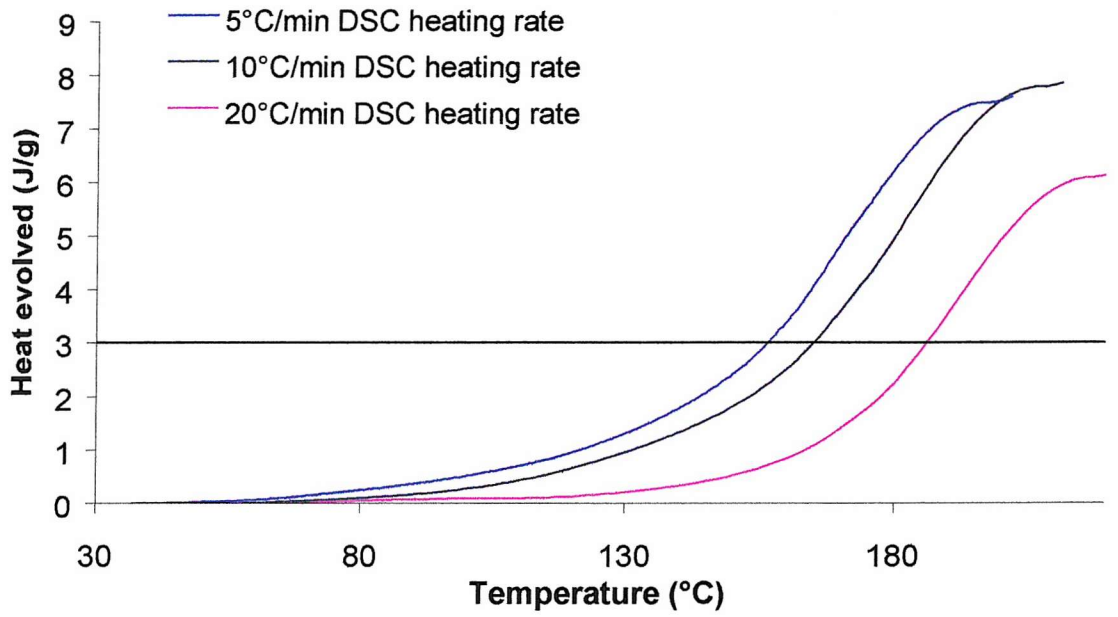

Figure 7.5: Curves of the integration of the first dissolution peak of 7449T651 DSC curves for different heating rate.

From Fig. 7.5, three T_{fi}-β_i combination are determined. These combinations are then plotted according to the Kissinger method in Eq. 7.11 (Fig. 7.6). According to the Kissinger method, the trendline slope of these points is then proportional to the activation energy.

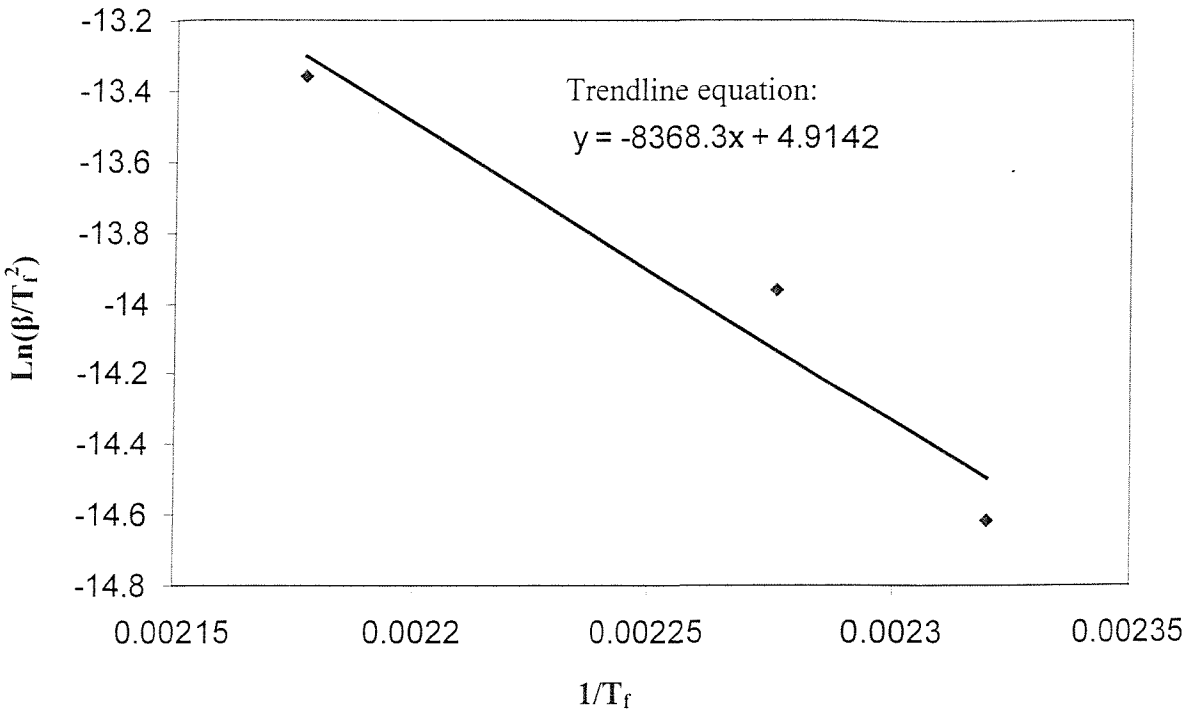

Figure 7.6: Kissinger method applied to the total heat evolved of the first endothermic peak of 7449T651

This procedure gives:

$$\frac{E_a}{k_B} = 8400K$$

The activation energy of η′ dissolution is then 70kJ.mol^{-1}. It should be noted that different heat evolved values along the linear part of these curves can produce E_a values that vary by about 10% from the value given above. This error may affect the accuracy of the modelling performed below.

Analysis of retrogressed samples

In a preliminary investigation, two RRA treatments for thin plate, described in Table 7.2, to use as a reference were investigated using DSC, Vickers hardness tests and tensile tests.

DSC experiments on retrogressed 7449 alloy are shown in Fig. 7.7.

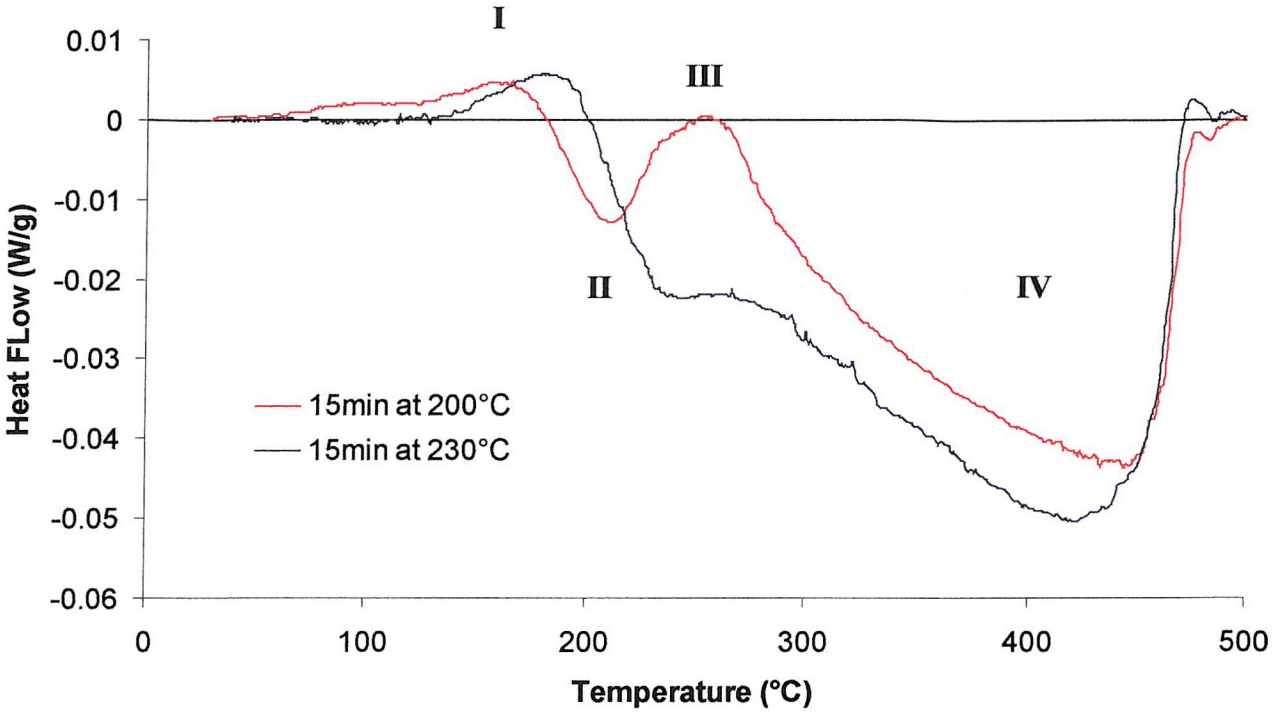

Figure 7.7: DSC curves of the 7449 alloy for two different retrogressed heat treatments.

The features shown in this figure are similar to previous studies on retrogressed 7xxx alloys [89,110]. Papazian [91] suggested that the first exothermic peak (peak I) represents the re-precipitation of η′ precipitates dissolved during the retrogression treatment; with the following endothermic peak (peak II) representing their re-dissolution during the DSC run. Subsequently η precipitates can form (peak III) for the alloy retrogressed at 200°C followed by η dissolution; or if most of η precipitates have been formed prior to the DSC experiment a transition to η dissolution can occur directly as for the alloy retrogressed at 230°C [89]. However, Park and Ardell have proposed another interpretation [110]. They observed that peak I occurs over the same temperature range as the η′ dissolution peak in alloys treated to T6 type conditions. As precipitation must take place at lower temperature compared to the dissolution reaction they described that first exothermic peak as the effect of the re-growth of partially dissolved η′ precipitates. The theory of thermally activated reactions indicates that precipitation will lead to a different shape peak as compared to re-growth [111]. Park and Ardell [110] also argue that the transformation of η′ into η precipitates occurs during peak I. Therefore, at this stage there

is a bimodal distribution of η precipitates in the alloy due to the presence of very small η precipitates formed during the DSC run and η precipitates formed during the heat treatment. Peak II then represents the dissolution of the small η precipitates and peak IV represents the dissolution of larger η precipitates. In this interpretation peak III does not represent a precipitation peak but an absence of reaction between small η precipitates dissolution (peak II) and large η precipitates dissolution (peak IV). The absence of peak III for the alloy treated at 230°C suggests that there is a wider range of η precipitate sizes in this alloy.

These two DSC curves suggest that the sample retrogressed at 200°C contains more η′ precipitates and/or small η precipitates than the one retrogressed at 230°C. The presence of peak I in both conditions indicates that a certain amount of η′ dissolution has occurred during both retrogression treatments.

Optimum re-ageing treatment has been determined by conducting Vickers hardness tests for samples heat treated at 120°C (see Fig. 7.8) The optimum re-ageing time is about 16 hours at 120°C.

Figure 7.8: Vickers hardness results of 7449 in two different retrogressed conditions re-aged for various length of time.

Tensile tests have then been conducted for both RRA conditions (Table 7.2).

	UTS (MPa)	σ_{ys} (MPa)	Elongation (%)	n	K_A
RRA 1: T6+retrogressed at 200°C for 15 min. +re-aged at 120°C for 16 hours	622	604	9.8	0.036	283
RRA 2: T6+retrogressed at 230°C for 15 min. +re-aged at 120°C for 16 hours	499	420	13.5	0.107	584

Table 7.2: Tensile tests results

Due to the limited availability of specimens no toughness tests were performed on RRA treated material. Howener, model I predicts a linear relation between the toughness, K_{Ic}, and $\frac{K_A^{\gamma}}{\sigma_{ys}^{\gamma-0.5}}$ (see Chapter 6). Therefore, $\frac{K_A^{\gamma}}{\sigma_{ys}^{\gamma-0.5}}$ can give a good indication of toughness level, see Fig. 7.9.

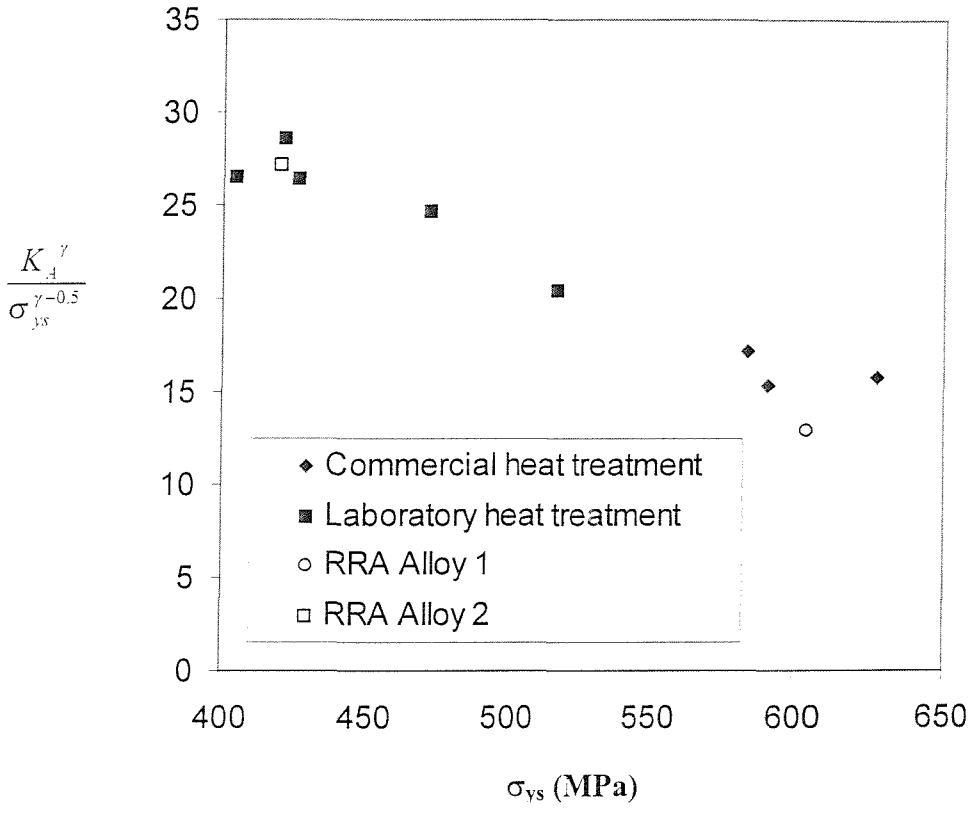

Figure 7.9: yield strength vs. $n\sqrt{\sigma_{ys}}$ for the 7449 alloy in various heat treated conditions.

Figure 7.9 shows the sensitivity of the 7449 alloy to retrogression treatment. Though retrogression treatment duration is short (15 minutes) and the temperature difference is 30°C between the two conditions, RRA 2 appears to be significantly overaged compared to RRA 1. The $n\sqrt{\sigma_{ys}}$-σ_{ys} combination of both RRA treated samples are in the same range as the other heat treated alloys. Therefore, these results suggest that RRA treatment will not benefit the toughness-yield strength relation in 7449 (but to confirm this toughness tests would be needed). As discussed before, the main benefit of RRA treatments will be found in an improved SCC resistance.

7.4.2 Retrogression heat treatment modelling

The aim of this study is to determine the applicability of RRA treatments to thick 7449 plates. The retrogression treatment is the critical step in this process. Therefore, this study was focused on determining critical parameters that affect the retrogression treatment and establish how these parameters influence the retrogression treatment and its suitability, i.e. obtaining a good balance of mechanical properties (strength-SCC resistance). This has been achieved applying the following modelling procedure: the basic principles of heat transfer, reviewed in part 7.2.1, enabled us to model the temperature at every point throughout the plate at all time of the given retrogression treatment (see Fig 7.10); thus, the specific heat treatment at a particular position within the plate is deduced. This heat treatment cause a specific microstructure to develop and, hence, specific mechanical properties. The equivalent time is evaluated for each position within the plate and comparison of equivalent time value near the surface of the plate, at the plate centre and quarter plate give significant data on possible variability in properties and, hence, on the suitability of retrogression treatments for thick 7xxx aluminium plate.

The temperature profile, as shown in Fig 7.10, evolves with time. Figures 7.11, 7.12 and 7.13 show the evolution of temperature with time for different positions within the plate. Plates heated linearly in an oven (see Figs. 7.11 and 7.12) show the same temperature-time curve features. A transitional behaviour appears in the first few minutes of the process. Subsequently, the plate heats up linearly following the oven temperature gradient; at this stage there is a time lag in the behaviour of the different positions within the plate. Finally, the plate temperature reaches the oven holding temperature. The temperature profile of an alloy immersed in a pre-heated medium layer is illustrated in Fig. 7.13. The alloy and the surrounding medium temperature show a transition behaviour where the plate is heated to the holding temperature. In Fig. 7.11 the plate is heated from 293K to 453K in around 5 minutes.

A detailed analysis was performed to elucidate the effects of various parameters on the heating of the plate. It was found that the retrogression treatment parameters can modify the temperature profiles in the following ways:

- Heating rate: As shown in Fig. 7.14, a slow heating gives a less pronounced transition behaviour with a smaller difference in temperatures for the plate surface and plate center. A faster heating rate results in a more noticeable transition step and an increased time lag between the plate surface and plate center temperature.
- Medium thickness: a larger difference appears in the temperature profile of alloys in a 10cm air layer as compared to those in a 50cm air layer (Fig. 7.15). For the alloy in a 50cm air layer the transitional behaviour is much longer. Therefore at the end of the treatment the plate temperature is critically below the retrogression temperature.
- Type of medium: in the absence of a medium the temperature profile of the plate surface follows the oven temperature program. The medium nature (air or oil) modify only slightly the temperature profile (Fig. 7.16).

The temperature-time relation for critical positions within the plate, i.e. near the plate surface, at the quarter of the plate and at the plate centre, was used together with Eq. 7.18 (with E_a=70kJ/mol) to calculate the equivalent times for the different retrogression treatments at these positions. The results are gathered in Table 7.3 to 7.9.

The equivalent time is a measure of the microstructural state of the alloy (see part 7.3.1). However, the relevance of the retrogression treatment for a thick 7xxx aluminium plate requires two conditions to be fulfilled: a microstructure similar to a retrogressed thin 7xxx plate (that can be evaluated using the equivalent time) and the homogeneity of the alloy properties throughout the plate. The latter property can be measured by the percentage difference between the plate surface equivalent time and the plate center equivalent time, this can be expressed as:

$$\%Diff = \frac{t_{eq}(surface) - t_{eq}(center)}{t_{eq}(surface)} \times 100 \qquad (7.19)$$

The calculation of the difference for each treatment and each parameters are displayed in Table 7.3 to 7.9. The concept of "homogeneity of the plate" used in the following part of this study will refer directly to these values, *%Diff.*

The results presented in Table 7.3 to 7.9 can be analysed by comparing the influence of the different parameters:

- Heating rate: the equivalent time increases with decreasing heating rate as the time to reach the holding temperature increases, i.e. longer treatments will give higher equivalent time. However, the difference in equivalent time between the plate surface and the plate center decreases with decreasing heating rate.
- Holding temperature: the equivalent time more than doubles going from 453K to 473K. The homogeneity of the plate is similar for both holding temperatures.
- Holding time: the relative importance of the holding temperature is strongly affected by the preceding ramp speed. For example, in Table 7.3 considering a 473K holding temperature for 1h with 100K/h heating rate, the ramp heat treatment represents less than 10% of the total equivalent time, whereas for considering a 453K holding temperature for 10min with 10K/h heating rate, the ramp heat treatment represents more than 90% of the total equivalent time. The equivalent time also obviously increases with longer retrogression treatment while the difference in equivalent time between the plate surface and the plate center decreases.
- Type of medium: the equivalent time is slightly less for the direct heat transfer case as compared to heat transfer in presence of air. The latter has an improved homogeneity. The equivalent time also decreases using oil as a medium instead of air but the homogeneity is similar for both mediums.
- Medium thickness: the comparison between 10cm and 50cm air layer shows much lower equivalent time for the 50cm air layer. However this is related to the plate temperature not reaching the retrogression treatment set holding temperature, as is illustrated in Fig. 7.16.
- Immersion in hot bath: The medium does not seem to influence this treatment. Short retrogression time give high inhomogeneity values, up to 25%, at both retrogression temperatures. Longer treatments give higher equivalent time with with homogenity values below 10%.

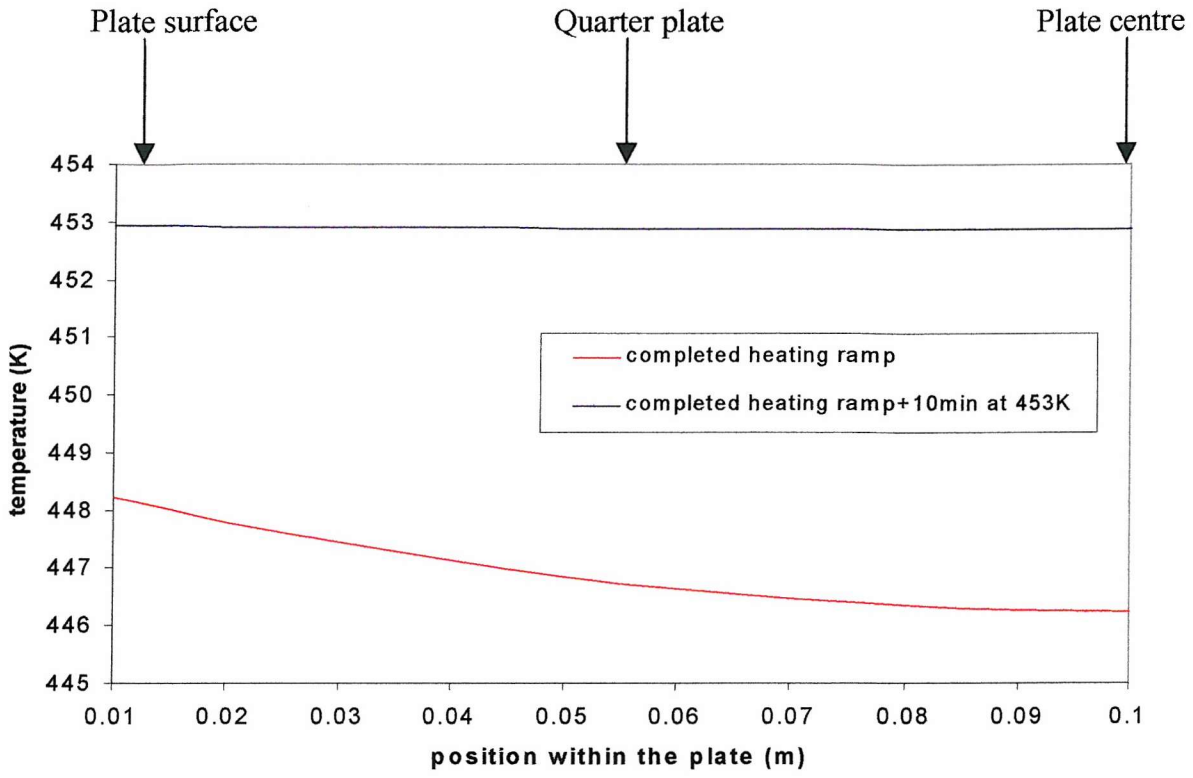

Figure 7.10: Temperature profile through a 20cm thick 7449 aluminium alloy plate (half-width represented) immersed in a 10cm air layer at different stages of a retrogression treatment conducted at 453K with a heating ramp of 100K/h.

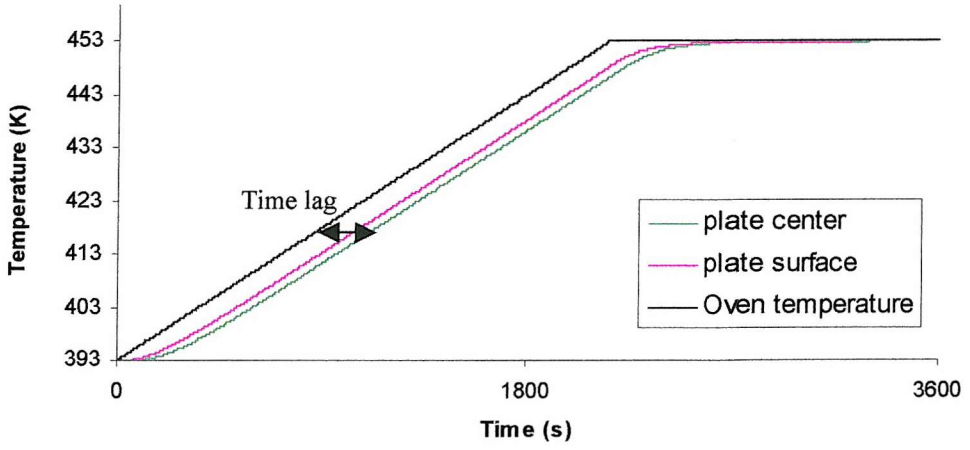

Figure 7.11: Temperature profile of an aluminium plate immersed in 10cm air layer heated from 393K to 453K at 100K/h

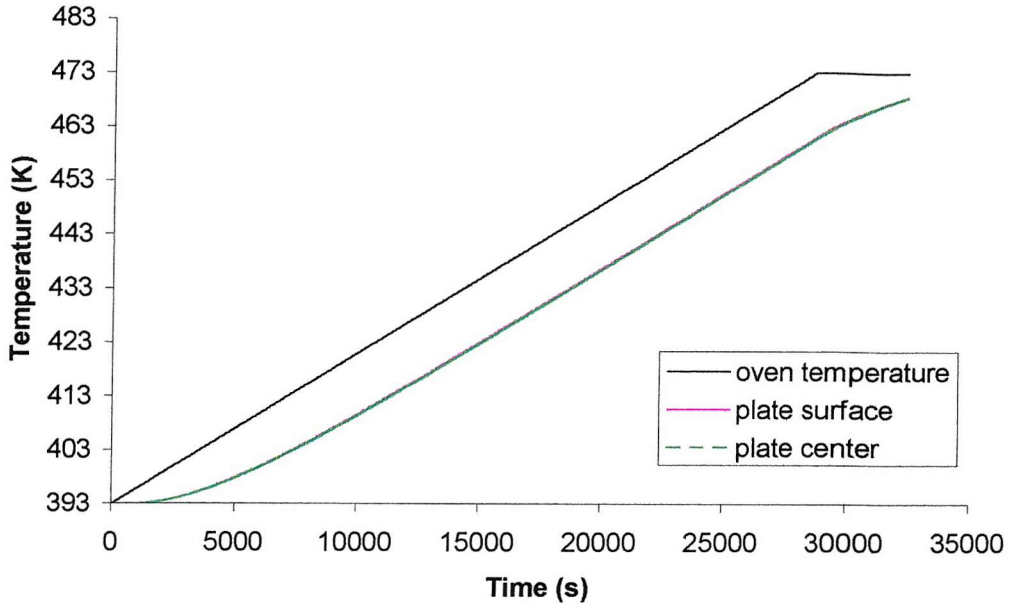

Figure 7.12: Temperature profile of an aluminium plate immersed in 50cm air layer heated from 393K to 473K at 10K/h

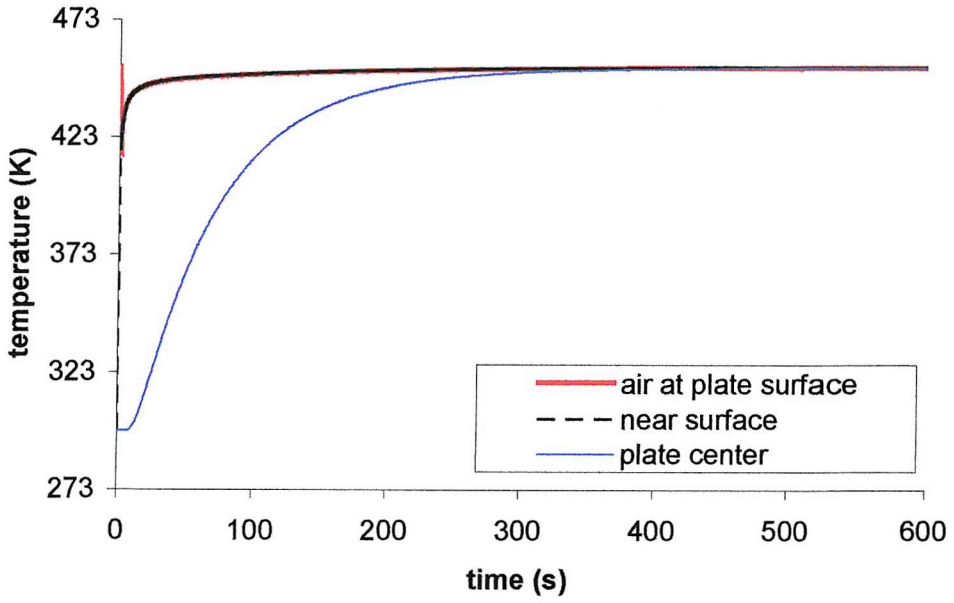

Figure 7.13: Temperature profile of an aluminium plate immersed in 10cm air layer heated 453K.

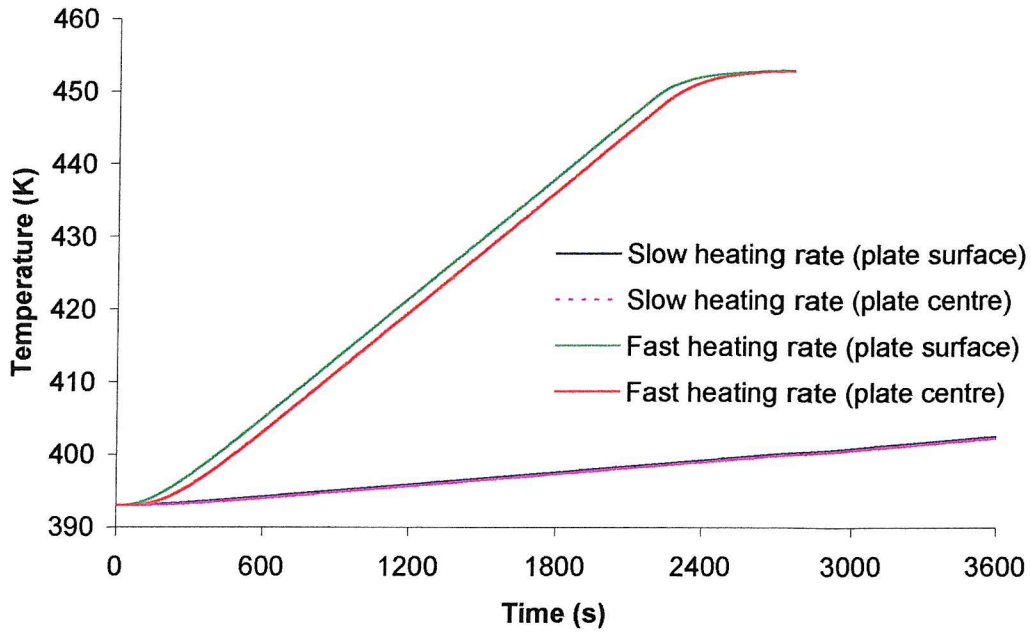

Figure 7.14: Temperature profile of a 20cm thick 7449 aluminium alloy plate heated in a 10cm air layer from 393K to 453K with a fast heating rate (100K/h) and a slow heating rate (10K/h) and maintained at 453K for 10min.

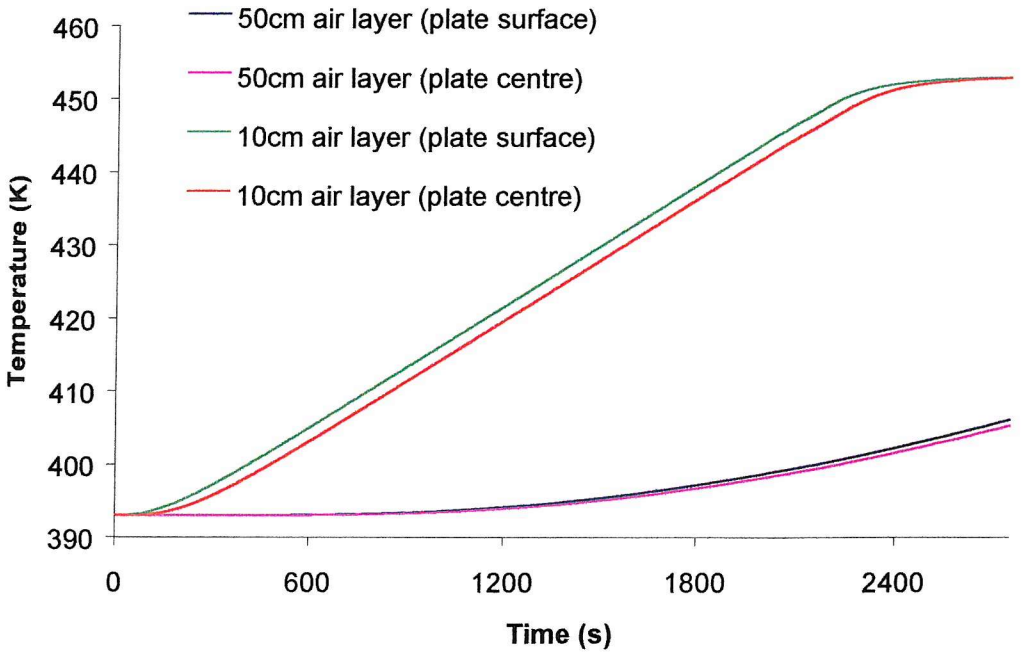

Figure 7.15: Temperature profile of a 20cm thick 7449 aluminium alloy plate heated in a 10cm and in a 50cm air layer from 393K to 453K with 100K/h and maintained at 453K for 10min.

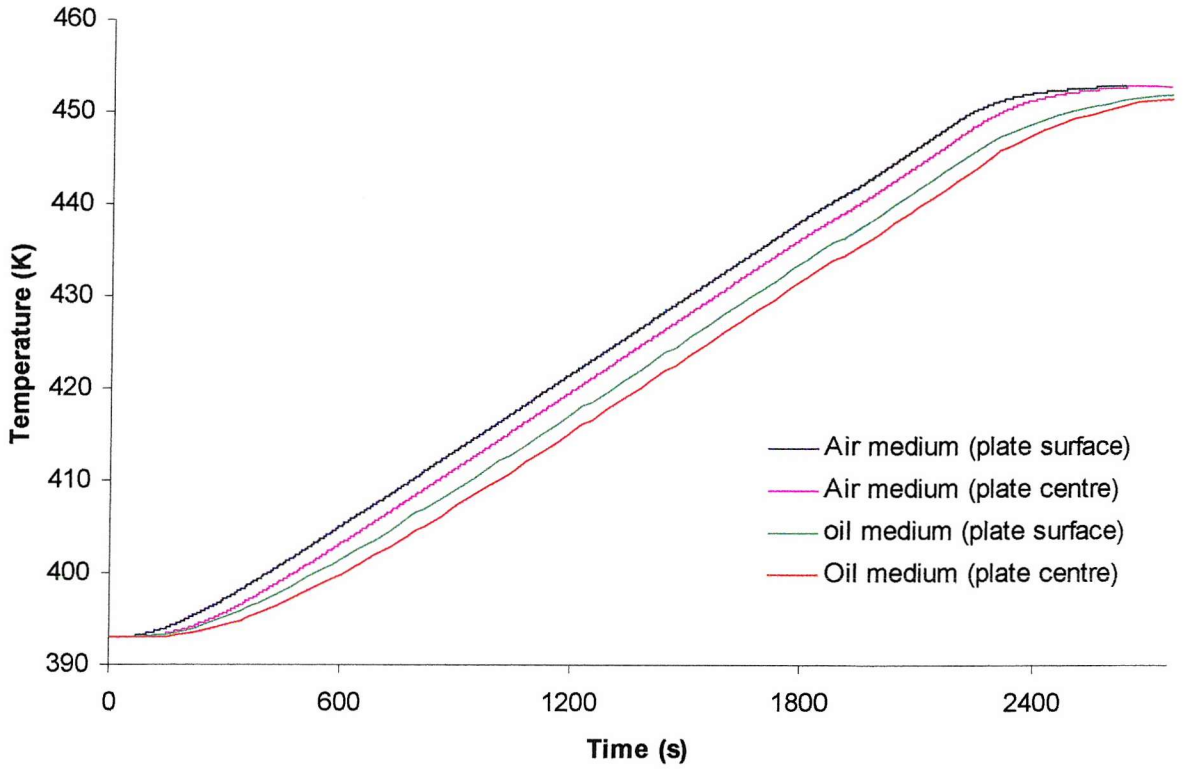

Figure 7.16: Temperature profile of a 20cm thick 7449 aluminium alloy plate heated in a 10cm thick medium layer from 393K to 453K with 100K/h and maintained at 453K for 10min

holding temperature:		180°C				200°C			
heating rate	eq. Time (h)	ramp	10min	30min	1h	ramp	10min	30min	1h
100°C/h	near surface	3.02	7.74	11.39	19.88	7.45	13.43	27.81	44.39
	1/4 plate	2.84	7.52	11.17	19.65	7.04	12.93	27.31	43.88
	1/2 plate	2.77	7.42	11.07	19.55	6.86	12.71	27.09	43.66
	Diff (%)	8.3	7.6	2.8	1.7	7.9	7.4	2.8	1.6
50°C/h	near surface	6.58	9.35	17.00	23.49	16.16	22.24	34.63	53.20
	1/4 plate	6.38	9.13	14.78	23.27	17.71	21.74	34.13	52.70
	1/2 plate	6.30	9.03	14.69	23.17	17.51	21.53	33.91	52.48
	Diff (%)	4.3	3.4	2.1	1.4	4.0	3.2	2.1	1.4
10°C/h	near surface	37.26	38.08	43.73	52.22	86.27	92.44	104.82	123.40
	1/4 plate	37.05	37.86	43.52	52.00	87.79	91.95	104.33	122.91
	1/2 plate	34.96	37.77	43.42	51.90	87.57	91.73	104.11	122.69
	Diff (%)	0.9	0.8	0.7	0.6	0.8	0.8	0.7	0.6

Table 7.3: Equivalent time for various retrogression treatments applied to 7xxx alloy plate of 20cm thickness in the presence of an 10cm air layer

holding temperature:		180°C				200°C			
heating rate	eq. Time (s)	ramp	10min	30min	1h	ramp	10min	30min	1h
100°C/h	near surface	3.57	6.39	12.04	20.51	8.19	14.96	27.19	47.92
	1/4 plate	3.27	6.06	11.70	20.17	7.54	14.20	26.44	47.16
	1/2 plate	3.16	7.93	11.58	20.04	7.29	13.91	26.15	44.88
	Diff (%)	11.6	7.2	3.8	2.3	10.9	7.0	3.8	2.3
50°C/h	near surface	7.19	10.02	17.68	24.17	17.58	23.78	36.17	54.76
	1/4 plate	6.88	9.69	17.35	23.84	16.87	23.04	37.43	54.02
	1/2 plate	6.76	9.57	17.22	23.71	16.60	22.75	37.14	53.74
	Diff (%)	6.0	4.5	2.9	1.9	7.6	4.3	2.8	1.9
10°C/h	near surface	36.39	39.14	44.63	53.13	88.53	94.72	107.12	127.44
	1/4 plate	36.07	38.82	44.31	52.80	87.80	94.00	106.39	124.72
	1/2 plate	37.94	38.69	44.18	52.68	87.52	93.71	106.11	124.43
	Diff (%)	1.2	1.1	1.0	0.8	1.1	1.1	0.9	0.8

Table 7.4: Equivalent time for various retrogression treatments applied to 7xxx alloy plate of 20cm thickness with no medium layer.

holding temperature:		180°C				200°C			
heating rate	eq. Time (s)	ramp	10min	30min	1h	ramp	10min	30min	1h
100°C/h	near surface	2.55	7.05	10.67	19.15	6.35	11.88	24.19	42.76
	1/4 plate	2.41	4.84	10.45	18.93	6.00	11.39	23.68	42.26
	1/2 plate	2.34	4.75	10.35	18.83	7.85	11.18	23.46	42.04
	Diff (%)	8.2	7.9	3.0	1.7	7.9	7.9	3.0	1.7
50°C/h	near surface	6.04	8.69	14.33	22.81	14.91	20.76	33.11	51.68
	1/4 plate	7.86	8.48	14.11	22.59	14.49	20.27	32.61	51.18
	1/2 plate	7.78	8.38	14.01	22.49	14.31	20.05	32.39	50.96
	Diff (%)	4.3	3.6	2.2	1.4	4.0	3.4	2.2	1.4
10°C/h	near surface	34.66	37.45	43.10	51.58	84.89	91.02	103.39	121.97
	1/4 plate	34.45	37.24	42.89	51.37	84.42	90.53	102.90	121.48
	1/2 plate	34.36	37.14	42.79	51.27	84.21	90.31	102.68	121.26
	Diff (%)	0.9	0.8	0.7	0.6	0.8	0.8	0.7	0.6

Table 7.5: Equivalent time for various retrogression treatments applied to 7xxx alloy plate of 20cm thickness in presence of an 10cm oil layer.

		time		
holding temperature (K)		10min	30min	1H
453	surf	2.64	8.29	16.76
	1/4plate	2.10	7.76	16.22
	1/2plate	1.99	7.64	16.11
	diff(%)	24.6	7.8	3.9
473	surf	7.76	18.14	36.69
	1/4plate	4.58	16.96	37.51
	1/2plate	4.33	16.70	37.25
	diff (%)	24.8	7.9	3.9

Table 7.6: Equivalent time for various retrogression treatments applied to 7xxx alloy plate of 20cm thickness immersed in hot air (10cm layer).

		time		
holding temperature (K)		10min	30min	1H
453	surf	2.64	8.28	16.75
	1/4plate	2.10	7.73	16.20
	1/2plate	1.98	7.61	16.08
	diff(%)	27.0	8.1	4.0
473	surf	7.77	18.11	36.64
	1/4plate	4.56	16.89	37.42
	1/2plate	4.31	16.63	37.17
	diff (%)	27.3	8.2	4.0

Table 7.7: Equivalent time for various retrogression treatments applied to 7xxx alloy plate of 20cm thickness immersed in hot oil bath (10cm layer).

		180°C			200°C		
heating rate	eq. Time (s)	10min	30min	1h	10min	30min	1h
100°C/h	near surface	0.97	1.94	4.48	1.51	3.12	8.36
	1/4 plate	0.95	1.89	4.36	1.46	3.01	8.11
	1/2 plate	0.94	1.86	4.31	1.44	2.96	8.00
	Diff (%)	3.1	4.1	3.8	4.6	7.1	4.3
50°C/h	near surface	2.21	3.70	7.24	4.16	7.20	14.82
	1/4 plate	2.16	3.62	7.09	4.05	7.00	14.48
	1/2 plate	2.14	3.58	7.02	4.00	6.91	14.32
	Diff (%)	3.2	3.2	3.0	3.8	4.0	3.4
10°C/h	near surface	23.41	27.38	33.98	58.04	66.68	81.75
	1/4 plate	23.21	27.16	33.72	57.57	66.15	81.16
	1/2 plate	23.13	27.06	33.61	57.36	67.92	80.89
	Diff (%)	1.2	1.2	1.1	1.2	1.1	1.1

Table 7.8: Equivalent time for various retrogression treatments applied to 7xxx alloy plate of 20cm thickness in presence of an 50cm air layer.

	180°C			200°C		
holding time	10min	30min	1h	10min	30min	1h
eq. time (h)	2.83	8.48	16.96	6.19	18.58	37.15

Table 7.9: Equivalent time for retrogression various retrogression treatments applied to thin 7xxx aluminium alloy plate.

7.5 Discussion

To achieve a suitable RRA treatment for a thick plate, the retrogression treatment equivalent time has to be as close as possible to the thin plate retrogression treatment equivalent time, with a small difference between the treatment received by the surface of the plate and the middle of the plate, i.e. good homogeneity of the properties throughout the plate. The present results show the difficult balance between these requirements: a low equivalent time is generally associated with high heating rate, and good homogeneity is associated with low heating rate. Thus, a balance must be sought.

A suitable means of analysing this balance is by plotting the equivalent time of a treatment (at the centre of the plate) vs. a parameter describing the homogeneity of the microstructure. For the latter we have chosen to use $\frac{t_{eq}(surf)-t_{eq}(centre)}{t_{eq}(surf)}\times 100$. A schematic of a plot of $\frac{t_{eq}(surf)-t_{eq}(centre)}{t_{eq}(surf)}$ vs. t_{eq} is presented in Fig. 7.17. It illustrates the constraints on the applicability of the retrogression treatment. The homogeneity requirements limit the speed of the heating rate and impose a minimum duration on the retrogression treatment. On the other hand, the equivalent time requirements impose a maximum duration on the retrogression treatment and require relatively fast heating rates. The different retrogression temperatures and medium conditions will move the curves, i.e. in Fig. 7.17 treatment B curve is situated closer to the axis compared to treatment A. It is clear that the closer the curve is to the axes, the larger the portion of the curve situated in the "valid" section delimited by the homogeneity requirement and equivalent time requirement will be. In Fig. 7.17, if the heating rate and duration of the treatment are chosen correctly, treatment B will satisfy all requirements and will possibly be a valid retrogression treatment, whereas treatment A will fail to satisfy both requirements in all cases. Therefore, the closer the curve is to the axis the better possibilities for a suitable retrogression treatment will be.

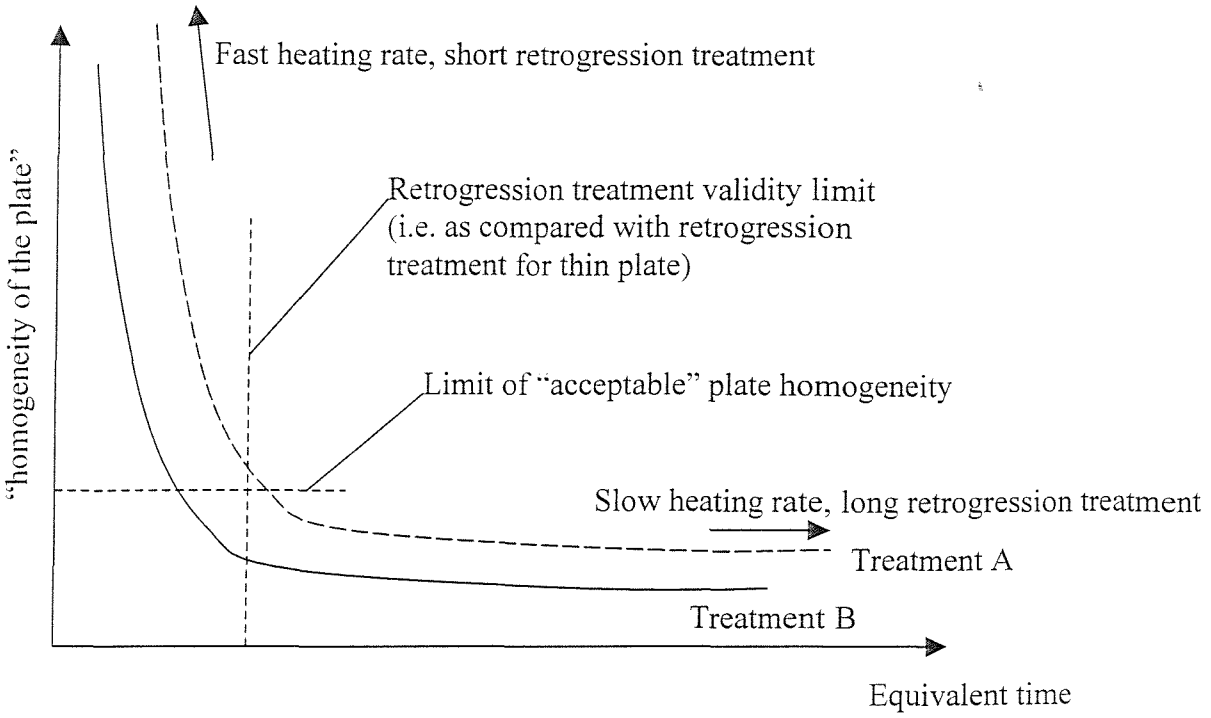

Figure 7.17: Schematic t_{eq} *vs.* $\frac{t_{eq}(surf)-t_{eq}(centre)}{t_{eq}(surf)}\times 100$ *curve for two given retrogression temperature associated with a given medium, treatment A and B.*

Fig. 7.18 and 7.19 show the influence of the different parameters on these types of plots. Figure 7.18 illustrates the influence of the addition of a medium on equivalent time and equivalent time difference through the plate. It is clear that the presence of a medium lowers both properties compared to the direct heat transfer through a plate. Decreasing temperature also contributes to lower these values. Low heating rates (around 10K/h) give good homogeneity but very high equivalent time, i.e. well above the equivalent time for retrogression treatment for thin plate. On the other hand, high heating rates (around 100K/h) give valid equivalent time as compared to valid retrogression treatment for thin plate but with poor plate homogeneity: the percentage difference is estimated between 5 and 10%.

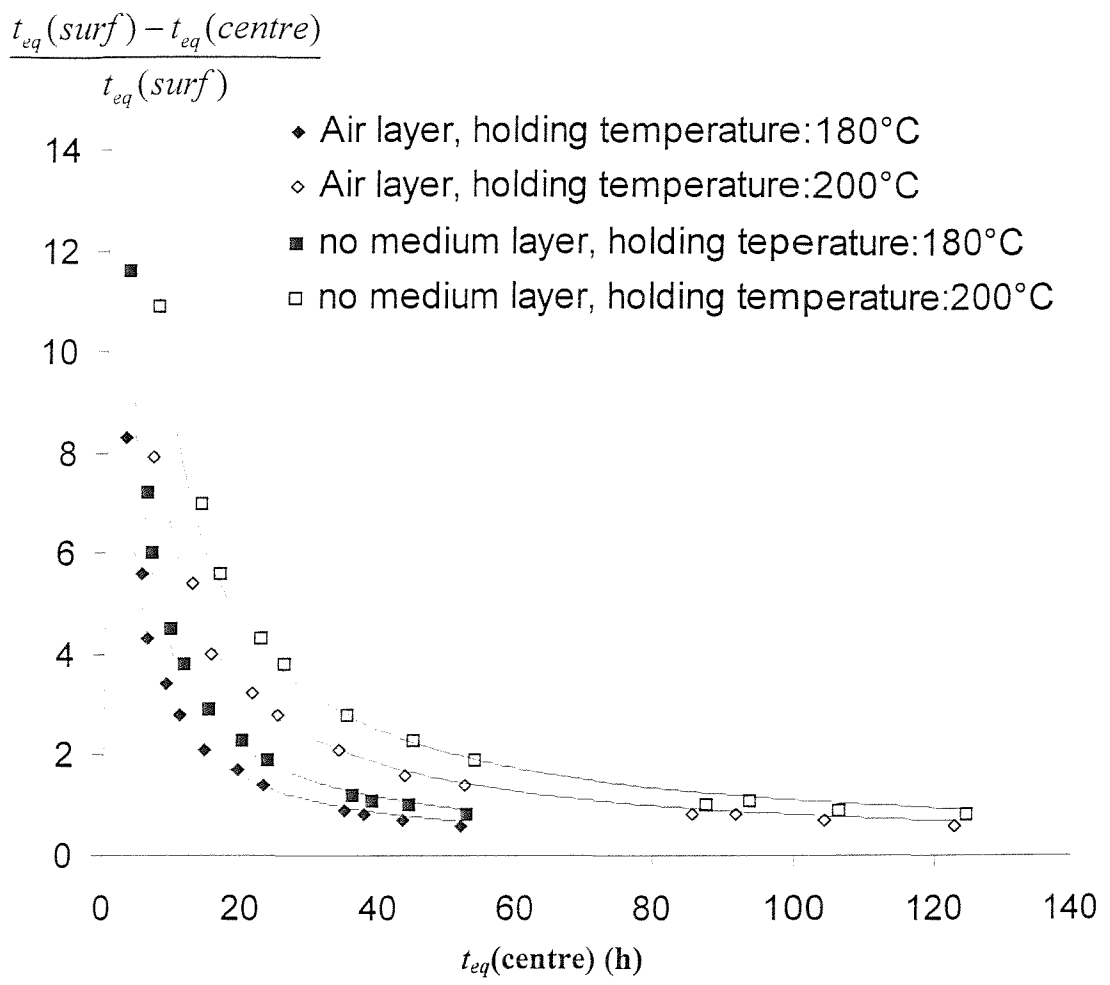

Figure 7.18: The percentage difference in equivalent time between the retrogression treatment received by the plate surface and the treatment received by the plate centre vs. the equivalent time at the plate centre for various retrogression treatments applied to the 7xxx alloy.

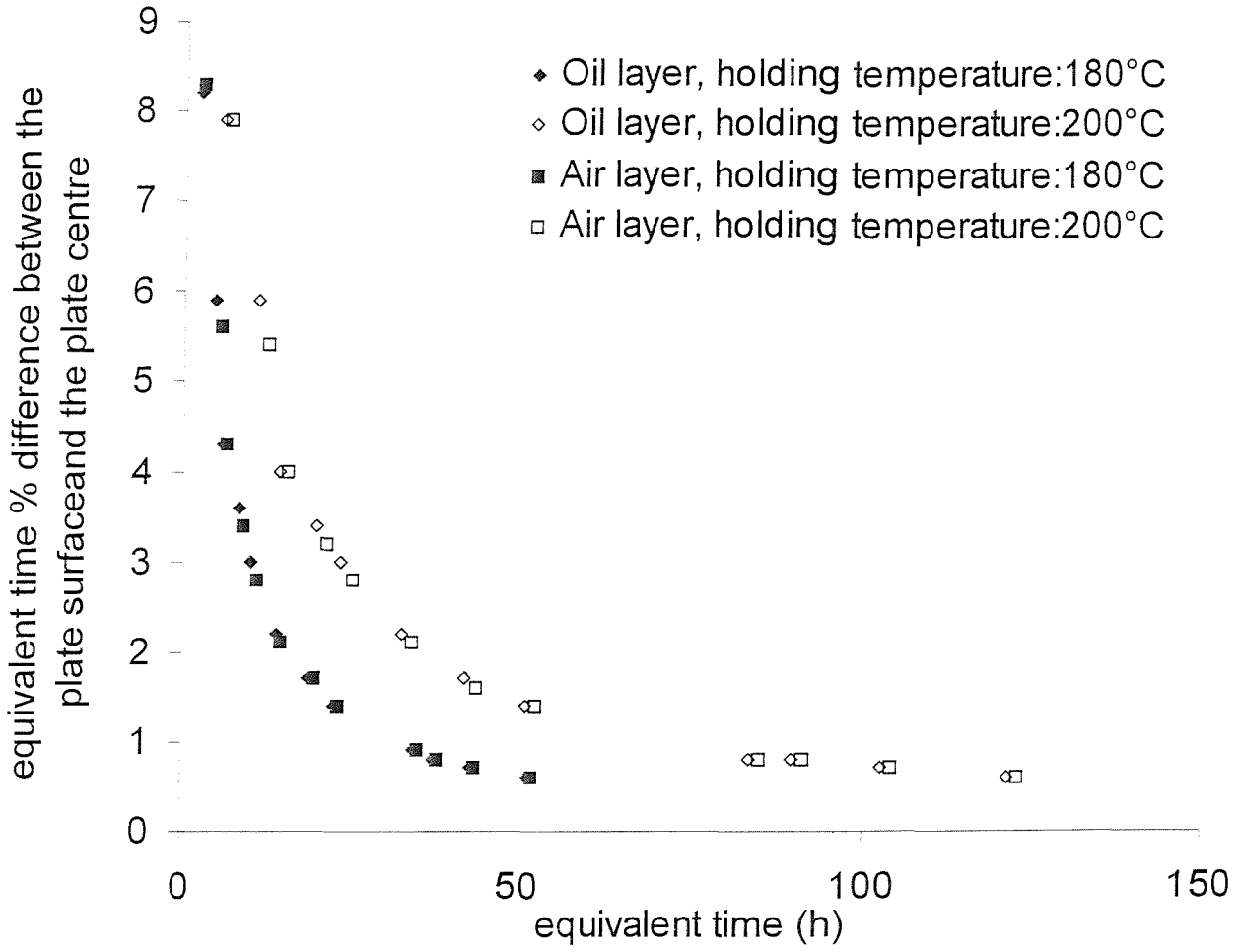

Figure 7.19: The percentage difference in equivalent time between the retrogression treatment received by the plate surface and the treatment received by the plate centre vs. the equivalent time at the plate centre for retrogression treatments applied to the 7xxx alloy in two different medium.

Figure 7.19 shows the influence of varying the type of medium. Although the diffusivity coefficient of the oil is less than half the value of the air diffusivity, no significant difference on the heat treatment of plate is found, and differences are dominated by the holding temperature.

In analysing Figs. 7.18 and 7.19 it was noted that the data could be fitted well using an equation of the form:

$$\%diff. = C\left(\frac{1}{t_{eq}}\right)^{q} \tag{7.19}$$

Where C and q are constants depending on heat treatment type. Examples of these fits are given in Fig. 7.18. A fixed value of q for each condition of 0.88 and a varying C value seems to provide a good fit for all the conditions. C values are summarised in Table 7.10. These results show that the presence of a medium and lower holding temperatures are beneficial to the reversion treatment, i.e. they yield lower values of C.

	Holding temperature	180°C	200°C
medium	No medium	30	64
	Air	22	46
	Oil	22	47

Table 7.10: C values for different temperature and medium.

From this investigation, several retrogression treatments valid for 7xxx thick plates are proposed for products immersed in a medium:

- 100°C/h heating ramp to 200°C and no isothermal step.
- 100°C/h heating ramp to 190°C+10min isothermal step
- 100°C/h heating ramp to 180°C+10min isothermal step
- 50°C/h heating ramp to 180°C+10min isothermal step
- immersion for 30min in a bath at 180°C

7.6. Conclusions

A heat transfer model together with an internal state variable approach has been used to evaluate the applicability of RRA treatments to thick 7449 aluminium plates. Several observations have been drawn from the results of this modelling work:

- During the immersion of a cold plate in a hot bath, the heat up of the plate produces a large difference between the temperature at the surface of the plate and at the plate interior. This treatment gives low equivalent times for longer retrogression treatment compared to heating ramp+holding time configuration.
- Heating rates of 10°C/h give in all conditions a high equivalent time compared to equivalent time for thin plates.
- The difference in equivalent time is below 10% in all heating ramp+holding temperature configurations. This difference decreases with the heating rate and going to longer isothermal treatment duration. This difference is not significantly affected by varying holding temperature.
- The equivalent time more than doubles on going from 180°C to 200°C holding temperature.
- The equivalent time also increases with decreasing heating rate, though the difference in heat treatment between the surface and the interior of the plate decreases with decreasing heating rate.

There may be a narrow theoretical "window" of applicability for RRA treatments to thick plates. Holding temperatures between 200°C and 180°C with heating rates around 50°C/h and holding time less than 30minutes may be suitable candidates (SCC data also required). Experimental work on thick plates would be required to validate this model.

Pages 164-167 are missing from volume

Appendix I

Two different analytical models of work hardening have been considered in this study: the Ramberg-Osgood model (see Section 6, Eq. 6.), and the Ashby model (see Section 2, Eq. 2.). The correlation between the strain hardening exponent n and the work hardening factor K_A is derived from the following equivalence:

$$\sigma = A\varepsilon^n = \sigma_{ys} + K_A\sqrt{\varepsilon} \tag{I.1}$$

However it is not possible to derive directly mathematically n as a function of K_A and σ_{ys} from this equation. Therefore, a curve fitting approach was used. For yield strength levels relevant to high strength 7xxx aluminium alloys (i.e. between 400 and 600MPa), K_A values were systematically varied between 300 and 500MPa$\sqrt{m}$. Varying the plastic strain between 0.01 and 0.05, a modeled stress is obtained from Eq. 2.2, (see Figure I.1,2).

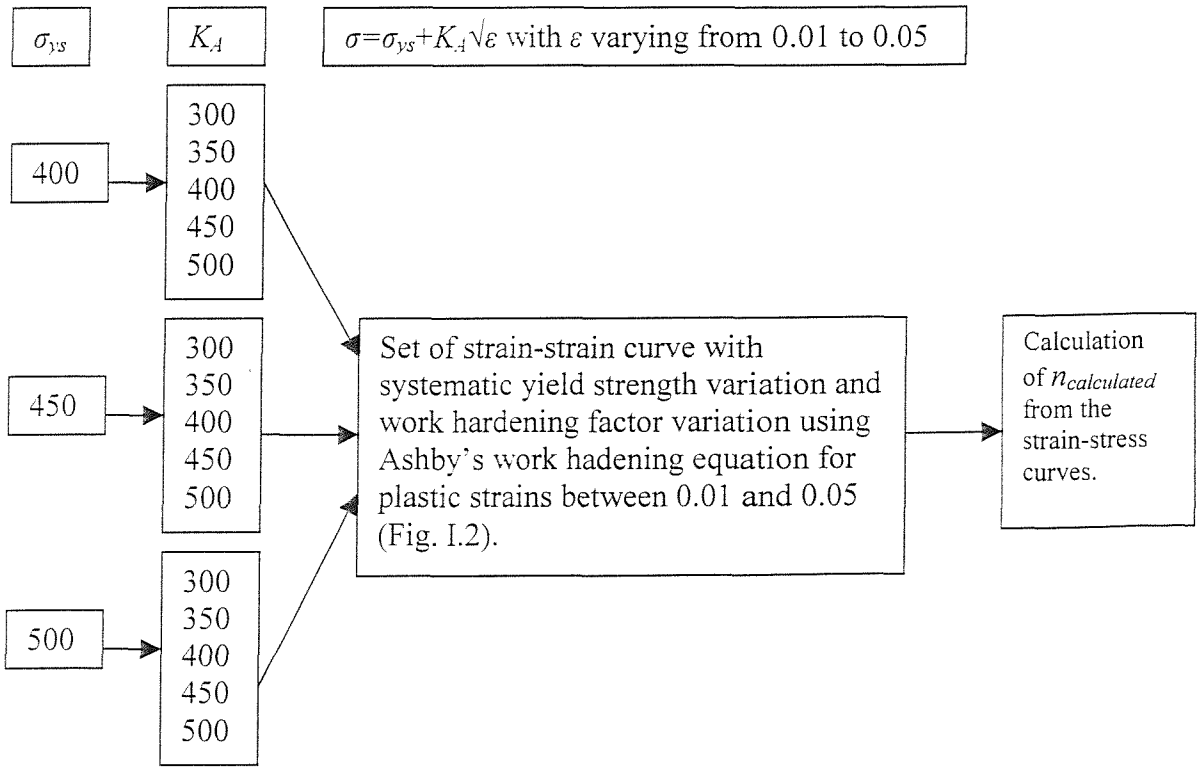

Figure I.1: Schematic diagram of the modeling process.

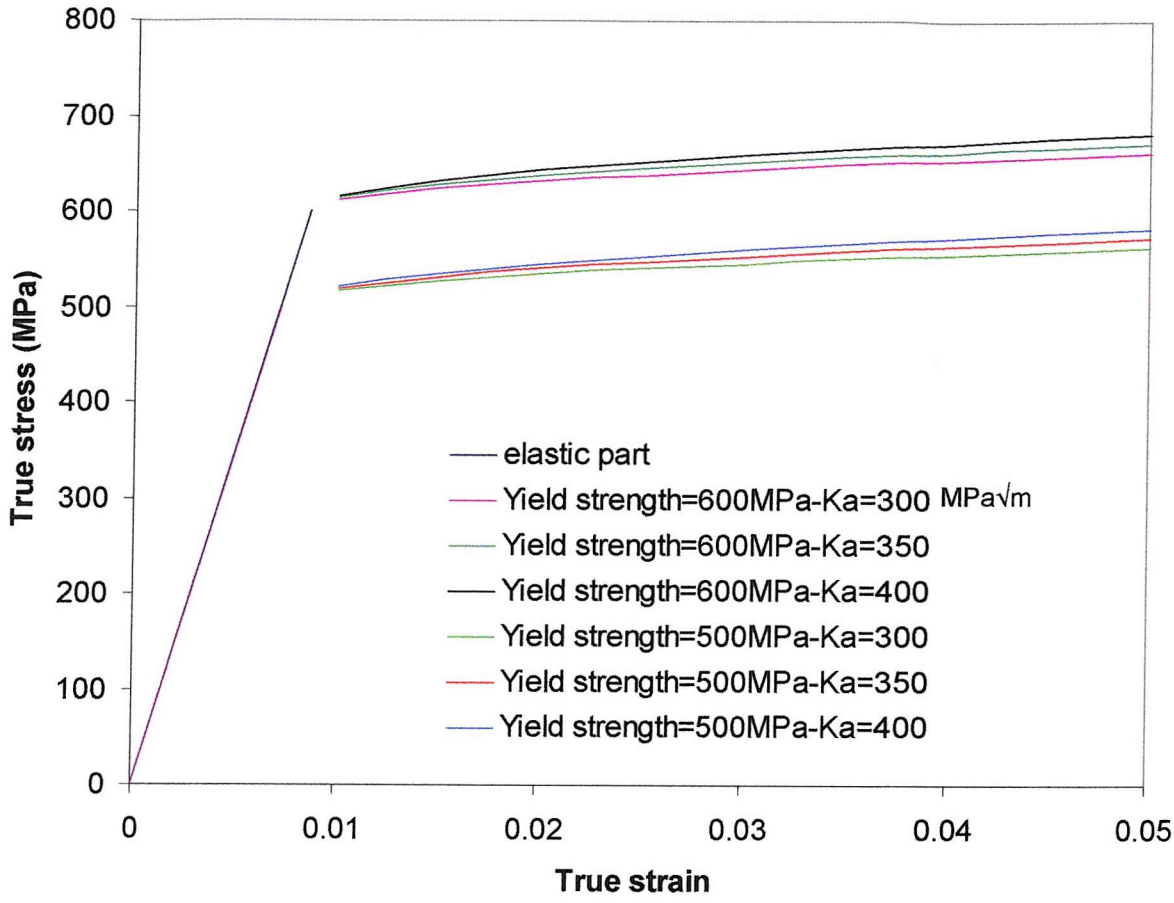

Figure I.2: Example of stress-strain curves plotted using varying K_A values, yield strength values for a strain value varying between 0.01 and 0.05.

From each stress-strain curve obtained a $n_{calculated}$ value is derived using Ramberg-Osgood equation. A $n_{modeled}$ value can be derived from Eq. 6.5. Subsequently C_1 and γ are used as fitting parameters between $n_{calculated}$ and $n_{modeled}$ over a comprehensive range of yield strength and work hardening values typical of 7xxx aluminium alloys.

Figure I.3 shows the linear relationship between ln(n) and ln(K_A/σ_{ys}) for the 7449, 7449 (Mn) and 7150 alloys. Plots for the 7150 alloys are in the same range as those for the 7449. The plots for the 7449 (Mn) are below this range but their trendline slope is similar to the trendline slope for 7150 and 7449, i.e. γ is considered to be constant over this range of high strength aluminium alloys, whereas C_1 is a constant specific to a given alloy.

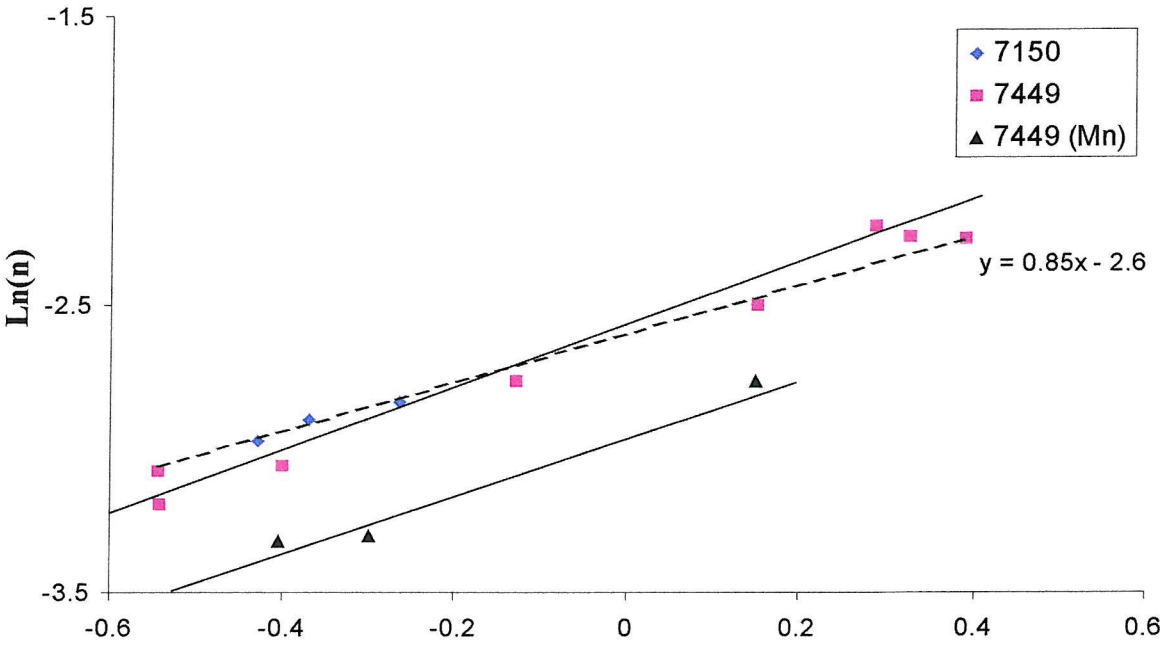

Figure I.3: ln(n) vs. ln(K_A/σ_{ys})

For the present alloys, γ is about 0.97(±0.1), and C_1 varies from 0.08 for the 7449 and 7150 alloys to 0.05 for the 7449 (Mn) alloy. However, any modelling attempt would aim to be reproducible over a range of alloys as large as possible. Hence, the average value for γ obtained from a larger range of alloys will be used in the assessment of the toughness models. Fig. I.3 demonstrates that γ=0.85 is consistent with our present alloys considering the scatter of the data.

APPENDIX II

```
'declare constant
--Heat treatment duration
Const total_time = 7000
--plate thickness 20cm
Const plate_width = 0.2
--number of thickness division of the media and alloy for incremental calculation
Const oil_length_step = 9
Const Al_length_step = 10
--Alloy and media diffusivity constant
Const Al_diffusivity = 0.0000572547
Const Oil_diffusivity = 0.0000318926
--starting temperature
Const Ti = 393

'declare module level variables
--the temperature of the alloy and media at a time t are stored in a first vector
(each vector value correspond to the temperature a thickness division).
Temperature at a time t+Δt are stored in a second vector.
Dim rang1(10)
Dim rang2(10)
Dim rang1bis(11)
Dim rang2bis(11)

--Initialisation (temperature at t=0)
Sub iteration()
For n = 0 To oil_length_step + 1
rang1(n) = Ti
rang2(n) = 0
Next
```

```
For n = 0 To Al_length_step + 1
rang1bis(n) = Ti
rang2bis(n) = 0
Next

--Incremental variable
k2 = 1
k = 0

--A time step is chosen and the corresponding temperature step for the oven depending on the heating rate is deduced (here time step:0.5s and temperature step:0.01389°C/s (heating rate 100°C/h))
tempvar = Ti - 0.01389
For t = 0 To total_time Step 0.5

--Incrementing
k = k + 1
tempvar = tempvar + 0.01389

--The temperature of the medium in contact with the oven increases as the oven until it reaches the maximum temperature
If tempvar < 453
        Then rang2(0) = tempvar
        Else rang2(0) = 453
End If

--Calculation of the medium temperature using Eq 7.18 (defined as a customized function)
For x = 1 To oil_length_step
Ta = rang1(x - 1)
Tb = rang1(x)
```

```
Tc = rang1(x + 1)
rang2(x) = calcul_iteration(Ta, Tb, Tc, 0.5, 0.01, Oil_diffusivity)
--When temperature reaches the maximum limit the iteration is stopped
If rang2(x) > 453 Then rang2(x) = 453
Next

--Applying boundary condition between the medium and the aluminium
rang2(10) = rang1(10) + Oil_diffusivity * 0.5 * (rang1(9) - rang1(10)) / 0.01 ^ 2)
rang1bis(0) = rang1(10)
rang2bis(0) = rang2(10)
rang1bis(1) = (155 * rang1bis(0) + 0.024 * rang1bis(0) - 0.024 * rang1(9)) / 155)
rang2bis(1) = (155 * rang2bis(0) + 0.024 * rang2bis(0) - 0.024 * rang2(9)) / 155)

-- Calculation of the aluminium temperature
For x = 2 To Al_length_step
Ta = rang1bis(x - 1)
Tb = rang1bis(x)
Tc = rang1bis(x + 1)
rang2bis(x) = calcul_iteration(Ta, Tb, Tc, 0.5, 0.01, Al_diffusivity)
Next
rang2bis(11) = rang2bis(9)

--The temperature profile values (temperature at a time t and position x) are
  written in an excel worksheet at regular and significant time intervals
If (k = 60)
        Then k2 = k2 + 1
                k = 0
                If k2 = 2000
                        Then End
                        Else vCells(k2 + 2, 1) = t
                                For x = 0 To oil_length_step + 1
```

```
                Cells(k2 + 2, x + 2) = rang2(x)
                Next
                For y = 0 To Al_length_step + 1
                Cells(k2 + 2, y + 13) = rang2bis(y)
                Next
End If

--Reinitialise the first vector
For n = 0 To oil_length_step + 1
rang1(n) = rang2(n)
Next
For n = 0 To Al_length_step + 1
rang1bis(n) = rang2bis(n)
Next
Next
End Sub

--Define Eq. 7.16 as a function
Function calcul_iteration(T1, T2, T3, dt, dx, a)
calcul_iteration = T2 + a * dt * (T3 - 2 * T2 + T1) / dx ^ 2
End Function
```

REFERENCES:

1 J.T. Staley, D.J. Lege, "Advances in aluminium alloy products for structural applications in transportation", *J. Phys. IV*, 3, 1993, pp 179-190.

2 T.J. Warner, R.A. Shahani, P. Lassince, "Aluminium alloy developments for affordable airframe structures", *3rd ASM Conference on synthesis, processing and modelling of advanced materials*, Paris, France, June 1997.

3 P. Sainfort, C. Sigli, G.M. Raynaud, P. Gomiero, "Structure and property control of aerospace alloys", *Mater. Sci. Forum*, 242, 1997, pp 25-32.

4 R.J. Bucci, "Selecting aluminum alloys to resist failure by fracture mechanisms", *Engng. Fract. Mech.*, 12, 1979, pp 407-441.

5 I.J. Polmear, Light Alloys: Metallurgy of the light metals, 3rd edition. Butterworth-Heinemann, London, 1995.

6 A.K. Vasudevan and R.D. Doherty, Aluminium alloy-Contemporary research and applications, Academic press, London, 1989.

7 J. Liu, M. Kulak, "A new paradigm in the design of aluminium alloys for aerospace applications", *Mater. Sci. Forum*, 331-337, 2000, pp 127-140.

8 Pechiney Aerospace Technical Data Sheet, "7449-T651/T7951/T7651 New alloy-Plates. A choice of very high strength-corrosion resistant tempers", Pechiney-Rhenalu, France, 2001.

9 P.D. Pitcher, C.M. Styles, "Creep age forming of 2024A, 8090 and 7449 alloys", *Mater. Sci. Forum*, 331-337, 2000, pp 455-460.

10 B. Morere, "Recrystallisation d'un alliage d'aluminium 7010 apres deformation a chaud; influence de la tenacite", PhD thesis, Ecole nationale Superieure des Mines de Saint-Etienne-INPG, 1998.

11 R.H. Brown, L.A. Willey, "constitution of alloys" in Aluminium: Properties, physical metallurgy and phase diagram, K.R. Van Horn Ed., Pittsburgh, 1967, pp 31-54.

12 L.F. Mondolfo, Aluminium alloys, Butterworth & Co Ltd, London, 1976.

13 D.J. Strawbridge, W. Hume-Rothery, A.T. Little, "The constitution of Aluminium-Magnesium-Zinc alloys at 460°C", *J. Inst. Metals*, 74, 1948, pp 191-225.

References

14 P. Liang, T. Tarfa, J.A. Robinson, S. Wagner, P. Ochin, M.G. Harmelin, H.J. Seifert, H.L. Lukas, F. Aldinger, "Experimental investigation and thermodynamic calculation of the Al-Mg-Zn system", *Thermochimica Acta*, 314, 1998, pp 87-110.

15 N. Ryum, "Precipitation kinetics in an Al-Zn-Mg alloy", *Z. Metallkd.*, 66, 1975, pp 338-345.

16 C.E. Lyman, J.B. Vander Sande, "A Transmission Electron Microscopy investigation of the early stages of precipitation in an Al-Zn-Mg alloy", *Metall. Trans. A*, 7, 1976, pp 1211-1216.

17 H. Löffler, I. Kovács, J. Lendvai, "Review of Decomposition processes in Al-Zn-Mg alloys", *J. Mater. Sci.*, 18, 1983, pp 2215-2240.

18 K. Stiller, V. Hansen, M. Knutson-Wedel, G. Waterloo, J. Gjonnes, "Hardening precipitates and their precursor in 7xxx alloys", *Proceedings of ICAA-6*, 2, 1998, pp 615-620.

19 X.Z. Li, V. Hansen, J. Gjonnes, L.R Wallenberg, "HREM study and structure modeling of the η′ phase, the hardening precipitates in commercial Al-Zn-Mg alloys", *Acta Mater.*, 47, 1999, pp 2651-2659.

20 C. Garcia-Cordovilla, E. Louis, "A differential scanning calorimetry investigation of the effects of zinc and copper on solid state reactions in Al-Zn-Mg-Cu alloys", *Mater. Sci. Eng. A*, 132, 1991, pp 135-141.

21 A. Deschamps, F. Livet, Y. Bréchet, "Influence of predeformation on ageing in an Al-Zn-Mg alloy –I. Micrsostructure evolution and mechanical properties", *Acta Mater.*, 47, 1999, pp 281-292.

22 A. Deschamps, Y. Brechet, "Nature and distribution of quench-induced precipitation in an Al-Zn-Mg-Cu alloy", *Scripta Mater.*, 39, 1998, pp 1517-1522.

23 H. Auld, S. M. Cousland, "Structure of the metastable η′ phase in aluminium-zinc-magnesium alloys", *J. Aust. Inst. Metals*, 19, 1974, pp 194-199.

24 S.S. Brenner, J. Kowalik, Hua Ming-Jian, "FIM/probe analysis of a heat treated 7150 aluminium alloy", *Surface Sci.*, 246, 1990, pp 210-217.

25 A.K. Vasudevan, R.D. Doherty, "Grain boundary ductile fracture in precipitation hardened Aluminium alloys", *Acta Metall.*, 35, 1987, pp 1193-1219.

References

26 A. Deschamps, Y. Brechet, P. Guyot, F. Livet, "On the influence of dislocation precipitation in an Al-Zn-Mg alloy", *Z. Metallkd.*, 8, 1997, pp 601-606.

27 J.D. Embury, D.J. Lloyd, T.R. Ramachandran, "Strengthening mechanisms in aluminum alloys", in Aluminium alloy-Contemporary research and applications, Eds. A.K. Vasudevan and R.D. Doherty, 1989, pp 17-27.

28 P.J. Gregson, "Aluminium alloys: physical metallurgy, processing and properties", in High performance materials in aerospace, Eds. H.M. Flower, Chapman & Hall, 1995.

29 M.J. Starink, P. Wang, I.Sinclair, P.J. Gregson, "Microstructure and strengthening of Al-Li-Cu-Mg alloys and MMCs: II. Modelling of yield strength", *Acta mater.*, 47, 1999, pp 3855-3868.

30 W.D. Callister Jr., Materials Science and Engineering-An Introduction, 2nd edition, John Wiley & sons Inc, New York, 1985.

31 H.L. Ewalds and R.J.H. Wanhill, Fracture Mechanics, Edward Arnold, London, 1984.

32 M.F. Ashby, "Work hardening of Dispersion-hardened Crystals", *Phil. Mag.*, 14, 1966, pp 1157-1178.

33 J.W Hutchinson, "Elastic-plastic behaviour of polycrystalline metals and composites", *Proc. Roy. Soc. Lond. A*, 319, 1970, pp 247-272.

34 P. Gomiero, Y. Brechet, F. Louchet, A. Tourabi, B. Wack, "Microstructure and mechanical properties of A 2091 AlLi alloy-II. Mechanical properties: Yield stress and work hardening", *Acta Metall Mater.*, 40, 1992, pp 857-861.

35 G.T. Hahn, A.R. Rosenfield, "Metallurgical Factors affecting Fracture Toughness of Aluminium Alloys", *Metall. Trans. A*, 6, 1975, pp 653-670.

36 G. Lapasset, C. Renon, "Influence des facteurs métallurgiques sur la tenacité des alliages d'aluminium 7010 et 7050", *La Recherche Aérospatiale*, 5, 1982, pp. 313-326.

37 D.S. Thompson, "Metallurgical factors affecting high strength aluminium alloy production", *Metall. Trans. A*, 6, 1975, pp 671-683.

38 J. Yeh, K. Liu, "A study relating to the enhancement of transgranular fracture by iron in Al-Zn-Mg alloys", *Scripta Metall.*, 20, 1986, pp 329-334.

References

39 T. Ohira, T. Kishi, "Effect of Iron Content on Fracture Toughness and Cracking Processes in High Strength Al-Zn-Mg-Cu Alloy", *Mater. Sci. Eng. A*, 78, 1986, pp 9-19.

40 W.M. Garrison Jr., N.R. Moody, "Ductile Fracture", *J. Phys. Chem. Solids*, 48, 1987, pp 1035-1074.

41 A.J. Morris, R.F. Robey, P.D. Couch and E. De Ios Rios, "A Comparison of the Damage Tolerance of 7010 T7451 and 7050 T7451", *Mater. Sci. Forum*, 242, 1997, pp181-186.

42 M.R. Jarrett, J.S. Crompton, "The Development of Improved Fracture Toughness by Microstructural Process Control for an Al-Zn-Mg-Cu Alloy", *in Proceedings of Extrusion of Hard Alloys*, 1991, Milan, Italy, Associazione Italiana di Metallurgia, Milan, Italy.

43 R.C. Dorward, D.J. Beerntsen, "Grain structure and quench rate effects on strength and toughness of AA7050 Al-Zn-Mg-Cu-Zr alloy plate", *Metall. Mater. Trans. A*, 26, 1995, pp 2481-2484.

44 B. Morere, J.-C. Ehrstrom, P.J. Gregson, I. Sinclair, "Microstructural Effects on Fracture Toughness in AA7010 Plate", *Metall. Mater. Trans. A.*, 31, 2000, pp 2503-2515.

45 R. Shahani, J.-F. Verdier, P. lassince, G.-M. Raynaud, C. Sigli, P. Sainfort, "Thick AlZnMgCu alloy product with improved properties", *US patent n°6027582*, 2000.

46 C.Q. Chen, J.F. Knott, "Effects of dispersoid particles on toughness of high-strength aluminium alloys", *Metal Sci.*, 15, 1981, pp 357-365.

47 M.J. Haynes, R.P. Gangloff, "Elevated temperature fracture toughness of Al-Cu-Mg-Ag sheet: characterization and modelling", *Metall. Mater. Trans. A*, 28A, 1997, pp 1815-1829.

48 E. Di Russo, "Microfractographic characteristics and fracture toughness of 7000 and 2000 series aluminium alloys: proposal of a static fracture model", *Metall. Sci. Technol. A*, 4, 1986, pp 37-48.

49 O.E. Alarcon, A.M.M. Nazar, W.A. Monteiro, "The effect of microstructure on the mechanical behavior and fracture mechanism in a 7050 T76 aluminium alloy", *Mater. Sci. Eng. A*,138, 1991, pp. 275-285.

References

50 D.S. Thompson, R.E. Zinkham, "Effects of alloying and processing on the fracture characteristics of aluminium sheet", *Eng. Fract. Mech.*, 7, 1975, pp 389-409.

51 J.T. Staley, "Quench factor analysis of aluminium alloys", *Mater. Sci. Tech.*, 3, 1987, pp 923-935.

52 H.X. Li, X.R. Xiao, "An approach on the mode-I fracture toughness anisotropy for materials with layered microstructures", *Eng. Frac. Mech.*, 52, 1995, pp 671-683.

53 I. Kirman, "The relation between microstructure and toughness in 7075 Aluminium alloy", *Metall. Trans. A*, 2, 1975, pp 1761-1770.

54 T. Kawabata and O. Izumi, "The relationship between fracture toughness and transgranular fracture in an Al-6.0% Zn-2.5% Mg alloy", *Acta Metall.*, 5, 1977, pp 505-512.

55 D. Goddard, G. Lapasset, H. Octor, "Chracterization by electron microscopy of nucleation sites and phases nucleated during quenching of an AlZnMgCu alloy", *Proceeding of ICAA-6*, 2, 1998, pp 633-638, The Japan Institute of Light Metals, Japan.

56 N. Ryum, B. Haegland, T. Lindtveit, "Brittleness and Microstructure of some Al-Mg-Zn-Alloys", *Z. Metallkd.*,58, 1967, pp 28-31.

57 P.N.T. Unwin, G.C. Smith, "The microstructure and Mechanical properties of Al-6%Zn-3%Mg", *J. of the institute of metals*, 97, 1969, pp 299-310.

58 P.J. Gregson, H.M. Flower, "Microstructural control of toughness in aluminium-lithium alloys", *Acta Metall.*, 33, 1985, pp. 527-537.

59 B. Cina, *US patent n°3856584, 1974.*

60 J.K. Park, A.J. Ardell, "Effect of retrogression and reaging treatments on the microstructure of Al-7075-T7651", *Metall. Trans. A*, 15, 1984, pp1531-1543.

61 G. Deshais, S.B. Newcomb, "The influence of microstructure on the formation of stress corrosion cracks in 7xxx series aluminium alloys", Mater. Sci. Forum, 331-333, 2000, pp 1635-1640.

62 L. Christodoulou, H.M. Flower, "Hydrogen embrittlement and trapping in Al-6%Zn-3%Mg", *Acta Metall.*, 28, 1980, pp 481-487.

References

63 M. Talianker, B. Cina, "Retrogression and reaging and the role of dislocations in the stress corrosion of 7000-type aluminium alloys", Metall. Trans. A, 20A, 1989, pp 2087-2092.

64 V. Komisarov, M. Talianker, B. Cina, " The effect of retrogression and reaging on the resistance to stress corrosion of an 8090 type aluminium alloy", *Mater. Sci. Eng. A*, 221, 1996, pp 113-121.

65 S.M. Lee, S.-I. Pyun, Y.-G. Chun, "A critical evaluation of the stress-corrosion cracking mechanism in high-strength aluminium alloys", *Metall. Trans. A*, 22A, 1991, pp 2407-2414.

66 M.U. Islam, W. Wallace, "Retrogression and reaging response of 7475 aluminium alloy", Metals Technology, 10, 1983, pp 386-392.

67 K. Rajan, W. Wallace, J.C. Beddoes, "Microstructural study of a high strength stress-corrosion resistant 7075 aluminium alloy", *J. Mater. Sci.*, 17, 1982, pp 2817-2824.

68 N.C. Dahn, K. Rajan, W. Wallace, "A TEM study of microstrctural changes during retrogression and reaging in 7075 aluminum", *Metall. Trans. A*, 14A, 1983, pp 1843-1850.

69 K. Ural, "Study of optimization of heat-treatment conditions in retrogression and reageing treatment of 7075-T6 aluminium alloy", *J. Mater. Sci. Letters*, 13, 1994, pp.383-385.

70 J.F. Knott, *Fundamentals of fracture mechanics*, 1973, London, Butterworths.

71 J.R. Rice, "Limitations to the small scale yielding approximation for crack tip plasticity", *J. Mech. Phys. Solids*, 22, 1974, pp. 17-.

72 R.M. McMeeking, "Finite deformation analysis of crack-tip opening in elastic-plastic materials and implications for fracture", *J. Mech. Phys. Solids*, 25, 1977, pp. 357-.

73 R.H. Van Stone, J.A. Psioda, "Discussion of "Metallurgical Factors affecting Fracture Toughness of Aluminium Alloys"", *Metall. Trans. A*, 6, 1975, pp 668-670.

74 J.C. Ehrstrom, P. Achon, J.F. Hebert, A. Pineau, "Microstructural modelling of fracture toughness of Al alloys", *Mater. Sci. Forum*, 217-222, 1996, pp1539-1544.

75 G.T. Hahn, A.R. Rosenfield, "Sources of fracture toughness: the relation between Kic and the ordinary tensile properties of metals", *ASTM STP*, 432, 1968, pp 5-32.

References

76 G.G. Garrett, J.F. Knott, "The influence of Compositional and Microstructural Variations on the Mechanism of Static Fracture in Aluminium Alloys", *Metall. Trans. A*, 9, 1978, pp 1187-1201.

77 J.D. Embury, E. Ness, "On the tensile Fracture of Aluminium Alloys", *Z. Metallkd*, 65, 1974 , pp 45-55.

78 N.U. Deshpande, A.M. Gokhale, D.K. Denzer, John Liu, "Relationship Between Fracture Toughness, Fracture Path, and Microstructure of 7050 Aluminium Alloy: Part I. Quantitative Characterization", *Metall. Mater. Trans. A,* 29, 1998, pp 1191-1200.

79 E. Hornbogen, "On the grain size dependence of fracture toughness of precipitation hardened alloys", *Z. Metallkd.*, 66, 1975, pp 511-513.

80 E. Hornbogen, M. Graf, "Fracture Toughness of precipitation hardened alloys containing narrow soft zones at grain boundary", *Acta Metall.*, 25, 1977, pp 877-881.

81 A.M. Gokhale, N.U. Deshpande, D.K. Denzer, J. Liu, "Relationship Between Fracture Toughness, Fracture Path, and Microstructure of 7050 Aluminium Alloy: Part II. Multiple Micomechanisms-Based fracture Toughness Model", *Metall. Mater. Trans. A,* 29A, April 1998, pp 1203-1210.

82 M. Sugamata, C.P. Blankenship, Jr., E.A. Starke, Jr., "Predicting plane strain fracture toughness of Al-Li-Cu-Mg alloys", *Mater. Sci. Eng. A*, 163, 1993, pp 1-10.

83 H.J. Roven, "A model for fracture toughness predictions in aluminium alloys exhibiting the slip band decohesion mechanism", *Scripta Metall. Mater.* , 26, 1992, pp 1383-1388.

84 V.J. Griffin and P.G. Laye, "Differential Thermal Analysis and Differential Scanning Calorimetry", in *Thermal Analysis-Techniques and Applications,* Eds. E.L. Charsley and S.B. Warrington, Leeds Metropolitan University, 1984.

85 M.J. Starink, A.J. Hobson, P.J. Gregson, "DSC sample preparation for Al-based alloys", *Scripta Mater.*, 34, 1996, pp 1711-1716.

86 *Annual Book of ASTM standards*, vol. 3.01, E399-90, 1996.

87 *Aluminum and aluminum alloys*, ASM specialty handbook, Ed. J.R. Davis, USA, 1993.

References

88 X. Li, M.J. Starink, "Analysis of precipitation and dissolution in overaged 7xxx aluminium alloys using DSC", *Mater. Sci. Forum*, 331, 2000, pp 1071-1076

89 R. DeIasi, P.N. Adler, "Calorimetric studies of 7000 series aluminium alloys: I. Matrix precipitates characterisation of 7075", *Metall Trans. A*, 1977, pp 1177-1183.

90 M.J. Starink, D. Peskett and N. Kamp, unpublished research, University of Southampton, 2001.

91 J.M. Papazian, "Calorimetric studies of precipitation and dissolution kinetics in aluminium alloys 2219 and 7075", *Metall. Trans. A*, 13, 1982, pp 761-769.

92 X. Li, M.J. Starink, "Effect of compositional variations on characteristics of coarse intermetallic particles in overaged 7000 aluminium alloys", *Mater. Sci. Tech.*, 17, 2001, pp 1324-1328.

93 D.S. Park, S.W. Nam, "Effects of manganese dispersoid on the mechanical properties in Al-Zn-Mg alloys", *J. Mater. Sci.*, 30, 1995, pp 1313-1320.

94 J. Chang, I. Moon, C. Choi, "Evolution of microstructure and tensile strength of rapidly solidified Al-4.7 Pct Zn-2.5 Pct Mg-0.2 Pct Zr- X Wt Pct Mn Alloys", *Metall. Mater. Trans. A*, 29A, 1998, pp 1873-1882.

95 J.W. Hancock, M.J. Cowling, "Role of state of stress in crack tip failure processes", *Metal Sci.*, 1980, pp 293-304.

96 G.M. Ludtka, D.E Laughlin, "The influence of microstructure and strength on the fracture mode and toughness of 7xxx series aluminium alloys", *Metall. Trans. A*, 13A, 1982, pp 411-425.

97 E. Hornbogen, K.H. Zum Garh, "Distribution of plastic strain in alloys containing small particles", *Metallography*, 8, 1975, pp 181-202.

98 N.O. Kong, S.W. Nam, "Investigation of growth mechanism and orientation relationship of Mn-dispersoid in an Al-Zn-Mg-Mn alloy", *Mater. Letter*, 28, 1996, pp 385-391.

99 M.J. Starink, "The phase diagram of Al-Zn-Mg-Cu at about 440-490°C", *unpublished research*, University of Southampton, 1999.

100 M.F. Ashby, in *Strengthening methods in crystals*, ed. A. Kelly and R.B. Nicholson, Elsevier, Amsterdam, The Netherlands, 1971, pp 137-192.

References

101 H.S. Carslaw, J.C. Jaeger, "Conduction of heat in solids", 2nd ed., Oxford univ. press, 1986.

102 H.R. Shercliff, M.F. Ashby, "A process model for age hardening of aluminium alloys", *Acta Metall. Mater.*, 38, 1990, pp 1789-1812.

103 M.F. Ashby, "Physical modelling of materials problems", *Mater. Sci. Tech.*, 8, 1992, pp 102-111.

104 O.R. Myhr, O. Grong, S.J. Andersen, "Modelling of the age hardening behaviour of Al-Mg-Si", *Acta Mater.*, 49, 2001, pp 65-75.

105 H.R. Shercliff, M.F. Ashby, "Modelling thermal processing of aluminium alloys", *Mater. Sci. Tech.*, 7, 1991, pp 85-88.

106 B. Dubost, J. Bouvaist, "Process for thermal treatment of thin 7000 series aluminium alloys and products obtained", *US patent 4189334*, 1980.

107 B. Dubost, J. Bouvaist, "Process for the thermal treatment of thick products made of copper containing aluminium alloys of the 7000 series", *US patent 4200476*, 1980.

108 M.J. Starink, "A new method for the derivation of activation energies from experiments performed at constant heating rate", *Thermochimica Acta*, 288, 1996, pp 97-104.

109 M.J. Starink, "On the applicability of isoconversion methods for obtaining the activation energy of reactions within a temperature-dependent equilibrium state", *J. Mater. Sci.*, 32, 1997, pp 6505-6512.

110 J.K. Park, A.J. Ardell, "Correlation between microstructure and calorimetric behavior of aluminium alloy 7075 and Al-Zn-Mg alloys in various temper", *Mater. Sci. Eng. A*, 114, 1989, pp.197-203.

111 M.J. Starink, A.M. Zahra, "Determination of the transformation exponent s from experiment at constant heating rate", *Thermochim. Acta*, 298, 1997, pp 179-189.